ISSN 1344-6320

PHOTON FACTORY ACTIVITY REPORT

1999

PART A

HIGH LIGHTS
AND
FACILITY REPORT

#17

High Energy Accelerator Research Organization, KEK

KEK Progress Report 2000-1
November 2000
A/M

KEK Reports are available from:

Information Resources Division
High Energy Accelerator Research Organization (KEK)
1-1 Oho, Tsukuba-shi,
Ibaraki-ken, 305-0801
JAPAN

Phone : (81)-298-64-5137
Fax : (81)-298-64-4604
Internet: http://www.kek.jp

Photon Factory Activity Report

1999

Staff members and visitors of the Photon Factory

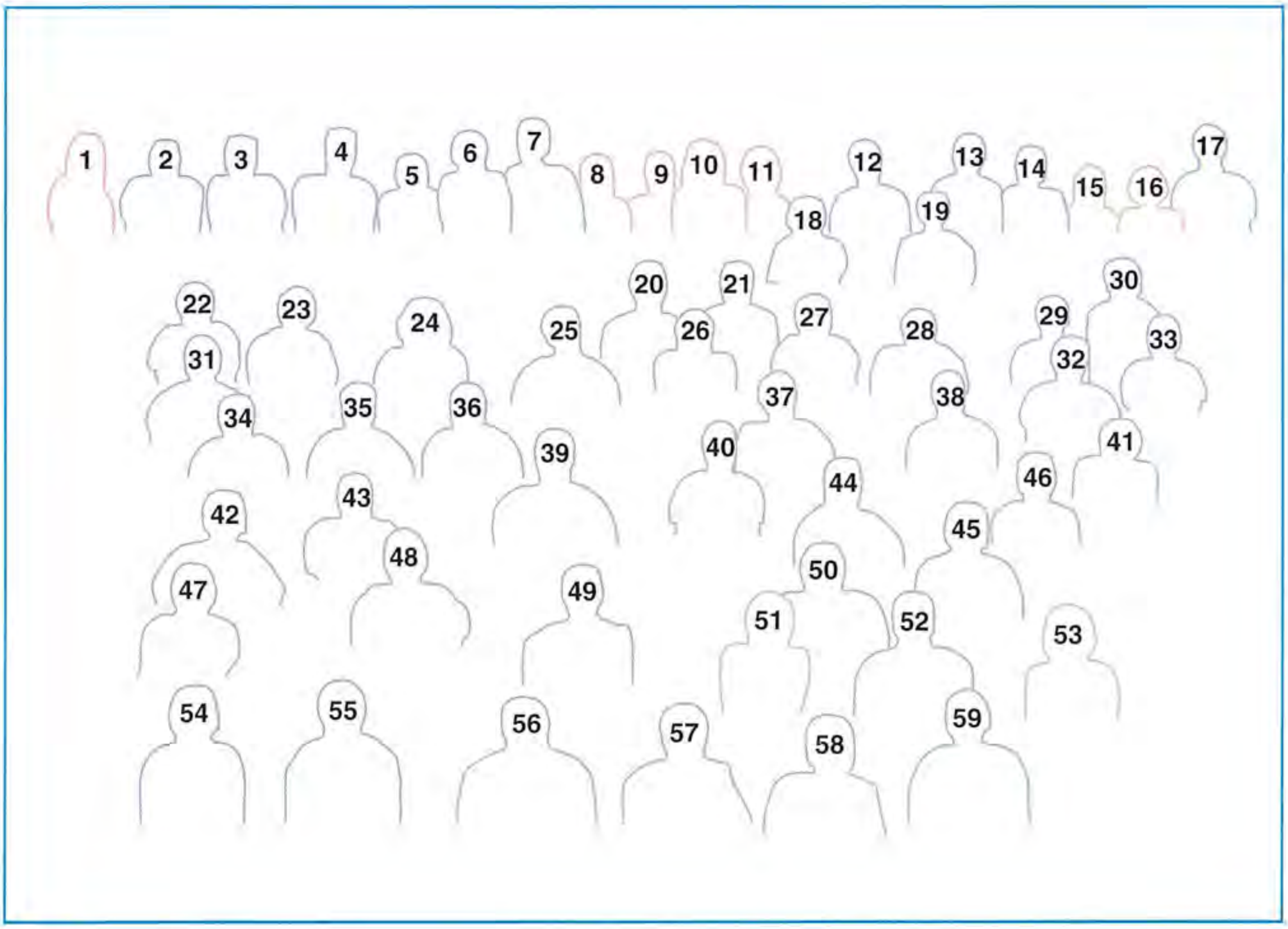

1. Y. Takahashi
2. Y. Miyata
3. M. Tanaka
4. A. Yagishita
5. K. Ito
6. S. Yamamoto
7. A. Mishina
8. S. Takano
9. S. Isoyama
10. A. Kikuchi
11. H. Furubayashi
12. T. Kurihara
13. H. Kawata
14. N. Tomita
15. H. Toyama
16. K. Kojo
17. Y. Kitajima
18. Y. Tanimoto
19. M. Nomura
20. K. Tsuchiya
21. T. Uchiyama
22. S. Kishimoto
23. A. Ueda
24. J. Sternberg
25. Y. Azuma
26. Y. Hori
27. T. Takahashi
28. T. Nogami
29. T. Aoto
30. T. Miyajima
31. K. Kobayashi
32. H. Yoshii
33. K. Isari
34. A. Iida
35. J. Adachi
36. J. Harris
37. K. Ono
38. C.-O. Pak
39. N. Igarashi
40. T. Honda
41. H. Mizouchi
42. H. Nakao
43. T. Saitoh
44. M. Kubota
45. Y. Saito
46. H. Ohsumi
47. T. Kikegawa
48. H. Kamikubo
49. K. Nasu
50. T. Kosuge
51. F. Mori
52. Y. Murakami
53. N. Usami
54. K. Ishii
55. M. Kobayashi
56. K. Ohsumi
57. Y. Kimura
    (Director of IMSS)
58. T. Matsushita
59. A. Kakizaki

You can jump to the article by clicking its title.

CONTENTS

INTRODUCTION

HIGHLIGHTS

EXPERIMENTAL FACILITIES

CONTENTS

ACCELERATORS OPERATIONS, RESEARCH AND DEVELOPMENTS

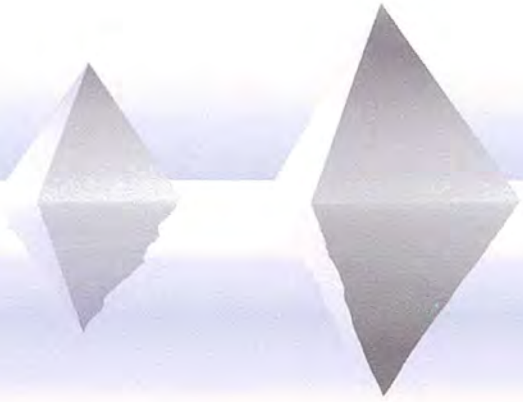

Introduction

In fiscal 1999(April 1999 - March 2000), operation of the Photon Factory facility was carried out remarkably well by recording the longest operational hours in the history of the Photon Factory both for the 2.5 GeV and 6.5 GeV rings.

The total operational hours of the 2.5GeV ring logged 5264 hours (219 days), providing users with synchrotron beam time of 4248 hours(177 days) The initial current of the 2.5 GeV ring has been increased up to 450 mA since October, 1999. The life time of the electron beam was improved to 50 hours from 25 hours by a small phase modulation on an rf accelerating voltage as described in ACCELERATORS section.


Tadashi Matsushita

Operation of PF-AR(6.5 GeV electron storage ring) was much improved compared with that in the previous year. The total operational hours was 4064 hours at the end of March, 2000. However, the lifetime of the electron beam has still been only 2.5 hours at 40mA. For improving the electron beam life time, an additional budget from the government was approved in November 1999 to replace the vacuum system of the ring. Many vacuum components are now being manufactured by industries, and complete replacement of the vacuum system will start in February 2001. Commissioning of the ring with the new vacuum system will start in autumn of 2001.

A possibility of increasing number of straight sections of the 2.5 GeV ring was discussed in the Photon Factory symposium(PF users meeting) in December 1999. According to the proposal, 7 additional straight sections for insertion devices will be created in addition to existing 7 straight sections by replacing quadrupole and sextupole magnets with thinner ones and placing those closer to neighboring bending magnets. During FY 2000, more detailed and extended study will be made to prepare an official proposal.

In recent years, competition for the beam time allocation is much harder on insertion device beamlines(6 beamlines on 2.5 GeV ring and 2 on 6.5 GeV ring) than on bending magnet beamlines. The Photon Factory is seeking possibilities and will make every effort to construct new insertion device beamlines both on 2.5 GeV and 6.5 GeV rings. A new insertion device beamline for protein crystallography/X-ray absorption spectroscopy has been designed for installation in the existing north building of PF-AR and many beamline components have been ordered. Installation of those beamline components will start in February 2001. If construction of the north-west building of PF-AR is approved and realized, two more insertion device beamlines will be constructed.

Bending magnet beamlines are still very important and useful resources for many basic and applied researches. With an emittance of 36 nm-rad and an initial beam current of 450 mA of the 2.5 GeV ring, the Photon Factory bending magnet beamlines are able to offer comparable brightness of radiation with bending magnet beamlines on third generation synchrotron sources. Continued efforts have been made in improving existing bending magnet beamlines as described in EXPERIMENTAL FACILITIES section. The BL-9A for XAFS spectroscopy is now equipped with two bent conical mirrors before and after a double-crystal monochromator and provides 8 times more intensity with a better energy resolution than obtained by optics having conventional double-crystal monochromator plus a bent cylinder mirror. This kind of optics will be also very efficient if installed on multipole wiggler beamlines. The beamline 7A, build and operated by the Research Center for Spectrochemistry of University of Tokyo, is being upgraded by preparing new optics. Installation of new optical components and commissioning will occur in summer and fall of 2000, respectively. The second CCD based two dimensional X-ray detector was commissioned on BL-18B for data collection of protein crystal diffraction. Together with BL-6A, we now have two stations equipped with CCD detectors, which play complimentary roles with imaging plate system. Data collection on those two stations(BL-6A and 18B) is now automated and load on protein crystallography users are greatly reduced. New experimental systems such as a multi anvil cell system for the structural study under high temperature and high pressure(BL-14C2) and a diffractometer for the structural study under high pressure/low temperature(BL-1B) were commissioned and are now used routinely.

In HIGHLIGHTS section, typical examples of experimental results are presented, which are distributed in wide spectrum of research disciplines. Such diversity makes it somewhat difficult to summarize highlights. However, we find in-situ measurements or quick feed back of experimental results to next beam time assignment is one of key factors in many of those experiments. The Photon Factory will extend its support to such areas in addition to its efforts in delivering stable and intense photon beams.

T. Matsushita

Tadashi Matsushita
Deputy Director

Activities of the Photon Factory Users Organization

Masaharu Oshima, The University of Tokyo

The Photon Factory Users Organization (PFUO) is a union for PF users. Every year we hold a Photon Factory Symposium at KEK. The 16th PF Symposium was held on March 11-12, 1999, and the 17th PF Symposium was held on December 21-22, 1999. The chairman for both symposia was Prof. Shunji Kishimoto. During these symposia, general meetings of the PFUO were held. At the 17th symposium, special discussions on Synchrotron Radiation(SR) dreams and future plans for the PF were held. User Group(UG) activities were reported, and the management of the PF, especially on the beam-time allocation, utilities and future plans, was discussed. Furthermore, during the Joint Symposium of the Japanese Society for Synchrotron Radiation Research with SR facilities and their users' organizations, an extended meeting for PFUO executive members was held on January 7, 2000, mainly to discuss the above mentioned agenda.

Masaharu Oshima

Several years ago, 14 UG, for example, XAFS, surface chemistry and protein crystallography, were organized for various scientific areas in the PFUO; these groups made enthusiastic efforts to convey the users requests and opinions to the PF. In 1999, two more user groups, namely the quantum nano-spectroscopy UG, and the nuclear resonance scattering UG were started. Now, 16 user groups are active in the PFUO. On January 19, 2000, a User Group Leaders Meeting was held to discuss how to manage or encourage UG activities, meetings, seminars, and so on.

Furthermore, PFUO has organized two seminars on SR sources and SR optics for users in 1999 and 2000.

In order to encourage the exchange of important information for users, PFUO set up its own home page in 1998, which has been updated frequently. Various discussions in meetings and on the web were organized and from time to time conveyed to KEK and IMSS. So far, PFUO has sent three letters to the Director of KEK and the Director of IMSS regarding Independent Administration Agency issue, the sudden change of the AR machine time, and improvements of the accommodation conditions of user lodges.

Regarding the third request, KEK responded promptly by repairing the facility and setting up a users' opinion box.

In order to maintain the best environment for SR science, we believe that PFUO should keep in close contact with the PF staff and frankly discuss current user issues together.

Aerial view of KEK

Site map of KEK

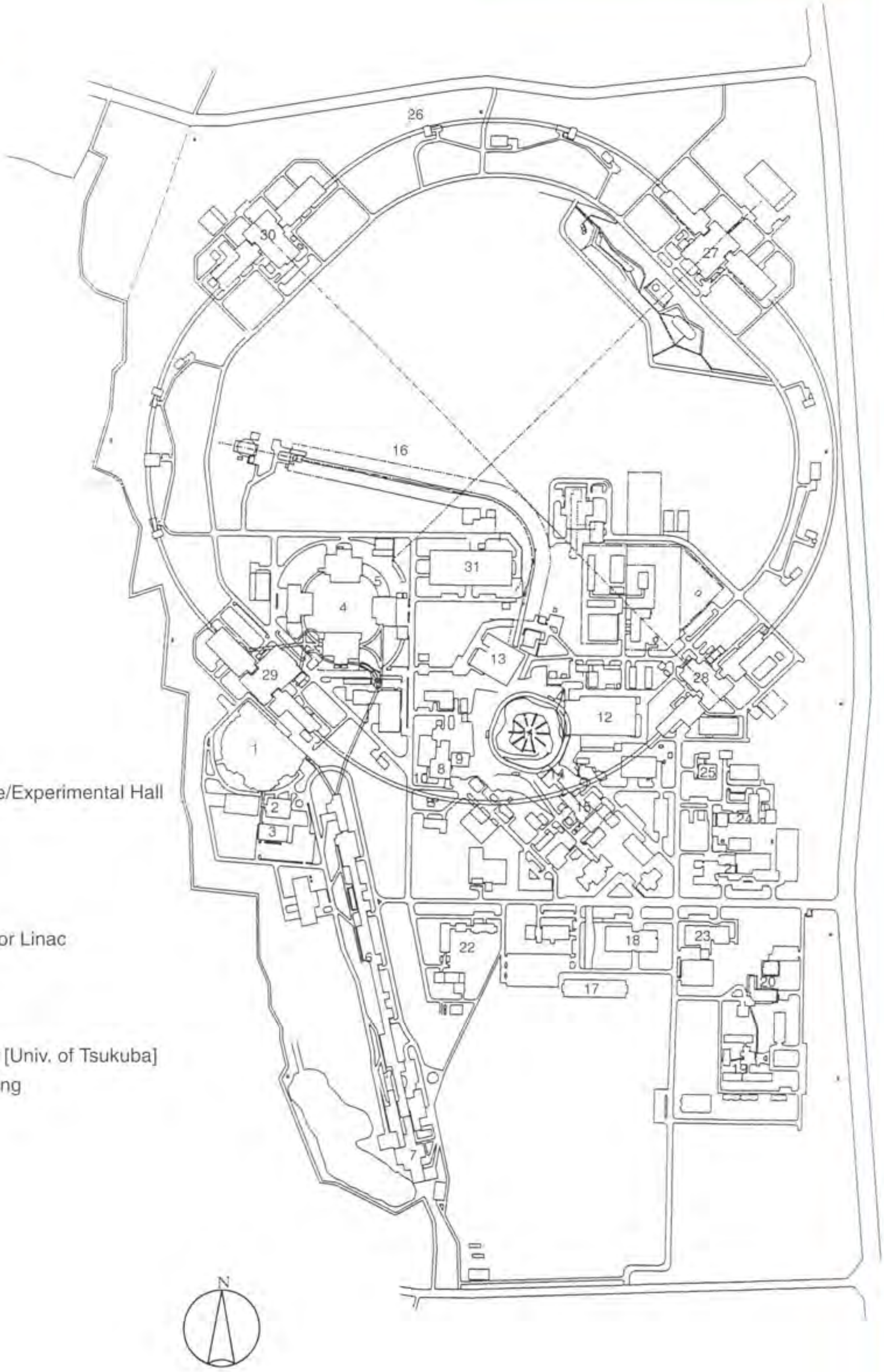

1. PF (Photon Factory) Light Source/Experimental Hall
2. PF Office Building
3. PF Preparation Laboratory
4. PF-AR (PF Advanced Ring)
5. PF-AR Experimental Hall
6. PF/KEKB (KEK B-Factory) Injector Linac
7. Slow Positron Facility
8. Neutron Science Laboratory
9. Meson Science Laboratory
10. Proton Medical Research Center [Univ. of Tsukuba]
11. PS (Proton Synchrotron) Main Ring
12. PS East Experimental Hall
13. PS North Experimental Hall
14. PS Booster
15. PS Injector Linac
16. Neutrino Beamline
17. Building No.4 (IMSS Office)
18. Libray/Users Office
19. Dormitory/Guest House
20. Restaurant/Cafeteria
21. Administration Building
22. Radiation Science Center
23. Computing Research Center
24. Cryogenics Science Center
25. Mechanical Engineering Center
26. KEKB LER (Low Energy Ring) and HER (High Energy Ring)
27. KEKB Tsukuba Laboratory (BELLE Detector)
28. KEKB Oho Laboratory
29. KEKB Fuji Laboratory
30. KEKB Nikko Laboratory
31. ATF (Accelerator Test Facility)

Members of Board of Councilors

AWAYA, Yoko	Musashino Art University
CHIKAWA, Jun-ichi	CAST Hyogo
FUJIMORI, Hiroyasu	The Research Institute for Electric and Magnetic Materials
FUKUYAMA, Hidetoshi	The Institute for Solid State Physics, The University of Tokyo
GOHSHI, Yohichi	National Institute for Environmental Studies
HIROTA, Eiji	The Graduate University of Advanced Studies
ITO, Mitsuo	Okazaki National Research Institute
KAMITSUBO, Hiromichi	The Institute of Physical and Chemical Research
KITAHARA, Yasuo	University of Tsukuba
KURODA, Haruo**	The Science University of Tokyo
KYOGOKU, Yoshimasa	Fukui University of Technology
NAGAOKA, Yosuke*	Kansai University
OGIUE, Koichi	Tokyo Metropolitan University
SAHARA, Makoto	National Museum of Japanese History
SASAKI, Kazuo	Okazaki National Research Institute
SUGANO, Takuo	Toyo University
TAKAYANAGI, Kazuo	The University of Tokyo
TAKEDA, Yasutsugu	Hitachi Corporation
YAMADA, Yasusada	Waseda University
YASUOKA, Hiroshi	Japan Atomic Energy Research Institute

Members of Advisory Council for Scientific Policy & Management

ARAI, Masatoshi	Neutron Science Lab., IMSS
ENDO, Yasuo	Tohoku University
FUJII, Yasuhiko	The University of Tokyo
GO, Nobuhiro	Kyoto University
IIDA, Atsuo	Photon Factory , IMSS
IKEDA, Susumu	Neutron Science Lab., IMSS
KOBAYASHI, Masanori	Photon Factory, IMSS
KUROKAWA, Shinichi	Accelerator Lab., KEK
MATSUSHITA, Tadashi**	Photon Factory, IMSS
NAGAMINE, Kanetada	Meson Science Lab., IMSS
NISHIDA, Nobuhiko	Tokyo Institute &Technology
OHSUMI, Kazumasa	Photon Factory , IMSS
OHTA, Toshiaki	The University of Tokyo
OSHIMA, Masaharu	The University of Tokyo
SHIBATA, Tokushi	Applied Research Lab., KEK
SUEMATSU, Hiroyoshi*	The University of Tokyo
TAKATA, Koji	Accelerator Lab., KEK
TSUJI, Kazuhiko	Keio University
TSUKIHARA, Tomitake	Osaka University
YAGISHITA, Akira	Photon Factory , IMSS
YOSHIWARA, Keitaro	Japan Advanced Institute of Science & Technology

** Chairman * Vice-Chairman

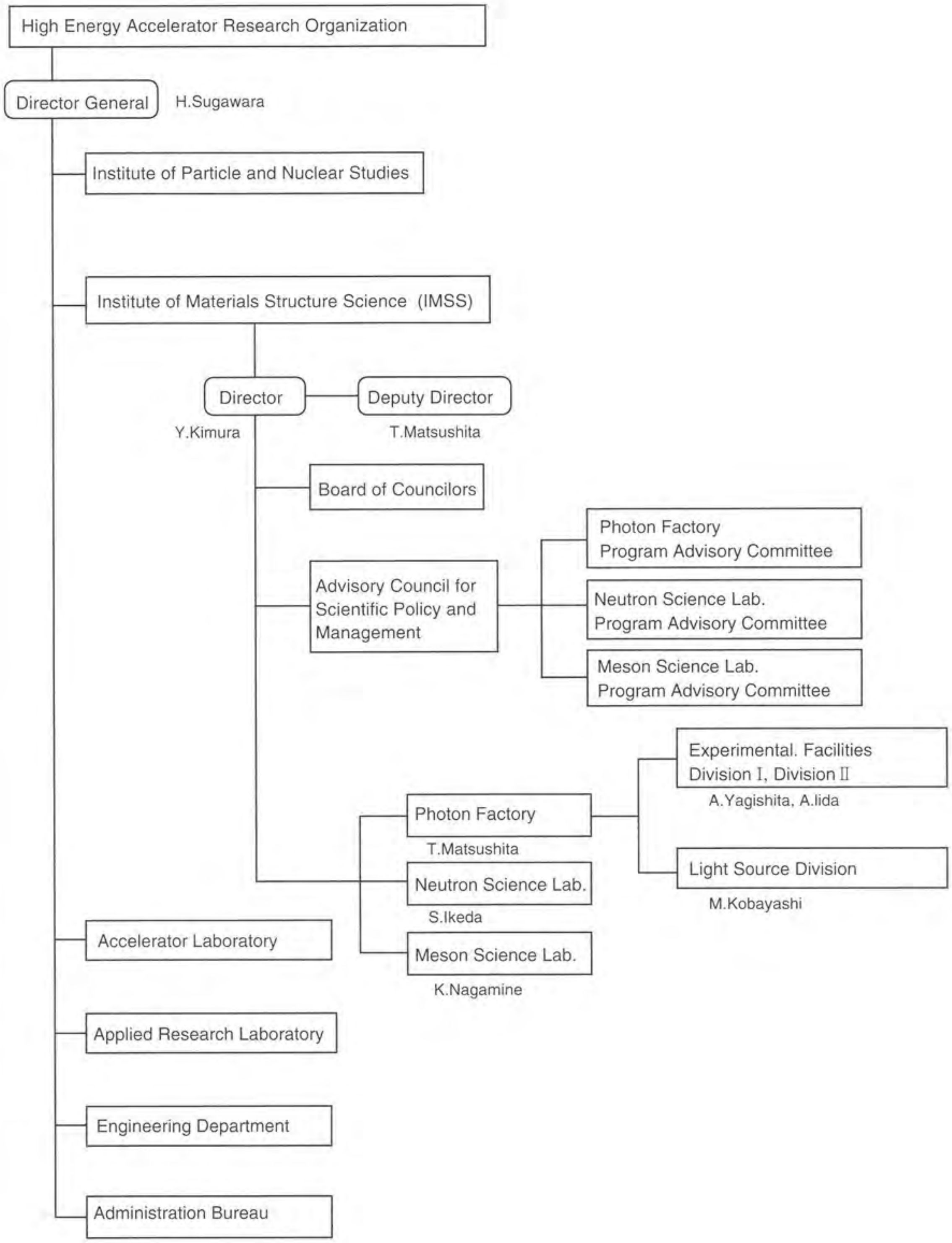
High Energy Accelerator Research Organization
Director General
H.Sugawara
Institute of Particle and Nuclear Studies
Institute of Materials Structure Science (IMSS)
Director
Y.Kimura
Deputy Director
T.Matsushita
Board of Councilors
Advisory Council for Scientific Policy and Management
Photon Factory Program Advisory Committee
Neutron Science Lab. Program Advisory Committee
Meson Science Lab. Program Advisory Committee
Photon Factory
T.Matsushita
Experimental. Facilities Division I, Division II
A.Yagishita, A.Iida
Light Source Division
M.Kobayashi
Neutron Science Lab.
S.Ikeda
Meson Science Lab.
K.Nagamine
Accelerator Laboratory
Applied Research Laboratory
Engineering Department
Administration Bureau

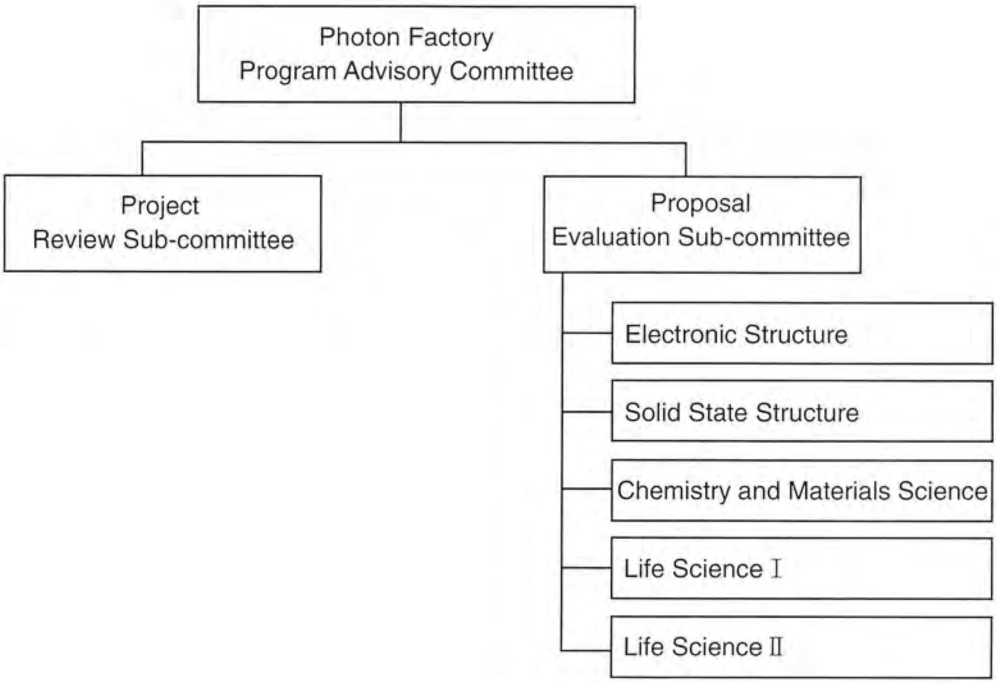
Photon Factory
Program Advisory Committee
Project
Review Sub-committee
Proposal
Evaluation Sub-committee
Electronic Structure
Solid State Structure
Chemistry and Materials Science
Life Science Ⅰ
Life Science Ⅱ

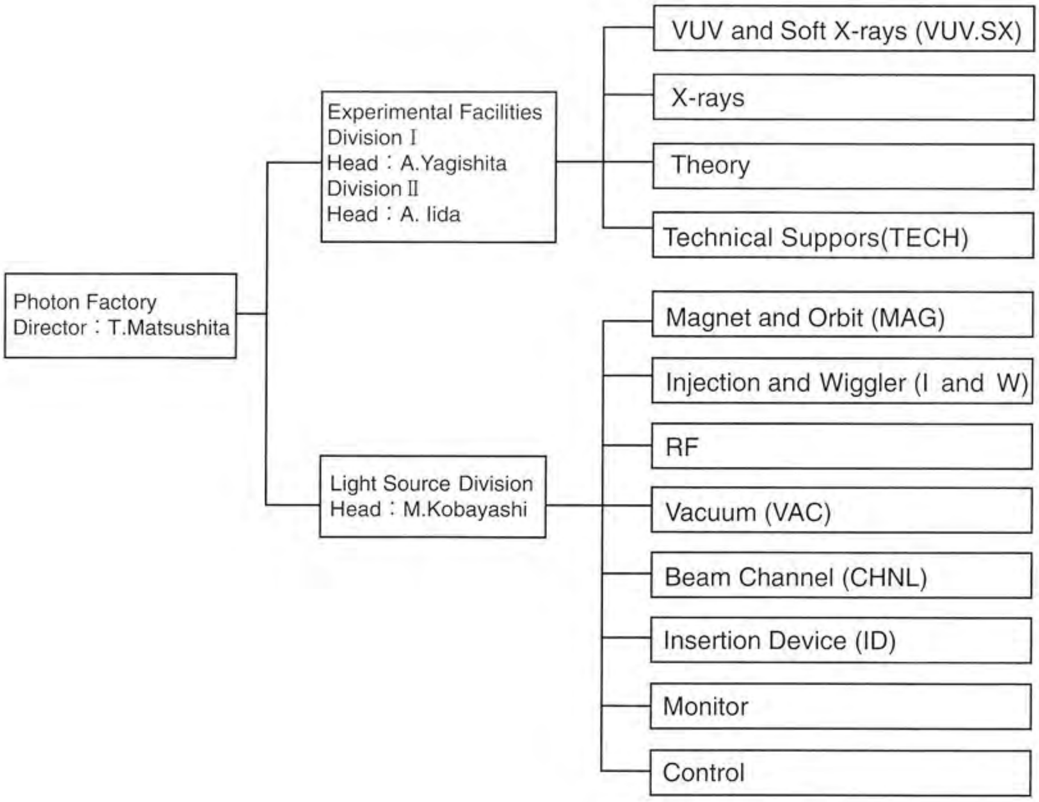
Photon Factory
Director：T.Matsushita
Experimental Facilities
Division Ⅰ
Head：A.Yagishita
Division Ⅱ
Head：A. Iida
Light Source Division
Head：M.Kobayashi
VUV and Soft X-rays (VUV.SX)
X-rays
Theory
Technical Suppors(TECH)
Magnet and Orbit (MAG)
Injection and Wiggler (I and W)
RF
Vacuum (VAC)
Beam Channel (CHNL)
Insertion Device (ID)
Monitor
Control

Staff members of the Photon Factory

Name	Responsibility	e-mail address
Research Staff		
MATSUSHITA, Tadashi	Director	tadashi.matsushita@kek.jp
Experimental Facilities Division I & II		
ADACHI, Hiromichi	X-rays	hiromichi.adachi@kek.jp
ADACHI, Junichi 1)	VUV-SX	adachij@post.kek.jp
ANDO, Masami	X-rays	masami.ando@kek.jp
AZUMA, Yoshiro	VUV-SX	yoshiro.azuma@kek.jp
HIRANO, Keiichi	X-rays	keiichi.hirano@kek.jp
HYODO, Kazuyuki	X-rays	kazuyuki.hyodo@kek.jp
IGARASHI, Noriyuki	X-rays	noriyuki.igarashi@kek.jp
IIDA, Atsuo	X-rays	atsuo.iida@kek.jp
ITO, Kenji	VUV-SX	kenji.ito@kek.jp
IWANO, Kaoru	Theory	iwano@nasuws1.kek.jp
IWAZUMI, Toshiaki	X-rays	toshiaki.iwazumi@kek.jp
KAKIZAKI, Akito	VUV-SX	akito.kakizaki@kek.jp
KAMIKUBO, Hironari	X-rays	hironari.kamikubo@kek.jp
KAWATA, Hiroshi	X-rays	hiroshi.kawata@kek.jp
KIKEGAWA, Takumi	X-rays	takumi.kikegawa@kek.jp
KISHIMOTO, Shunji	X-rays	syunji.kishimoto@kek.jp
KITAJIMA, Yoshinori	X-rays	yoshinori.kitajima@kek.jp
KOBAYASHI, Katsumi	X-rays	katsumi.kobayashi@kek.jp
KOIDE, Tsuneharu	VUV-SX	tsuneharu.koide@kek.jp
KURIHARA, Toshikazu	VUV-SX	toshikazu.kurihara@kek.jp
MASE, Kazuhiko 2)	VUV-SX	kazuhiko.mase@kek.jp
MURAKAMI, Youichi	X-rays	youichi.murakami@kek.jp
NAKAO, Hironori 2)	X-rays	hironori.nakao@kek.jp
NASU, Keiichiro	Theory	knasu@nasuws4.kek.jp
NOMURA, Masaharu	X-rays	masaharu.nomura@kek.jp
OHSUMI, Kazumasa	X-rays	kazumasa.ohsumi@kek.jp
SAITOH, Tomohiko	VUV-SX	tomohiko.saitoh@kek.jp
SHIGEMASA, Eiji 3)	VUV-SX	
SUGIYAMA, Hiroshi	X-rays	hiroshi.sugiyama@kek.jp
SUZUKI, Mamoru	X-rays	mamoru.suzuki@kek.jp
TANAKA, Masahiko	X-rays	masahiko.tanaka.pf@kek.jp
TOMITA, Norikazu	Theory	tomita@nasuws4.kek.jp
USAMI, Noriko	X-rays	noriko.usami@kek.jp
WATANABE, Masamitsu 4)	VUV-SX	
WATANABE, Nobuhisa 5)	X-rays	
YAGISHITA, Akira	VUV-SX	akira.yagishita@kek.jp
YAMAMOTO, Shigeru	X-rays	shigeru.yamamoto@kek.jp
ZHANG, Xiaowei	X-rays	zhang.xiaowei@kek.jp

Name	Responsibility	e-mail address
Light Source Division		
HAGA, Kaiichi	MONITOR	kaiichi.haga@kek.jp
HONDA, Tohru	MONITOR	tohru.honda@kek.jp
HORI, Yoichiro	VAC	yoichiro.hori@kek.jp
ISAWA, Masaaki	RF	masaaki.izawa@kek.jp
KANAYA, Noriichi 4)	CHNL	
KASUGA, Toshio	MAG	kasugat@post.kek.jp
KATOH, Masahiro 6)	MAG	
KATSURA, Tomotaro	MONITOR	tomotaro.katsura@kek.jp
KOBAYASHI, Masanori	VAC	masanori.kobayashi@kek.jp
KOBAYASHI, Yukinori	MAG	yukinori.kobayashi@kek.jp
MAEZAWA, Hideki	CHNL	hideki.maezawa@kek.jp
MITSUHASHI, Toshiyuki	I&W	toshiyuki.mitsuhashi@kek.jp
OBINA, Takashi	CONTROL	takashi.obina@kek.jp
OHMI, Kazuhito	I&W	ohmi@post.kek.jp
PAK, Cheol On	CONTROL	cheol-on.pak@kek.jp
SAKANAKA, Shogo	RF	shogo.sakanaka@kek.jp
TANIMOTO, Yasunori	VAC	yasunori.tanimoto@kek.jp
TSUCHIYA, Kimichika	ID	kimichika.tsuchiya@kek.jp
Technical Staff		
Experimental Facilities Division I & II		
KIKUCHI, Takashi	TECH	takashi.kikuchi@kek.jp
KOSUGE, Takashi	TECH	takashi.kosuge@kek.jp
KOYAMA, Atsushi	TECH	atsushi.koyama@kek.jp
MIKUNI, Akira	TECH	akira.mikuni@kek.jp
MORI, Takeharu	TECH	takeharu.mori@kek.jp
OKAMOTO, Wataru	TECH	wataru.okamoto@kek.jp
SAITO, Yuuki	TECH	yuuki.saito@kek.jp
SATOH, Masato	TECH	masato.satoh@kek.jp
TOYOSHIMA, Akio	TECH	akio.toyoshima@kek.jp
UCHIDA, Yoshinori	TECH	yoshinori.uchida@kek.jp
Light Source Division		
ASAOKA, Seiji	CHNL	seiji.asaoka@kek.jp
MISHINA, Atsushi	CONTROL	Atsushi.MISHINA@kek.ac.jp
MIYAJIMA, Tsukasa 2)	CHNL	tsukasa.miyajima@kek.jp
NOGAMI, Takashi	I&W	takashi.nogami@kek.jp
SATO, Yoshihiro	CONTROL	ysatopf@post.kek.jp
SHIOYA, Tatsuro	ID	tatsuro.shioya@kek.jp
TADANO, Mikito	MONITOR	mikito.tadano@kek.jp
TAKAHASHI, Takeshi	RF	takeshi.takahashi@kek.jp
UCHIYAMA, Takashi	VAC	takashi.uchiyama@kek.jp
UEDA, Akira	I&W	akira.ueda@kek.jp

Name	Responsibility	e-mail address
Guest Professor		
GO, Nobuhiro	(Kyoto Univ.)	
HYODO, Toshio	(The Univ. of Tokyo)	
ITOH, Masahisa	(Himeji Inst. of Tech.)	
KATAOKA, Mikio	(Nara Inst. Sci. Tech.)	
MIYAHARA, Tsuneaki	(Tokyo Metro. Univ.)	
OSHIMA, Masaharu	(The Univ. of Tokyo)	
SHIN, Shik	(The Univ. of Tokyo)	
TAKAHASHI, Toshio	(The Univ. of Tokyo)	
COE Staff		
AN, Ki-Seok [7]	VUV-SX	
HUANG, Ming-Tie [8]	VUV-SX	
KIYAMA, Takashi [2], [4]	X-rays	
MIZOUCHI, Hideo	Theory	mizouchi@nasuws4.kek.jp
SAITOW, Akihiro	X-rays	
SEKINE, Taketoshi [2]	VUV-SX	taketoshi.sekine@kek.jp
YOSHII, Hiroshi [2]	VUV-SX	yoshii@mail.kek.jp
The Graduate University for Advanced Studies		
HUAI, Ping		
MATSUMOTO, Isao		
NAKAJIMA, Hideki [2]		
RAHMAN Md. Obaidur		
TAKAHASHI, Yumiko		
YAMAZAKI, Masahiro		

---

[1] Oct. 1, '99 joined [2] Apr. 1, '99 joined [3] Apr. 30, '99 left [4] Mar. 31, 2000 left
[5] Sept. 30, '99 left [6] Feb. 29, 2000 left [7] July 31, 2000 left [8] June 22,'99 left

Highlights

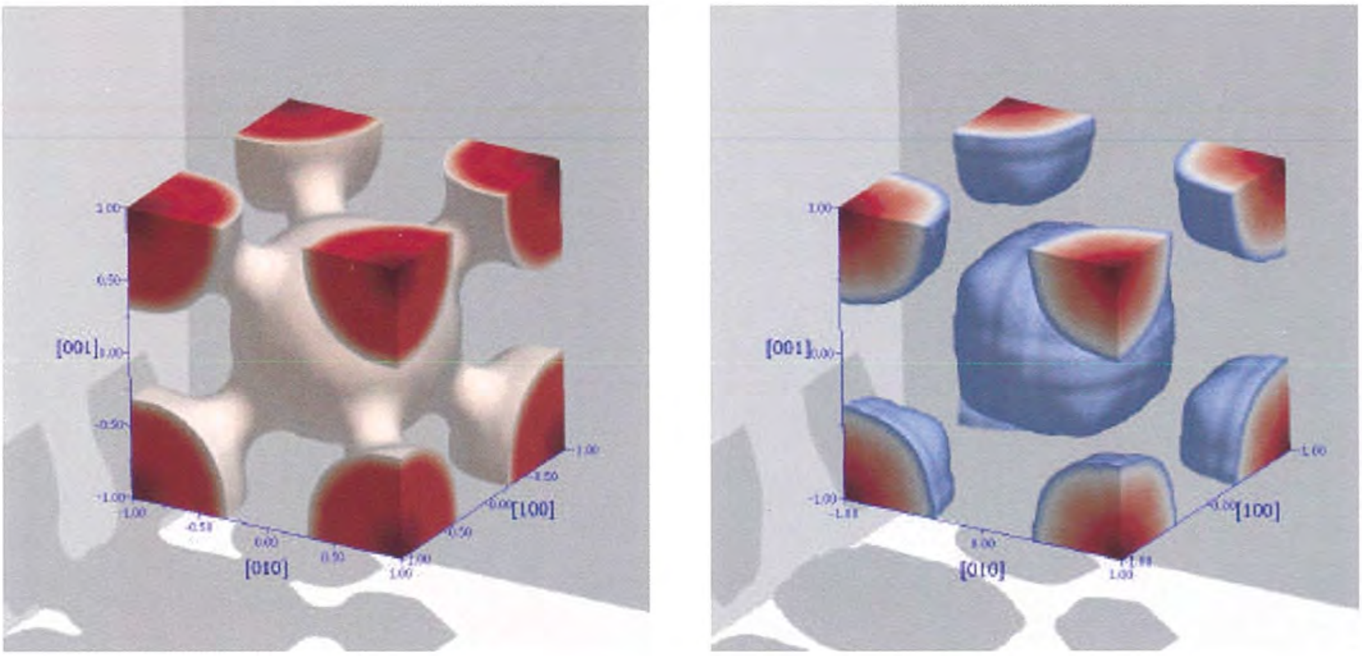

(a) pure Cu

(b) Cu -28at%Pd

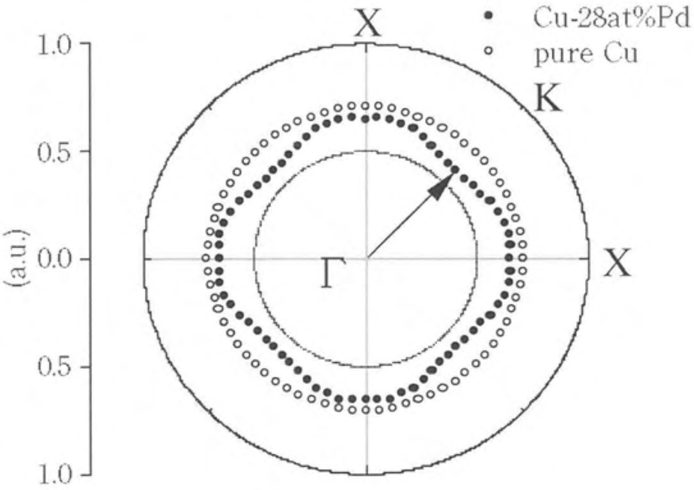

(c) (100) cross -section

Three-dimensional Fermi surface of pure Cu (a) and Cu-28at%Pd (b). (c) The Fermi surface on the (100) cross-section.

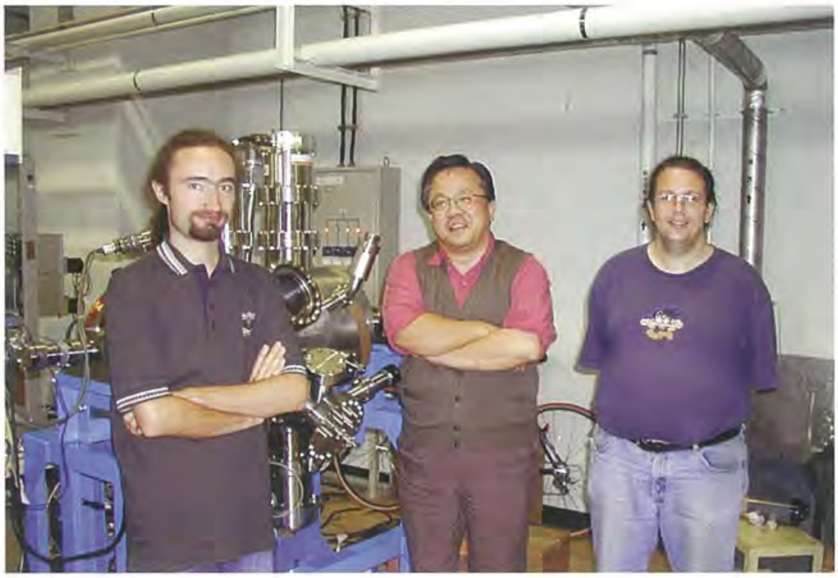

1

Atomic and Molecular Science

1 Atomic and Molecular Science

1-1 Decay Channels of Triply Photoexcited Lithium

The lowest triply excited state of the neutral Li atom, assigned as $2s^22p\ ^2P$, can decay either into a Li^+ ion by emitting one electron, or into a Li^{2+} ion by emitting two electrons. In the latter case, the decay proceeds through one-step double autoionization with the simultaneous ejection of two electrons since this $2s^22p\ ^2P$ state is located below the lowest doubly excited state of the singly charged Li ion, $2s^2\ ^1S$, and two step sequential electron emission processes are not possible. Wehlitz et al. have measured the photoion yield spectra for both Li^+ and Li^{2+} ion production over the photoexcitation resonance.

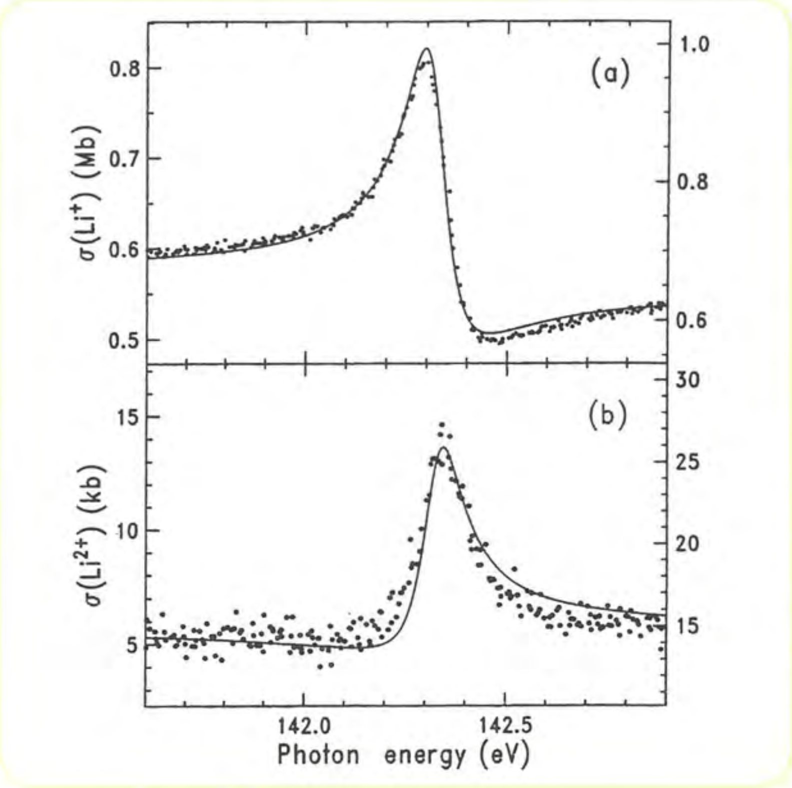

Figure 1.
Comparison experimental results with calculations. (a) Li^+ partial photoionization cross section; (b) Li^{2+} partial photoionization cross section.

Figure 1 shows their spectra compared with R-matrix calculations. The Li^+ spectrum exhibits the typical asymmetric Fano profile due to the interaction of the resonance with the one electron continuum. Although not as pronounced as in the Li^+ case, some asymmetry is also found in the Li^{2+} yield spectrum. This is an evidence of the importance of the correlation between the triply excited state and the two electron continua.

Reference
R. Wehlitz et al., Phys. Rev. A, 60 (1999) R17.

1-2 Electron-Electron Coincidence Spectroscopy of Kr Atoms

The 3d ionization of the Kr atom is embedded in the double and triple ionization continua and the 3d hole states decay into the various states of Kr^{2+} and Kr^{3+} ions through Auger decay. As the photoionization cross sections of the inner shells are much larger than those for direct double photoionzation, the inner-shell processes can be used to great advantage to study ionic states of doubly charged ions. The excess energy, (photon energy) - (state energy of the doubly charged ion), is shared by the two ejected electrons. When these two electrons are detected in coincidence, the spectral width of the energy spectrum of the electrons is determined solely by the band pass of the incident photons and the energy resolution of the electron spectrometers. This situation is common to both direct double photoinization and indirect double photoionization via Auger. In the latter case, the core hole states are intermediate states that one can look on as resonances in the double ionization continuum. Hikosaka et al. have built a new apparatus for electron-electron coincidence spectroscopy. One electron spectrometer is a, so-called, "threshold"

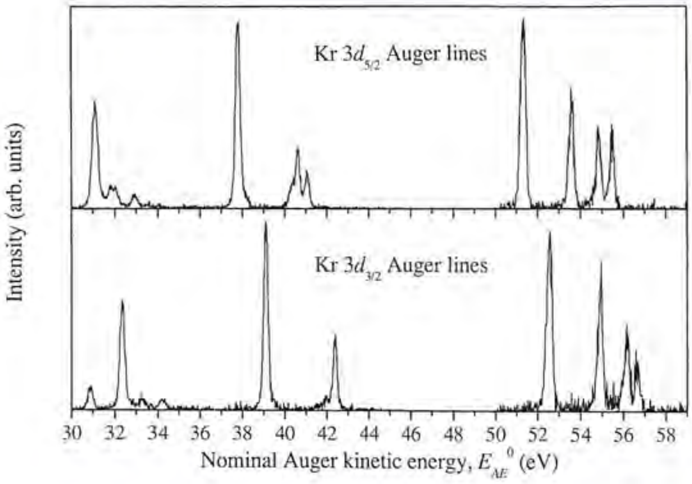

Figure 2.
Kr $M_4N_1M_{23}$, $M_4N_{23}N_{23}$ and $M_5N_1N_{23}$, $M_5N_{23}N_{23}$ "Auger electron spectra" measured in coincidence with the M_4 and M_5 "threshold photoelectrons."

electron spectrometer to detect zero-energy electrons with high efficiency and resolution, and the other is an electrostatic hemispherical analyzer that detects energetic electrons. Figure 2 shows the zero-energy electron, "photoelectron"- energetic electron, "Auger electron", coincidence spectra, which were measured at near the photon energies of the $3d_{5/2}$ and $3d_{3/2}$ thresholds. Compared to conventional normal Auger spectra, these coincidence spectra have two prominent features; first, the spectra from the initial $3d_{5/2}$ and $3d_{3/2}$ core hole states are perfectly separated and, second, the linewidths are free from lifetime broadening of the core hole states.

Reference
Y. Hikosaka et al., Measurements Sci.Tech., impress.

1-3 Dissociation of Rare Gas Dimers

The van der Waals interaction has been intensively studied by the photoionization of rare gas dimers. Figure 3 shows potential curves of the Xe_2^- ion. Yoshii et al. have observed 27 vibrational levels between the first and second dissociation limits of the Xe_2^+ ion in the threshold photoelectron specrum, and assigned this progression to the C_2 1/2 state of the Xe_2^- ion. They have measured the threshold photoelectron-photoion coincidence spectra between the first and second dissociation limits of the Xe_2^+ ion to elucidate the dissociation mechanism of the van der Waals molecule. Figure 4 shows the threshold photoelectron-photoion coincidence spectra taken at the Xe^+ $^2P_{1/2}$ threshold(a), at the v'=0 peak of the Xe_2^+ C_1 3/2 state(b), and at

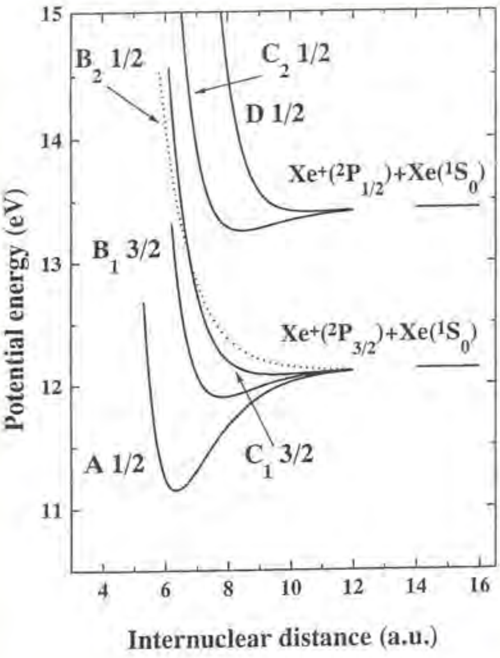

Figure 3.
Potential curves of the electronic states of Xe_2^-.

the v'=6 peak of the Xe_2^+ $C_2 1/2$ state(c). The sharp peaks in Figures 4 (a) and (b) correspond to the Xe^+ and Xe_2^+ ions, respectively. In contrast to these peak profiles, a very broad peak is observed in Figure 4 (c). It implies that the threshold electrons are mostly in coincident with the Xe^+ ions with appreciable kinetic energies. That is, the van der Waals Xe_2^+ ion of the $C_2 1/2$ state dissociates or predissociates, and produces a pair of fast Xe^+ and Xe.

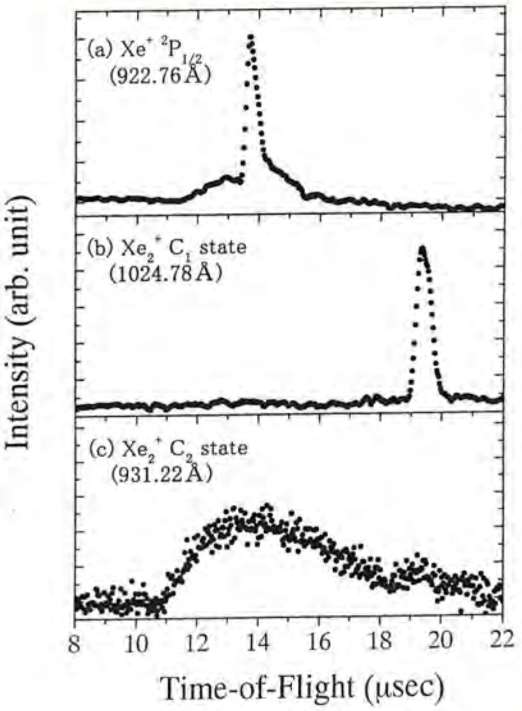

Figure 4.
Time-of-flight mass spectra in coincidence with threshold photoelectrons at photon energies of Xe^+ $^2P_{1/2}$ (a), Xe_2^+ $C_1 3/2$ (b), and Xe_2^+ $C_2 1/2$ (c). Figures (a) and (b) show sharp peaks, because atomic Xe^+ and dimer Xe_2^+ ions produced at the Xe^+ $^2P_{1/2}$ and Xe_2^+ $C_1 3/2$ thresholds have no kinetic enegy.

Reference
H. Yoshii et al. to be published.

1-4 Manifestation of Many-Electron Correlations in the K-Shell Photoionization of N_2 Molecule

One of the most interesting features of the K-shell photoabsorption specrta of diatomic molecules is a broad resonance above the ionization threshold, called a σ^* shape resonance, which does not exist in the corresponding atomic K-shell spectra. Dehmer and Dill interpreted the σ^* shape resonance as the $1s\sigma_g \rightarrow \varepsilon f\sigma_u$ single-channel enhancement based on single-electron multiple-scattering calculations. Also, this interpretation of the shape resonance has been widely accepeted for a long time. However, this situtation has recently been changed when the angular distributions of photoelectrons ejected from fixed-in-space N_2 molecules were measured at the Photon Factory. They contain much more information compared to the photoelectron angular distributions from randomly oriented N_2 molecules. Cherepkov et al. have performed calculations of the K-shell photoabsorption cross sections by a random phase approximation, which takes into account electron-electron correlations. Figure 5 shows their theoretical results. Surprisingly, it has been revealed that not only the $1s\sigma_g \rightarrow \varepsilon\sigma_u$ channel, but also the $1s\sigma_u \rightarrow \varepsilon\sigma_g$ channel is strongly enhanced in the the σ^* shape resonance region. This new finding has been explained by intershell interactions bewteen the $1s\sigma_g$ and $1s\sigma_u$ shells. To confirm their interpretation of the shape resonance, they have also calculated the angular distributions of the 1s photoelectrons from fixed-in-space N_2 molecules, and measured them. Comparisons between the theoretical and experimental results are shown in Figure 6. As can be seen from this figure, the contributions of the $1s\sigma_u \rightarrow \varepsilon\sigma_g$ channel to the σ^* shape resonance are certainly appreciable. This remarkable result is the first bench-mark investigation, which has pointed out the importance of the intershell interactions in the inner-shell molecular photoionization.

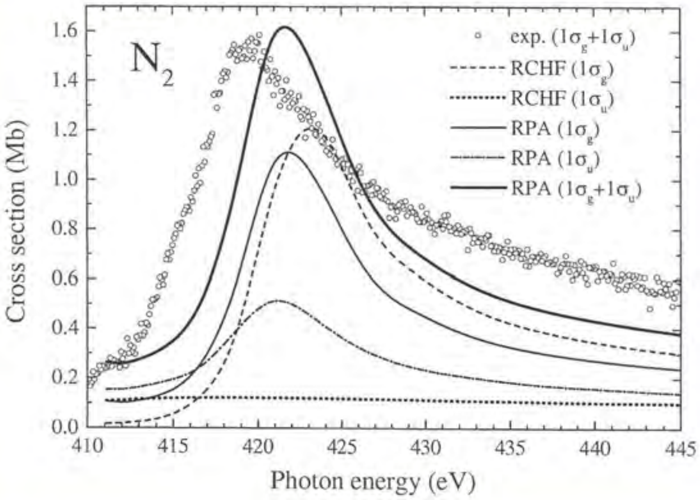

Figure 5.

Photoionization cross section for the K shell of a N_2 molecule, calculated using the relaxed-core Hartree-Fock and random-phase approximation.

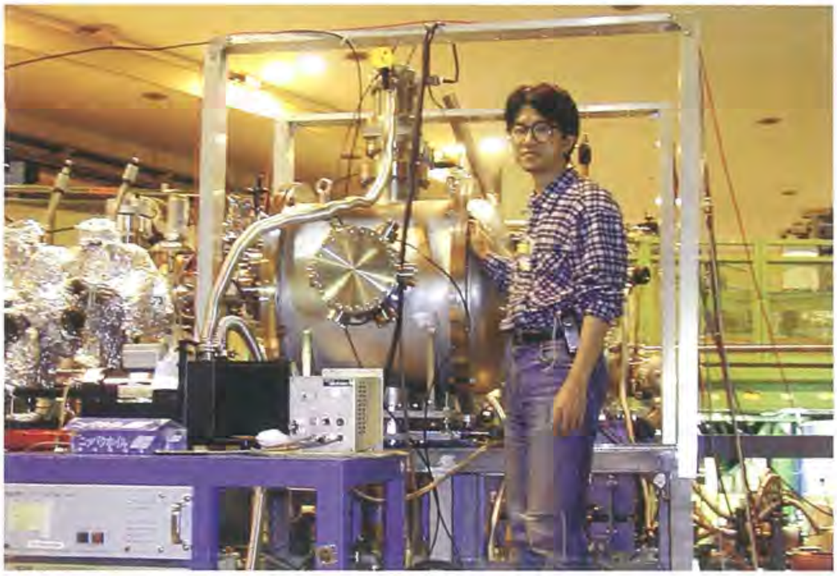

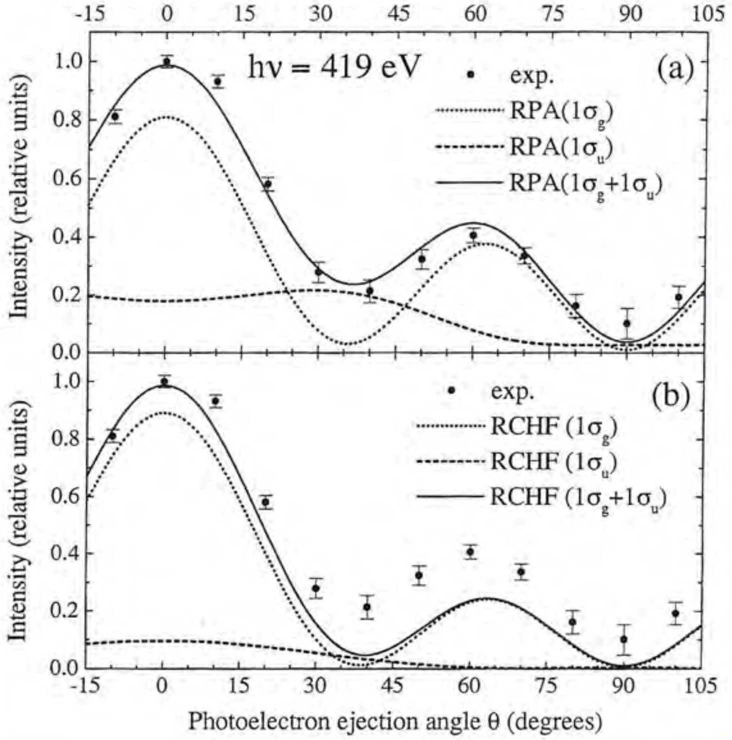

Figure 6.

Contributions of the $1\sigma_u \rightarrow \varepsilon\sigma_g$ and the $1\sigma_g \rightarrow \varepsilon\sigma_u$ channels to the photoelectron angular distributions in the random phase (a) and relaxed-core Hartree-Fock (b) approximations in the maximum of the σ^* shape resonance, compared with the experiment.

Reference

N. A. Cherepkov et al., Phys. Rev. Lett., 84 (2000) 250.

J. L. Dehmer and D. Dill, J. Chem.Phys., 65 (1976) 5327.

2 Chemistry

Many challenging investigations have been carried out using synchrotron radiation in the field of chemistry, which include catalysts, surface adsorbates, organic thin films, solutions and clusters. From among these studies, five topics are introduced in the following sections.

2-1 Site-Selective X-ray Absorption Fine Structure (XAFS) Spectroscopy Applied to a Cr/SiO$_2$ Catalyst

X-ray absorption fine structure (XAFS) spectroscopy is a powerful tool to clarify local geometric and electronic structures of catalysts. The information available in conventional XAFS, however, is limited to the average of the sites involved in the sample. Yasuo Izumi et al.

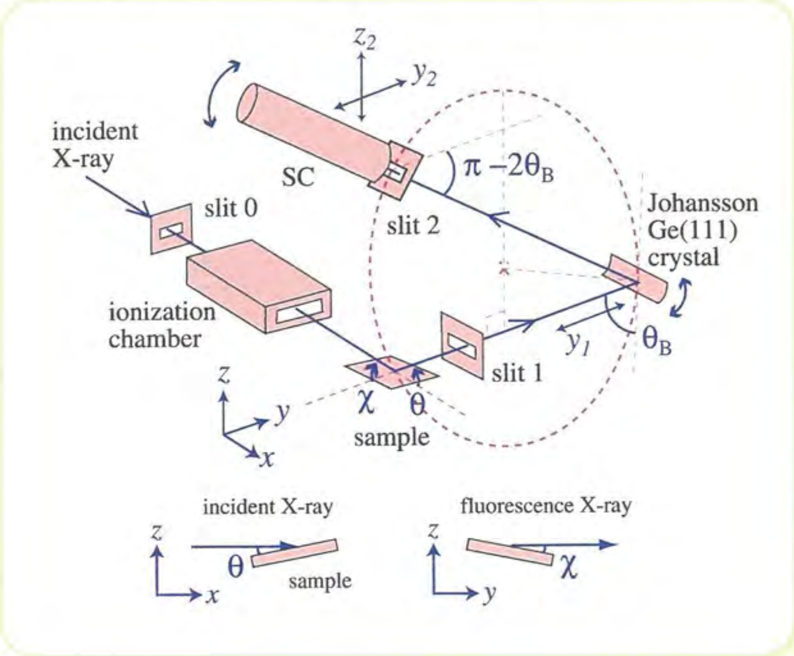

Figure 1.
Configuration of fluorescence spetrometer.

have developed a site-selective XAFS apparatus combined with a Rowland-type X-ray fluorescence spectrometer, as shown in Fig.1 [1]. They measured site-selective X-ray absorption near edge structure (XANES) spectra for chromium supported on silica (Cr/SiO_2) catalyst at BL-7C by taking advantage of the chemical shift in X-ray fluorescence [2]. Cr/SiO_2 is an important catalyst for the dehydrogenation of ethanol. The Cr/SiO_2 sample (Cr 15 wt%) was evacuated at 293 K and interacted with 10 kPa of ethanol at 373 K for 5 hours. A site-selective XANES spectrum was successfully measured by tuning the fluorescence spectrometer to Cr^{III} K β_1 ($h\nu$ = 5947.5 eV), as shown in Fig.2(a). By analyzing the correlation of the chemical shift between Cr^{III} and Cr^{VI} ($\Delta h\nu$ = 1.6 eV) and the X-ray fluorescence peak width, the contribution of the Cr^{III} site to the site-selective XANES was estimated to be 94±3%.

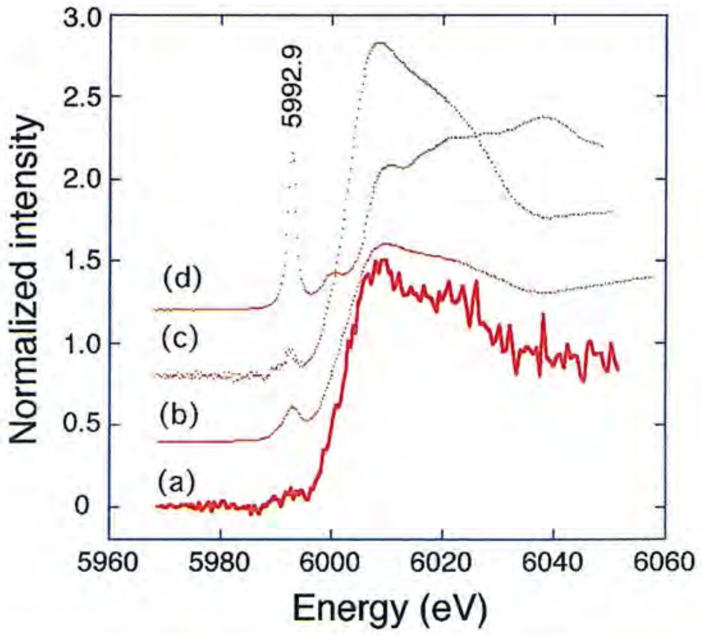

Figure 2.
(a) Site-selective XANES spectrum of Cr/SiO_2 catalyst by tuning the fluorescence spectrometer at 5947.5 eV corresponding to the Cr^{III} site. Conventional XANES spectra are also shown for (b) Cr/SiO_2, (c) Cr_2O_3 (Cr^{III}) and (d) K_2CrO_4.(Cr^{VI}). The Cr^{III} site-selective XANES of Cr/SiO_2 (a) resembles to the XANES of Cr_2O_3 (Cr^{III}) (c).

References

[1] Y. Izumi, H. Oyanagi and H. Nagamori, Bull. Chem. Soc. Jpn. 73 (2000) 2017.

[2] Y. Izumi and H. Nagamori, Bull. Chem. Soc. Jpn. 73 (2000) 1581.

2-2 In-Situ X-Ray Absorption Fine Structure (XAFS) Spectroscopy Applied for a Rhodium Catalyst under High-Temperature High-Pressure CO_2 Hydrogenation Conditions

In-situ X-ray absorption fine structure (XAFS) spectroscopy is an ideal technique to clarify the structure of active sites under reaction conditions, which is essential for designing better catalysts. However, in-situ experiments have scarcely been carried out so far due to problems in gas handling under sever reaction conditions. K.K. Situ Bando et al. managed to overcome these problems and measured in-situ XAFS spectra of a rhodium (Rh) catalyst under high-temperature high-pressure conditions at the BL-10B [1]. The rhodium catalyst was prepared by an ion-exchange method, replacing Na ions in NaY-type zeolite by Rh ions (RhY), which was found to exhibit a high activity in the hydrogenation of CO_2. During a pretreatment for CO_2 hydrogenation, the RhY catalyst was reduced under an atmospheric pressure with a flow of 20%H_2/Ar with increasing temperature from 286 K to 723 K. The XAFS spectra under the reduction conditions displayed a significant change, as shown in Fig.3, which indicates the generation of Rh metal clusters from Rh-O. After 30 min. of CO_2 hydrogenation at a pressure of 3 MPa with a flow of 25%CO_2/H_2 (100 ml/min.) at 523 K the peak intensity assigned to Rh-Rh scattering was observed to increased significantly in Fourier transformed extended XAFS (EXAFS). This change corresponded to an increase in the catalytic activity; the maximum activity of the RhY catalyst was observed after 30 min. of CO_2 hydrogenation. These results evidence an advantage of in-situ XAFS analyses over conventional ones in elucidating the structure of the active site responsible for the catalytic activity and selectivity.

Reference

[1] K.K. Bando et al., J. Synchrotron Rad., in press.

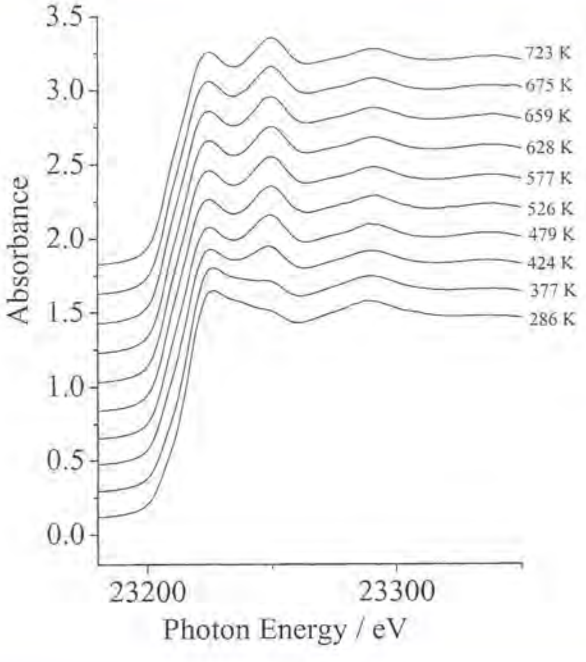

Figure 3.
In-situ XAFS spectra observed during H_2 reduction of a 5 wt% RhY catalyst.

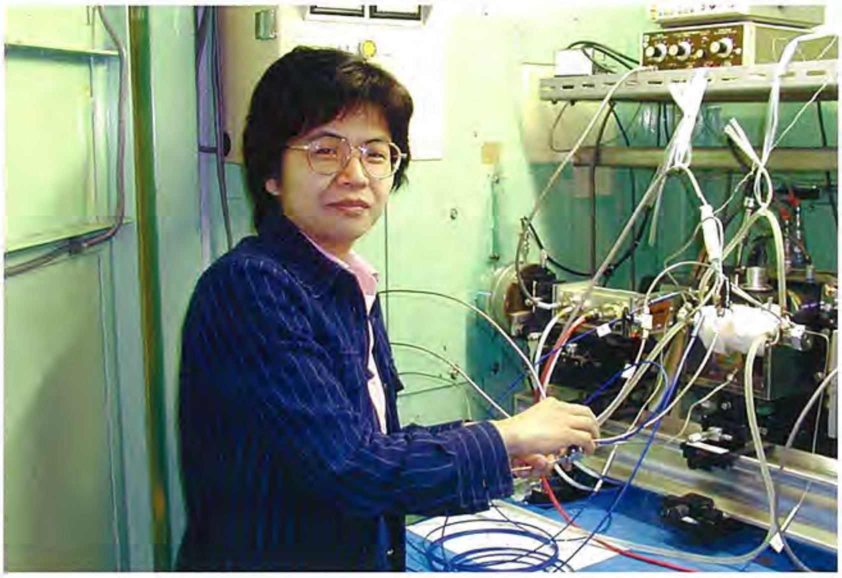

2-3 Anharmonicity in the Metal-Oxygen Bonding Potential for 3d Transition Metal Ions in Aqueous Solutions Studied by Extended X-Ray Absorption Fine Structure (EXAFS) Spectroscopy

Information on anharmonicity in the interatomic bonding potential can be obtained from the temperature dependence of the extended X-ray absorption fine structure (EXAFS) spectra. Takafumi Miyanaga et al. applied this method to aqueous solutions of 3d transition metal ions [1]. EXAFS spectra of aqueous solutions of Cr^{3+}, Fe^{3+}, Fe^{2+}, Ni^{2+}, Co^{2+} and Zn^{2+} (0.5-1.0 mol dm^{-3}) were measured for 20-80 ℃. Assuming Morse-type interatomic potentials, the dissociation energies of ligand water from metal ion have been evaluated based on the temperature dependence of the harmonic Debye-Waller factor and the anharmonic third-order cumulant. Assuming that ligand water-exchange reaction is dominated by a dissociation process, the dissociation energy was

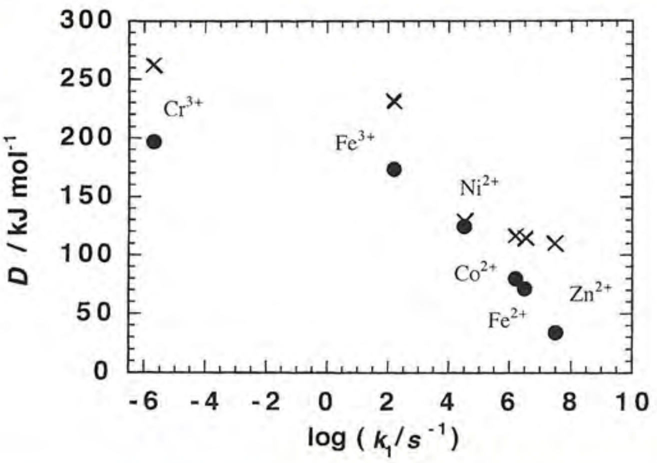

Figure 4.
Relation between the dissociation energy (D) evaluated from EXAFS (solid circles) and log k_1, where k_1 is the ligand exchange rate constant. The crosses represent the theoretical results by Akesson et al. [2].

considered to be equal to the activation energy of the water-exchange reaction. The deduced dissociation energies were found to correlate with those predicted by theory and with the experimental water-exchange rate constant as shown in Fig.4.

References

[1] T. Miyanaga et al., Phys. Chem. Chem. Phys. 2 (2000) 2361.
[2] R. Akesson et al., J. Am. Chem. Soc.116 (1994) 8705.

2-4 Reduction Process of Cu-ZSM-5 Catalyst Studied by Time-Resolved XAFS

Time-resolved measurements of the structural change of catalysts are essential to clarify the reaction mechanisms and to find preferable reaction conditions. For this purpose, Masaharu Nomura et al. have developed dispersive X-ray absorption fine structure (DXAFS) spectroscopy at the BL-9C. By using a bent silicon (111) crystal, a polychromatic X-ray beam was focused on a sample, and the diverging X-rays were detected by a position-sensitive X-ray detector consisting of a phosphor-coated fiber-plate and 1024 sensing elements photodiodes (0.025 mm wide, 2.5 mm high) (HAMAMATSU Photonics). A Pt-coated mirror was set between the sample and the detector to suppress higher order reflections. The energy range and resolution were 8800-9800 eV and 3-5 eV, respectively.

By using the DXAFS apparatus, Aritomo Yamaguchi et al. investigated the structural changes of Cu catalysts during temperature-programmed reduction [1]. The sample was prepared by an ion-exchange method, replacing H ions in HZSM-5 zeolite by Cu ions (Cu-ZSM-5). The Cu K-edge DXAFS spectra were recorded at an interval of 1 s in H_2 of 5.3 KPa at a heating rate of 5 K min^{-1} in the range from 300 K to 700 K. The analysis of the XAFS data revealed that the isolated Cu^{2+} species in the channels of zeolite were reduced stepwise, that is, $Cu^{2+} \rightarrow Cu^{+}$ at 400-450 K and $Cu^{+} \rightarrow Cu^{0}$ at 550-650 K. On the contrary, CuO particles on the outer surfaces were reduced directly to Cu^0 metallic particles at around 450 K. These results demonstrate that DXAFS is useful for monitoring the structural change of a catalyst during chemical reactions.

Reference

[1] A.Yamaguchi et al., Catal. Lett.68 (2000) 139.

2-5 Coulomb Explosion Following Core Excitations of Selenium Clusters Studied by Photoelectron Photoion Coincidence Spectroscopy

Clusters are attractive targets because they are considered to be intermediate states between atoms and condensed matter. Most X-ray absorption studies of clusters in the gas phase, however, so far have been limited to the soft X-ray region. Tetsuichiro Hayakawa et al. have studied the multiply charged ion formation of selenium clusters, Se_2 and "Se_5" (the mixture of Se_5 and small amounts of Se_6 and Se_7), in the Se K-edge region at the BL-12C by using photoelectron photoion coincidence (PEPICO) spectroscopy [1]. In the PEPICO spectra of Se_2, broad peaks corresponding to z/n = 1 to 7 were observed, as shown in Fig.5, where z and n represent numbers of charge and atom, respectively. Most of the peaks are split into asymmetric doublets. These results indicate that energetic Se^{z+} ions are produced by Coulomb explosion following cascade Auger processes after core excitations. The PEPICO peak widths were interpreted quantitatively by assuming the maximum charge before the Coulomb explosion is equal to 8. The difference in the branching ratios of Se_2 and "Se_5" was well reproduced by considering that the charges are randomly distributed within the clusters before the Coulomb explosion.

Reference

[1] T. Hayakawa et al., J. Phys. Soc. Jpn. 69 (2000) 2039.

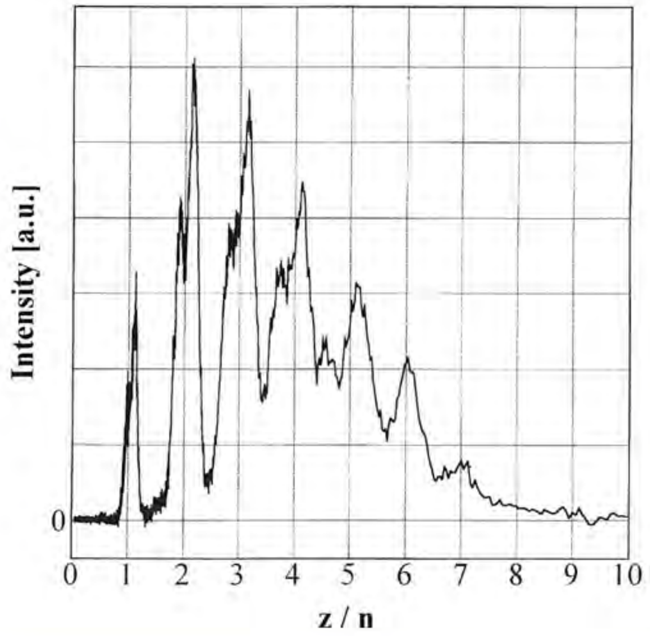

Figure 5.
PEPICO spectra of Se_2 at the photon energy of 12.68 keV, which is slightly higher than the 1s ionization potential, shown as a function of z/n.

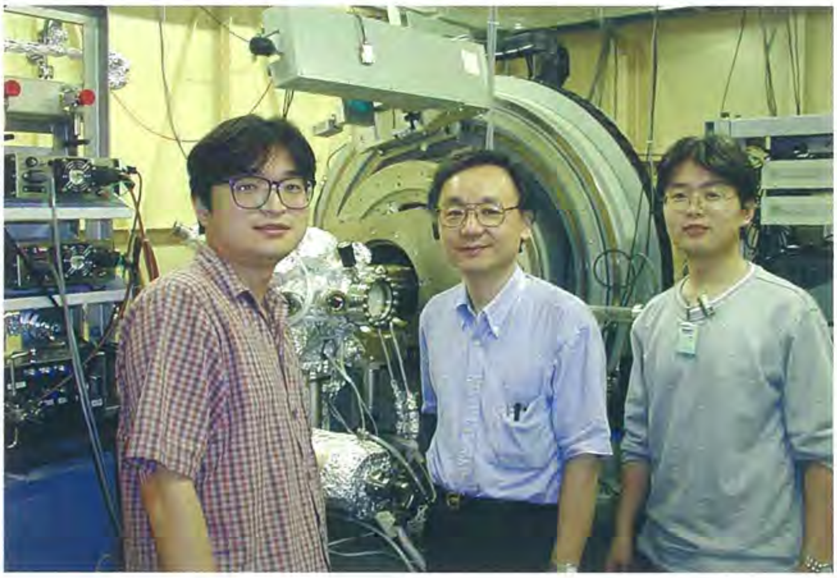

3 Surfaces and Interfaces

3-1 Pseudomorphic Growth of a Pd Monolayer on an Au(111) Electrode Surface

For studies on electrode-electrolyte interfaces, surface X-ray diffraction (SXD) is a unique technique, because it is not much influenced by the solution encapsulating the sample surface. Also, the penetrating feature of X-rays allows a determination of the crystallographic relationship between the overlayer and the substrate. Thus, SXD is complementary to electrochemical scanning probe microscopy, which is sensitive only to the outermost layer.

Takahasi et al. [1] have studied the surface structure of a Pd monolayer electrochemically deposited onto Au(111) by SXD. The specular rod profile is shown in Figure 1(a). According to convention, hexagonal coordinates with $a = [1/2,0,1/2]_{\mathrm{bulk}}$, $b = [-1/2,1/2,0]_{\mathrm{bulk}}$ and $c = [1,1,1]_{\mathrm{bulk}}$ are used. Compared with the profile for an ideally terminated Au(111) surface (dotted line), the observed intensity decreases remarkably between neighboring bulk Bragg peaks. This destructive interference effect results from a uniform Pd monolayer formed on Au(111). A least-squares fitting gives the calculated curve (solid line) corresponding to the Pd-Au interlayer spacing, 2.27 Å. The lateral adsorption site of Pd is ascertained by a measurement of the (01) rod shown in Fig.1(b). The observed profile agrees well with the adsorption to the cubic closest packing site (solid line). Other adsorption sites, such as the hexagonal closest packing site (dashed line) and the atop site (dot-dashed line), fail to reproduce the observation. The Pd-Au bond length was calculated to be 2.82 Å, which is close to the sum of the atomic radii of Pd and Au in each bulk.

It is noteworthy that such a pseudomorphic smooth Pd layer, as obtained by the electrochemical method, is not available in a vacuum.

The formation of a stable Pd layer in an electrolyte is ascribable to a lifting of the 23×√3 surface reconstruction of the Au substrate.

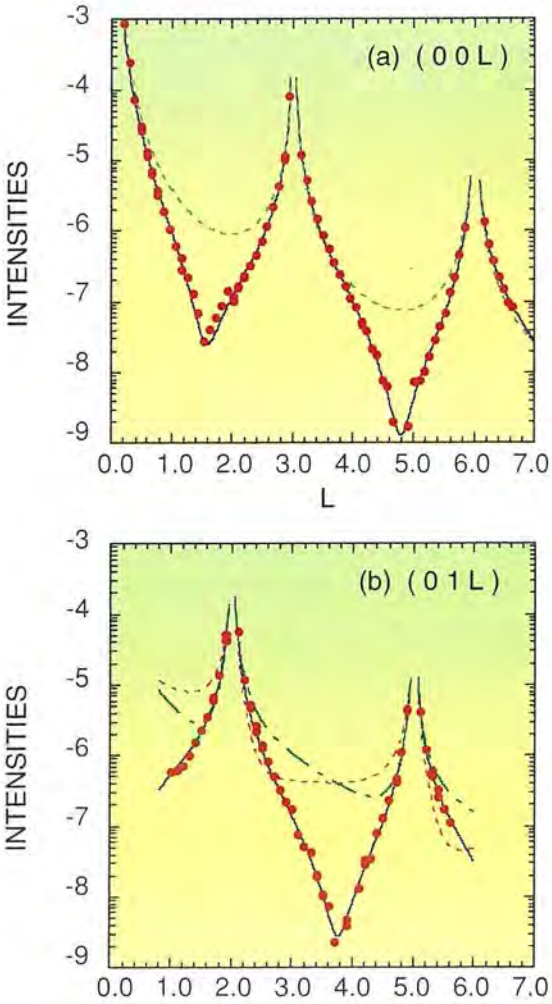

Figure 1.
Rod profiles obtained for the structure of Pd (1ML) / Au (111) : (a) 00 rod, and (b) 01 rod.

Reference

[1] M. Takahasi, Y. Hayashi, J. Mizuki, K. Tamura, T. Kondo, H. Naohara, and K. Uosaki, Surf. Sci., 461 (2000) 213.

3-2 Effect of Bragg Reflection on Surface X-ray Diffraction

Diffraction spots in SXD are observed in the directions where the Ewald sphere intersects with the reciprocal rods perpendicular to the surface, reflecting the two-dimensional periodicity of the crystal surface. Due to the weak interaction of X-rays with the crystal, the interactions among those rods can usually be neglected. However, when Bragg reflection is excited at one of the rods, the intensities of the diffraction spots on other rods are influenced by Bragg reflection.

Takahashi et al. [1] have measured the intensity change of the specular reflection from a Si(001) crystal under excitation of 555 Bragg reflection of the (05) rods, as shown in Fig.2 (a). Since the excited point is close to the 004 Bragg point in this experiment, the intensity change is not very sensitive to the structure of the monolayers, but is rather sensitive to a strain to near to the surface extending into a depth of a few hundreds of Å. The dotted curve, calculated for a model terminated by the ideal surface, well reproduces the experimental results, but differs slightly from them. A more-detailed analysis (the solid curve) indicates that the native oxide layer, about 30 Å in thickness, formed on the crystal surface generates a strain ranging to a depth of 310 Å with $\Delta d/d = 0.0005$, if we assume a model in which a uniform lattice distortion is produced by the oxide layer and is localized only near to the surface to a depth much smaller than the extinction distance of X-rays.

Yashiro et al. [2] have obtained the intensity change when a point far from the Bragg point on the specular rod was excited under the diffraction condition, as illustrated in Fig.2 (b). In this case, the profile of the intensity modulation becomes sensitive to the surface structure, and one can obtain not only the amplitude, but also the phase of the X-ray wave scattered by the native oxide layer on the crystal. This means that, in principle, one can obtain the structure of the native oxide layer model-independently by a Fourier Transform if one measures such intensity modulations at a number of points on the specluar rod by changing the wavelength.

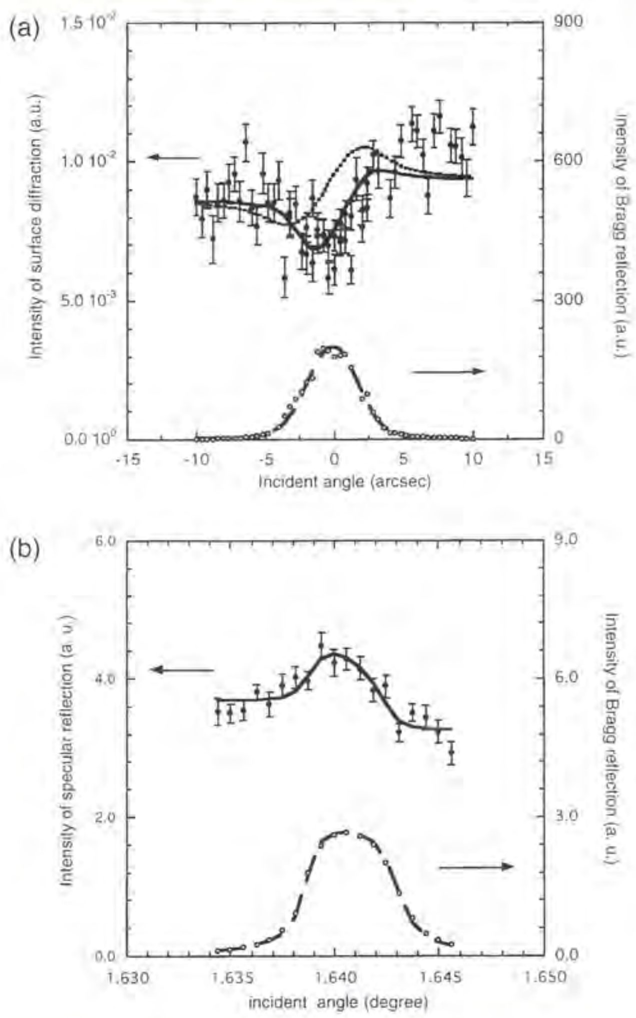

Figure 2.
Variations of CTR scattering as a function of incident angle under the Bragg condition obtained for Si(001) crystals with native oxide layers: CTR scattering (a) near 004 Bragg point and (b) near 000 point.

References

[1] T. Takahashi, W. Yashiro, M. Takahasi, S. Kusano, X.W. Zhang, and M. Ando: Phys. Rev. B 62 (2000) 3630.

[2] W. Yashiro, K. Shimizu, K. Hirano, and T. Takahashi: submitted to Phys. Rev. B.

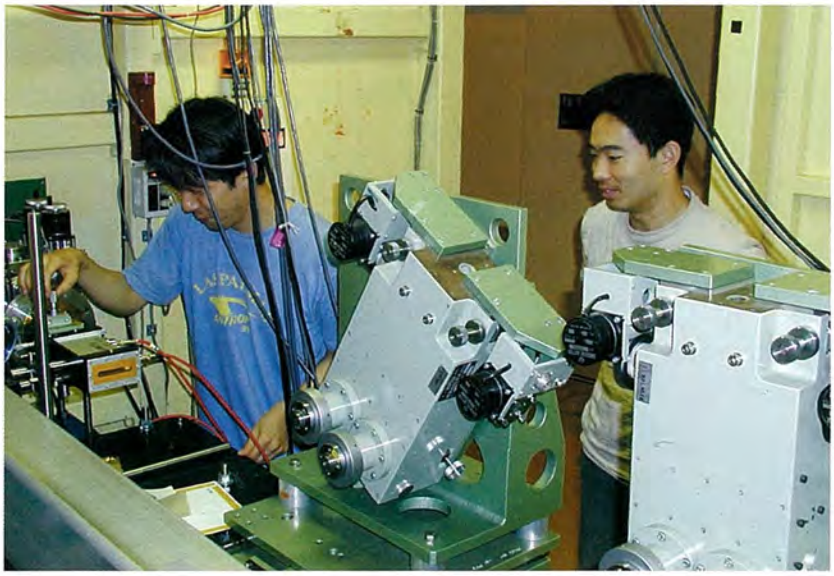

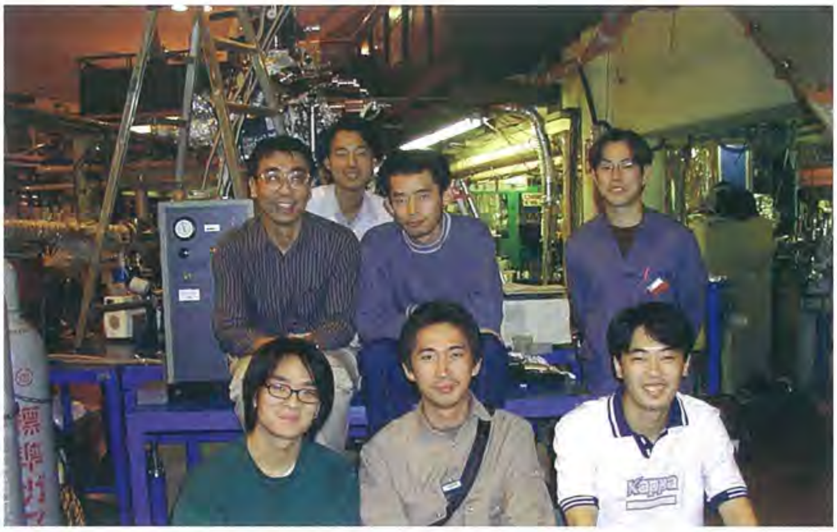

4

Electronic Structure of Condensed Matter

4 Electronic Structure of Condensed Matter

Investigations of the electronic structure of condensed matter have been one of the main topics of synchrotron-radiation science. So far, the developments of experimental techniques, such as magnetic circular dichroism, spin-resolved photoemission and photoelectron diffraction, as well as the preparation of new samples with interesting properties, have continuously brought this field new aspects. We present below two excellent experiments which have been carried out at the Photon Factory in the preceding years.

4-1 Observation of the Bonding Orbital between a C_{60} Molecule and the Dangling Bonds of Si Surfaces

The recent observation of epitaxial silicon carbide (SiC) formation by the thermal reaction of C_{60} molecules with Si(111)-(7×7) and Si(001)-(2×1) surfaces [1] has led to increased interest in the nature of the bond between C_{60} and Si surfaces. In order to determine the bonding nature, Sakamoto et al. have studied the coverage-dependent [2] and temperature-dependent electronic structures [3] of C_{60} molecules adsorbed on Si(111)-(7×7) and Si(001)-(2×1) surfaces.

Figure 1 (a) shows the coverage-dependent valence band spectra of a C_{60} adsorbed Si(111)-(7×7) surface. The spectral features at a coverage of 5.0 monolayer (ML) are the same as those of bulk C_{60}, in which C_{60} molecules interacted with the van der Waals force. The highest occupied molecular orbital (HOMO) and the second HOMO (HOMO+1) are observed at 2.0 and 3.3 eV, respectively. No difference is observed in the spectrum at 1.0 ML, indicating that most C_{60} molecules interact with the van der Waals force with the surface at this coverage. At a coverage of 0.25 ML, the full width at half-maximum (FWHM) of all molecular orbitals increases. Moreover, the HOMO seems to split into two peaks having binding energies of 1.8 and 2.4

eV. Taking into account the polarization dependence of the valence band spectra and the results of the Si 2p and C 1s core levels, it is found that the 2.4-eV peak is the covalent bonding state between a C_{60} molecule and the Si substrate, and that the 1.8-eV peak is a shifted HOMO. The bonding state was also observed between the C_{60} molecule and a Si(001)-(2×1) surface at a coverage lower than 0.25 ML, and after annealing the 1.0 ML C_{60} film adsorbed Si(111)-(7×7) and Si(001)-(2×1) surfaces at 500 K. The latter result suggests a change in the bonding nature at 500 K. Figure 1 (b), presents the energy-level scheme of the bonding state in terms of the symmetry of the HOMO.

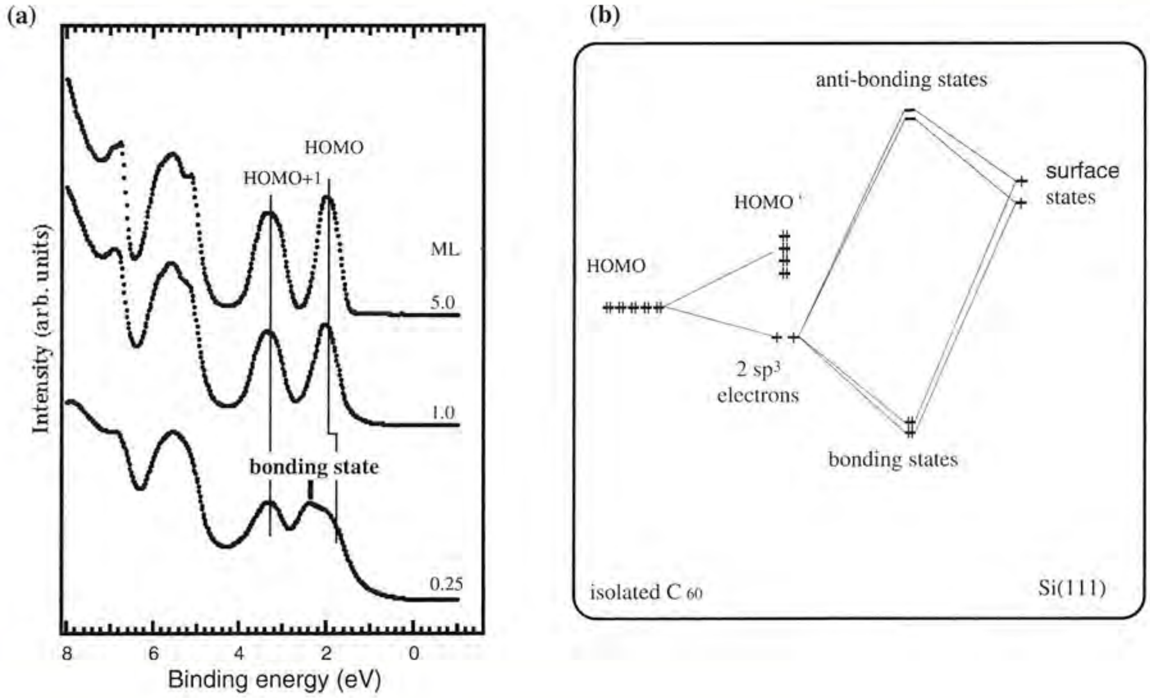

Figure 1.

(a) Coverage-dependent valence band spectra of the C_{60} adsorbed Si(111)-(7×7) surface measured with a photon energy of 21.2 eV.

(b) Schematic diagram of the energy levels for the adsorption of a C_{60} molecule on the Si(111)-(7×7) surface at a coverage lower than 0.25 ML.

References

[1] A.V. Hamza, M. Balooch, and M. Moalen, Surf. Sci. 317 (1994) L1129.

[2] K. Sakamoto, M. Harada, D. Kondo, A. Kimura, A. Kakizaki, and S. Suto, Phys. Rev. B 58 (1998) 13951.

[3] K. Sakamoto, D. Kondo, Y. Ushimi, M. Harada, A. Kimura, A. Kakizaki, and S. Suto, Phys. Rev. B 60 (1999) 2579.

4-2 Orbital Moments of Oxygen Atoms of CO Adsorbed on Ni/Cu(001) Films [1]

Perpendicular magnetic anisotropy (PMA) is one of the main subjects on magnetic thin films. Thin Ni films on Cu(001) are especially interesting, since the system shows two thickness-dependent phase transitions; in the thickness range of about 10-50 ML the Ni films exhibit PMA. The adsorption of H and CO on Ni/Cu(001) is also interesting. It was found that H and CO adsorption further stabilizes PMA; the magnetization easy axis of Ni film with 7-11 ML thickness is changed from the surface parallel to the surface normal upon adsorption [2].

In order to understand the adsorption effect on PMA, Yokoyama et al. measured the O *K*-edge XMCD (X-ray magnetic circular dichroism) spectra at the BL-11A for CO on Ni/Cu(001) by varying the Ni thickness. Figure 2 shows the O *K*-edge spectra of CO adsorbed on 6 ML, 10 ML, and very thick Ni films. The most striking observations should be different signs of the XMCD signals appearing at the $2\pi^*$ transitions. In the in-planar magnetization cases of 6 ML and very thick films, small positive peaks were detected, while in the 10 ML Ni film (PMA) a strong negative feature was observed. In the perpendicular magnetization case, the observed negative XMCD

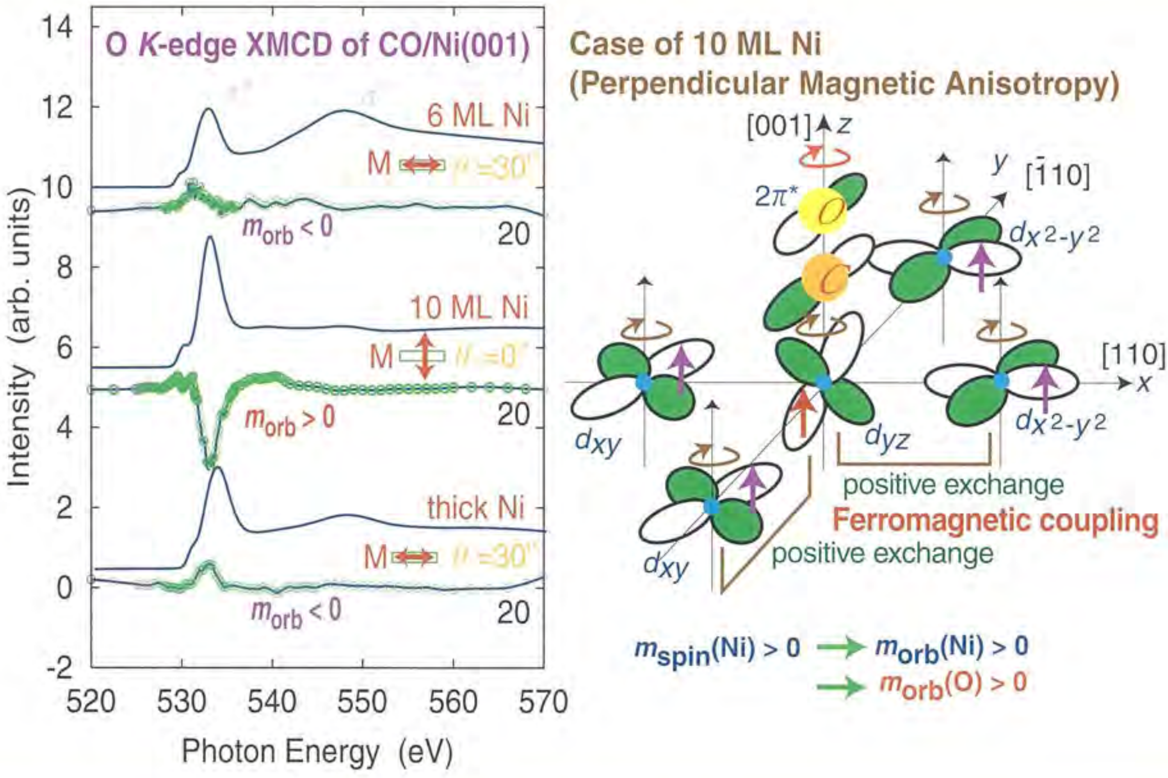

Figure 2.
(Left) O *K*-edge XMCD spectra of CO on 6 ML, 10 ML, very thick Ni films on Cu(001) and (Right) interpretation of the ferromagnetic coupling between the O orbital moment and the substrate magnetization.

signal indicates a positive orbital moment, which implies ferromagnetic coupling between the O orbital moment and the total magnetization. On the contrary, the positive XMCD signs observed in the in-planar magnetization indicate negative orbital moments at the O atoms and antiferromagnetic coupling. The antiferromagnetic coupling in the latter case is consistent with their previous observation on CO/Co/Cu(001) (in-plane magnetization) [3].

In the case of the 10 ML Ni film (PMA), the CO $2\pi^*$ orbital is hybridized with the $3d_{yz}$ orbital of the surface Ni atom, as shown in Fig. 2. The orbital moments of the surrounding surface Ni atoms originate from a pair of $3d_{xy}$ and $3d_{x^2-y^2}$. Since the symmetry of the $3d_{yz}$-$2\pi^*$ hybridized orbital is different from those of $3d_{xy}$ and $3d_{x^2-y^2}$ of the surrounding Ni atoms, the hybridized orbital forms no chemical bonding with those orbitals, leading to a positive exchange interaction. The spin and, thus, the orbital moments of the hybridized orbital are consequently coupled ferromagnetically with the total Ni magnetization. In the case of in-planar magnetization, the present results should indicate that CO-adsorbed Ni atoms also show antiferromagnetic coupling with the total magnetization, though the detailed interpretation may be more complicated.

The present XMCD measurements allow us to obtain more detailed information about the chemical-bonding picture between adsorbates and substrates, including magnetic interactions.

References

[1] T. Yokoyama, K. Amemiya, M. Miyachi, Y. Yonamoto, D. Matsumura and T. Ohta, Phys. Rev. B in press.

[2] R. Vollmer, Th. Gutjahr-Löser, J. Kirschner, S. van Dijken and B. Poelsema, Phys. Rev. B60, 6277 (1999).

[3] K. Amemiya, T. Yokoyama, Y. Yonamoto, M. Miyachi, Y. Kitajima, and T. Ohta, Jpn. J. Appl. Phys. Exp. Lett. 39, L63 (2000).

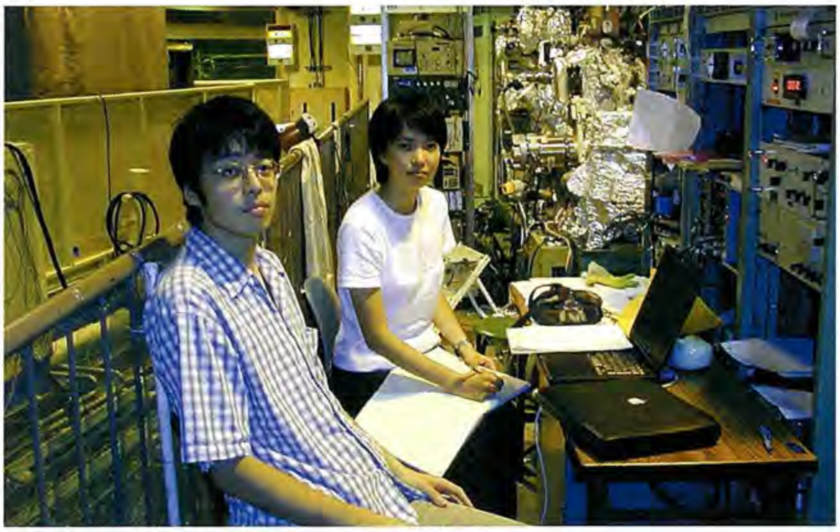

5 Materials Science

5-1 Direct Observation of Antiferroquadrupole Ordering; Resonant X-Ray Scattering Study of DyB_2C_2

Antiferroquadrupolar (AFQ) ordering has been conjectured in several rare-earth compounds to explain their anomalous magnetic properties. No direct evidence for AFQ ordering, however, has been reported. Using the resonant X-ray scattering technique near to the Dy L_{III} absorption edge with a six-axis diffractometer at the BL-16A2, K.Hirota and his group have succeeded in observing the AFQ order parameter in DyB_2C_2 and analyzing the energy and polarization dependence [1].

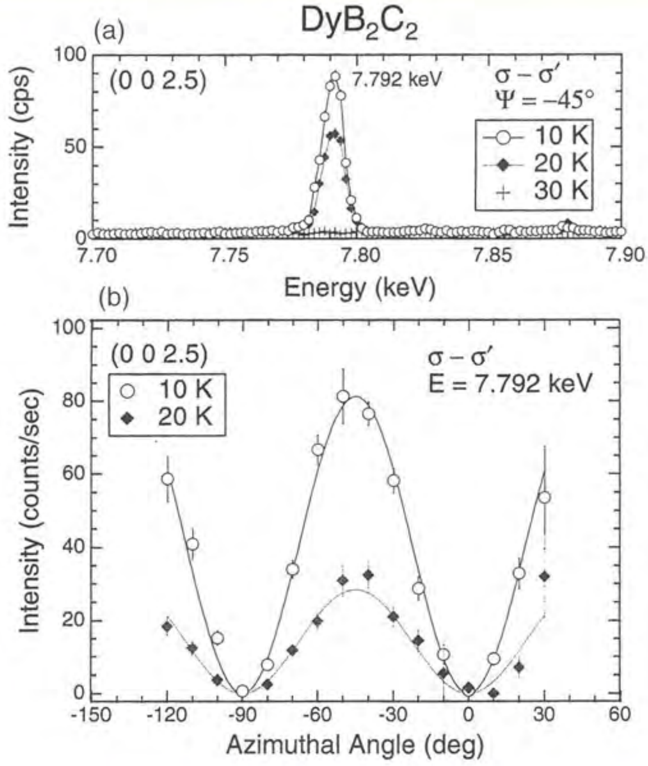

Figure 1.
Incident energy dependences (a) and azimuthal angle dependences (b) of the (0 0 2.5) peak for σ - σ' polarization.

Three superlattice peaks of q_M =(1 0 0), q_{Q1} =(0 0 1/2) and q_{Q2}=(1 0 1/2) were investigated. Figure 1(a) shows the incident-energy dependences of the (0 0 2.5) peak, i.e., the q_{Q1} point, which exhibits a sharp enhancement at the Dy L_{III} edge. The (0 0 1/2) peaks appearing below T_Q =25 K in both the σ-π' and σ-σ' scattering processes have been observed. On the other hand, the (1 0 0) and (1 0 1/2) peaks in the σ-π' scattering process appear only below T_N =15 K, corresponding to a magnetic order consistent with previous neutron-scattering results.

In addition to the enhancement, it is expected that the resonant ATS scattering from AFQ ordering would show an azimuthal angle (Ψ) dependence reflecting the shape of the *f* electron distribution. As shown in Fig.1(b), they measured the azimuthal angle dependence for the two different polarizations by rotating the crystal around the scattering vector kept at (0 0 2.5), which demonstrates that the σ-σ' scattering exhibits a characteristic four-fold oscillation, compatible with the AFQ ordering in tetragonal symmetry. The intensity approaches zero at Ψ=0 and π/2.

The much weaker coupling between the orbital degrees of freedom and the lattice in 4*f* electron systems than in 3*d* compounds makes them an ideal platform to study orbital interactions originating from electronic mechanisms.

Similar studies were also done by Tanaka and the co-workers almost simultaneously [2].

References

[1] K. Hirota et al., Phys. Rev. Lett. 84 (2000) 2706.

[2] Y. Tanaka et al., J. Phys. Condens. Matter 11 (1999) L505.

5-2 Structural and Magnetic Properties of K-Absorbing Zeolite LTA

Zeolite LTA, $M_{12}Si_{12}Ai_{12}O_{48}(H_2O)_n$, where *M* is an alkali-metal, is a synthetic hydrated aluminosilicate, where a (-Si-O-Al-O-) framework forms two kinds of cages, called α and β. The dehydrated LTA can absorb additional alkali-atoms, whose 4s-electrons are delocalized in the cavities of α-cages in the crystal, and exhibit novel properties. In 1992, Nozue et al. reported a ferromagnetic-like transition in K-absorbing K-ion type LTA, K_x- $K_{12}Si_{12}Ai_{12}O_{48}$, with *x* from 3 to 5 [1]. In a naive picture, the electrons occupy the 1*s* and 1*p* quantum states formed in the cavities with a spherical potential well. Then, the ferromagnetism appears when the 1*p* states are partially filled.

Recently, a systematic study on the structure and magnetism was performed by Maniwa et al. in K-absorbing K-ion type LTA [2]. Figure 2 shows examples of powder X-ray diffraction profile as a function of the K-absorbing density, *x*. The peaks for *x* = 0 are indexed as those of a simple cubic lattice, as shown in the bottom. Upon increasing *x*, we can see new peaks assigned to a superlattice with doubling the lattice constants for each direction. This implies that there are two kinds of α-cage with different K-density (so-called mass density wave; MDW). Magnetic susceptibility measurements of the same samples clarified that the ferromagnetic moment coexists with the lattice modulation, suggesting a possibility of ferrimagnetism. From this point of view, ^{29}Si-NMR experiments were also performed [3]. The spectra actually indicated the presence of two different kinds of magnetic moments. A detailed analysis of the spectra to determine the magnetic structure is now in progress.

Finally, it should be emphasized that high-performance X-ray diffraction experiments using synchrotron radiation on the BL-1B made it possible to discover the new aspect of the ferromagnetic zeolite LTA.

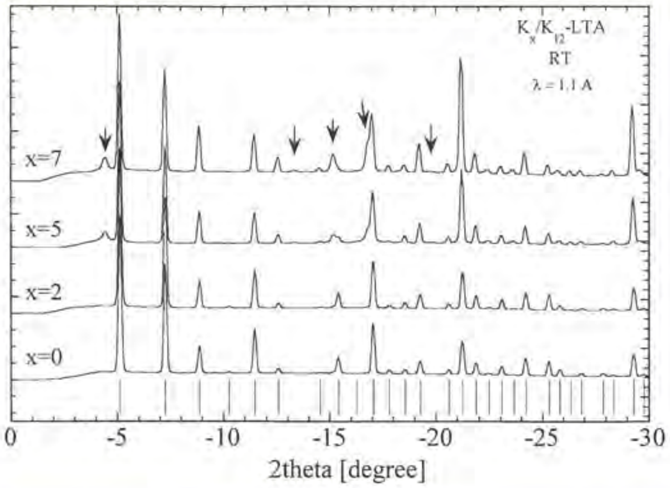

Figure 2.
Powder X-ray diffraction profiles in K-absorbing K-ion type LTA.

References
[1] Y. Nozue et al., Phys. Rev. Lett., 68 (1992) 3789.
[2] Y. Maniwa et al., J. Phys. Soc. Jpn., 68 (1999) 2902.
[3] H. Kira et al., to be appeared in J. Magn. Magn. Mater.

5-3 Observation of the Fermi Surface Flattening in Cu-28at%Pd by Compton Scattering

The Cu-Pd alloy exhibits a variety of phase transformations according to the composition and temperature. Many structural investigations have been carried out using X-ray or electron-beam diffraction methods. It is thought from these investigations that the conceivable driving force of the phase transformation and the occurrence of short-range order is related to the geometry of the Fermi surface. In particular, it has been predicted that a flattening of the Fermi surface due to alloying is responsible for the occurrence of a short-range order. However so far, a direct measurement of the

Fermi surface of the alloy has not been performed, because traditional methods for studying Fermiology can not be applied to concentrated alloys. Very recently, it becomes possible to study the Fermiology of alloys at the AR-NE1A1 by Compton scattering, which does not require long mean free paths of electrons, and the method has been applied to test the above-mentioned theoretical prediction.

Matsumoto et al. present direct evidence of a flattening of the Fermi surface in a disordered Cu-28at%Pd alloy which exhibits a short-range order at high temperatures [1]. Twenty two directional Compton profiles of the alloy and of pure Cu were measured, and are being used to reconstruct the 3D momentum density by the direct Fourier method. The 3D occupation number density is obtained from the obtained 3D momentum density via the LCW folding method.

Figure 3 shows the Fermi surface of pure Cu (a) and that of the alloy (b). It is easily seen that the neck at L in pure Cu disappears in the alloy. Figure 3(c) shows the (100) cross-section through Γ, which clearly demonstrates that the Fermi surface of the alloy flattens in the [110] direction. This is the first experimental evidence which supports the theoretical prediction on the driving force of the short range order in this system.

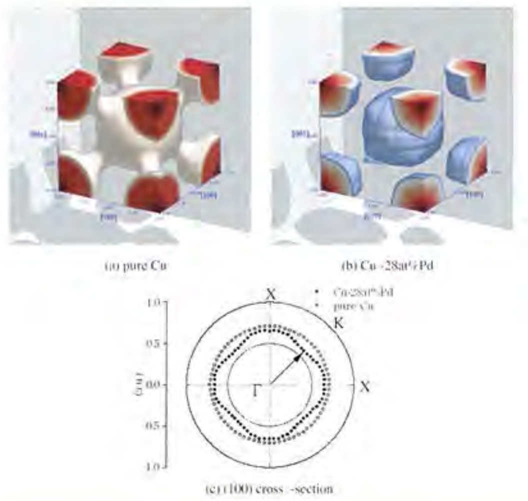

Figure 3.
Three-dimensional Fermi surface of pure Cu (a) and Cu-28at%Pd (b). (c) The Fermi surface on the (100) cross-section.

Reference

[1] I.Matsumoto, H.Kawata and N.Shiotani. Phys. Rev. Lett. submitted.

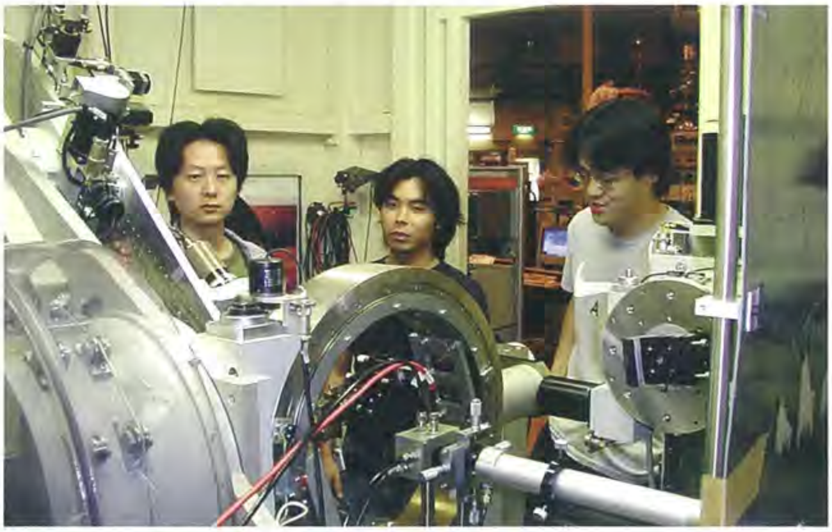

6 Crystallography

Powder X-ray diffraction has been developing as a useful and convenient method for crystal-structure analysis, when combined with synchrotron radiation and/or advanced analytical methods, such as the Rietveld method. We would like to mention it, as the highlight of crystallography and introduce here the recent developments of synchrotron powder X-ray diffraction experiments.

6-1 *Ab initio* Structure Determination using Synchrotron Radiation Powder Diffraction Data

The *ab initio* structure determination is still one of the most challenging topics in powder diffraction. Direct methods are major tools for phasing in powder methods as well as in single-crystal methods. However, they sometimes fail to give complete structure solutions because of incompleteness of the observed structure amplitudes derived from reflection data with severe overlap [l-2].

Recently, powerful methods, such as those which apply the Monte-Carlo method or the simulated annealing method, have been developed for solving crystal structures from powder data in direct space [3-5]. At BL-4B2, Yamazaki, S. (INAX Co. Ltd.), et al. are interested in solving the crystal structure *ab initio* from high-resolution synchrotron radiation powder diffraction data. In the following two examples, which apply the Monte-Carlo method for finding missing atoms, are described.

In the structure determination of the monoclinic-2,2-bis(hydroxymethyl)butanoic acid (*m*-BHBA) [$C_6H_{12}O_4$: space group $P2_1/c$, $Z = 4$, $a = 6.3980(1)$ Å, $b = 11.0866(3)$ Å, $c = 11.2095(4)$ Å, $\beta = 106.108(2)^\circ$], the positions of seven atoms among ten non-hydrogen atoms in a unit cell were first found by the direct method. The positions of the remaining three atoms were successfully found after

20000 Monte-Carlo moves without applying any constraints on these atoms [6]. Figure 1 shows the crystal structure of *m*-BHBA finally obtained by a Rietveld refinement.

In the case of the tobermolite-11 Å [$Ca_5(Si,Al)_6O_{16}H_2 \cdot 4H_2O$: space group *Bm*, $Z = 2$, $a = 6.7296(7)$ Å, $b = 7.3550(6)$ Å, $c = 22.610(2)$ Å, $\gamma = 123.242(8)^\circ$], the "frame structure [$Ca_4(Si,Al)_6O_{16}H_2$]" has already been known [7-8]. However, the positions of one Ca atom and four water molecules, existing as "zeolitic ions", have not yet been determined. The application of the Monte-Calro method was again successful in finding the positions of these atoms. The derived structure model, having 51 atomic parameters, was further refined by the Rietveld method. Figure 2 shows the refined crystal structure of tobermolite-11 Å.

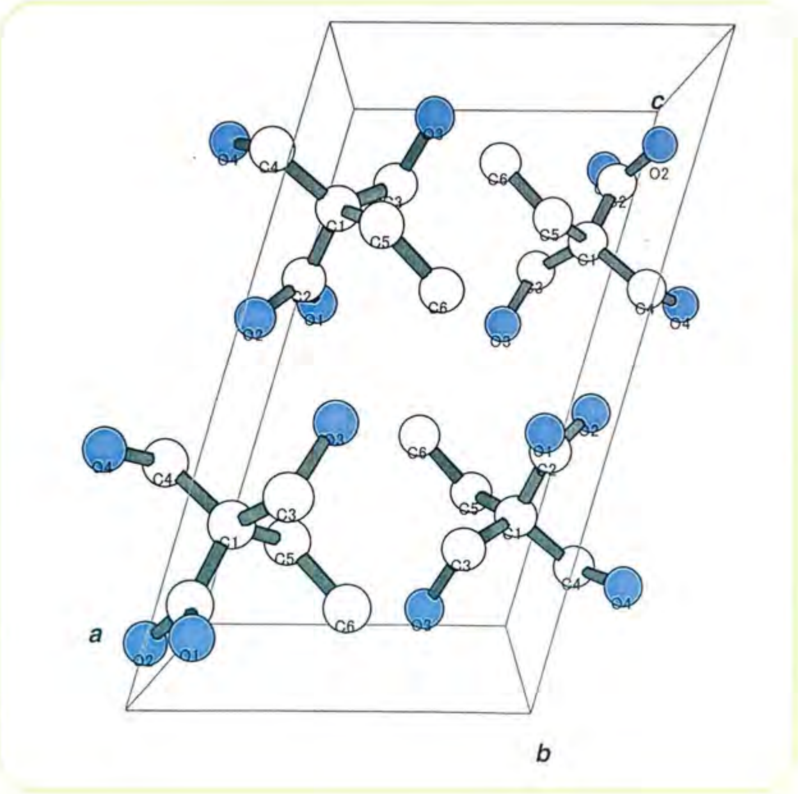

Figure 1.
Crystal structure of *m*-BHBA.

The Monte-Carlo methods for structure solution is generally used with a rigid-body model, which constrains the atomic positions of individual atoms for reducing the number of variables and avoiding to fall into false minima [9]. In the present study, it has been demonstrated that the method is powerful for finding missing atoms without using the rigid-body model, and that it compensates the direct methods for any incompleteness of powder data [6].

References

[1] C. Giacovazzo, Acta Cryst., A52 (1996) 331.
[2] A. Altomare, C. Giacovazzo, A. Guagliardi, A. G. G. Moliterni and R. Rizzi, J. Appl. Cryst., 29 (1996) 667.
[3] K. D. M. Harris M. Tremayne, Chem. Mater., 8 (1996) 2554.
[4] S. Wu-Pei, Acta Cryst., A51 (1995) 845.
[5] J. R. Holden, Z. Y. Du and H.L. Ammon, J. Comput. Chem., 14 (1993) 422.
[6] Y. Tanahashi, H. Nakamura, S. Yamazaki, Y. Kojima, T. Ida and H. Toraya: In preparation .
[7] S. Komarneni and M. Tsuji: J. Am. Cerm. Soc., 72 (1989) 1668

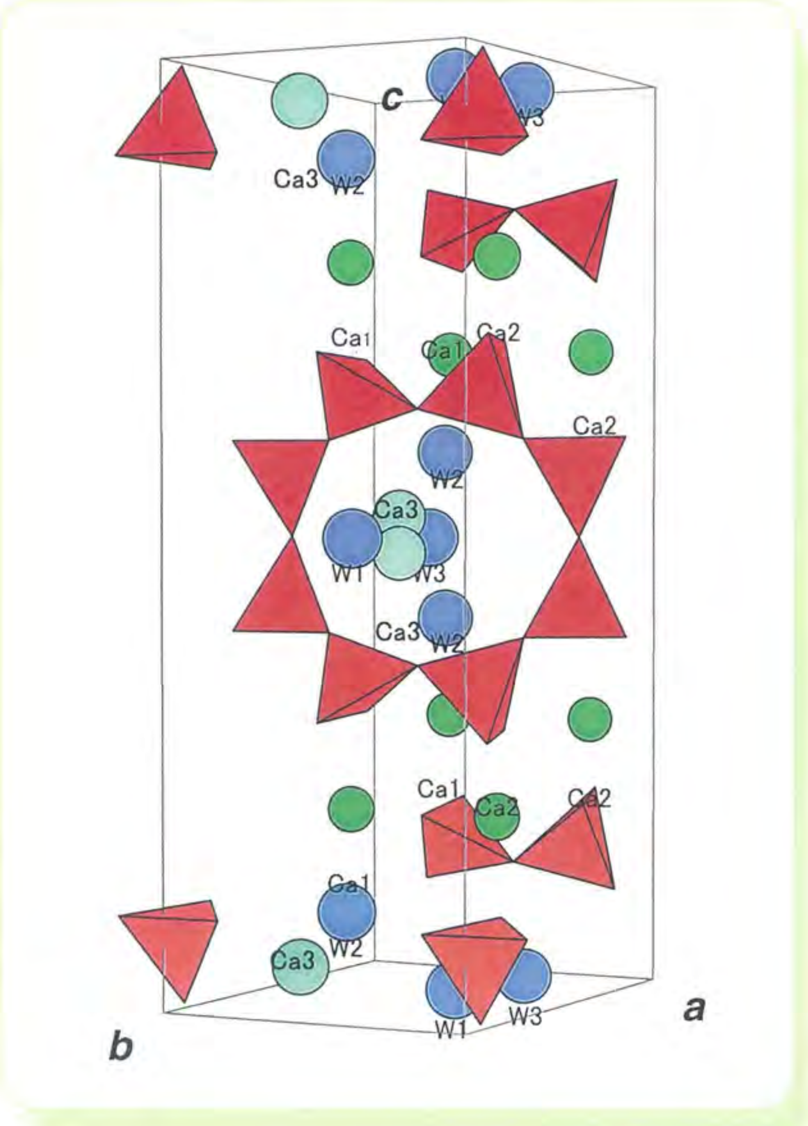

Figure 2.
Crystal structure of tobermolite-11 Å. SiO_4(or AlO_4) is illustrated as tetrahedra and the occupancy of the Ca3 position is 0.5.

[8] S. Merlino, E. Bonaccorsi and T. Armbruster: Amer. Mineral., 84 (1999) 1613.

[9] K. D. M. Harris, M. Tremayne, P. Lightfoot and P. G. Bruce: J. Am. Chem. Soc., 116 (1994) 3543.

6-2 A New Furnace for Synchrotron Powder X-Ray Diffraction at BL-3A and its Application to High-Temperature Crystal-Structure Studies of Rare-Earth Alminium Oxide

A new apparatus for high-temperature X-ray powder diffraction experiments has been developed for the diffractometer at BL-3A and has been applied to crystal-structure studies of perovskite-type oxide, $CeAlO_3$, under high temperature.

Synchrotron powder X-ray diffraction is a very powerful method for investigating the structural phase transition, as mentioned below. 1) It can be applied to a material that is hard to synthesize a single crystal. 2) It can easily observe a change in the powder diffraction profile caused by the sample environment. 3) If synchrotron radiation is used as the X-ray source, it can obtain extremely high-resolution diffraction data without any $K\alpha_1 K\alpha_2$ contamination. Many low-temperature X-ray powder diffraction apparatus are provided to experimental stations in the PF for material physics. On the other hand, high-temperature powder X-ray diffraction is expected to be a useful method in the field of earth or planetary material science. Tanaka, M. (Photon Factory, KEK), et al. thus developed a new

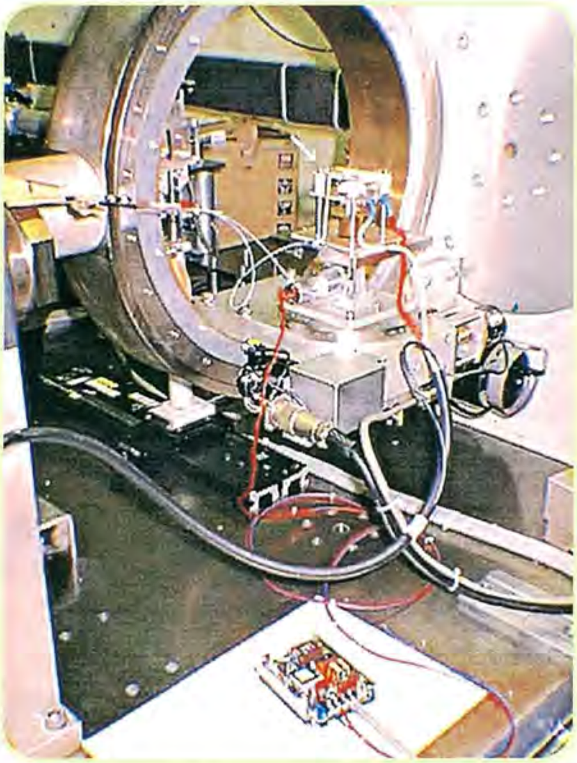

Figure 3.
New furnace for high-temperature powder X-ray diffraction attached to the BL-3A diffractometer ϕ -stage. The arrow indicates the heater and sample holding. An alminium chamber covers the heater and sample holder.

powder X-ray diffraction furnace for the 3-axis 4-circle diffractometer at the BL-3A [1]. This new furnace is designed to enable atmosphere control and sample rotation at 1 rps under heating to avoid the grain-size or grain-growth problem. The expected highest sample temperature is about 900K. Figure 3 is a photograph of the furnace attached to the BL-3A diffractometer. The performance is summarized on Table 1.

This furnace has been applied to powder diffraction experiments on the $CeAlO_3$ crystal structure under high temperature at BL-3A. $CeAlO_3$ is one of the compounds of a series of rare-earth alminium oxide, which takes a perovskite-type structure. In this series of compounds the crystal symmetry changes systematically according to the ionic radius of the rare-earth element. The compounds containing the smaller ion-radius rare-earth elements are orthorhombic structure and the compounds containing the larger ion-radius rare-earth elements are rhombohedral structure [2-4]. However, only $CeAlO_3$ is an exception to this tendency. There were many trials to further analyze the crystal structure [5], but the deviation from a cubic perovskite is so small that the structure has not been made clear indetal until now. The experimental condition is as follows. The furnace is installed on the ϕ -rotation stage of the BL-3A diffractometer. 1.0 Å X-rays monochromatized from synchrotron radiation by a Si (111) double-crystal monochromator were used. The powder-diffraction profiles of selected diffraction peaks were observed in the temperature range from 300K to 880 K. Figure 4 is the obtained powder diffraction profiles. These patterns clearly show the change in crystal symmetry. For example, the double-peak around 2θ =15.5(deg.) becomes single-peak according to the ascent of temperature. It was concluded that the crystal system was orthorhombic below 443 K and changed into rhombohedral above 514 K, as the result of an analysis on the diffraction-peak split pattern.

As mentioned, this new furnace was successfully applied to observe the symmetry change of $CeAlO_3$, and will be a new useful apparatus to investigate high-temperature structural phase transitions. The authors presently provide it for PF user experiments and expect it to be utilized for high-temperature diffraction studies.

Table 1 Performance of the new synchrotron powder X-ray diffraction furnace.

Heater : Platinum

Temperature range : 300～900K

Temperature deviation : ±2 K at 1000 K

Sample size : 10mm ϕ ×0.5mm

Sample rotation : 1 rotation／second

Temperature measurement : Pt-PtRh13 thermo couple

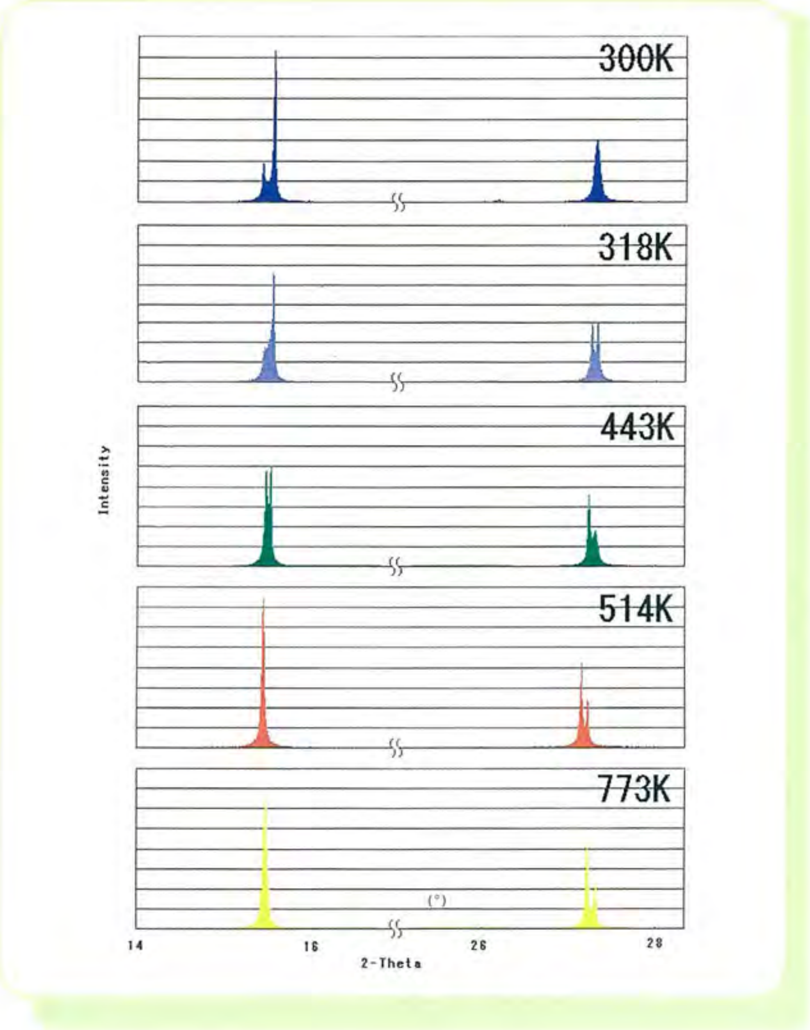

Figure 4.
Powder-diffraction patterns of $CeAlO_3$ under heating.

References

[1] K. Kawasaki et al., Rev. Sci. Instrum. 63 (1992) 1023.

[2] A. Yoshikawa et al., J. Alloys and Compounds, 266 (1998) 104.

[3] H. Horiuchi et al., Proc. of PRICM 3 Eds. M.A.Iman et al., The MMM Soc., (1998)1417.

[4] A.Saitow et al., J. Appl. Crystallogr. 31(1998) 663.

[5] M. Tanaka et al., J. Alloys and Compounds, 192 (1993) 87.

6-3 Structural Study of Spinel-Type $CuIr_2S_4$ at Low Temperatures by High-Resolution Powder Diffraction

A spinel-type compound, $CuIr_2S_4$, shows a metal-insulator transition (MIT) at T_t = 226 K, which is accompanied by a structural phase transition [1]. Although many efforts have been made to clarify the origin of the MIT of $CuIr_2S_4$, the precise crystal structure of the low-temperature phase as well as the origin of the MIT remains unknown. Ishibashi, H, (Osaka Pref. Univ.), et al. carried out high-resolution powder diffraction experiments to examine the crystal structure of the low-temperature phase of $CuIr_2S_4$ in detail.

High-resolution powder diffraction experiments at 50 K were performed using a four-circle diffractometer with high-angle resolution installed at the BL-3A. The cryostat of the helium closed-cycle type was used to cool the sample. Further, a flat Si(111) crystal analyzer was used in front of the counter to obtain diffraction data with much higher resolution. The other layout of the experiment is similar to that reported previously [3]. The wavelength used was $\lambda = 1.547$ Å. The powder pattern was measured in $2\theta/\theta$ step scanning with a step width of 0.002°.

Figure 5(a) shows the observed powder pattern of the low-temperature phase of $CuIr_2S_4$. The fundamental reflections were indexed by assuming that the crystal structure has an orthorhombic symmetry. Figure 5(b) shows detailed profiles of the 404, 044 and 440

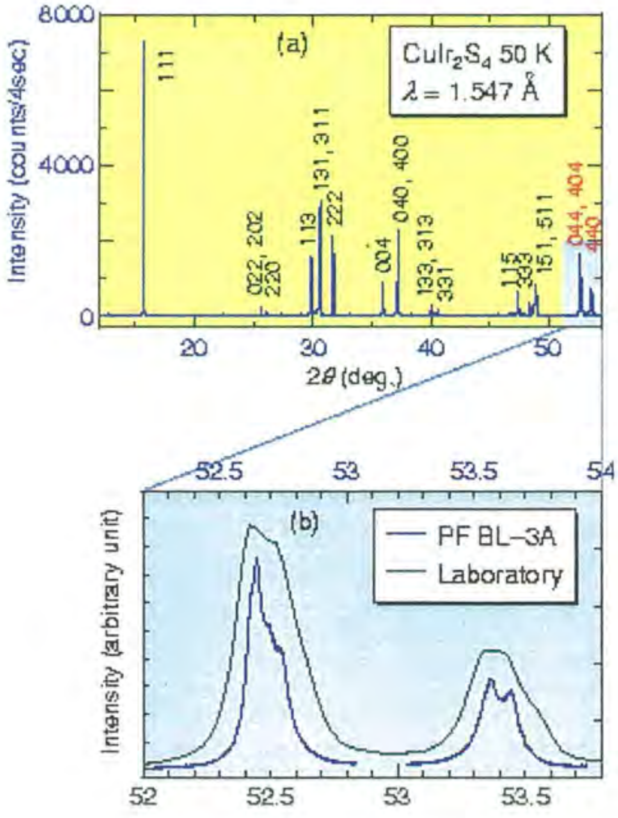

Figure 5.
(a) Powder pattern of $CuIr_2S_4$ at 50 K obtained by a synchrotron radiation source at BL-3A station.
(b) Blue lines showing the detailed profiles of the 044, 404 and 440 reflections. The green lines show the profiles obtained by Cu Kα radiation at laboratory for a comparison with the present result.

reflections together with those obtained by a laboratory X-ray source (using Cu Kα radiation) for a comparison. As can be seen in this figure, the peak width becomes remarkably narrow by using a synchrotron radiation source. As a result, it is found that each peak is clearly splitting into two peaks, i.e., the 440 reflection of the high-temperature phase is divided into six independent reflections. These splittings mean that the crystal structure has a triclinic symmetry. Furthermore the existence of extra weak reflections, such as 3/2 1/2 1/2, are clearly observed, which means that atomic displacements of Ir ions take place below T_t. These results support a charge in the ordering of Ir^{3+} and Ir^{4+}, which is considered to be the origin of the MIT. A possible model of the charge ordering and the correlation with the physical properties are now in progress.

References

[1] T. Furubayashi, T. Matsumoto, T. Hagino and S, Nagata, J. Phys. Soc. Jpn. 63, (1994)3333 .

[2] R. Oshima, H. Ishibashi, K. Tanioka and K. Nakahigashi, Proc. International Conf. on Solid-Solid Phase Transformations '99, (1999)895 .

[3] A. Saitow, A. Yoshikawa, H. Horiuchi, T. Shishido, T. Fukuda, M. Tanaka, T. Mori , S. Sasaki, J. Appl. Cryst. 31 (1998) 663.

6-4 Study of High-Tc Compounds by X-Ray Powder Diffraction Near the Cu K-Absorption Edge

Cu ions play a very important role in a high-Tc material and their valence states can be monovalent, divalent, or trivalent according to the configuration of the neighboring atoms. The high-Tc property very sensitively depends on the configuration. Ishida, K. (Science University of Tokyo) et al. studied the valence state of Cu ions and the electron density around the ions in high-Tc compounds by X-ray powder diffraction (XPD).

Though XPD is a very powerful method to determine crystal structure, it is not very good for the electronic state of ions in a crystal. It is well known that the X-ray absorption edge depends on the valence state of an atom. Therefore, the dispersion curves of ions reflect their electronic state. In order to obtain dispersion curve, for a start, structural parameters were determined by Rietveld analysis of XPD data taken with an X-ray wavelength far from the Cu K absorption edge. XPD measurements were carried out with a number of X-ray wavelengths near the absorption edge. The real and imaginary parts of the scattering factor of Cu ions near the edge were obtained by Rietveld analysis, in which both parts were parameters to be determined; other structure parameters determined far from the edge were adopted for the analysis.

As for electron distribution density, the Maximum Entropy Method (MEM) is a very powerful method to determine the density from XPD data without assuming any structure model. In the present work, however, the structure factors brought out by the Rietveld analysis were also used for MEM, since the final reliable factors of the MEM charge density obtained using the parameters was better than that without using them.

High-Tc compounds, YBCO and Nd-Ce-Cu, were prepared by the conventional method. Super- and non-super-conducting samples were obtained by heat treatments for YBCO and Ce doping for Nd-Ce-Cu.

The X-ray measurements were carried out at room temperature on the BL-4B2. The XPD data for YBCO were collected by high-resolution powder diffractometer and, for Nd-Ce-Cu, by high-resolution powder diffractometer with multiple detector system.

Figure 6 shows the dispersion curves of the real part of the atomic scattering factor of Cu(1) and Cu(2) in YBCO. The curves of Cu(1) and Cu(2) cannot be distinguished. Moreover, any significant difference isn't observed in the curves of tetragonal and orthorhombic compounds. For the edge of the Cu (1) ions, the energy of the tetragonal phase is slightly lower than that of the orthorhombic ones, but the difference is not as large as that expected for the Cu^+ ion [1].

Figure 7 shows the MEM charge densities of Nd-Ce-Cu obtained by using the structure factors brought out by the Rietveld method. A reliable factor of the MEM charge density was 2.5 %. From the charge

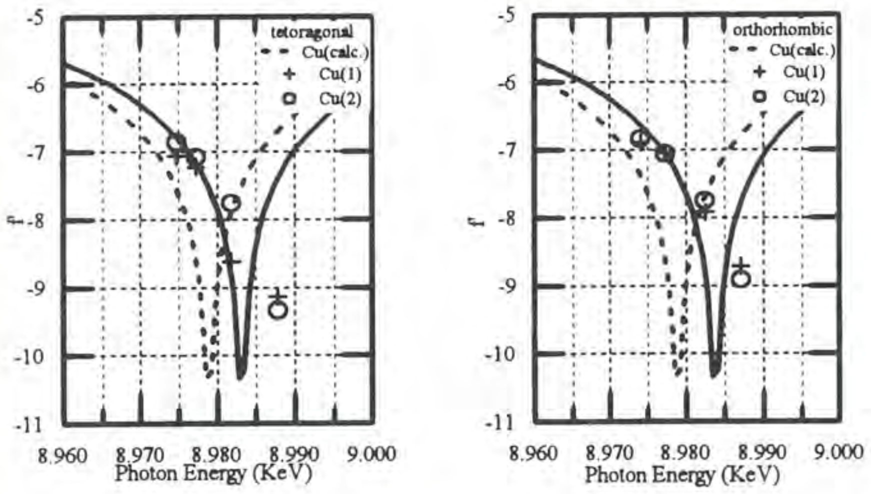

Figure 6.
Real part of the anomalous scattering factor of YBCO near the Cu K-edge. Tetragonal (left) and orthorhombic (right) phases. The curve is dispersion curve for Cu free atom (calculation). The solid curve is the same shape as the broken curve but with the edge shifted by 6 eV.

density of the (002) plane, directional robe of the density from the Cu atom to the surrounded O atoms can be observed. This shows the Cu($3d_{x^2-y^2}$)-O(2p) orbital hybridization charge and the strong bonding between the Cu and O atoms in the CuO_2 plane. It is also seen in the lower figure that the plane is composed of weakly bonding upper and lower planes.

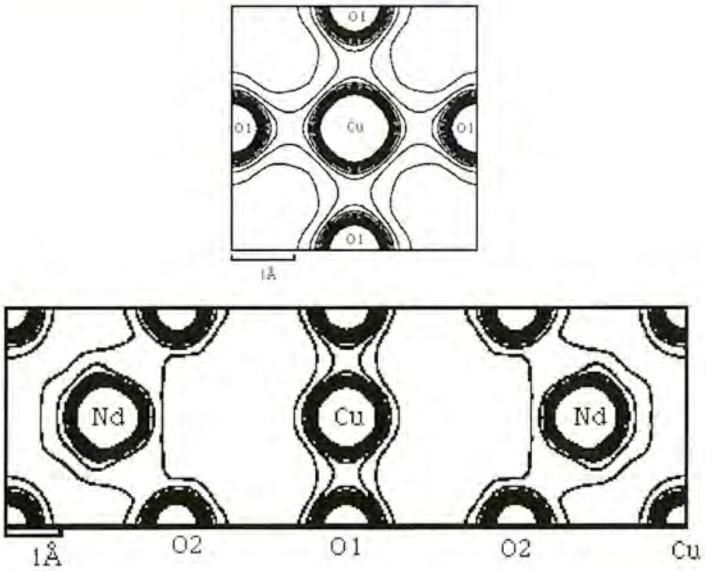

Figure 7.
MEM charge densities for (002) (upper) and (200) (lower) of superconducting $(Nd,Ce)_2CuO_4$. The contour lines are drawn from 0.5 to 5.0 with 0.3 (e/Å^3) intervals.

Reference
[1] M. Nakaura et al.: J. Phys. Soc. Jpn. 64 (1995) 3336.

7 High Pressure Science

7-1 High-Pressure Study of Hydrogen Bond Symmetrization on HCl

HCl is a member of the hydrogen halide system, and is a very popular material for high school students. It is one of the most simple molecular crystals containing a hydrogenbond. Among the research field of the hydrogen-bond system, symmetrization (proton is placed just in between two adjacent atoms) is an advanced topic: when and how a hydrogen-bond gains a single-well potential while losing its double-well potential. Hydrogen-bond symmetrization, which has been observed for H_2O ice at 60 GPa, can be expected to occur in hydrogen halide systems as well. With decreasing temperature, HCl gas becomes frozen to a solid state at ambient pressure, which takes three kinds of molecular crystals in different temperature ranges. They are known as Phase-I, Phase-II and Phase-III and their temperature ranges for existence are 159 K>T>120 K, 120 K>T>98 K and 98 K>T, respectively. Phase-I and Phase-II have orientationally disordered hydrogen bonds. As for Phase-II, a hydrogen atom occupies a symmetrically reversal position. Phase-III has a planar zigzag chain of hydrogen bonds.

X-ray powder diffraction experiments on solid HCl were carried out by H. Fujihisa et al. with a diamond anvil cell at room temperature at BL-18C. A pressure-induced transition was observed at 18 GPa and no other phase transition was found up to 61 GPa. The high-pressure phase was identified as Phase-III with space group $Cmc2_1$ and pressure effects on its lattice constants and atomic positional parameters were also measured by using a Rietvelt analysis.

At 61GPa the interchain Cl-Cl distances in Phase III decrease to the 89% value, which is shorter than a doubled van der Waals radii of chlorine. A continuous color change from brown to black can be explained by this pressure effect on the interchain interaction. The intrachain Cl-H···Cl distance reaches only a value 5% larger than the doubled intramolecular distance around 50 GPa. Hydrogen bond symmetrization should take place here, judging from this and the disappearance of molecular vibration in high-pressure Raman spectroscopy[1]. Figure 1 shows the atomic arrangements of HCl in Phase-III before hydrogen-bond symmetrization at 18 GPa [A] and after symmetrization at 55 GPa [B]. It is noted that the pressure-induced hydrogen bond symmetrization means molecular dissociation in HCl solid simultaneously.

Reference

[1] K. Aoki et al., Physica B 265 (1999) 83.

Figure 1.
Atomic arrangements of HCl in Phase III before and after hydrogen bond symmetrization, at 18 GPa [A] and at 55 GPa [B], respectively.

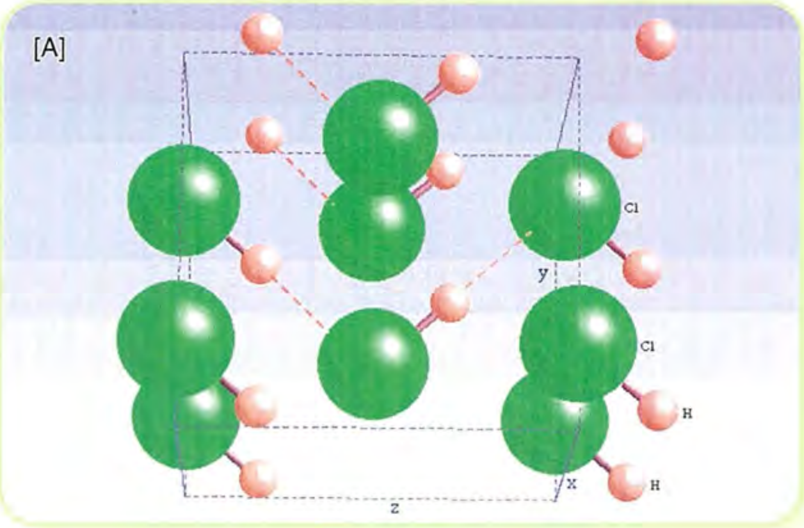

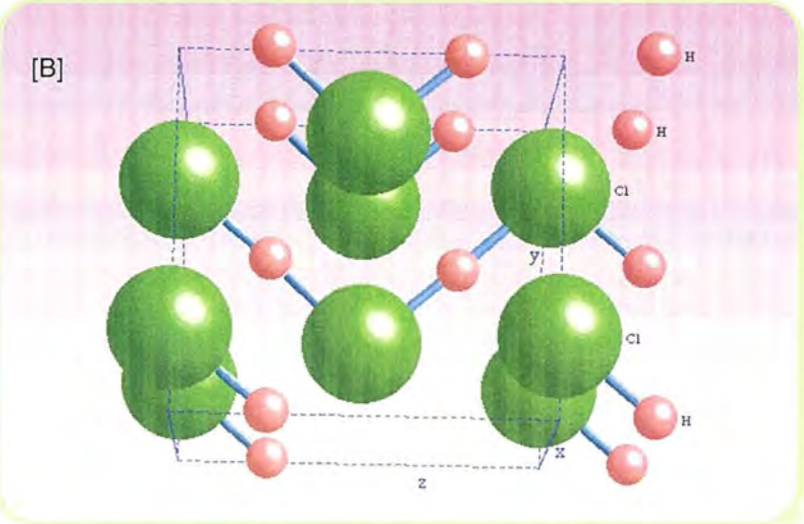

7-2 Phase Transitions of Sulfur at High Pressure and High Temperature.

In ordinary elements, pressure-induced phase transitions have been well studied in the pressure range below a few tens GPa. Moreover, the phase transitions over 100 GPa are becoming clear using *in-situ* X-ray measurements with a diamond-anvil cell. As for sulfur, many high-pressure and high-temperature experiments have been carried out because of the interest of material science and earth science, but they still lose consistency. In most of the previous experiments, many phases under slightly different conditions have been found using a quenching method. In addition, even a room temperature X-ray diffraction experiment shows only a complex of broad peaks up to about 20 GPa and an amorphous pattern in between 20 to 40 GPa.

The behavior of sulfur under high-pressure and high-temperature conditions has been revealed for the first time in the range of $P < 16$ GPa and $T < 900$℃. Kusaba and Kikegawa carried out a high-temperature high-pressure *in-situ* X-ray diffraction experiment using multi-anvil press MAX80 installed in AR-NE5C. Ge-SSD was used for the energy-dispersive powder X-ray diffraction method. Magnesia as a grain growth obstruction material at elevated temperature was mixed with sulfur powder in 20% weight. NaCl powder, in which magnesia was also mixed with in the same way, was used as a pressure marker.

Typical X-ray diffraction patterns are shown in Fig. 2. An orthorhombic normal-condition phase (a) is well known as alpha-sulfur with crown-shaped S_8 circular molecules (Fig. 3). Three kinds of new high-pressure phases (b-d) were found in this experiment. All these high-pressure phases appearing by elevating temperature to above 300℃ had not been observed in the usual room-temperature high-pressure experiments. They could be frozen in the room temperature but became unstable with decreasing pressure. Thus, these phases could not keep under the normal condition. This result indicates that it is impossible to observe the behavior of sulfur at high pressure and high temperature by the quenching method.

The second high-pressure phase is explained as hexagonal sulfur, which consists of 18 atoms with three S_6 circular molecules in a unit cell (Fig. 4). The hexagonal sulfur is known to be in a quasi-stable phase at ambient pressure. It is made by a re-crystallizing method from the solvent, and has the 6% higher density than that of the orthorhombic phase.

In the phase transition from the ambient-pressure phase to the second high-pressure phase, the crown-shaped S_8 molecules start an open-ring reaction and reconstruct into another type of circular molecule, S_6.

As for the two other high-pressure phases, structure analyses are now proceeding by the DDX (dual dispersive X-ray diffraction) method [1].

Reference

[1] T. Kikegawa, J. Chen, K. Yaoita and O. Shimomura, Rev. Sci. Instrum., 66 (1995) 1335.

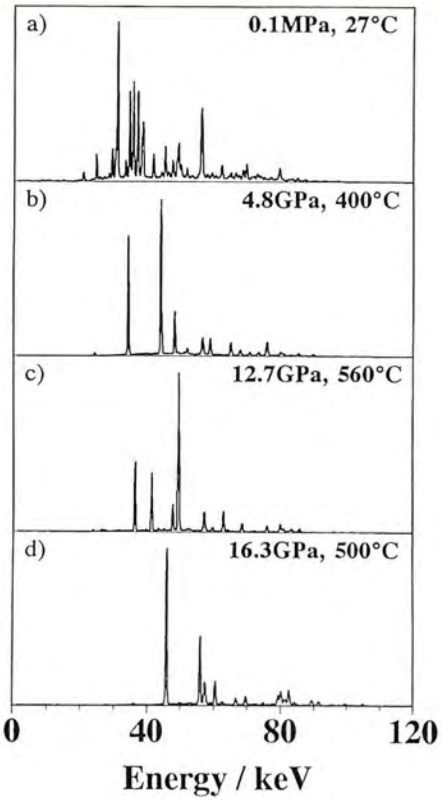

Figure 2.
X-ray diffraction patterns of sulfur for a) the ambient-pressure phase, b) the high-pressure phase I, c) the high-pressure phase II, and d) the high-pressure phase III.

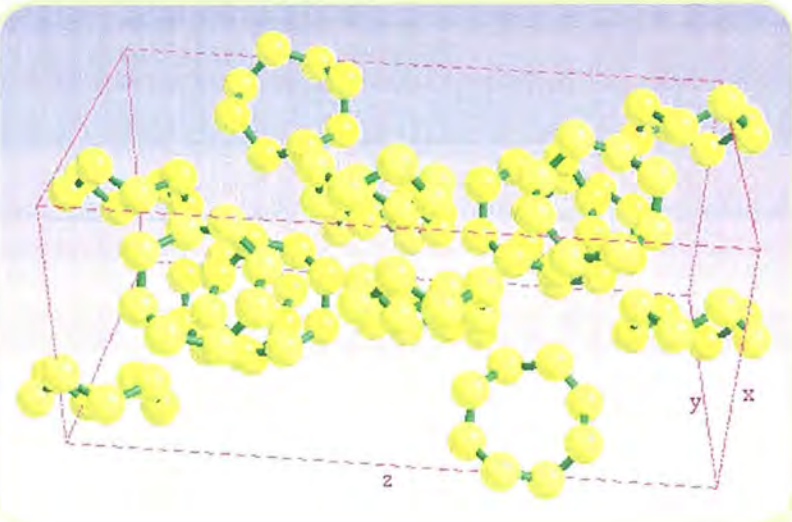

Figure 3.
Atomic arrangement of alpha-sulfur in the ambient-pressure phase. 128 sulfur atoms form 16 crown-shaped S_8 circular molecules in a unit cell.

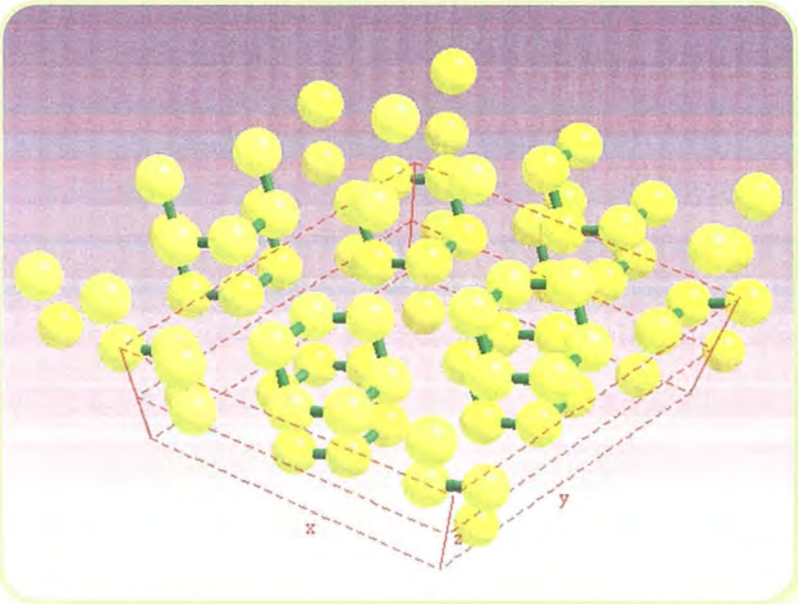

Figure 4.
Atomic arrangement of high-pressure phase II. 18 sulfur atoms form three S_6 circular molecules in a unit cell.

8 Biological Science

The application of synchrotron radiation to an analysis of the crystal structures of biological molecules is spreading. It is important not only for academic research, but also for industrial requirements. The Tsukuba Advanced Reseach Alliance (TARA) project is more suitable to fulfill these demands. In this section, two topics involving TARA project are discussed: one is the RNA-dependent RNA polymerase of Hepatitis C virus; the other is phycobiliproteins. The former was obtained by JT company, and the latter by international collaboration.

Two other topics to be pursued by crystal structural analyses of proteins are the use of the MAD method and the refined analysis of proteins. Recently, it has become feasible to analyze bound water around protein molecules.

It is now more recognized that proteins in motion are important to elucidate their function. Above many efforts in this trend, X-ray scattering is widely applied to elucidate protein folding, because X-ray scattering gives uniquely direct evidence of protein compactness. In parallel with the development of a CCD detector, it becomes feasible to investigate the protein folding pathway by a combined method with stopped-flow and a CCD detector. Here, results on the folding of α-lactalbumin (α-LA) are discussed.

8-1 Crystal Structure Analysis of the RNA-Dependent RNA Polymerase of Hepatitis C Virus

Hepatitis C virus (HCV) is a positive single-stranded-RNA [(+)ssRNA] virus and the major etiological agent of hepatocellular carcinoma. The World Health Organization has estimated that there are 170 million chronic HCV carriers in the world today [1], although the risk of acquiring HCV by transfusion has been dramatically reduced since the development of an assay for the virus. About 80% of HCV-infected patients develop chronic hepatitis, 20% of them progress to cirrhosis and eventually develop hepatocellular carcinoma. At present, no vaccine is available and there is no broadly effective therapy for all genotypes of HCV, although extensive research has been focused on the development of anti-HCV agents. The NS5B protein of HCV is the RNA dependent RNA polymerase (RdRp) which has the full-functionality of HCV RNA genome replication [2], and is one of the potential targets for anti-HCV agents.

The three dimensional structure of HCV RdRp was determined by X-ray crystallography at 2.5 Å resolution (Fig. 1) [3-5]. The structural basis of the RNA selectivity of HCV RdRp was elucidated from its crystal structure [5].

The compact HCV RdRp structure resembles a right hand, but has more complicated fingers and thumb domains than those of the other known polymerases, with a novel α-helix rich subdomain (α fingers) as an addition to the fingers domain. The other fingers' subdomain (β fingers) is folded in the same manner as the fingers' domain of human immunodeficient virus reverse transcriptase, another RNA-dependent polymerase.

HCV RdRp strictly discriminates between RNA and DNA for the template as well as between ribonucleoside-triphosphate (rNTP) and deoxy-ribonucleoside triphosphate (dNTP). The primary substrate discriminating factor is a hydrogen bond between Asp225 and 2'-OH of rNTP. It is consistent with the proposition of Hansen *et al* [6]. Further, more HCV RdRp possesses a shallow hydrophilic pocket with bound water molecules around the corresponding residue. The pocket is composed of residues that are highly conserved among (+)ssRNA RdRps (Asp225, Ser282, Thr287 and Asn291). The hydrophilic pocket of HCV RdRp should better accommodate the more polar and bulkier ribose of rNTP without dehydration. Coupled with the enthalpic gain from forming a hydrogen bond with Asp225, this should contribute to

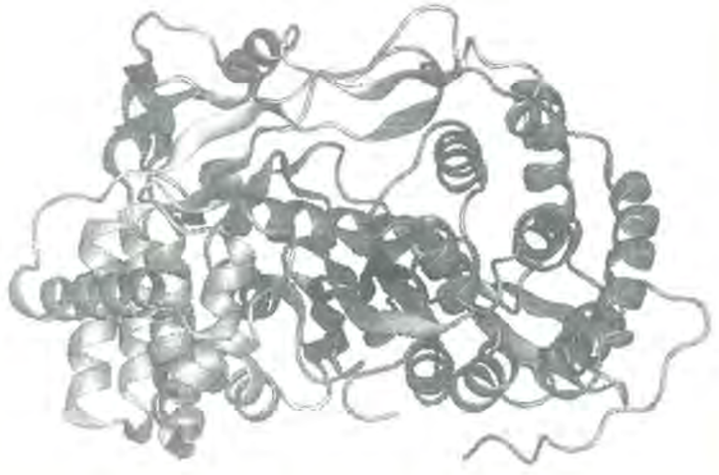

Figure 1.
Crystal structure of HCV RdRp. The α fingers, β fingers, palm and thumb domains are colored by green, blue, red and violet, respectively.

substrate selectivity. The unique α fingers might represent a common structural discriminator of a template-primer duplex that distinguishes the difference in the conformation between RNA and DNA during the replication of (+)ssRNA by viral RdRps. According to a docking study of the HCV RdRp and RNA duplex, the phosphodiester backbone of the RNA template lies in the vicinity of the electrostatically positive concave surface on the α fingers. Furthermore, the backbone of the RNA primer also comes close to the other side of the positively charged surface of the α fingers. The multisequence alignment of RdRps using PSI-BLAST [7] shows that the basic residues corresponding to Lys106 and Arg109 in the α fingers are significantly conserved in several (+)ssRNA viruses.

References

[1] WHO, *J. Viral Hepatitis* **6** (1999) 35.
[2] J.W. Oh *et al.*, *J. Virol.* **73** (1999) 7694.
[3] C.A. Lesburg, *Nat. Struct. Biol.* **10** (1999) 937.
[4] S. Bressanelli *et al.*, *Proc. Natl. Acad. Sci. USA* **96** (1999) 13034.
[5] H. Ago *et al.*, *Structure* **7** (1999), 1417.
[6] J.L.H. Hansen *et al.*, *Structure* **5** (1997) 1109.
[7] S.F. Altschul *et al.*, *Nucleic Acids Res.* **25** (1997) 3389.

8-2 Crystal Structure of Phycobiliproteins

The light-harvesting system of algae is formed by phycobilisomes, which are composed of different phycobiliproteins: phycoerythrin (PE), phycocyanin (PC) and allophycocyanin (APC). Light energy was harvested and transferred in the direction of PE → PC → APC → photosynthetic reaction center with very high efficiency. Phycobiliproteins all carry different chromophores, such as phycoerythrobilin (PEB), phycocynobilin (PCB), phycovilobilin (PVB) and phycourobilin (PUB); these chromophores were arranged in a specific position and orientation in the protein to form a specific network for energy transfer.

The crystal structures of R-phycoerythrin from *Polysiphonia urceolata* (1.9 Å) [1, 2], R-phycocyanin from *Polysiphonia urceolata* (2.4 Å) and allophycocyanin from *Porphyra yezoensis* (2.2 Å) [3] have been solved by Liang's group and all of the high-resolution diffraction data of these proteins were collected at the BL-6B .

The crystal structure of R-PE (Fig.2) was solved by the MIR method and the three-dimensional structure of PUB was determined for the first time. According to the crystal structure of R-PE, the distances between chromophores were calculated and possible energy transfer pathways were suggested.

PC can be classified into two groups, as R-PC and C-PC, by the spectrum characteristic. Although C-PC only carries chromophore

PCB, we determined that R-PC contains both PEB and PCB. A structural comparison of R-PC and C-PC has revealed that the different spectrum characteristic was influenced by the different microenvironment of the chromophores.

The observation of the APC structure suggests that APC may exert biological function as a "loose hexamer", and that the aromatic pathways may play a very important role in energy transferring.

Energy-transfer pathways inside each phycobiliprotein (R-PE, R-PC and APC) and phycobilisome have been proposed.

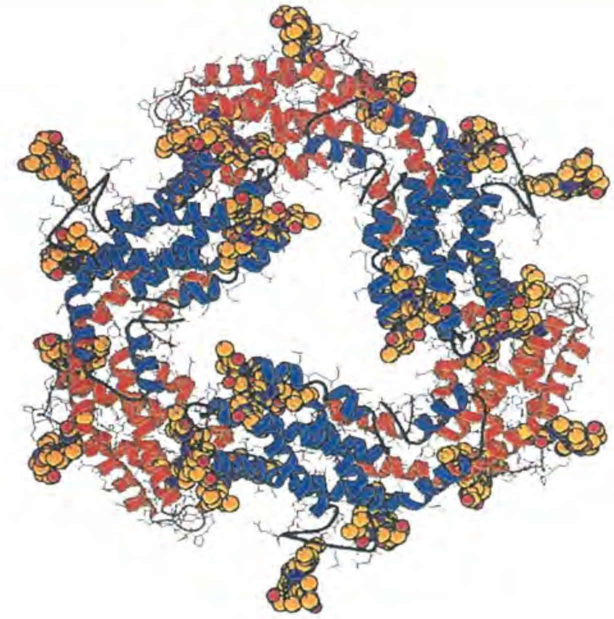

Figure 2.
Ribbon model of R-phycoerythrin from the *Polysiphonia urceolata* α subunits and β subunits, represented as ribbon, and chromophores, represented as the CPK model.

References
[1] W.R. Chang et al., *J. Mol. Biol.*, 262 (1996) 721.
[2] T. Jiang, J. P. Zhang, and D. C. Liang, *PROTEINS: Structure, Function, and Genetics*, **34** (1999) 224.
[3] J. Y. Liu, T. Jiang, J. P. Zhang, and D. C. Liang, *J. Biol. Chem.*, **274** (24) (1999) 16945.

8-3 Contribution of Water Molecules in the Interior of a Protein to the Conformational Stability

The conformational stability of globular proteins is low, only 40 kJ/mol, resulting from the combination of a hydrophobic effect, hydrogen bonding, conformational entropy, and other effects. In order to estimate the contribution of each factor to protein stability, changes in the stability and the structure due to mutations have been examined by differential scanning calorimetry and X-ray analysis, respectively, using many mutant human lysozymes (more than 100 mutants) with systematic and comprehensive substitutions. When the crystals of mutant proteins were small (less than 0.1 mm of a width), data collection for X-ray analysis of the mutant proteins was performed at Photon Factory. As shown in Fig.3, a new water molecule was found in the created cavity when a residue in the interior of a protein was substituted by a smaller residue (for example Ile to Val). Using a database of the stability/structure of mutant human lysozymes, it was estimated that (1) when one water molecule is newly introduced to the interior of the mutant protein, it destabilizes by 7.8 kJ/mol due to a decrease in the entropy of transferring the water molecule from the solvent to the interior of a protein, and (2) when a hydrogen bond in which the length is 3.0 Å is removed due to substitution, the mutant protein is destabilized by 5.1 kJ/mol for a protein-water interaction. Therefore, it could be concluded that a water molecule in a cavity created in the interior of a protein favorably contributes to the conformational stability, because most water molecules in the interior of a protein form three or four hydrogen bonds [1, 2].

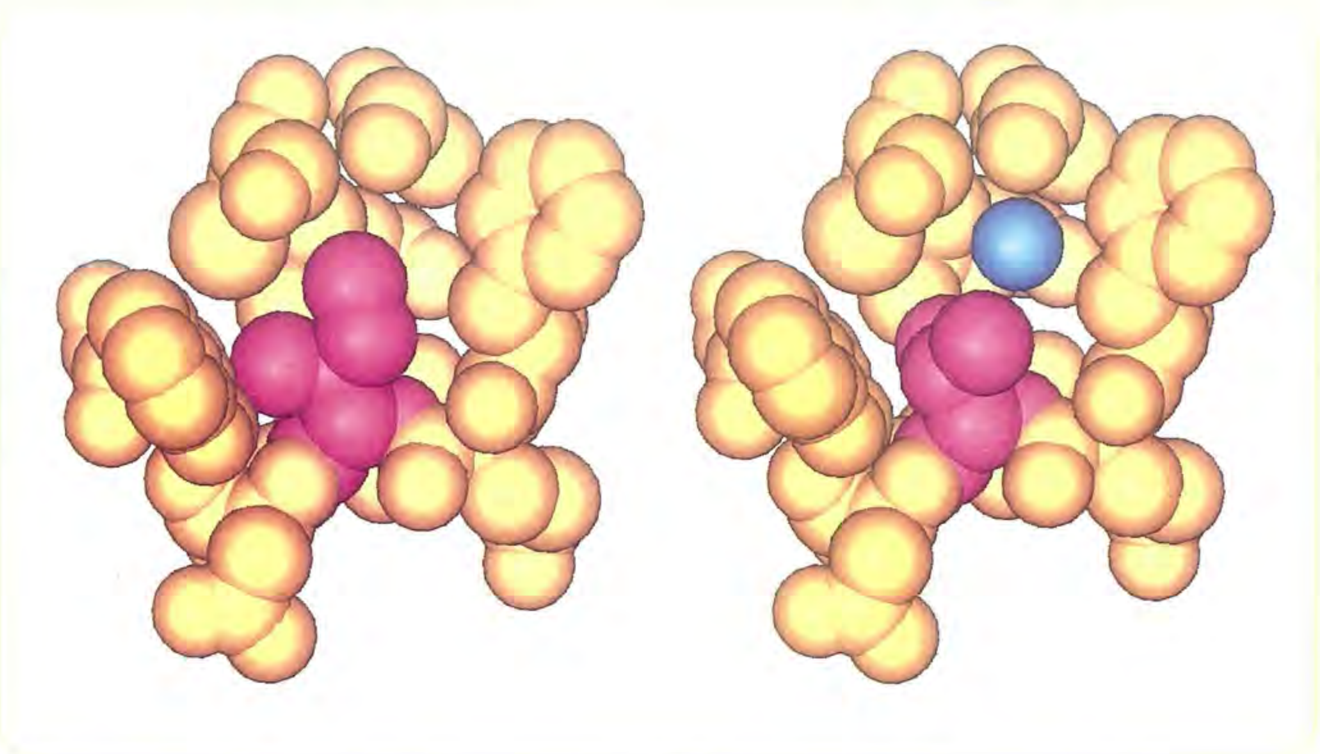

Figure 3.

Estimated contribution of a water molecule newly introduced to the interior of the mutant protein to the conformational stability. The structures in the vicinity of residue 59 in the wild-type human lysozyme and the mutant protein (Ile59 → Val) are shown in the left and right panels, respectively. The side-chain atoms at position 59 and an introduced water molecule are represented by purple and blue, respectively.

References

[1] K. Takano, J. Funahashi, Y. Yamagata, S. Fuzii, and K. Yutani, *J. Mol. Biol.* 274 (1997) 132.

[2] K. Takano, Y. Yamagata, J. Funahashi, Y. Hioki, S. Kuramitsu, and K. Yutani, *Biochemistry* 38 (1999) 12698.

8-4 Protein Folding Studied by Stopped-Flow X-Ray Solution Scattering using a CCD-Based X-Ray Detector

Knowledge of the molecular size and shape of a kinetic folding intermediate is inevitable in understanding the protein folding mechanism [1]. To obtain information about the size and shape of the intermediate, a stopped-flow X-ray scattering technique using synchrotron radiation is the most effective [2,3]. Although the signal-to-noise (S/N) ratio of the time-resolved X-ray scattering measurement using a one-dimensional position-sensitive proportional counter (PSPC) is low, a recently-developed charge-coupled device (CCD)-based X-ray detector has enabled us to increase the S/N ratio dramatically [4]. The scattering curves obtained by the CCD-based X-ray detector are coincident with those obtained by PSPC after corrections for image distortion, for non-uniformity of response and for contrast reduction of the X-ray image intensifier (XRII). The image distortion is due to the convex shape of the XRII, the non-uniformity of response is due to parallax effect and the effective pixel size changes, and the contrast reduction of the XRII is caused by the internal scattering of the XRII. These correction software programs have been developed by Ito [5]. Using this detector, the time-resolved X-ray scattering measurement of the kinetic refolding reaction of α-lactalbumin (α-LA) was performed. Figure 4 shows the time-dependent changes in the radius of gyration (R_g) of the protein. The results show that R_g of the kinetic folding intermediate formed within

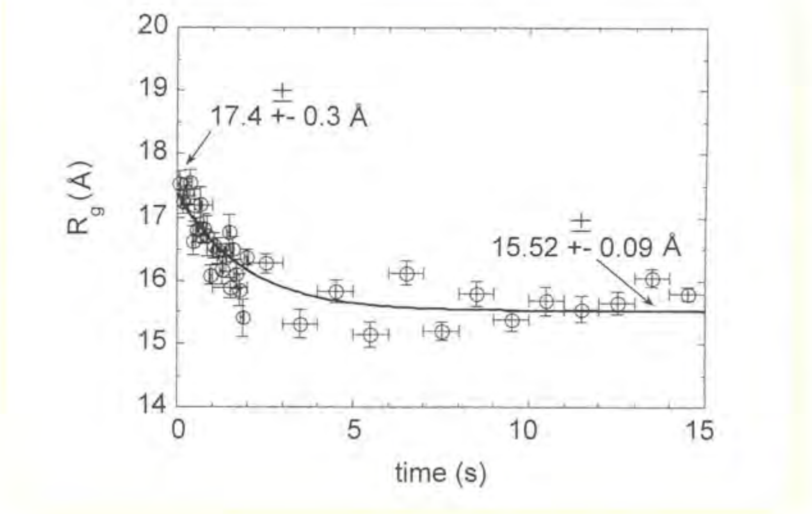

Figure 4.
Time-dependent changes in the R_g of α-LA. The solid line is a fitting curve assuming an exponential change in the R_g^2 with a rate constant of 0.55 s^{-1}. Conditions: 50 mM sodium cacodylate, 50 mM NaCl, 1 mM $CaCl_2$, pH 7.0, 5 °C, 4 mg/ml α-LA, 4→0.77 M GdnHCl (40-times accumulation).

100 ms of the refolding reaction (17.4 ± 0.3 Å) is the same as that of the equilibrium molten globule state (17.2 ± 0.2 Å [6]). Moreover, the Kratky plot of the folding intermediate is coincident with that of the equilibrium molten globule. Therefore, the size and shape of the early folding intermediate of α-LA are coincident with those of the equilibrium molten globule state. Combined with the previous results by stopped-flow circular dichroism [1], it is concluded that the folding intermediate of α-LA is the molten globule state, which has been proposed as a general intermediate in protein folding [1].

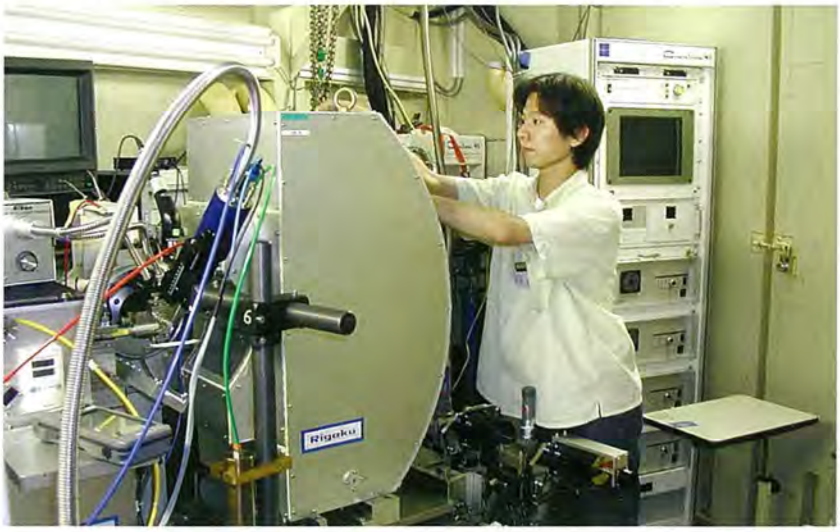

References

[1] M. Arai and K. Kuwajima, *Adv. Protein Chem.* **53** (2000) 209.
[2] H. Kihara, *J. Synchrotron Rad.* **1** (1994) 74.
[3] M. Arai et al., *J. Mol. Biol.* **275** (1998) 149.
[4] Y. Amemiya *et al., Rev. Sci. Instrum.* **66** (1995) 2290.
[5] K. Ito, Doctoral Thesis at the Graduate Univ. for Adv. Sci. **6** (1997).
[6] M. Kataoka *et al., Protein Sci.* **6** (1997) 422.

9 Medical Applications

9-1 Intravenous Coronary Angiography

Clinical applications of intravenous coronary angiography using a two-dimensional imaging system, an image intensifier - TV system (II-TV), was resumed at the PF-AR in May, 1999, after a long shut down of the AR. This work was done under collaboration between the University of Tsukuba and the Institute of Materials Structure Science.

Figure 1 shows a diagram of the new imaging system. We prepared a special hutch for clinical applications at a multi-pole wiggler (MPW) beam line, the AR-NE1, as shown in Fig.2. A large Si (311) crystal with the size of 650 mm by 80 mm was set in the AR-

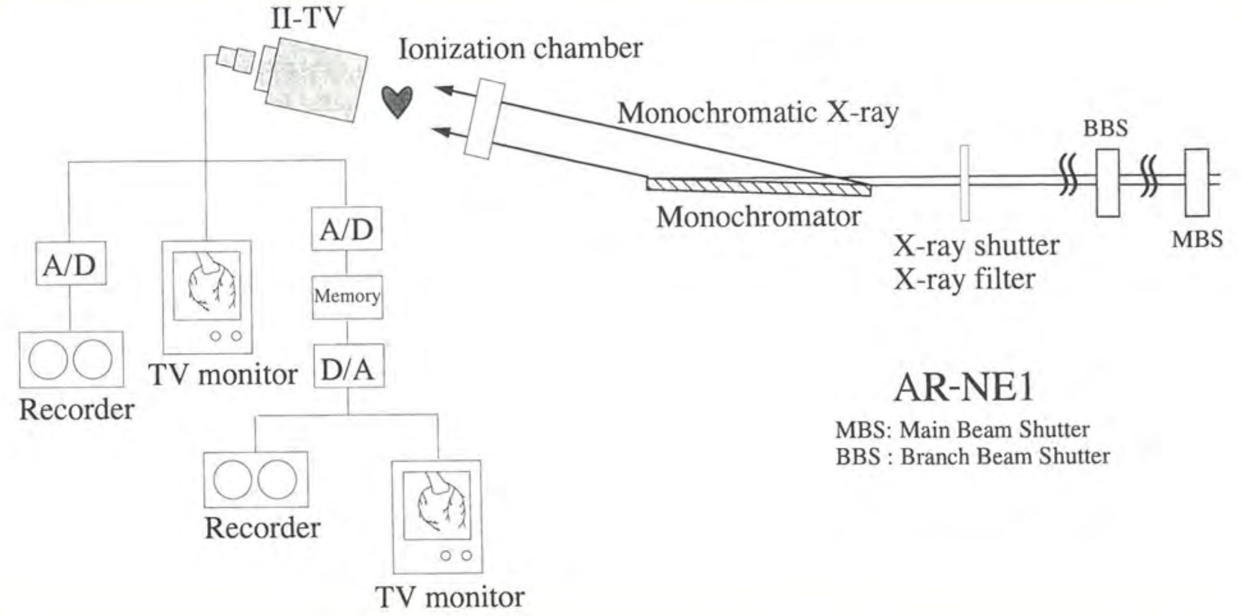

Figure 1.
Clinical imaging system using intense SR from the MPW at the AR-NE1. Asymmetrical reflection from a Si crystal was used to enlarge the vertical beam size. Images were taken by an Image Intensifier - TV (II-TV) system.

NEA2 station at about 40 m apart from the source point. The dimensions of the X-ray radiation were 8 mm vertically by 73 mm horizontally at the point as a characteristic feature of the MPW beam line. The vertical beam size of 8 mm was increased to approximately 120 mm by asymmetrical reflection from the crystal. For the purpose of reducing the X-ray exposure dose to patients as much as possible, a new high-speed X-ray shutter synchronized with TV operation and a high-speed-driven aluminum filter were placed before the crystal. The new high-speed X-ray shutter chosen was of the rotating-disk type, having aperture windows for the transmission of the radiation beam within a range of 2 ms to 33 ms. We can easily change the exposure time to take one image and the exposure rate by the shutter. The intensity of monochromatic X-ray radiation of 33 keV could be modulated within a range of 1/1-1/1000 by changing the thickness of an aluminum filter within a range of 0 mm to 30 mm. The monochromatic X-ray radiation was transmitted to the hutch through a pipe in a direction 13 degrees upwards from the crystal. At an entrance of the clinical hutch, a calibrated 20-ml ionization chamber of free air type was arranged for measuring the X-ray exposure dose to patients. The total maximum surface dose was limited for each patient by medical doctors.

Eight patients, from forty-five years old to seventy-five years old, were examined using the system. The PF-AR was operated at 5.0 GeV to decrease the 3rd higher harmonics X-ray photons from the single silicon crystal. The average stored current was 34 mA. Images were taken at above the K-edge energy of iodine (33.4 keV or 35 keV).

Three or four injections were made for seven patients at the LAO (left anterior oblique) position and the RAO (right anterior oblique) position to evaluate the right and left coronary arteries, and one injection was made for a patient at the LAO position to evaluate the right coronary artery. Contrast material (total amount of 35-40 ml) was

Figure 2.
Picture of inside the clinical hutch. A special chair for patients and a two-dimensional X-ray imaging system (II-TV) can be seen.

injected into the carotid vein at a rate of 17 - 20 ml/s. X-ray images were taken in 5 to 10 s at a rate of 10 images/s using a high-speed X-ray shutter; those images were recorded by a digital video-tape recorder. The right and left coronary arteries of seven patients and the right coronary artery of the one patient could be clearly detected with some stenosis regions. The advantage of the two-dimensional imaging system for coronary angiography was confirmed by the examinations; we plan to continue clinical applications.

References

[1] K. Hyodo, M. Ando, Y. Oku, S. Yamamoto, T. Takeda, Y. Itai, S. Ohtsuka, Y. Sugishita and J. Tada, J. Synchrotron Rad. 5 (1998) 1123.

[2] S. Ohtsuka, Y. Sugishita, T. Takeda , Y. Itai, J. Tada, K. Hyodo, M. Ando, British Journal of Radiology 72 (1999)24.

10 Applied Science

10-1 In-situ Observation of the Growth of a Crystalline SiO_2 Layer at the Interface during the Thermal Oxidation of Silicon by X-Ray Truncation Rod Scattering

Thermal oxide SiO_2 is a very important component of Si-LSI as a gate-insulating film of a MOS-FET. An ultra-thin film, such as 3nm, is required for Gbit-LSI. Thus, control of the SiO_2/Si interface is a very important issue to prevent increase in the leakage current for a thin film.

Thin films of SiO_2 were studied with X-ray reflectivity and crystal truncation rod (CTR) scattering; the results indicated the existence of

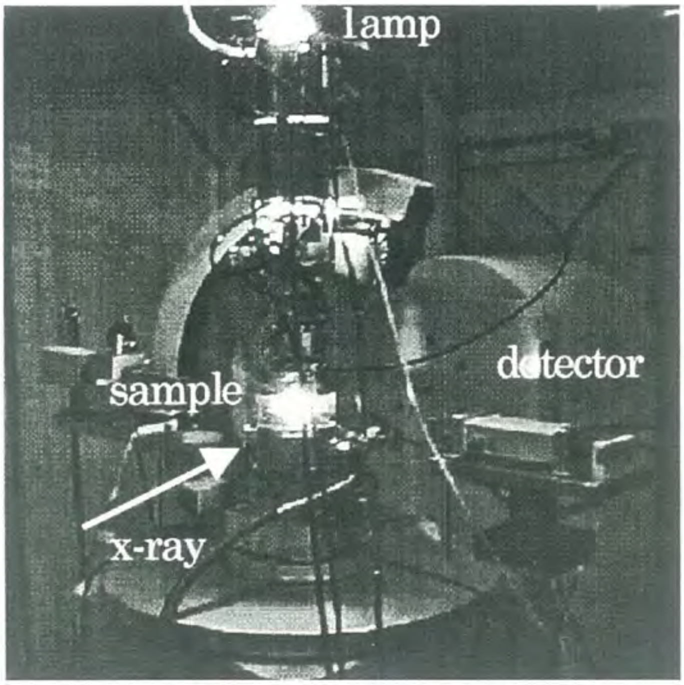

Figure 1.
Lamp annealing equipment set on the diffractometer.

a highly dense transition layer of about 1nm thick caused by crystalline SiO_2 at the interface. Here, an *in-situ* observation of the growth of crystalline SiO_2 during the oxidation of Si by N.Awaji et al. is introduced[1].

A focusing-type lamp annealing equipment is set on an in-plane diffractometer for an *in-situ* observation, as shown in Fig. 1. A Si(001) wafer was heated up to 900℃ from 300℃ after 3min by illumination from an infrared lamp. CTR scattering along the (1,1,L) rod was measured during oxidation at 900℃ in a diluted oxygen gas flow of O_2:N_2=1:9, where an asymmetric grazing-incident arrangement was used for sensitive detection. Figure 2 shows the CTR profile, the film thickness and structure estimated from CTR profiles with a peak around (1,1,0.52). The mechanism of thermal oxidation of Si is explained as follows. Although the crystalline SiO_2 generates at the initial stage and grows to a few nm, the thickness decreases to 1nm after being cooled at room temperature. This thickness is coincident with the previous results observed in oxide films prepared under various conditions. Therefore, the generation of crystalline SiO_2 at the interface is a fundamental phenomenon concerning thermal oxidation of Si, where the interface means the front of oxidation during a thermal treatment. However, it may be unstable because of a large interface stress, and it can exist only as 1-2 layers at the interface at room temperature.

Reference

[1] N.Awaji, Y.Sugita, and Y.Horii, Appl. Phys. Lett. 74 (1999) 2669.

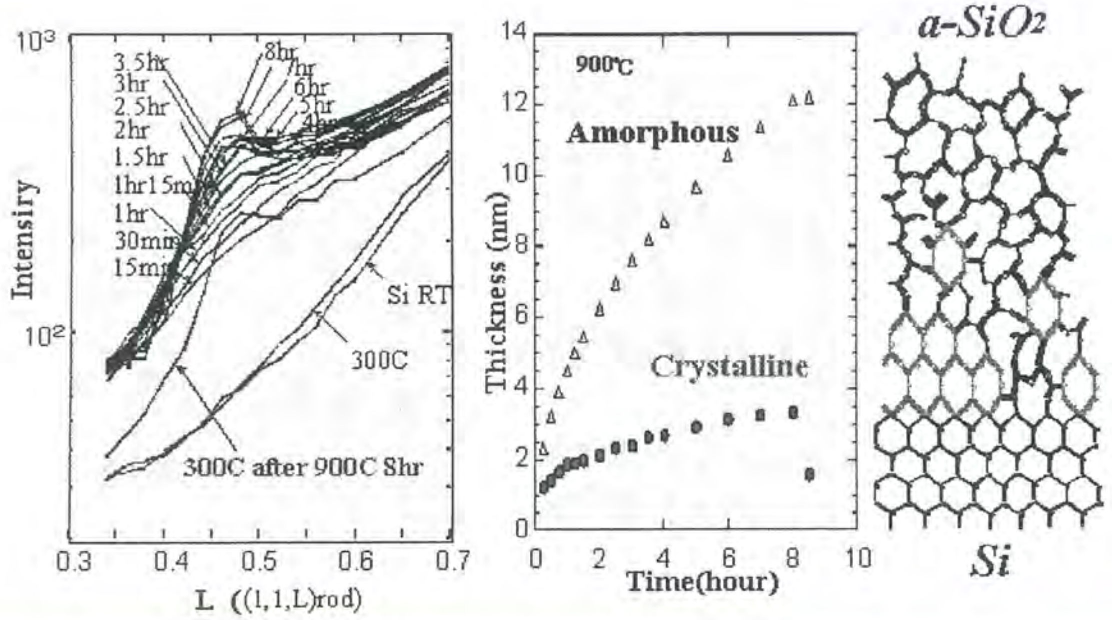

Figure 2.

CTR profiles along the (1,1,L) rod during thermal oxidation, the thickness of amorphous and crystalline SiO_2, and structure estimated from CTR.

10-2 XAFS Characterization of the Local Structure around Er in InP Grown by MO-CVD

Erbium is an interesting impurity as an emission center in compound semiconductors. Er-doped InP films was grown by MO-CVD in the temperature region of 530-610℃. The doping level was 2-8×10^{18} cm^{-3}. The photoluminescence intensity was high for samples grown at temperatures lower than 550℃.

H.Ofuchi et al. have studied the local structure around Er in InP thin films with XAFS [1]. The results are shown in Fig.3. The spectra are divided into two groups concerning the growth temperature, that is, lower or higher than 550℃. The XAFS spectra were calculated with FEFF6 [2] for four models and compared with measurements. The calculated spectrum for the substitution and interstitial structures were coincident with measurements for samples grown at low and high temperatures, respectively. The best fit for the former measurements are given in Table 1. The nearest bond lengths and coordination

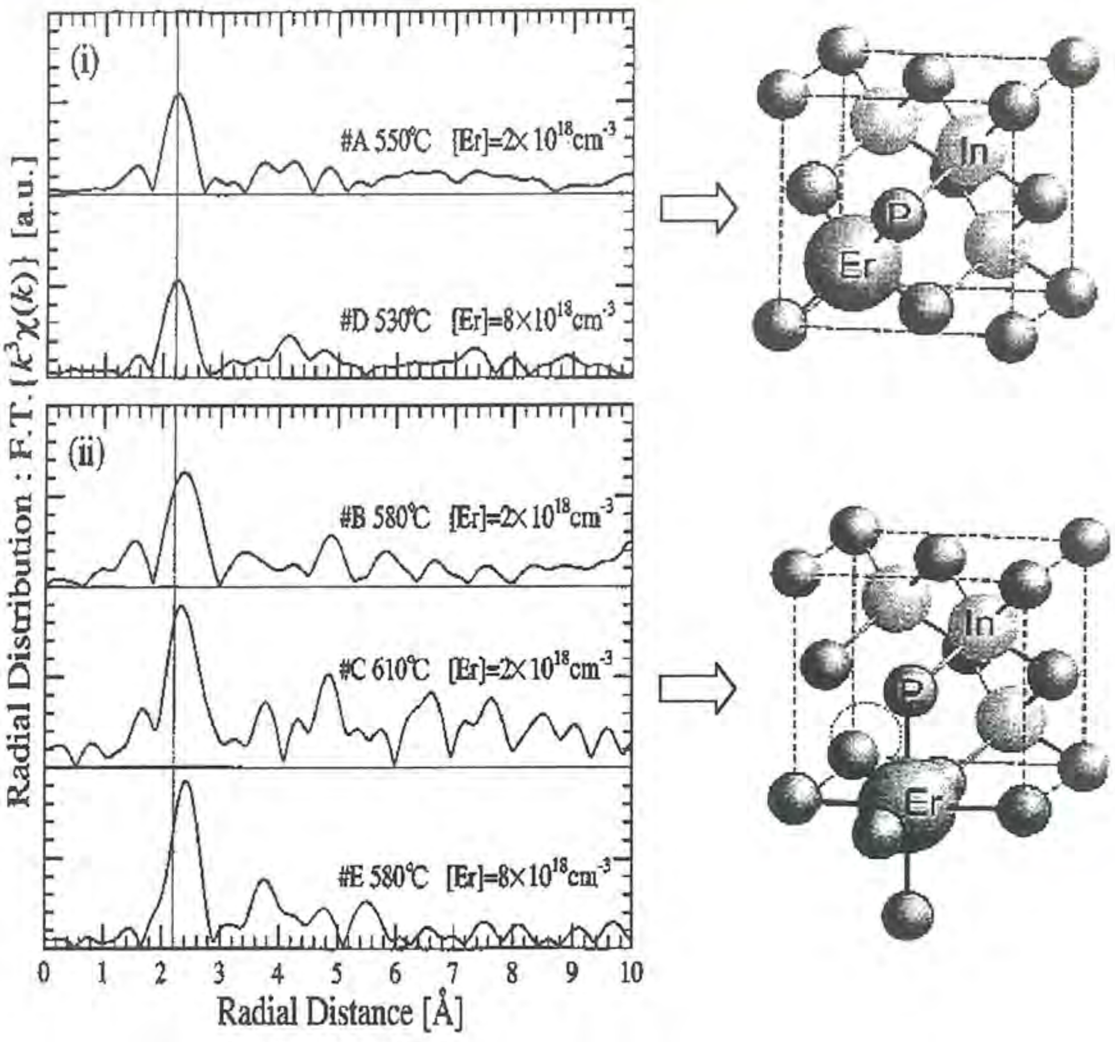

Figure 3.
Fourier-transformed spectra and the estimated local structure around Er in InP films grown by MO-CVD.

numbers agree with the substitution and interstitial structure, each other. [1].

Therefore, the growth temperature dependence of the photoluminescence efficiency in Er-doped InP films is due to the local structure around Er atoms. Er atoms substitute in-sites and form an Er-P zincblende structure at the row temperature, and the Er atoms occupy the interstitial site between P-P and form a rocksalt structure at high temperature during MO-CVD growth.

Table 1 Best-fit values of the parameter. Tg: growth temperature; n: doping level; r: bond length; N: coordination number.

Tg[˚C]	n[cm^{-3}]	r[Å]	N
550	2x10^{18}	2.67	3.8
530	8x10^{18}	2.67	3.9
580	2x10^{18}	2.77	6.2
610	2x10^{18}	2.78	6.1
580	8x10^{18}	2.77	7.3

References

[1] H.Ofuchi, D.Kawamura, J.Tsuchiya, N.Matsubara, M.Tabuchi, Y.Fujiwara, and Y.Takeda, J. Synchrotron. Rad. 5 (1998) 1061.

[2] S.I. Zabinsky, J.J. Rehr, A. Ankudinov, R.C. Albers and M.J. Eller, Phys. Rev. B52 (1995) 2995.

10-3 Construction of a Beamline with X-Ray Photoemission together with MBE

A system that joins angle-resolved X-ray photoemission with MBE a high-vacuum path has recently been constructed for studying semiconductor surfaces. Studies on a reconstructed surface on GaAs(100) or (111)B, InAs quantum dots on GaAs and a GaAs/AlAs quantum well are progressing. Here, photoemission spectroscopy for a (2×4) reconstructed GaAs(100) surface by K. Ono et al. is introduced.

A GaAs epitaxial layer was grown on GaAs(100) by MBE after removing of native oxide at 580˚C, where the surface was flattened by growing a buffer layer of 30 nm in thickness at a growth rate of 1ML/sec. The surface was observed by RHEED during growth and by LEED afterwards. The photoemission spectra around As 3*d* from a (2×4) reconstructed structure on GaAs(100) is shown in Fig. 4, where the incident X-ray energy was 100eV and θ_e is an angle detecting photoelectron. It has been revealed that the spectra are composed of a bulk component and three surface components caused by the (2×4) reconstructed structure. Also, the surface components were observed sensitively under the condition of θ_e= 60 deg.

Figure 4.
Photoemission spectra around As 3*d* from a (2×4) reconstructed structure on GaAs(100).

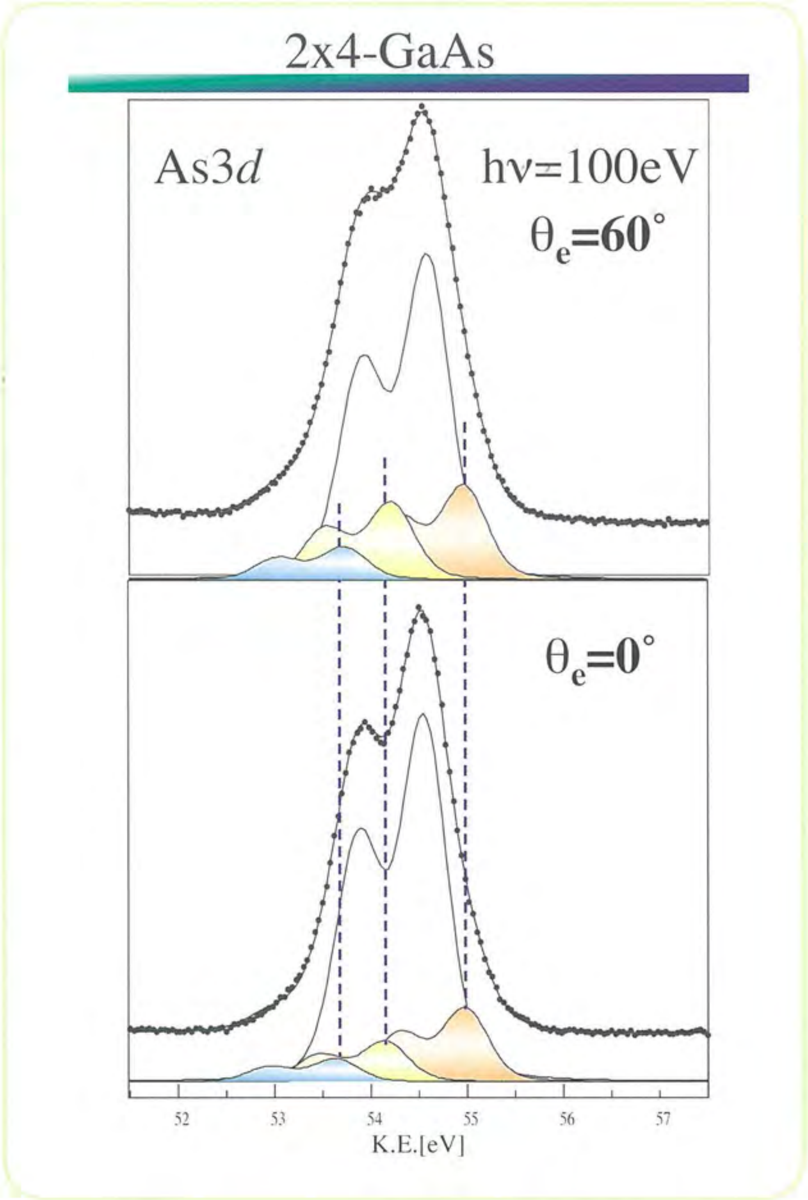

11 Instrumentation and Technique

11-1 A High-Resolution CCD-Based X-Ray Imaging System

X-ray CCD systems are often used for the detection of X-ray images. This type of system has the advantage of the classical photographic film or a plate, since it can be used for real-time imaging and shows higher linearity and a wider dynamic range. However, the spatial resolution is limited by the pixel size of the CCD, which is much larger than the grain size of a photographic plate. Sato et al. have developed a CCD-based X-ray micro imaging system combined with an X-ray magnifier using asymmetric Bragg reflection [1]. The system will be used for an X-ray polarization microscope.

The experimental setup is shown in Fig.1. The energy of the incident beam was tuned at 7.709 or 8.232 keV by using a Si(111) double crystal monochromator installed at the BL-15C. The monochromatic X-ray beam passed through a mesh was used as a reference, the vertical beam size being magnified by an asymmetrically cut Si(111) crystal, and detected by a CCD (Hamamatsu C4880-40) coupled with a phosphor screen and focusing optics. The CCD consists of 1280×1024 pixels of 6.7 μm square.
The magnification factor (M) could be controlled by changing the angle α between the diffracting plane and the crystal surface as

$$M = \frac{\sin(\theta_B + \alpha)}{\sin(\theta_B - \alpha)}$$

where θ_B is the Bragg angle. Four crystals with α = 0.0, 8.1, 10.9 and 12.8 degrees were prepared. With these asymmetrically cut crystals M could be controlled between 1 and 12.8 when the X-ray energy was 7.709 keV. M could be increased to 23.4 when the X-ray energy was increased to 8.232 keV. The results are shown in Fig.2. spatial resolution measured with a knife-edge test was 1.2 μm when

M= 23.4, which is much improved compared with that of 9.5 μm when M=1.

Also, a two-dimensional imaging system has been realized by placing another set of X-ray magnifiers perpendicularly. Real-time X-ray micro-imaging will be realized by using this CCD detection system.

Reference

[1] K. Sato, Y. Hasegawa, K. Kondo, K. Miyazaki, T. Matsushita and Y. Amemiya, Rev. Sci. Instrum., to be published.

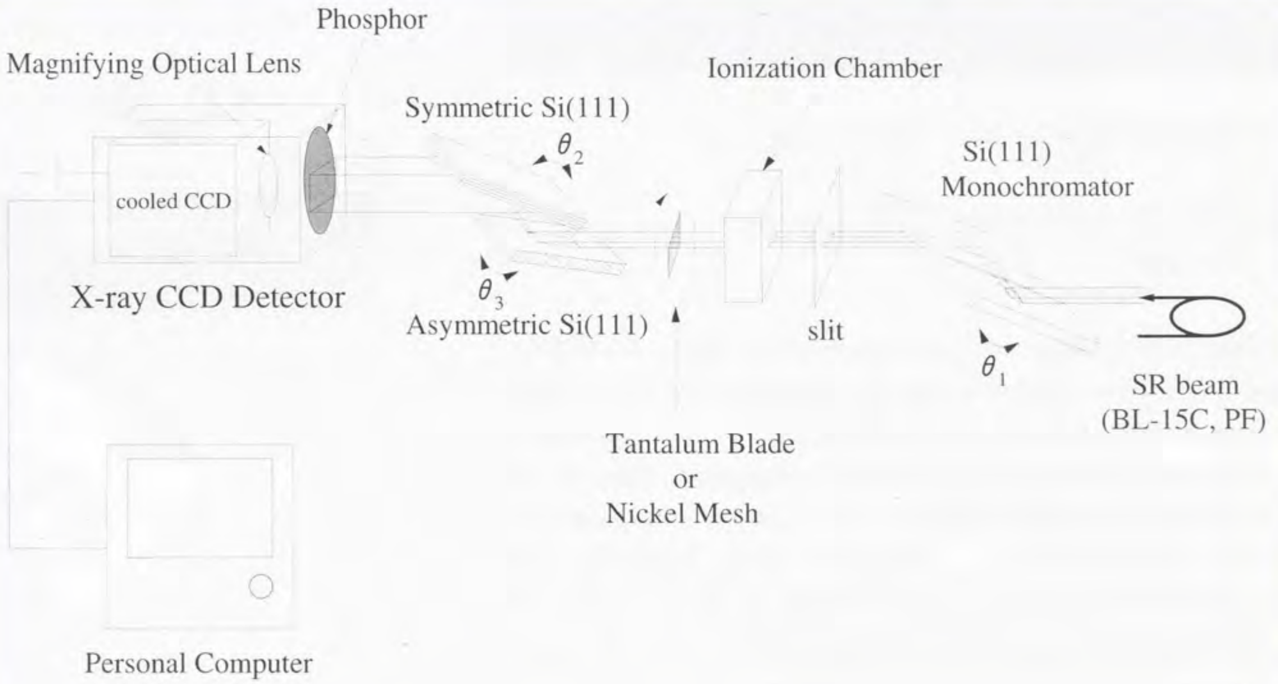

Figure 1.
Experimental setup of a high spatial-resolution x-ray CCD detector with a one-dimensional x-ray magnifier.

Figure 2.
Images of nickel meshes with 20 μm spacing taken with an X-ray CCD camera with one-dimensional X-ray magnification.

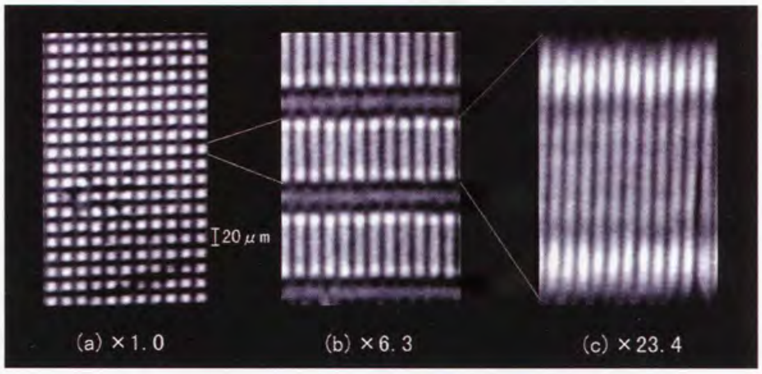

12 Theory

The theory group has been working on many subjects, such as second-order optical processes in the X-ray region, photoinduced phase transitions, and strongly correlated electron systems. Here, a few of our recent results are briefly introduced.

12-1 Electronic Relaxation Dynamics in Characteristic X-Ray Radiation Processes of Y Compounds

Mizouchi et al. have studied the electronic relaxation dynamics in the characteristic X-ray radiation processes of Y compounds. In recent years, the following second order optical processes have been experimentally observed in various insulators. First, an electron is excited from a deep core level to a conduction band by an incident X-ray. Then, another X-ray is radiated by a subsequent electronic transition from a shallow core level to a deep one. Especially, in YF_3 and YCl_3, three components appear in these radiation spectra as the result of this electronic transition. The peak position of one of these components is fixed, irrespective of the incident X-ray energy, while those of the other two components depend linearly on the incident energy. As for the X-ray absorption spectra in this energy region, they have only one peak with a long tail in its higher energy side. In order to explain these results, they consider a many-body problem in a four-band model composed of dispersionless deep, shallow core bands and conduction and valence bands. The Coulomb interactions among the conduction electrons and the valence holes are taken into account. In their model, the tail in the absorption spectra is due to new conduction-electron valence-hole pair creation through we can see a Coulomb interaction(Fig.1(a)). In the radiation spectra, we can see a peak whose position is fixed. It is due to luminescence which occurs after the electronic relaxation. This relaxation is such a one that the newly created electron-hole pairs go away from the sites where they were created (A in Fig.1(a)) The other two peaks are Raman-

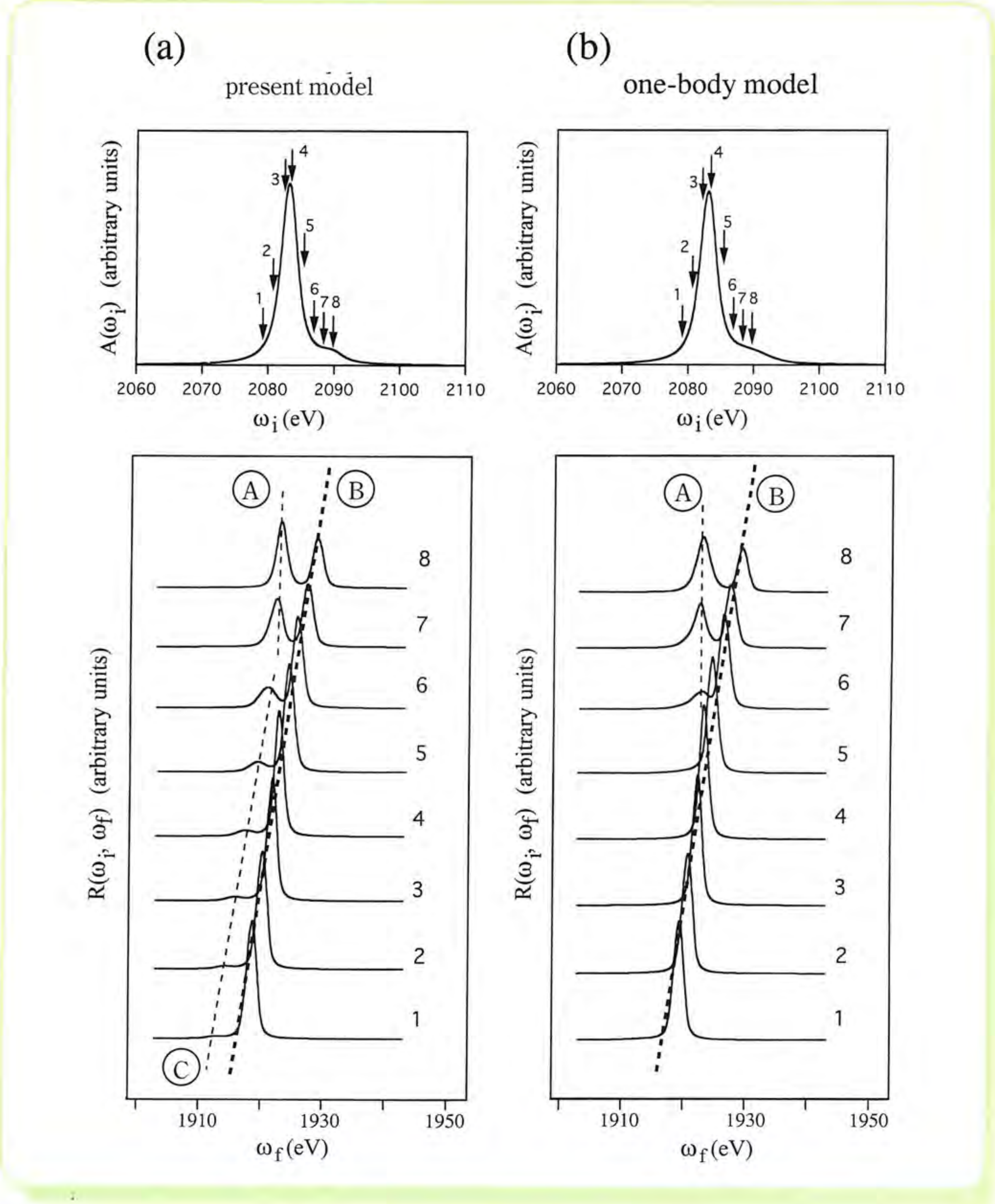

Figure 1.
Absorption (upper side, $A(\omega_i)$) and radiation (lower side, $R(\omega_i, \omega_f)$) spectra calculated with the present model (a) and a one-body model (b). ω_i and ω_f are the incident and radiated X-ray energies, respectively. The incident X-ray energies of the radiation spectra are indicated by the arrows in the absorption spectrum. A, B and C are components appearing in the radiation spectra. In (b), only two components A and B appear in the radiation spectra.

scattering peaks. In one of these final states, only one conduction electron remains (B in Fig.1(a)). In the other final state, one conduction electron remains together with one conduction-electron valence-hole pair (C in Fig.1(a)). With this model, the experimental results have been well-explained. On the other hand, the appearance of the three components cannot be explained by a one-body picture with two different conduction bands, although the characteristics of the absorption spectrum can be explained (Fig.1(b)).

12-2 Lattice Relaxation Dynamics of Excitons in Photoinduced Structural Phase Transitions

Mizouchi and Nasu have studied the lattice-relaxation dynamics of a photogenerated single exciton, which finally results in a macroscopic domain in insulating solids[1]. This domain-formation phenomenon is usually called a "photoinduced structural phase transition"(PSPT). In the relaxation processes which can finally produce in such a macroscopic domain, the exciton does not stay within a single adiabatic potential surface, but transits diabatically between the different potential ones. Hence, a full-quantum-mechanical treatment is indispensable. As one of the models for this

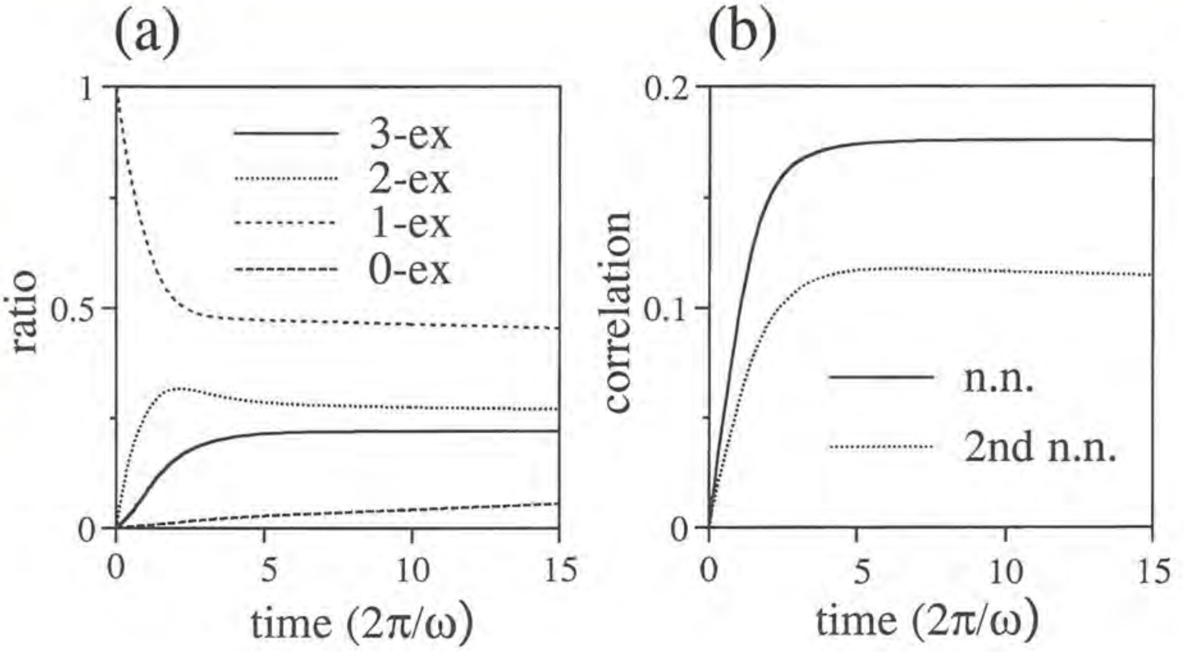

Figure 2.
Proliferation process of excitons. The time evolutions of the ratios of exciton states (a) and the density-density correlation functions between excitons (b) are shown. In (a), n-ex denotes the ratio of n-exciton states. In (b), n.n. and 2nd n.n. denote the correlation functions between nearest-neighboring excitons and the 2nd nearest-neighboring ones, respectively. The initial state is the Franck-Condon state with a single exciton.

type of phase transition, they considered a strongly coupled many exciton-Einstein phonon system interacting with a reservoir. Through the interaction between the system and the reservoir, we can take into account the dissipation of phonons as well as the radiative and nonradiative transitions of excitons. Within the Markov approximation for the reservoir, the time evolution of the density matrix is numerically calculated. As a first work, they have shown the characteristics of the early time dynamics of the domain formation, against dissipations and nonradiative relaxation processes. In Fig. 2, we show the proliferation of excitons. The initial state is the Franck-Condon state with a single exciton. As the time passes, the ratio of 1-exciton states reduces. The ratios of 2- and 3-exciton states increase, and then maintain finite values for a long time (Fig.2(a)). The density-density correlation functions between the nearest-neighboring excitons, and between second nearest-neighboring ones, also increase, and then maintain finite values for a long time (Fig.2(b)). Therefore, a photogenerated single exciton proliferates during the relaxation processes, and then these excitons aggregate with each other.

Reference
[1] H. Mizouchi and K. Nasu, J. Phys. Soc. Jpn. 69(2000)1543.

EXPERIMENTAL FACILITIES

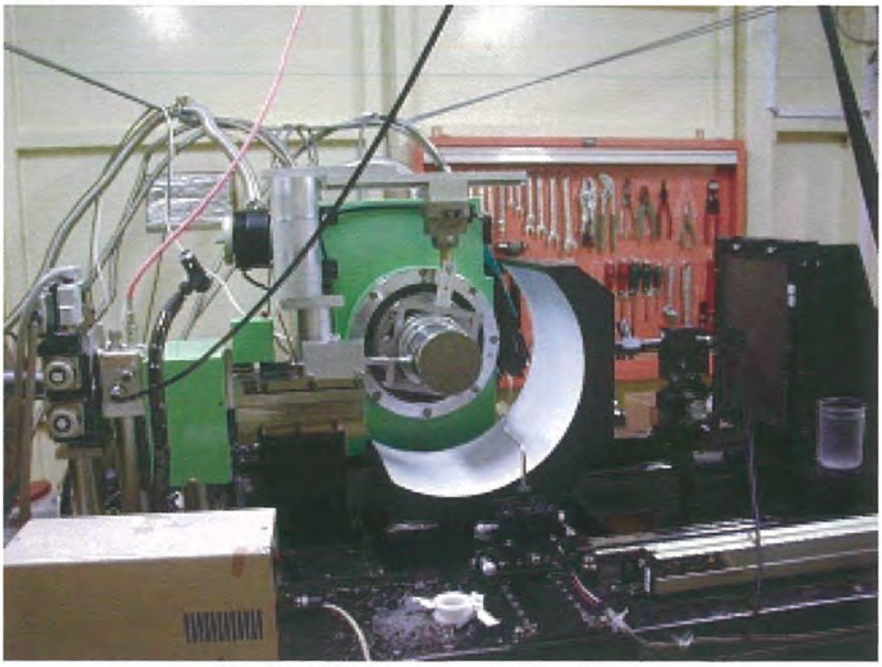

BL-1B MPD system reconstructed for single-crystal analysis at low temperature

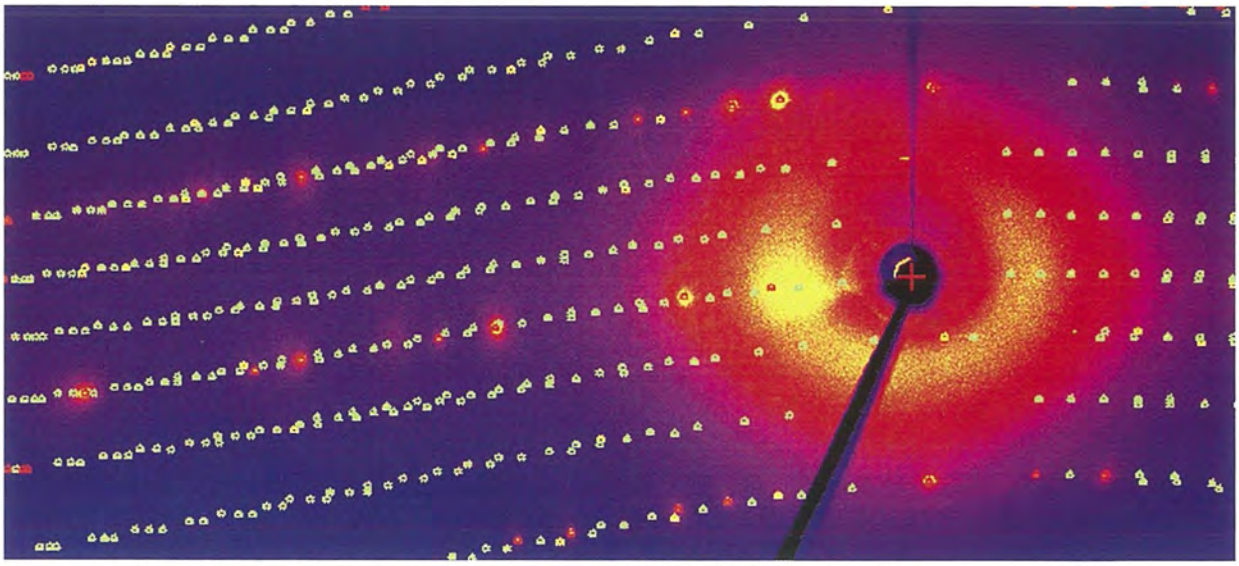

An oscillation photograph of a single crystal $(DBr\text{-}DCNQI)_2Cu$ at room temperature

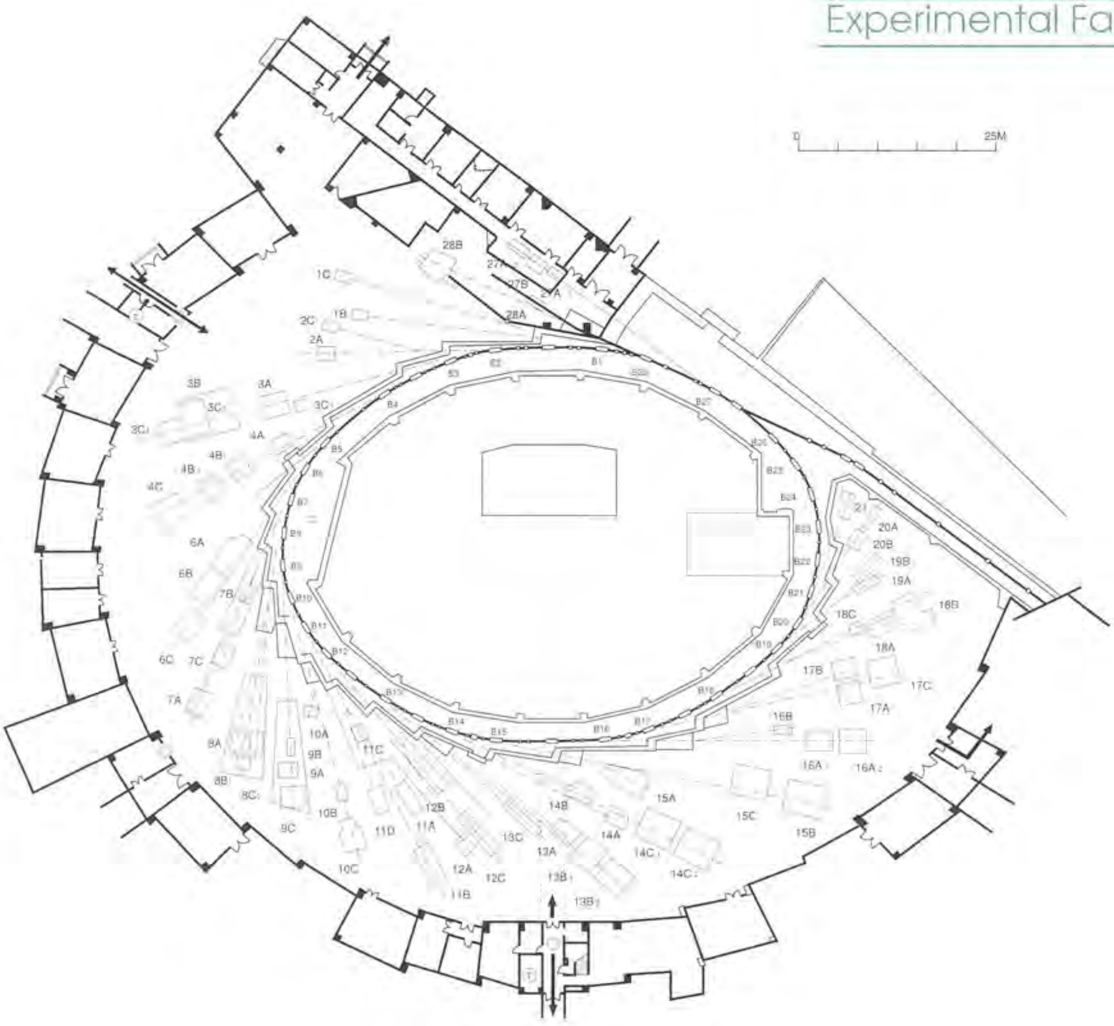

PF 2.5 Gev ring and beamlines.

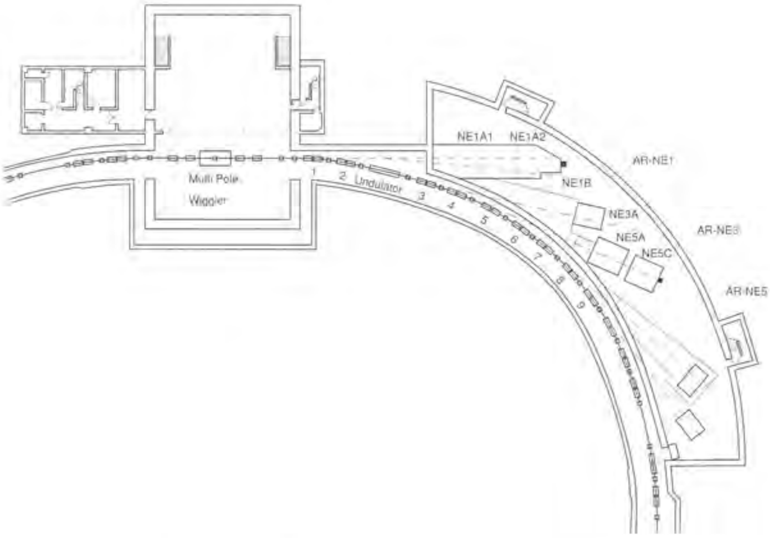

PF-AR (6.5 Gev) beamlines.

Summary of Experimental Stations

1

Table 1 List of Experimental Stations at PF Storage Ring

Experimental Station			Spokesperson
BL-1			
	A	X-ray powder diffraction under extreme condition	H.Nakao
	B	Soft X-ray photoelectron spectroscopy (under construction)	T.Saitoh
BL-2		(Undulator)	
	A	Soft X-ray spectroscopy	Y.Kitajima
	B	Soft X-ray spectroscopy	A.Yagishita
BL-3			
	A	X-ray diffraction and scattering	M.Tanaka
	B	VUV and soft X-ray spectroscopy	Y.Azuma
	C1	X-ray diffraction	H.Adachi, H.Kawata
	C2	Characterization of X-ray optical elements	M.Ando
	C3	X-ray magnetic Bragg scattering by means of white X-rays	H.Adachi, H.Kawata
BL-4			
	A	Trace element analysis, X-ray microprobe	A.Iida
	B1	Micro-crystal and -area structure analysis	K.Ohsumi
	B2	Powder diffraction	M.Tanaka
	C	X-ray diffraction and scattering	Y.Murakami
BL-6			
	A	Macromolecular crystallography by Weissenberg camera	N.Igarashi
	B	[TARA] Macromolecular crystallography by Weissenberg camera	N.Sakabe [TARA], M.Suzuki
	C	[TARA] Macromolecular crystallography by Weissenberg camera	N.Sakabe [TARA], M.Suzuki
BL-7			
	A	[RCS] Soft X-ray photoelectron spectroscopy	K.Amemiya [RCS], K.Ito
	B	[RCS] Surface photochemical reaction and angle resolved photoelectron spectroscopy	K.Amemiya [RCS], K.Ito
	C	X-ray spectroscopy and diffraction	M.Nomura
BL-8			
	A	[Hitachi] Soft X-ray spectroscopy	K.Ogata [Hitachi], K.Mase
	B	[Hitachi] EXAFS	K.Ogata [Hitachi], K.Mase
	C	[Hitachi] X-ray tomography and X-ray microscopy	K.Ogata [Hitachi], K.Mase

Experimental Station			Spokesperson
BL-9			
	A	XAFS	M.Nomura
	C	[NEC] EXAFS and X-ray toptgraphy/diffraction	H.Kimura [NEC], M.Nomura
BL-10			
	A	X-ray diffraction/scattering, crystal structure analysis	M.Tanaka
	B	XAFS	N.Usami
	C	Small-angle X-ray scattering of solution sample	K.Kobayashi
BL-11			
	A	Soft X-ray spectroscopy	Y.Kitajima
	B	Surface EXAFS, soft X-ray spectroscopy	Y.Kitajima
	C	VUV spectroscopy(solid state)	A.Kakizaki
	D	Angle-resolved photoelectron spectroscopy(under construction)	T.Saitoh
BL-12			
	A	Characterization of VUV-SX optical elements, soft X-ray spectroscopy	A.Yagishita
	B	VUV high-resolution spectroscopy	K.Ito
	C	XAFS	M.Nomura
BL-13		(Multipole Wiggler/Undulator)	
	A	High pressure X-ray diffraction (under construction)	T.Kikegawa
	B1	Surface-sensitive XAFS, X-ray diffraction	T.Kikegawa
	B2	High pressure & high temperature X-ray diffraction	T.Kikegawa
	C	Soft X-ray photoemission spectroscopy and XAFS	K.Mase
BL-14		(Vertical Wiggler)	
	A	Crystal structure analysis, EXAFS	S.Kishimoto
	B	High-precision X-ray optics	K.Hirano
	C1	Medical applications and General purpose (X-ray)	K.Hyodo
	C2	High pressure and High temperature X-ray diffraction	T.Kikegawa
BL-15			
	A	Small-angle X-ray scattering of muscle and alloys	H.Kamikubo
	B1	White X-ray topography and X-ray magnetic Bragg scattering	H.Kawata
	B2	Surface and interface diffraction	H.Sugiyama, H.Kawata
	C	High-resolution X-ray diffraction	K.Hirano
BL-16		(Multipole Wiggler/Undulator)	
	A1	General purpose (X-ray)	Y.Murakami
	A2	X-ray diffraction and scattering	Y.Murakami
	B	Soft X-ray spectroscopy	J.Adachi
BL-17			
	A	[Fujitsu] XAFS	S.Komiya [Fujitsu], A.Iida
	B	[Fujitsu] Photochemical vapor deposition	S.Komiya [Fujitsu], A.Iida
	C	[Fujitsu] Grazing incident X-ray diffraction, X-ray fluorescence analysis	S.Komiya [Fujitsu], A.Iida
BL-18			
	A	[ISSP] Angle-resolved photoelectron spectroscopy of surfaces and interfaces	T.Kinoshita [ISSP], A.Kakizaki
	B	Macromolecular crystallography(Weissenberg and Laue)	M.Suzuki
	C	High pressure X-ray powder diffraction	T.Kikegawa

Experimental Station			Spokesperson
BL-19		(Revolver Undulator)	
	A	〔ISSP〕 Spin-resolved photoelectron spectroscopy(Mott detector)	T.Kinoshita〔ISSP〕， A.Kakizaki
	B	〔ISSP〕 Spin-resolved photoelectron spectroscopy (SPLEED)	S.Shin〔ISSP〕， A.Kakizaki
		〔ISSP〕 Soft X-ray emission spectroscopy	
BL-20			
	A	VUV spectroscopy	K.Ito
	B	〔ANBF〕 White and monochromatic beam general purpose X-ray station	G.Foran〔ANBF〕， K.Ohsumi
BL-21		〔Light Source Division〕 Beam position monitoring	M.Kobayashi〔Light Source Div.〕
BL-27		(Beamline for experiments using radioisotopes)	
	A	Radiation biology， soft X-ray photoelectron spectroscopy	K.Kobayashi
	B	Radiation biology， X-ray diffuse scattering	N.Usami
BL-28		(Elliptical Multipole Wiggler/Undulator)	
	A	VUV and soft X-ray spectroscopy with circularly polarized undulator radiation	T.Koide
	B	Spectroscopy and scattering with polarized X-rays	T.Iwazumi
TARA		Tsukuba Advanced Research Alliance	
RCS		Research Center for Spectrochemistry， University of Tokyo	
ISSP		Institute for Solid State Physics， University of Tokyo	
ANBF		Australian National Beamline Facility	

Table 2 List of Experimental Stations at PF-AR

Experimental Station			Spokesperson
AR-NE1		(Elliptical Multipole Wiggler/Undulator)	
	A1	High resolution Compton and magnetic Compton scattering	H.Kawata
	A2	Coronary Angiography	K.Hyodo
	B	Spectroscopy with circularly polarized soft X-rays	T.Koide
AR-NE3		(Undulator)	
	A	Nuclear resonant scattering	X.Zhang
AR-NE5			
	A	Medical applications	K.Hyodo
	B	Bunch-purity and beam-position monitoring	S.Kishimoto
	C	High pressure and high temperature X-ray diffraction	T.Kikegawa
AR-NE9			
	B	〔Accelerator Department〕 Vacuum science and technology	K.Kanazawa〔Acc.Dept.〕

Table 3 X-Ray Beamline Optics

Branch Beamline	Acceptance Horiz. (mrad)	Type of Monochromator	Mirror	Photon Energy (keV)	Beam Size (H × V) (mm)	Photon Flux at Sample Position	Energy Resolution (ΔE/E) ×10^{-4}	Reference
BL-1B	2	Flat Double Crystal Si(111)	Bent Cylinder	6 ~ 21	0.5 × 0.3	8 × 10^{10}/4mm^2 (8.3 keV, 300 mA)	~ 5	
BL-3A	4	Double Crystal Si(111) Sagittal Focusing	Collimating Focusing Mirrors (Fused Quartz)	6 ~ 20	100 × 5 2 × 1		~ 2	1 - 3
BL-3C2	2	Double Crystal Si(111), Si(311)	None	4 ~ 20 6 ~ 34	5 × 2	1 × 10^{10} 2 × 10^9		
BL-3C3	2	Double Crystal Si(111)	None	5 ~ 30 or white	20 × 4 0.1 × 0.1			
BL-4A	6	Double Crystal Sagittal Focusing	None	4 ~ 20	50 × 4 4 × 1		~ 2	4
BL-4B1	4.5	Double Crystal Si(111)	None	4 ~ 35	50 × 5		~ 2	5
BL-4B2	4.5	Double Crystal Si(111)	Bent Cylinder	6 ~ 20	13 × 2		~2	
BL-4C	2	Flat Double Crystal Si (111)	Bent Cylinder	6 ~ 21	1.0 × 0.6		~5	6, 7
BL-6A	1.2	Bent Si(111) (α = 0, 6.0°, 7.8°, 9.5°, 11.4°, 13.7°, 16.5°)	Bent Plane Fused Quartz	5 ~ 25	2.5 × 1			8
BL-6B	1	Bent Si(111)	Bent Plane Si Pt-coated		1.7 × 0.2			9
BL-6C	2	BentSi (111)	Bent Plane Si Pt-coated					
BL-7C	4	Double Crystal Si (111) Sagittal Focusing	Double Mirror Fused Quartz Focusing	4 ~ 20 (4 ~ 13)	5 × 1	1 × 10^{10}/6mm^2 (8 keV, 300 mA) (1 × 10^{11} when focused)	~ 2	10 - 12
BL-8C1/C2	5	Channel-Cut Si(220), Si(111), Si(400)	None	5 ~ 40	50 × 5	6 × 10^9/mm^2 (10 keV, 300 mA)	~2	
BL-9A	3	Double Crystal Si (111)	Collimating and Focusing Bent Conical Mirrors (Rh Coated) Double Flat Mirror (Rh/Ni Coated)	2.2 ~ 15	1 × 0.3	4 × 10^{11}(9 keV, 300 mA)	2	32
BL-9C	3.5	Double Crystal Si(111), Si(311)	Bent Cylinder	4 ~ 23 or white	1 × 1		~ 2	

Experimental Facilities

Branch Beamline	Acceptance Horiz. (mrad)	Type of Monochromator	Mirror	Photon Energy (keV)	Beam Size (H×V) (mm)	Photon Flux at Sample Position	Energy Resolution (ΔE/E) $\times 10^{-4}$	Reference
BL-10A	1	Si(111), Si(311) Quartz(100), PG(002) Curved Si(111) ($\alpha \sim 4^\circ$, 8°)	None	5 ~ 25	10×3		10 ~ 5	13
BL-10B	2	Channel-Cut	None	6 ~ 30	5×1	1×10^{9}/7mm^2	1	
BL-10C	4	Double Crystal Si(111)	Bent Cylinder	4 ~ 10	2.4×0.6	~10^{11}/1.5mm^2 (8 keV, 400 mA)	2	
BL-12C	2	Double Crystal Si(111) Si(311)	Bent Cylinder	6 ~ 23	0.65×0.4	5×10^{10}/1mm^2 (8.0 keV, 300mA) w.Si(111)	~ 2	14
BL-13B1/B2	4	Double Crystal Si(111), Si(220) Sagittal Focusing	Bent Plane Fused Quartz	4 ~ 30	4×1		~ 2	15
BL-14A	1.28 (Vertical)	Double Crystal Si (111) Si (311) Si (553)	Bent Cylinder Pt-coated Fused Quartz	5.1 ~ 19.1 9.9 ~ 35.6 22.7 ~ 84.5	2×1 at focus 5×38		2	16
BL-14B	2.2 (Vertical)	Double Crystal Si(111),	None	10 ~ 57	5×14		2	
BL-14C	1.3 (Vertical)	Double Crystal Si(111), Si(220)	None	5 ~ 100 or white	6×35		2	
BL-15A	2	Bent Crystal Ge(111) ($\alpha = 8.0^\circ$)	Bent Plane, Fused Quartz Pt-coated	8.0 (fixed)	0.5×0.25	9×10^{10}/mm^2 (8.0 keV, 350 mA)	~ 10	17
BL-15B1/B2	2	Double Crystal Si (111)	Bent Cylinder	5 ~ 20 or white	0.6×0.4	10^{11}/1mm^2 (8.0keV, 350mA)	~ 2	
BL-15C	2	Double Crystal Si (111)	None	4 ~ 30	60×6			
BL-16A1/A2	1	Double Crystal Si(111) Sagittal Focusing	Bent Plane (Pt on SiC) for Vertical Collimating Bent Plane (Pt on SiO_2) for Vertical Focusing	4 ~ 25	1.3×0.4	~1×10^{13} (8.3 keV, 300 mA)	~ 1	18
BL-17A	4	Double Crystal Si(111)	None	5 ~ 13	100×10		~ 2	19
BL-17C	1	Double Crystal Si(111)	None	5 ~ 13	20×5		~ 2	20

Branch Beamline	Acceptance Horiz. (mrad)	Type of Monochromator	Mirror	Photon Energy (keV)	Beam Size (H×V) (mm)	Photon Flux at Sample Position	Energy Resolution (ΔE/E) $\times10^{-4}$	Reference
BL-18B	2	Double Crystal Si(111) Si(220) Ge(111) Ge(220)	Bent Cylinder Fused Quartz, Pt-coated	6 ~ 30	0.6×0.4	1.1×10^{10} (12.4 keV, 300 mA) Si(111)	~ 2	21
BL-18C	1	Double Crystal Si(111)	Cylinder Fused Quartz, Pt-coated	6~25	0.07×0.04		~2	
BL-20B	2	Channel Cut Si(111) Double Crystal Sagittal focusing Si(111)	None	4 ~ 25	26×3		~ 2	22
BL-27B	4	Double Crystal Si(111)	None	4 ~ 20	100×6		~ 2	23
BL-28B	H: 4 V:0.2	Double Crystal Si(111) Si (220) InSb(111)	Pre-mirror Bent Cylinder Si Pt- & Ni-coated Post-mirror Bent Plane Fused Quartz Pt- & Ni-coated	2 ~ 10	2.4×0.3	3×10^{10} (9 keV, 300mA Si(220) Pc ~ 0.5)	~ 2 (7.25 keV, Si(111)) ~ 0.2 (6.5keV, Si(311))	24
AR-NE1A1	2	Double Bent Crystal Si(111)		40 ~ 180	2×0.5	5×10^{12} (60 keV, 35mA)	8	25, 26
AR-NE1A2	2	Asym. cut Single Crystal Si(311)		33 ~ 38	75×120 ~140	10^{10}(33 keV)	60	25, 27
AR-NE3	H:0.3 V:0.03	Double Crystal Si(111) High-resolution Monochromator Nuclear Monochromator of Single Crystal $^{57}Fe_2O_3$(777)		5 ~ 25 8 ~ 26 14.4	15×2	1×10^{3} (14.4 keV)	1 5×10^{-3} 1×10^{-1}	28
AR-NE5A	10	Asym.Cut Single Crystal Si(311) (α = 4° ~ 6°) Double Crystal Si (311)		20 ~ 40 25 ~ 70	150×8 (33.2 keV)	5×10^{9}	60 1	29, 30
AR-NE5C	3	Double Crystal Si (111)		30 ~ 100	60×5		5	31

References

[1] S. Sasaki et al., Rev. Sci. Instrum. 63 (1992) 1047.
[2] K. Kawasaki et al., Rev. Sci. Instrum. 63 (1992) 1023.
[3] T. Mori and S. Sasaki, Rev. Sci. Instrum. 66 (1995) 2171.
[4] A. Iida et al., Rev. Sci. Instrum. 66 (1995) 1373.
[5] K. Ohsumi et al., Rev. Sci. Instrum. 66 (1995) 1448.
[6] H. Iwasaki et al., Rev. Sci. Instum. 60 (1989) 2406.
[7] Photon Factory Activity Report 1995 #13 (1996) E-1.
[8] N. Sakabe et al., Rev. Sci. Instrum. 66 (1995) 1276.
[9] Photon Factory Activity Report 1995 #13 (1996) C-1.
[10] M. Nomura and A.Koyama, KEK Internal 93-1 (1993) .
[11] M. Nomura et al., KEK Report 91-1 (1991).
[12] M. Nomura and A. Koyama, in "X-ray Absorption Fine Structure", ed. by S. S. Hasnain, Ellis Horwood, Chichester, 1991, p.667.
[13] S. Sasaki, Rev. Sci. Instrum. 60 (1989) 2417.
[14] M. Nomura and A. Koyama, KEK Report 95-15 (1996).
[15] Photon Factory Activity Report 1994 #12 (1995) C-6.
[16] Y. Satow and Y. Iitaka, Rev. Sci. Instrum. 60 (1989) 2390.
[17] Y. Amemiya et al., Nucl. Instrum. Meth. 208 (1983) 471.
[18] Photon Factory Activity Report 1994 #12 (1995) E-3.
[19] Photon Factory Activity Report 1988 #6 (1988) I-15.
[20] Y. Horii et al., Rev. Sci. Instrum. 66 (1995) 1370.
[21] N. Watanabe et al., Rev. Sci. Instrum. 66 (1995) 1824.
[22] R.F. Garret et al., Rev. Sci. Instrum. 66 (1995) 1351.
[23] H. Konoshi et al., Nucl. Insrtum. Meth. A 372 (1996) 322.
[24] T. Iwazumi et al., Rev. Sci. Instrum. 66 (1995) 1691.
[25] H. Kawata et al., Rev. Sci. Instrum. 60 (1989) 1885.
[26] Photon Factory Activity Report 1994 #12 (1995) E-4.
[27] T. Iwazumi et al., Rev. Sci. Instrum. 63 (1992) 419.
[28] X. Zhang et al., Rev. Sci. Instrum. 63 (1992) 404.
[29] K. Hyodo et al., Handbook on SR IV, (1991) 55.
[30] Y. Itai et al., Rev. Sci. Instrum. 66 (1995) 1385.
[31] T. Kikegawa et al., Rev. Sci. Instrum. 66 (1995) 1335.
[32] M. Nomura and A. Koyama, J. Synchrotron Rad. 6 (1999) 182.

Table 4 VUV and Soft X-ray Beamline Optics

Branch Beamline	Acceptance Horiz. (mrad)	Type of Monochromator	Grating Groove Density (l/mm)	Photon Enegy (eV)	Beam Size (mm)	Typical Resolving Power (E/ΔE) and Photon Flux (/s)	Reference
BL-2A Undulator	K = 0.5 ~ 2.2 λ_u = 6cm	Double Crystal InSb (111), Si (111)	——	1740 ~ 5000	< 1 ϕ	2000, 8000 10^{10}	1 - 3
BL-2C Undulator	K = 0.55 ~ 2.2 λ_u = 6 cm	Varied-Space Plane Grating	1000 2200	250 ~ 1400	0.9 × 0.1	5000 ~ 10000 10^{11} ~ 10^{10}	4, 5
BL-3B	10 2	Grazing Incidence R = 24 m $\alpha + \beta = 165^\circ$	200 600 1800	10 ~ 280	< 2 ϕ	200 ~ 3000 10^{12} ~ 10^{9}	6, 7
BL-7A (RCS)	6 1	Plane Grating	1200 2400	10 ~ 1000	2 × 1	500	8
BL-7B (RCS)	6 4	1m Seya-Namioka	1200 2400	5 ~ 50	1 × 1	1000	9
BL-8A (Hitachi)	0.5 1	SX700 Plane Grating	1221	38 ~ 2300	5 × 1	2000 10^{10}	
BL-8B (Hitachi)	3 0.5	Double Crystal InSb (111), Si (311)	——	1700 ~ 14000	1.9 × 0.5	5000	10
BL-11A	5 1	Varied-Line-Space Plane Grating	300 800 1200	70 ~ 1900	2 × 1	500 ~ 5000 10^{12} ~ 10^{9}	12 - 14 36
BL-11B	4 0.6	Double Crystal InSb (111), Ge (111)	——	1760 ~ 3910	5 × 2	2000 10^{10}	3, 15, 16
BL-11C	4.8 3	1m Seya-Namioka	1200	4 ~ 35	~1 ϕ	1000	17
BL-11D	4 2	Grazing Incidence On-blaze Mount R_1 = 52.5 m R_3 = 22.5 m	2400	G_3 20~280 G_1 200~1200			
BL-12A	2.2 0.34	Grazing Incidence R = 2 m $\alpha = 88^\circ$	1200	30 ~ 1000	2 × 3	1000 10^{9}	18
BL-12B	5 3.6	6.65 m Off-Plane Eagle	1200 4800	5 ~ 30	——	2.5 × 10^{5} 10^{4}	19 - 21
BL-13C Undulator	K = 0.3 ~ 4.2 λ_u = 18 cm	Grazing Incidence R = 50 m $\alpha + \beta = 173.2^\circ$	350 750	70 ~ 500 150 ~ 1000	5 × 1	1000 ~ 6000 10^{12} ~ 10^{10}	22, 23
BL-16B Undulator	K = 0.5 ~ 5.75 λ_u = 12 cm	Grazing Incidence R = 24 m $\alpha + \beta = 168.6^\circ$	400 900 2000	40 ~ 550	< 1 ϕ	1000 ~ 10000 10^{12} ~ 10^{10}	24 - 26
BL-17B (Fujitsu)	8 1	Toroidal Mirror	——	——	10 × 1	——	——

Experimental Facilities

Branch Beamline	Acceptance Horiz. (mrad)	Type of Monochromator	Grating Groove Density (l/mm)	Photon Enegy (eV)	Beam Size (mm)	Typical Resolving Power (E/ΔE) and Photon Flux (/s)	Reference
BL-18A (ISSP)	2 2	Grazing Incidence R = 3 m $\alpha+\beta = 160^\circ$ R = 6.65 m $\alpha+\beta = 167.5^\circ$	300 600 1200 500	15 ~ 150	< 1 ϕ	1000~2000 10^{11} ~ 10^{9}	27
BL-19A Revolver Undulator (ISSP)	K = 1.0 ~ 9.0 λ_u = 16.4 cm K = 0.5 ~ 1.25 λ_u = 5 cm K = 0.5 ~ 2.5 λ_u = 7.2 cm K = 1.0 ~ 5.0 λ_u = 10 cm	Grazing Incidence R = 2 m $\alpha+\beta = 160^\circ$ R= 4 m $\alpha+\beta = 170^\circ$	600 1200 600 1200	12 ~ 250	< 0.7 ϕ	1000 10^{12}	28, 29
BL-19B Revolver Undulator (ISSP)		Varied-space Plane Grating	800 2400	10 ~ 1200	< 0.5 ϕ	400~4000 10^{12} ~ 10^{11}	29
BL-20A	28 5	3m Normal Incidence	1200 2400	5 ~ 40	2 × 1	300 ~ 30000 10^{12} ~ 10^{8}	30
BL-27A	5 0.5	Double Crystal InSb (111)	——	1800 ~ 6000		2000	31
BL-28A Helical Undulator	K_x = 0.23 ~ 3 K_y = 0.23 ~ 6 λ_u = 16 cm	Grazing Incidence R = 2 m $\alpha+\beta = 160^\circ$ R = 4 m $\alpha+\beta = 170^\circ$	600 1200 600 1200	30 ~ 250	< 0.5 ϕ	1000 10^{10}	32
AR-NE1B Helical Undulator	Kx = 0.2 ~ 3 Ky = 0.2 ~ 6 λ_u = 16 cm	Grazing Incidence R = 10m $\beta = 89^\circ$	1200 2400	250 ~ 1800	~ 0.8 × 0.2	1000~5000 10^{11} ~ 10^{9}	33,34

References

[1] H. Maezawa et al., Nucl. Instrum. Meth. A246 (1986) 310.

[2] Y. Kitajima et al., Rev. Sci. Instrum. 63 (1992) 886.

[3] Y. Kitajima, J. Elec. Spec. Relat. Phenom. 80 (1996) 405.

[4] Y. Yan and A. Yagishita, KEK Report 95-9 (1995).

[5] M. Watanabe et al., Proc. SPIE Vol. 3150 (1997) 58.

[6] A. Yagishita et al., Nucl. Instrum. Meth. A306 (1991) 578.

[7] S. Masui et al., Rev. Sci. Instrum. 63 (1992) 1330.

[8] H. Namba et al., Rev. Sci. Instrum. 60 (1989) 1909.

[9] H. Namba et al., Rev. Sci. Instrum. 60 (1989) 1917.

[10] K. Ogata et al., Photon Factory Activity Report 1994 #12 (1995) 164.

[11] Photon Factory Activity Report 1988 #6 (1989) I-13.

[12] K. Amemiya et al., J. Synchrotron Rad. 3 (1996) 282.

[13] K. Amemiya et al., Proc. SPIE Proceedings 3150 (1997) 171.

[14] Y. Kitajima et al., J. Syncrotron Rad. 5 (1998) 729.

[15] T. Ohta et al., Nucl. Instrum. Meth. A246 (1986) 373.

[16] M. Funabashi et al., Rev. Sci. Instrum. 60 (1989) 1983.

[17] Photon Factory Activity Report 1982/1983 (1984) V-15.

[18] Photon Factory Activity Report 1992 #10 (1993) I-2.

[19] K. Ito et al., Appl. Opt. 25 (1986) 837.

[20] K. Ito et al., Appl. Opt. 28 (1989) 1813.

[21] K. Ito and T. Namioka, Rev. Sci. Instrum. 60 (1989) 1573.

[22] N. Matsubayashi et al., Rev. Sci. Instrum. 63 (1992) 1363.

[23] H. Shimada et al., Rev. Sci. Instrum. 66 (1995) 1780.

[24] E. Shigemasa et al., KEK Report 95-2 (1995).

[25] Photon Factory Activity Report 1995 #13 (1996) E-2.

[26] E. Shigemasa et al., J. Synchrotron Rad. 5 (1998) 777.

[27] S. Suzuki et al., Activity Report of SRL-ISSP 60 (1989).

[28] A. Kakizaki et al., Rev. Sci. Instrum. 60 (1989) 1893.

[29] A. Kakizaki et al., Rev. Sci. Instrum. 63 (1992) 367.

[30] K. Ito et al., Rev. Sci. Instrum. 66 (1995) 2119.

[31] H. Konishi et al., Nucl. Instrum. Meth. A372 (1996) 322.

[32] Y. Kagoshima et al., Rev. Sci. Instrum. 63 (1992) 1289.

[33] Y. Kagoshima et al., Rev. Sci. Insturm. 66 (1995) 1696.

[34] Y. Kagoshima et al., Rev. Sci. Instrum. 66 (1995) 1534.

[35] Y. Kitajima, J. Synchrotron Rad. 6 (1999) 167.

[36] Y. Kitajima et al., J. Elec. Spectrosc. Relat. Phenom. 101-103 (1999) 927.

Table 5 Timetable of the Machine Operation in FY 1999.

PF: PF ring

🟥 tuning and ring machine study

☰ ring machine study

short maintenance and /or machine study

experiment using SR (36 nmrad)

BA beam alignment

HC high curent study of beamline

3Gev SB: single bunch

MB: multi bunch

AR: PF-AR

▨ experiment using SR(full day)

BF/E B-factory commissioning and /or experiment using RS

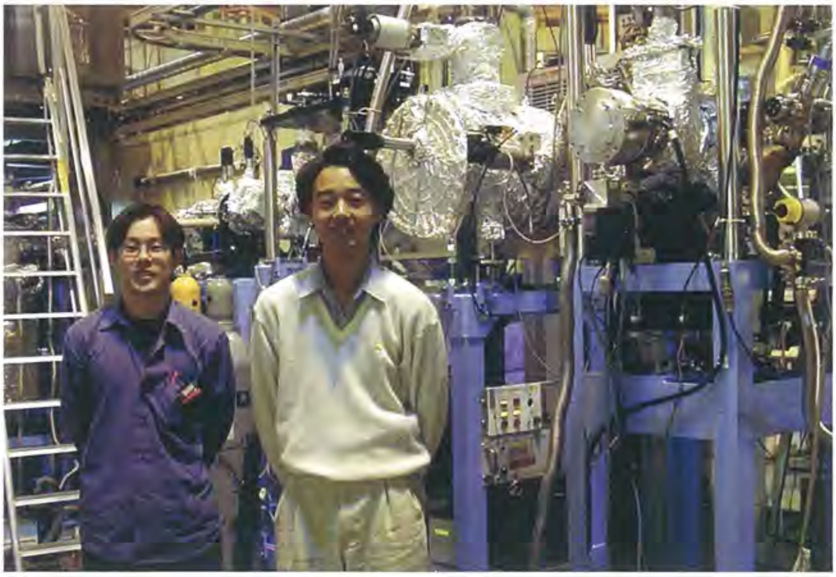

2 Reconstruction and Upgrading of Beamlines

2-1 BL-7A, New Soft X-Ray Beamline for Surface XAFS and XMCD Experiments

A new beamline, the BL-7A, is now being constructed by the Research Center for Spectrochemistry (Univ. of Tokyo) in collaboration with the Photon Factory. The main objective of this beamline is to perform surface XAFS and XMCD measurements at the K edges of light elements (C, N, and O) and the L edges of 3d transition metals. Since such experiments require intense and stable X-rays over a wide photon energy range, we have adopted a constant-included-angle monochromator equipped with a varied-line-spacing (VLS) plane grating. The layout of the beamline is schematically shown in Fig. 1. Three gratings, whose groove densities are 300, 650, and 1300 l/mm, are mounted with an included angle of 174.5°. Soft X-rays in the energy range of 100-1500 eV will be available. The ultimate resolving power is expected to be ~10000 with a photon flux of $\sim 10^9$ s^{-1}, while $\sim 10^{11}$ s^{-1} will be attained at a resolving power of 1000.

In addition to the conventional XAFS and XMCD measurements, the development of a novel experimental technique, 'surface dispersive XAFS', is being planned. The vertical dispersion plane of the X-rays at the exit slit (S2; ~2 mm width in this case) is rotated by 90° with a plane mirror (Mr), which is inclined by 45° around the light propagation. Thus, the horizontally dispersed X-rays illuminate the sample, and Auger electrons emitted from each position of the sample surface are collected at once by a position-sensitive electron analyzer (SCIENTA SES-2002). Accordingly, the Auger electron yield XAFS spectra can be obtained with one shot, and the data-acquisition time for the surface XAFS measurements is expected to be reduced to ~1/100 of that for the conventional method. This new technique will allow us to perform time-resolved observations of various surface reactions.

The commissioning of the beamline is scheduled for the autumn of 2000, and it will possibly be opened from April, 2001.

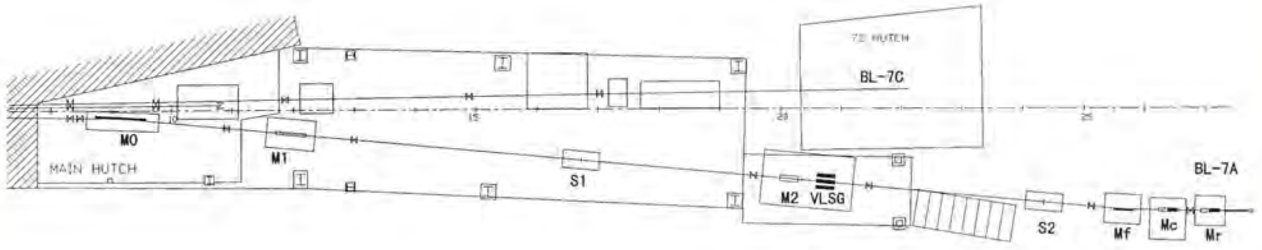

Figure 1. Plan view of BL-7A. VLSG varied-line-spacing plane grating.

2-2 BL-9A, Performance of a XAFS Beamline using Bent Conical Mirrors

A new XAFS beamline, the BL-9A, has been opened for users. The beam line consists of a Si(111) double-crystal monochromator sandwiched between a pair of bent conical mirrors. Since the first bent conical mirror collimates the diverging synchrotron radiation, there is practically no divergence in the beam at the monochromator position. Thus, it is not necessary to limit the beam size and/or the divergence in order to maintain an energy resolution sufficient for usual XAFS experiments. The second mirror is used to focus the beam at the sample position. Therefore, both high flux, high energy resolution and small focus size can be realized simultaneously. Detailed design parameters can be found in references 1 and 2.

The first beam, by using the above-described optics, was obtained in January 2000. As shown in Fig.1, a hump in the XANES spectrum of 6 μm thick copper foil is clearly observed, which is more prominent than the usual one taken with Si(111). The energy resolution did not change upon changing the beam size hitting the monochromator, which indicates that the first bent conical mirror functions as expected. Under this condition, the flux is estimated to be 4×10^{11} photons/s under a stored current of 300 mA, which is *ca.* 8-times higher compared with that realized at the BL-12C, which uses a bent cylindrical focusing mirror [3].

The ratio of higher orders can be reduced to less than *ca.* 10^{-6} of the fundamental by using a pair of flat mirrors for higher order elimination. The focus size, 1 mm×0.3 mm in FWHM, is larger than

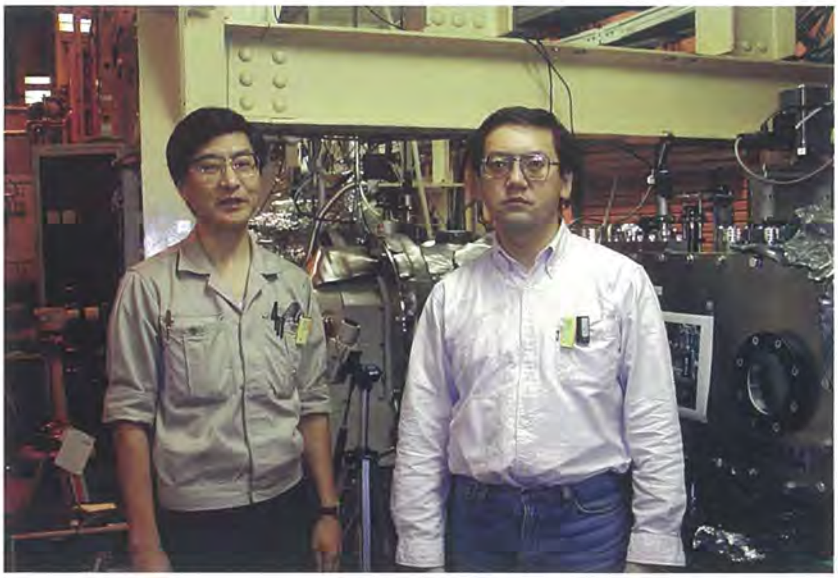

that expected from ray-tracing simulation. Several reasons are considered: 1) the alignment of the optical components is not optimized, 2) the deformation of the mirrors by clamping and/or bending and 3) the effect of the slope error is larger than estimated. However, since we could not obtain a smaller focus by limiting the beam size hitting the first mirror, the second reason will be excluded. Detailed peformance will be published elsewhere [4]. Presently, the further optimization of the beamline is progressing.

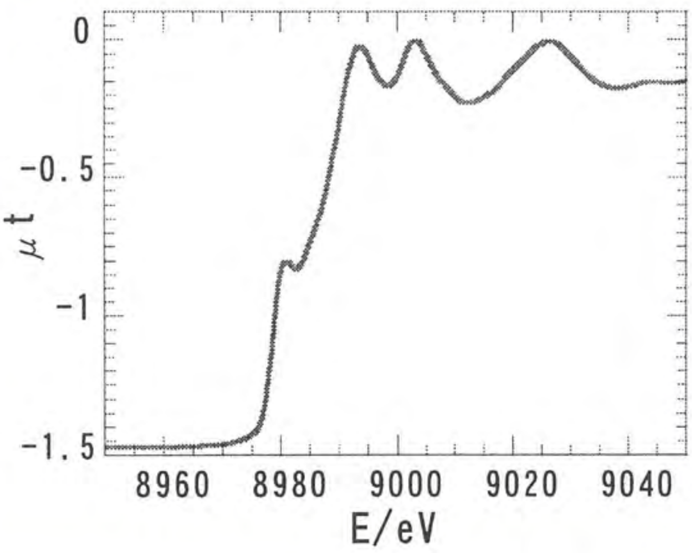

Figure 1.

XANES spectrum of a 6 μm thick copper foil. Both high flux, 4×10^{11} photons/s/300mA, and high energy resolution are realized simultaneously.

References

[1] Photon Factory Activity report #14 (1997) E-5.

[2] M.Nomura, and A. Koyama, J. Synchrotron Rad. 6 (1999)182.

[3] M. Nomura and A. Koyama, KEK Report 95-15 (1996).

[4] M. Nomura and A. Koyama, J.Syncro tron Rad. to be published.

2-3 Inprovement of the Experimental Hutch

BL-14C has been reconstructed to provide general-purpose hard X-rays from the superconducting vertical wiggler. The original BL-14C, which was constructed in 1983, having a main hutch for a double-crystal monochromator and an experimental hutch, had provided both vertically polarized white X-rays and monochromatic X-rays using a double-crystal monochromator for such experiments as topography, Compton-scattering experiments, high-temperature and high-pressure experiments, coronary angiography, micro-angiography, computed tomography and phase-contrast imaging. Improvements to the experimental hutch and the beamline monochromator were necessary to perform many kinds of experiments, of which the number had been increasing in recent years.

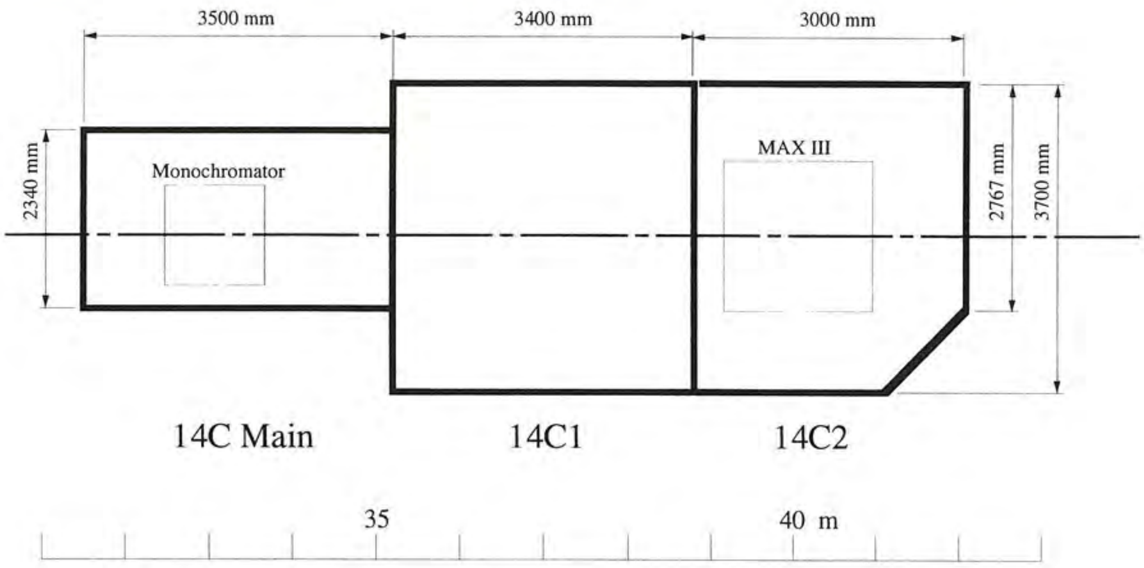

Figure 1.
Plan view of the BL-14C. There are two experimental hutches and a main hutch for a monochromator.

The improvements to the experimental hutch and the beamline monochromator are as follows:

1) The BL-14C experimental hutch is separated into two hutches in tandem: the upstream hutch is the BL-14C1 for general experiments, including phase-contrast imaging experiments using an X-ray interferometer (99S2-002); the downstream hutch is the BL-14C2 for high-temperature and high-pressure experiments, where a new experimental apparatus, MAX999, will be installed. White X-rays or monochromatic X-rays using a new double-crystal monochromator are available in both hutches. A vacuum pipe is installed in the BL-14C1 in the case of introducing white or monochromatic X-rays to the BL-14C2 through the BL-14C1. It is not necessary to remove MAXⅢ to perform the other kinds of experiments in the BL-14C1.

2) It was rather difficult to adjust the original double-crystal monochromator, which was installed in 1983, to obtain the desired monochromatic X-ray beam. A new double-crystal monochromator, which was adapted as a double-crystal monochromator, whose performances had already been verified at other beamlines, for the vertically polarized beam, is installed in the main hutch of the BL-14C .

Figure 1 shows a plan view of the new BL-14C. The double-crystal monochromator is located about 33.5 m apart from the source point in the main hutch. The walls of the hutches consist of a 10 mm Pb plate sandwiched by Fe plates for a radiation shield. A 4-plate water-cooling slit was installed upstream (32.75m) and downstream of (34.43m) the monochromator. Figure 2 shows a schematic layout of the double-crystal monochromator. The first and second crystals are placed on the same goniometer. O is the axis of rotation. The thickness of the second crystal is 20 mm to prevent bending of the crystal. The distance between the white X-ray beam and monochromatic X-ray beam, h, is 25 mm. The specifications of the monochromator are as follows:

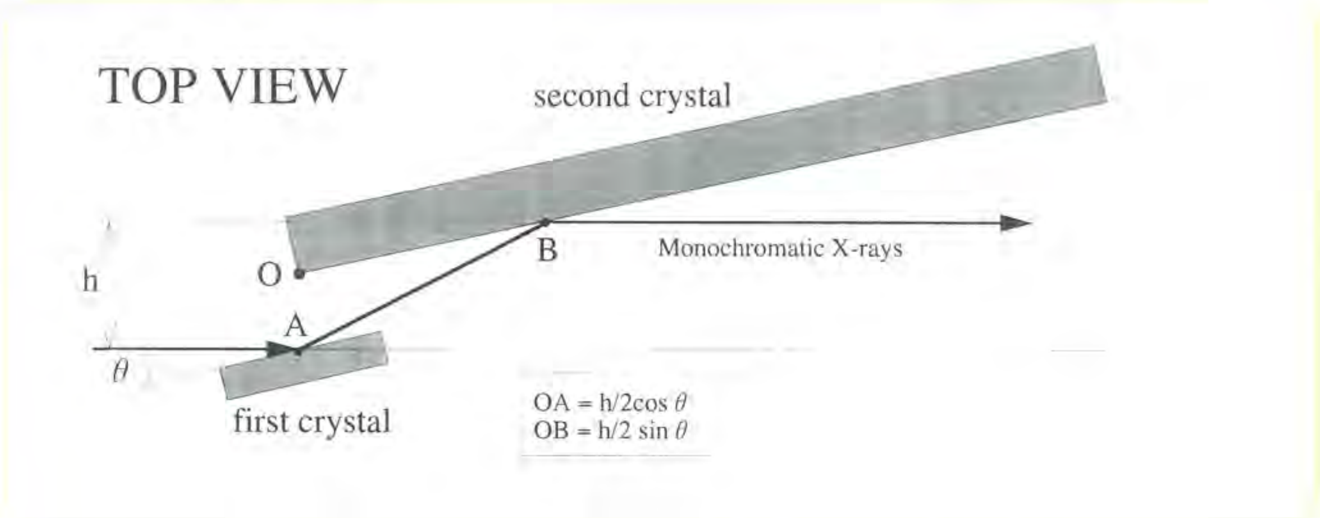

Figure 2.
Schematic layout of the double-crystal monochromator.

Reflecting planes: Si(220), Si(111), Si(311)
Crystal size: first 100(h)×60(v)×10 mm
second 280(h)×60(v)×20 mm
Energy range: 8 keV - 90 keV
Beam size: white beam 40(h)×6(v) mm
monochromatic beam 40(h)×1-6(v) mm

The BL-14C was opened for general users in April, 2000.

Reference

[1] Private communications with H. Kawata

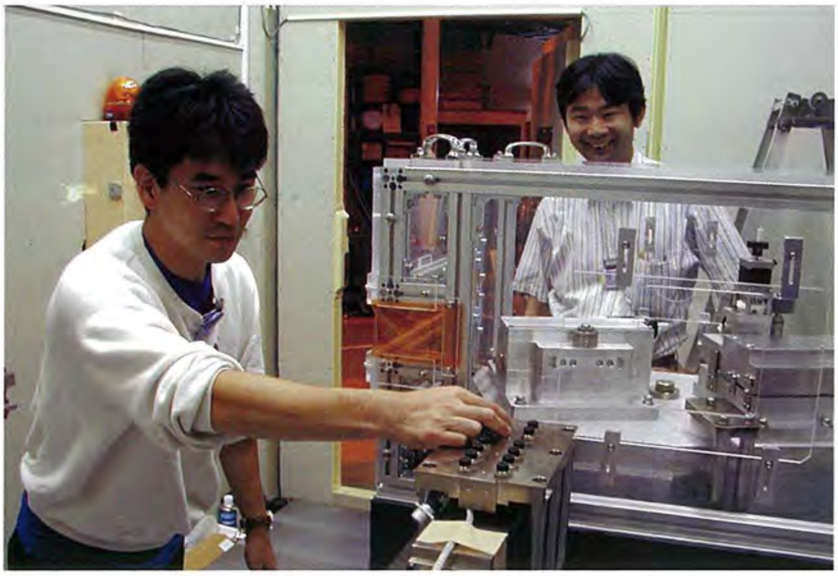

There are two primary-electron beam sources for the relocated slow-positron facility: the 1.5-GeV beam of the KEKB linac and the 45-MeV beam from a test linac. The nominal beam power of the 1.5-GeV beam is 0.75 kW (an energy of 1.5 GeV, charge of 10 nC, a pulse length of 10 ps and a pulse repetition rate of 50 pulse/s). Since the injection interval of the J-linac for the KEKB rings might be relatively short, a dedicated linac for slow-positron use only (the slow-positron generator linac named TEST LINAC) was installed utilizing the remnants of the J-linac upgrade plan. Figure 1 shows a schematic view of the slow-positron generator linac. An average beam power of 1 kW can be expected from a dedicated linac.

In 1999, we detected the first slow positron beam at a new relocated site. At that time, the 1.5-GeV beam of the KEKB linac was used as the primary-electron beam. We also installed a two-dimensional angular correlation of annihilation radiation (2D-ACAR) measurements system. We had already demonstrated the surface sensitivity of positrons with the time-of-flight spectra of orthopositronium. The 2D-ACAR measurements with monoenergetic positron beams will give us valuable information related to the surface electronic structure, rather than bulk structure. Figure 2 shows the insulation support guarders, which were installed to the 2D-ACAR beamline to perform energy-dependence measurements of positron-annihilation radiations. The energy range of the slow-positron beam is nearly from 10 eV to 60 keV. Compared with other positron beam

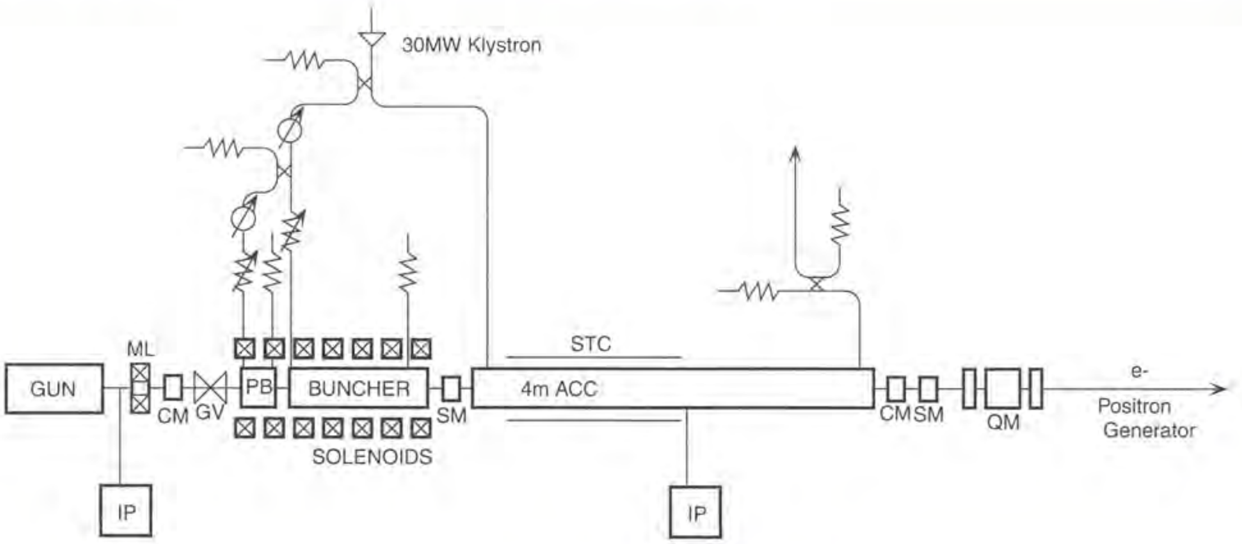

Figure 1.
Schematic view of the slow-positron generator linac.
ML: magnetic lens, CM: current monitor, GV: gate valve, PB pre-buncher, SM screen monitor, ACC accelerator tube, STC: steering coils, QM: quadruple magnet, IP: ion pump.

facilities[1], we have an advantage regarding the sample target position. We put the sample at ground potential. That means the target can be instrumented to allow *in-situ* annealing, cooling and other treatments.

Corona guards of high-voltage regions and a fence for a safety interlock will be installed in FY2000.

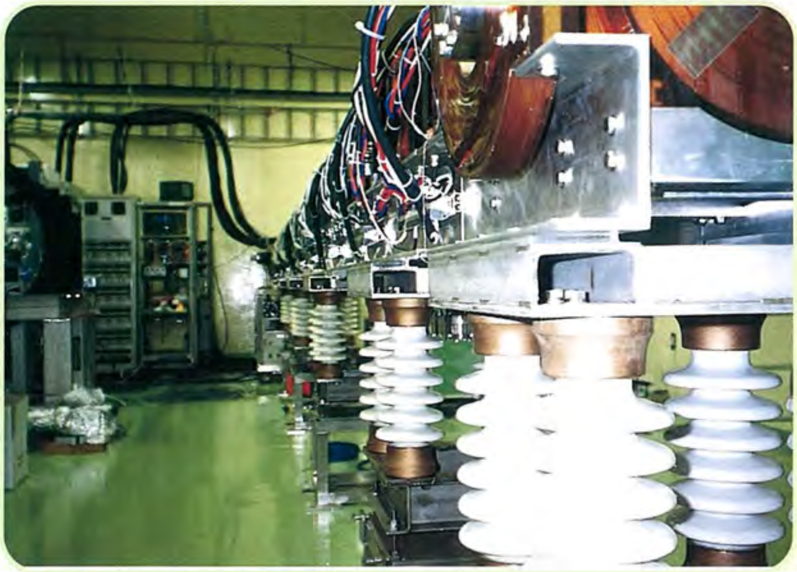

Figure 2.
The beamline capable of applying 60 kV in order to vary the energy of the positron beam.

Reference

[1] See for example, the case of the positron microprobe at Lawrence Livermore National Laboratory, Livermore, CA, USA. Web page: http:www-phys.llnl.gov/H-div/Positrons/

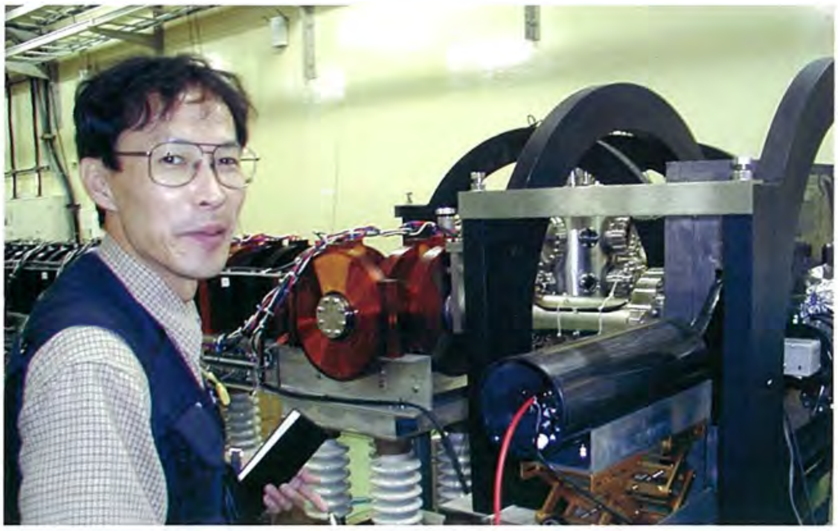

2-5 Experimental Facility of PF-AR

In 1999, a part of the budget for the PF-AR project (renewal of PF-AR for the establishment of a new scientific facility utilizing "single-bunch and high-flux synchrotron radiation in the X-ray region") was approved. We could then start renewal of the accelerator (vacuum system, monitor system and magnet system etc.) and construction of an X-ray undulator beamline for protein crystallography and also for time-resolved XAFS experiments.

The scientific purposes of the new X-ray undulator beamline are as follows:

(a) protein crystallography based on the MAD method

(b) Time-resolved protein crystallography to clarify the mechanism of reactions on biological macromolecules

(c) Time-resolved XAFS experiments

These scientific subjects require the following specifications in this beamline:

(1) In order to achieve the (a) MAD method and (c) XAFS experiments, it is necessary to achieve good energy tunability in the energy range 5~20 keV.

(2) Photon flux at the sample position for (a) protein crystallography be above 10^{12} photons/s under the conditions of a focused beam size less than 0.2×0.2 mm^2 and a beam divergence less than 1 mrad.

(3) Photon flux at the sample position for (c)XAFS experiments will be up to 10^{13} photons/s at a beam size less than 0.5×0.5 mm^2.

(4) In order to achieve time-resolved experiments like (b) and (c), it is necessary to focus white X-ray for Laue method or a dispersive XAFS arrangement at the beamline optics; it is also necessary to produce a relatively wider energy spread of the undulator synchrotron radiation from the insertion device.

In order to achieve the above-mentioned specifications, the details of the designed beamline are as follows. Figure 1 shows the plan view of the beamline.

The insertion device is an in-vacuum undulator having a period of 40 mm, which can cover the energy range of 5~20 keV by using the 1st and 3rd harmonics of the undulator synchrotron radiation. Further, the device has an optional mechanics to make a tapered undulator in order to obtain a relatively wider energy spread ($\Delta E/E \sim 10^{-1}$) for the 3rd harmonics.

The front end, which consists of a fixed mask, beam-position monitor, absorber, beam shutter, graphite heat absorber and Be windows, has already been constructed. The design of these components is similar to those of SPring-8, because the heat-load problem to be solved is almost the same.

Figure 2 (a) shows the typical beamline optics for monochromatic X-ray activity, like protein crystallography or high-intensity XAFS experiments. The main optical elements are a double-crystal monochromator and a double-focusing X-ray mirror, which are located at positions of 22.5 m and 25.3 m from the center of the insertion device, respectively. The double-crystal monochromator consists of flat silicon (111) crystals, which are cooled by liquid nitrogen in order to reduce any deformation caused by the heat load. The focusing mirror is a conical bent mirror in order to reduce the aberration of the focused beam. After the focusing mirror, there is a double-mirror system (cut-off mirrors) to reduce any contamination of the higher harmonics. If we want to carry out time-resolved Laue protein crystallography, the first crystal of the monochromator shifts downward so that white X-rays pass through the monochromator. Then, the mirror system also shifts downward in order to reflect the white X-rays; focused white X-rays are also available in the experimental hutch. Furthermore, if we want to perform time-resolved XAFS experiments by using a dispersive XAFS geometry, the double focusing mirror will be replaced by a flat mirror. Then, one of the cut-off mirrors will be bent at the meridian direction to produce vertical focused white X-rays, as shown in Fig. 2 (b). The horizontal beam divergence in Fig.2 (b) will be used for the dispersive condition for a bent-crystal monochromator in the experimental hutch.

Figure 3 shows the result of a ray-tracing analysis for a double-focused beam at the sample position corresponding to the optics in Fig. 2 (a). As shown in the figure, the focused beam size is about 0.5 mm horizontally and 0.2 mm vertically, respectively. Table 1 summarizes the expected performance of this beamline after a ray-tracing analysis under several conditions. As shown in this table, the expected performance is satisfactory compared with the above-mentioned specification for this beamline.

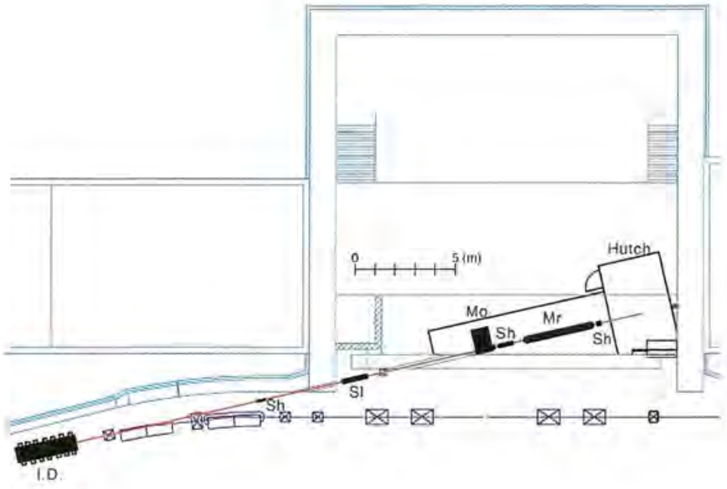

Figure 1.
Outline of beamline AR-NW2. I.D. : insertion device, Sh: beam shutter, Sl: slit, Mo: monochromator, and Mr: mirrors.

The time schedule of the construction is as follows. PF-AR will operate at the present performance until the middle of February, 2001. Then, replacement of the accerelator will start, and finish by the end of November, 2001. On the other hand, all of the beamline components will start, and finish by the end of November, 2001. On the other hand, all of the beamline components will be produced by the end of April, 2001, and the setting will be completed by the end of November, 2001. During the month of December, 2001, we will commission the accelerator and the beamline, and then at the beginning of 2002 we will observe the first beam in this new beamline.

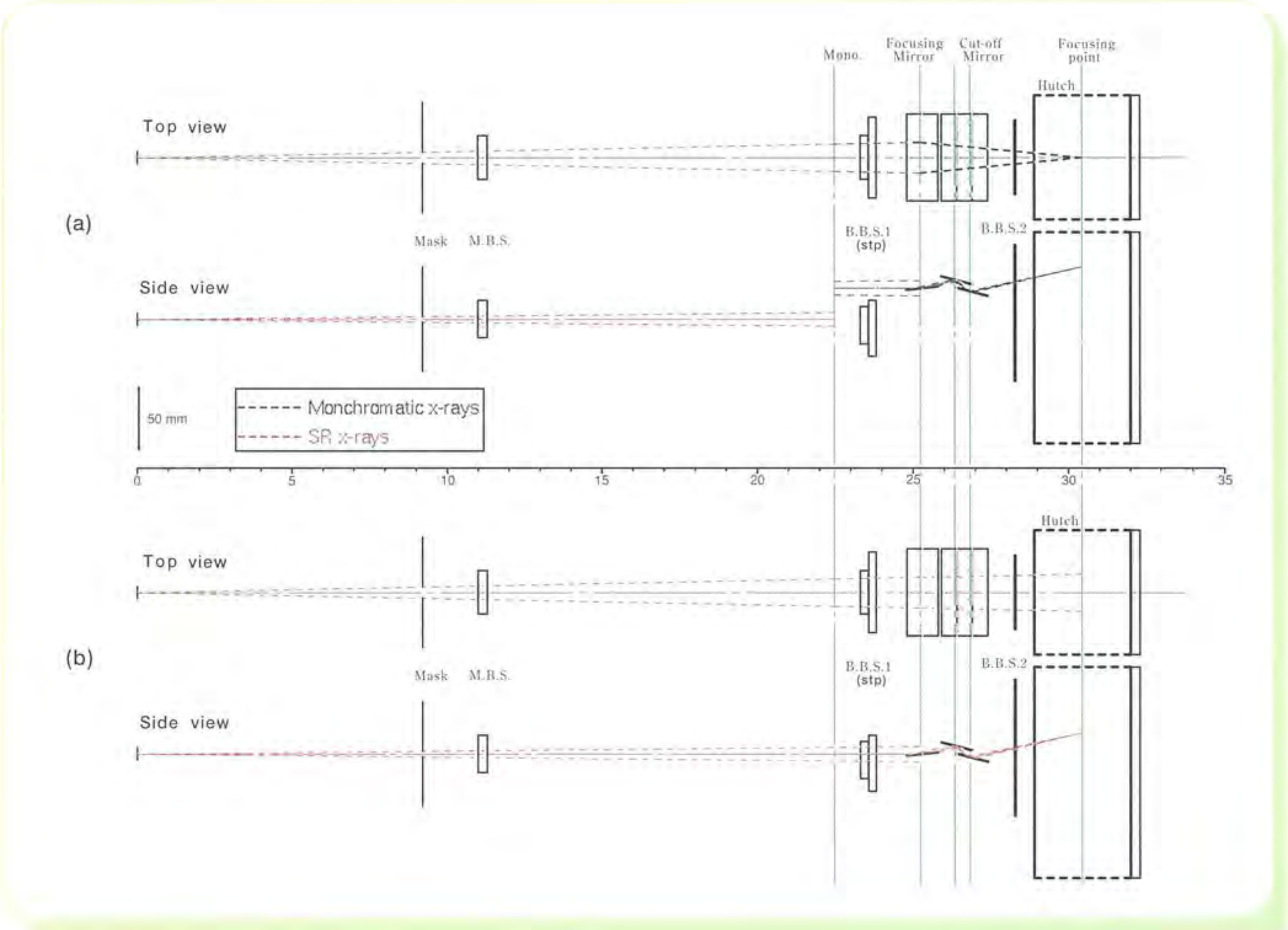

Figure 2. Optical design of beamline AR-NW2. a) protein crystallography and XAFS experiments, b) dispersive XAFS experiments.

Table 1 Expected performance of the beamline AR-NW2 under several conditions. Intensities are estimated for 10 keV X-rays at a ring current of 50 mA.

Application	Acceptance of the beam divergence (mrad)	Intensity (photons/s)	Focused beam size (hor.(mm) x ver.(mm))
XAFS experiments	1.0	1.2×10^{13}	0.6×0.2
Protein crystallography	0.2	2×10^{12}	0.2×0.2
Protein crystallography (Laue method)	0.2	White beam	0.2×0.2
Dispersive XAFS	1.0	White beam	30×0.08

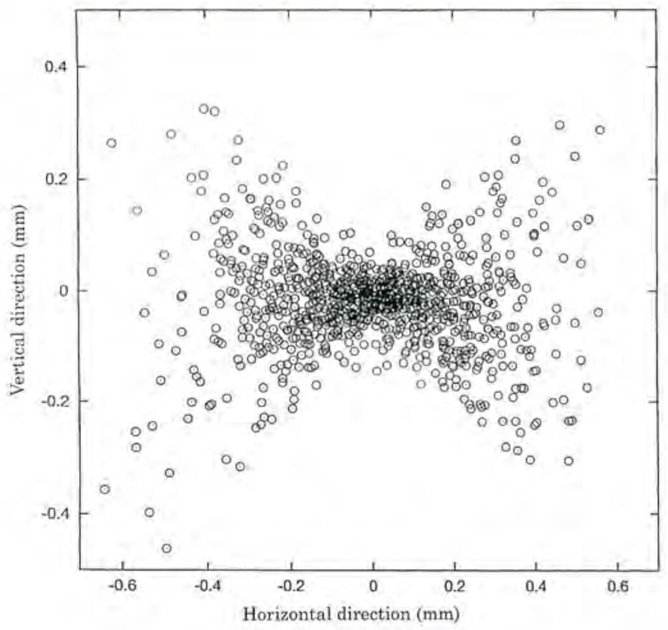

Figure 3.
Spot diagram for double-focused beam of the sample position.

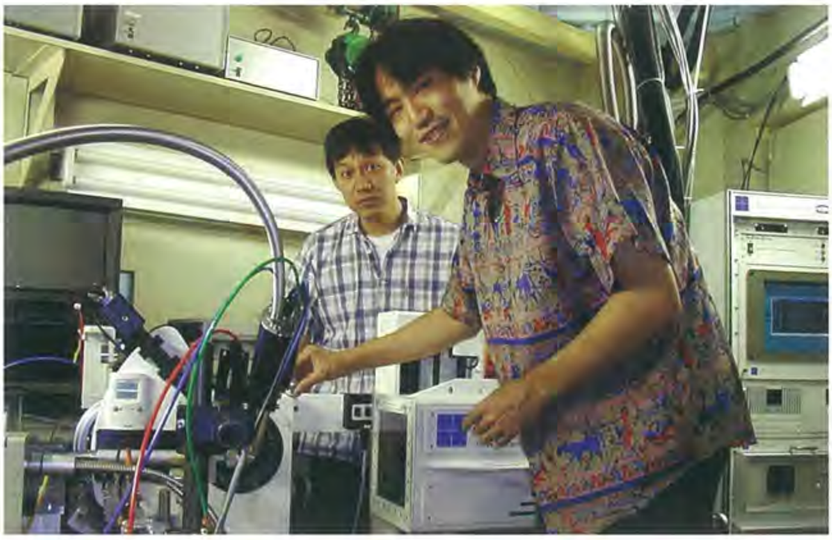

3 New Instrumentation

3-1 Installation of a CCD Automatic Data-Collection System to BL-6A and BL-18B for the Protein Crystallography.

The BL-6A was built in 1987, and a 3rd Weissenberg camera was installed in 1989. The BL-18B was built in 1993 for the purpose of Laue experiments and wavelength variable experiments, such as the MAD method. Both stations have played as a central role in protein crystallography in Japan. In the stations, data were recorded on an imaging plate (IP) and read-out of IP was done with an off-line scanner (FUJI BAS2000) or a large-format imaging-plate reader (RIGAKU IPR4080). The IP has been widely used in the field of protein crystallography because of its many excellent advantages: wide dynamic range, big active area, good uniformity of the sensitivity and ease of handling. However, it is difficult to speed-up the read-out time coupled with automation. CCD-based X-ray detectors have advantages in speeding up data collection with automation. Especially, detector coupled with a fiber-optic taper (FOT) has been developed for automated protein crystallography with synchrotron radiation. For the purpose of speeding up, automation and increasing the measurement efficiency , CCD automatic data-collection systems were installed in two stations (the BL-6A and the BL-18B).

This system is composed by three parts: a CCD detector, a goniostat and a control device, and is carried on the Weissenberg camera. The BL-6A goniostat with the CCD detector are shown in Fig. 1. That for the BL-18B is of the same design. All data collection is done with this system, and the Weissenberg camera is used as a base for any beam adjustment. Sharing the work makes it easy to remodel or renew any part of the system. In fact, a replacement of the base of the BL-6A is scheduled for the end of FY2000, as described below.

The installed CCD detector is a Quantum 4R of ADSC. The detector is coupled with a FOT, and four CCDs are arrayed with a 2×2 configuration to have a total active area size of 188×188 mm. The specifications are briefly listed in Table 1. The goniostat has a vertical drive mechanism for high-resolution measurements. The mechanism lifts the detector up to 45 degrees around the sample position as the center of rotation. The camera distance can be set up to 50-400 mm for the BL-6A or 50-500 mm for the BL-18B by the motor drive. Table 2 gives the maximum resolution. The CCD and the goniostat are controlled by linux computer and images are saved on a raid disk of 150 GB. Two other computers are available for data processing with the software of DPS-Mosflm. The data are backuped by three methods: DAT tape, FTP transfer to a SCSI hard disk or to the computers of users.

Table 1 Specifications of the ADSC Quantum 4R

The number of CCD	2×2
Active area	188×188 mm^2
Pixel number	2304×2304
Pixel size	82mm
Spatial resolution	90mm FWHM
Readout noise	$8e^-$/pixel/s
Dynamic range	10^4
Readout time (Fast, Nobins)	9s

Table 2 Maximum resolution (the wavelength of 1.0 Å).

Camera distance (mm)	$2\theta=0^\circ$	$2\theta=20^\circ$	$2\theta=45^\circ$
100	1.36 Å	0.95 Å	0.71 Å
150	1.81 Å	1.14 Å	0.80 Å
200	2.29 Å	1.30 Å	0.87 Å
250	2.80 Å	1.44 Å	0.92 Å
300	3.31 Å	1.56 Å	0.97 Å
400	4.34 Å	1.75 Å	1.03 Å
500	5.39 Å	1.89 Å	1.07 Å

The system was installed in BL-6A from February 1, and that BL-18B was ported at the end of FY1999. From the beginning of FY2000, both CCD systems are available.

At the end of FY2000, the 3rd Weissenberg camera in the BL-6A will be renewed. This camera was originally designed for IP cassettes, which are not heavier than the CCD system. Some motors do not have sufficient power to drive the heavy CCD system, and a problem arises concerning beam alignment. Thus, at the present, the wavelength is fixed at 1.0 Å in the BL-6A. The new camera bases are designed for only CCD use and for establishing a full-automated camera including a beam-tracing mechanism.

Figure 1.
CCD automatic data collection system.

3-2 MAX-III, New High-Pressure and High-Temperature Experimental System at the BL-14C2.

In the 1998/1999-winter shutdown, the succession device of the high-temperature high-pressure experimental system MAX90 was installed in the BL-14C2 station, which was also reconstructed at this time. After some modifications, the first experiment was carried out from April, 1999, by the construction group.

This system, MAX-III, will be open for users in the same way as MAX90 a few months after the starting period. The nickname of the new system was finally decided to be MAX *SANSEI* in Japanese (MAX the Third in English).

Yagi and Funamori have optimized the system for earth science

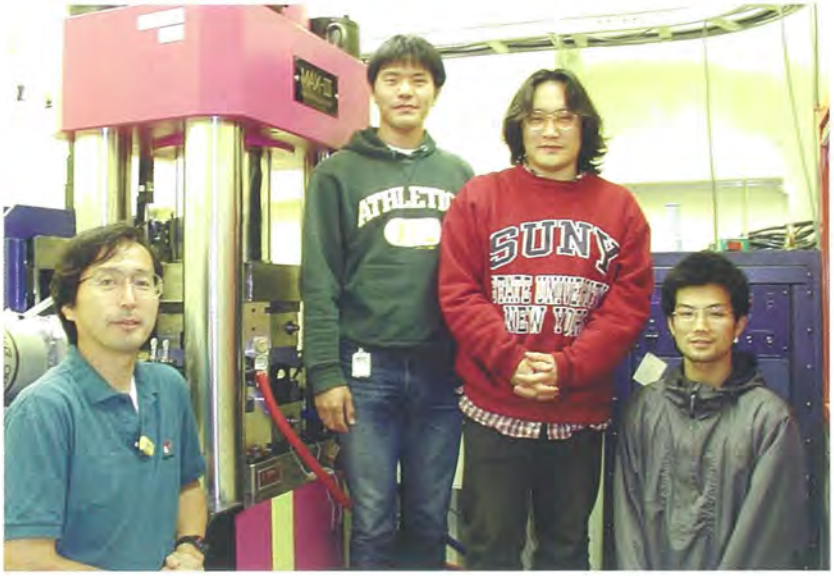

as the main research object. Though the basic character of MAX-III is almost the same as MAX80 and MAX90, the main difference is the maximum load of 700 tons, which exceeds 500 tons of the previous ones. The purpose of this system is to always show the best performance so that it can be devoted to the high-pressure research by exceeding the performance of MAX80 and MAX90.

Today, the circumstances of the research are changing to the normal stage from a stage, in which the high-pressure experiment using Synchrotron Radiation is special. It is being asked to harvest results of good quality from the reclaimed field as much as possible, although it was important to reclaim a new field with the most advanced tool. From that viewpoint, a big expectation is made to the third high-pressure high-temperature system at PF, MAX-III.

Figure 1.
Double stage (6-8) type anvil assembly. The sample is placed on 4 cubic shaped anvils (left).

Specifications of the device:

(1) Press: Maximum load 700 tons.
  Estimated maximum pressure is 30 GPa.
(2) Anvil system : [100] cubic type high pressure device
  Usually double stage (6-8) type anvils are operated.
  Sintered diamond anvils are used as second stage anvils.
(3) Diffraction system: one circle goniometer with a Ge-SSD for the energy dispersive X-ray diffraction experiment .
(4) Press size: 900mmW×1200mmL×2200mmH
  Total weight: more than 4 tons

3-3 Bunch-Purity Monitor Installed at the AR-NE5B

Beamline AR-NE5B was completed for setting up a beam-monitoring system in June, 1999. A detector system for measuring the bunch purity was installed in a hutch of the AR-NE5B. This is one of the improvements for time-resolved and time-spectroscopy studies that are intensively executed at the PF-AR.

One can obtain a pattern of the electron-bunch structure in a storage ring when measuring the time spectrum of synchrotron radiation compared with timing signals from the accelerator. In the time spectrum measured under single-bunch operation, we often observe sub-peaks due to side bunches around the main electron bunch. The intensity ratio of the sub-peaks and the main peak gives the purity of the single-bunch operation.

The detector system at the AR-NE5B is similar to that installed at the BL-21 of the PF ring. A detector using an avalanche photodiode (APD) detects X-rays of a white beam collimated by slits and a pinhole. The detector has a time resolution of 100 ps, and the peak width at 10^{-5} maximum is narrower than 2 ns [1]. The system can resolve a weak sub-peak of 2 ns apart from the main peak. The bunch purifying is performed just after 2.5-GeV injection to the PF-AR. The time spectra are remotely measured with the bunch-purity monitor from a control room of the PF-AR ring. Figure 1 shows the time spectrum of the bunch structure, measured with this system. We can see that the purity is less than 10^{-6}.

Reference

[1] S. Kishimoto, Nucl. Instrum. and Meth. A351 (1994) 554.

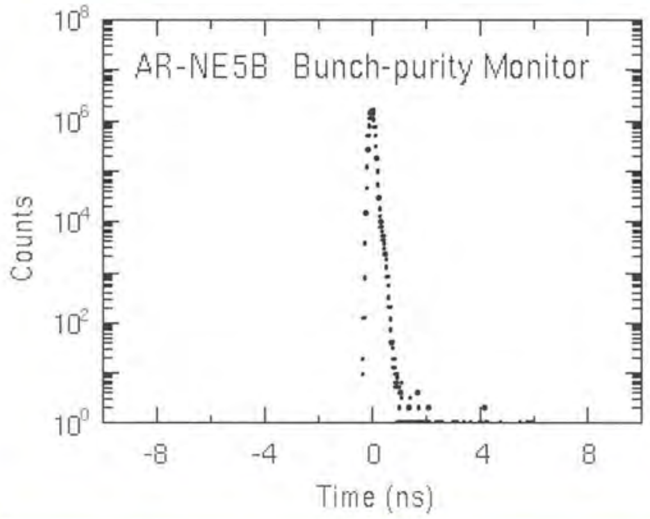

Figure 1.
Time spectrum of synchrotron radiation measured with the bunch-purity montoring system.

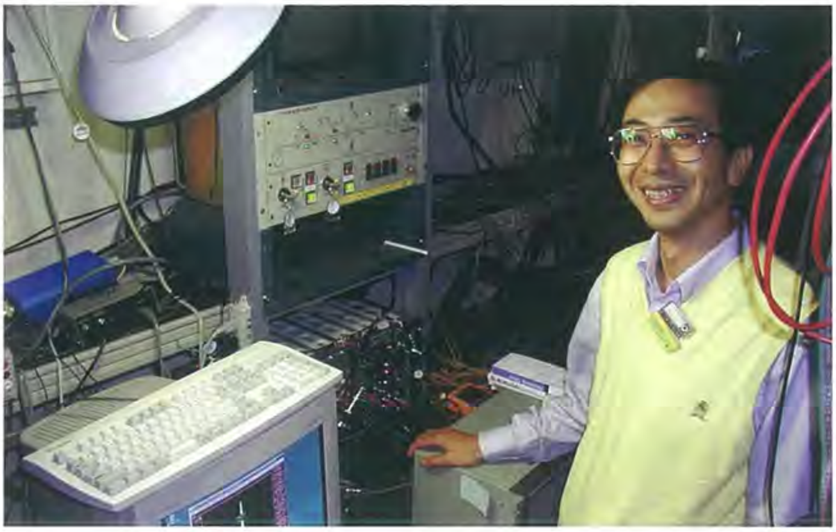

3-4 External Control System for the Beamline Interlock System

More than twenty beamlines are installed at the 2.5-GeV PF ring for the transport of synchrotron radiation to experimental stations. In order to protect the operators and the experimentalists from radiation hazards, each beamline is equipped with an interlock system, which controls the beamline components such as beam shutters, valves, hutches, etc. This BeamLine Interlock System (BLIS) consists of a main unit with a CPU, and station controllers located beside the experimental stations. With the station controllers, one can send the requests for opening or closing the beam shutters and valves to the main unit, which actuates the beam shutters if the condition of the beamline is satisfactory. So far, the procedure of sending such requests can be done manually by users with button switches on the station controllers. In the PF ring, the injection of electron beam is taken place at 9:00 am once a day, and one can continue data accumulation almost for 24 hrs. While in the PF-AR, due to a short lifetime of the stored electron, the injection of electron beam should be taken place so frequently as every two-four hours. In some experiments, once the experimental condition is fixed, the accumulation continues for over one week to have a good statistics. It has been requested for the security reason that the users should open the beam shutters after every injection. To avoid such inconvenience, we have introduced an "External Control System (ECS)", with which one can send the open/close requests to the BLIS using any kind of user's control system. We have discussed about the introduction of the ECS for a long time, and consulted also with the KEK radiation control. In conclusion we have decided to introduce the ECS under some restrictions such as; 1) we do not touch the main unit of the BLIS, controlling the security of the whole beamline, 2) the condition for the "External control mode" can not be satisfied by only the users, 3) we installed a voice alert system, announcing the opening of the beam shutters

In order to meet the restriction 1), the ECS consists of a personal computer (PC) equipped with a parallel I/O interface board, as shown in Fig.1, while an I/O box is attached to the BLIS for the communication with the ECS. The PC is connected with a user's control system through RS-232C. Once the experimental hutch is closed, the users can send the signals for opening/closing beamline shutters with the manual operation of the station controller. The ECS can make an equivalent role as the station controller except that the ECS accepts the signals from the user's control system. The ECS and the station controller cannot be operated simultaneously, because of a key, which activates one of them. Another important function of the ECS is to supply the information such as Beam Ready, and Beam Off, with which the users know the availability of synchrotron radiation beam at their experimental station.

The restriction 2) is satisfied by additional operation of the PC by a floor manager, who is responsible for the safety in the experimental hall during the ring operation. After the floor manager approves that the beamline is ready for the ECS mode, he will set the duration (maximum 7 days) of the ECS mode.

The beam shutters are opened after every injection during the ECS mode, and the voice alert system announces the opening of the shutters.

We have installed a prototype ECS at beamline AR-NE1, where they need a long accumulation to attain a good statistics. We have already experienced that the ECS works without any problem.

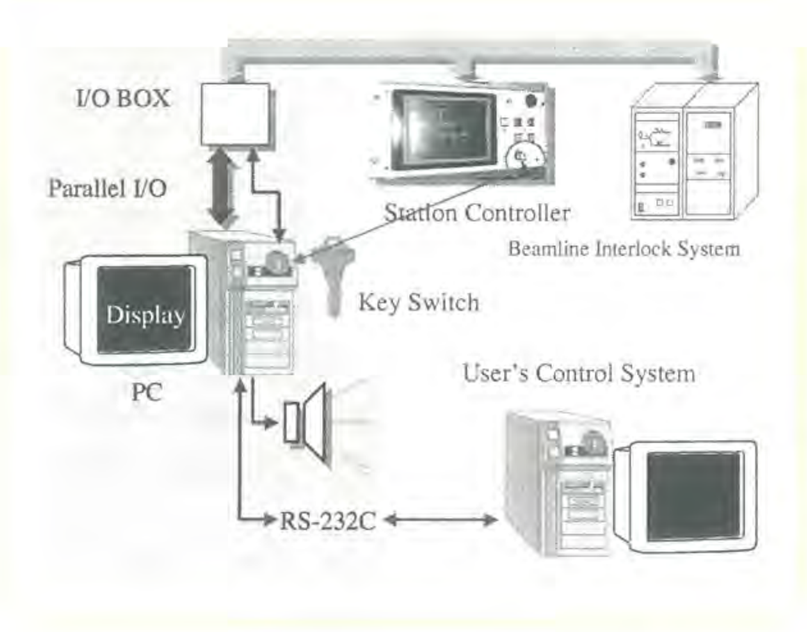

Figure 1.
Beamline Interlock System and External Control System.

3-5 BL-1B, X-ray Diffraction for Crystal Structure Analysis under Multiple Extreme Conditions

Beamline 1B was designed mainly for micro powder diffraction experiments at low temperature and/or under high pressure. In 1999, this line was modified also for single-crystal diffraction experiments.

The beamline consists of a monochromator, and horizontal and vertical focusing mirrors. The monochromator is a fixed-exit type with double flat crystals of Si (111), which covers the energy range 5-21 keV. The cylindrical mirror, which is coated by Rh on Si single crystal, is bent so as to focus the beam vertically and horizontally. The focused beam size was about 0.4 mm (vertical) by 0.7 mm (horizontal) in FWHM at E = 10 keV. The measured shift of the beam position in the energy range of 8 to 18 keV was 0.4 mm and 0.1 mm in the horizontal and vertical directions, respectively. The energy resolution is about $\Delta E/E = 5\times10^{-4}$.

The diffractometer is equipped with a two-dimensional detector of a curved imaging plate, and has been installed to carry out diffraction experiments in the fields of structure determination for a micro single crystal and of a phase transition induced by pressure or temperature. A package of programs was prepared for the analysis of X-ray diffraction data collected from single crystals. This package consists of three programs: visualization of the diffraction patters, data reduction (indexing) and integration, and the merging and scaling of intensities.

One can use this beamline for experiments at low temperature (10~300 K) and high pressure (<50 GPa) in which a diamond anvil cell is installed on a cold head of a closed-cycle cryostat. The pressure at low temperature is changed by the helium gas pressure of a metal-membrane cell.

Figure 1.
BL-1B MPD system reconstructed for single-crystal analysis at low temperature.

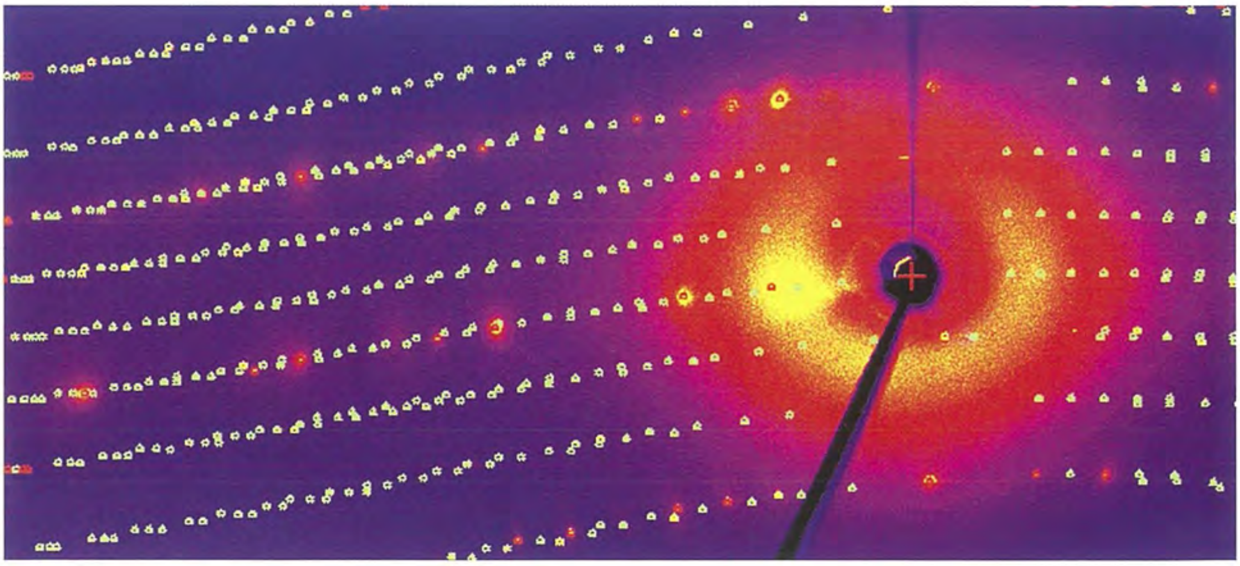

Figure2.
An oscillation photograph of a single crystal (DBr-DCNQI) $_2$Cu at room temperature.

ACCELERATORS OPERATIONS, RESEARCH AND DEVELOPMENTS

Power Supplies for New Kicker Magnets

Test of New Kicker Magnets

ACCELERATORS OPERATIONS, RESEARCH AND DEVELOPMENTS

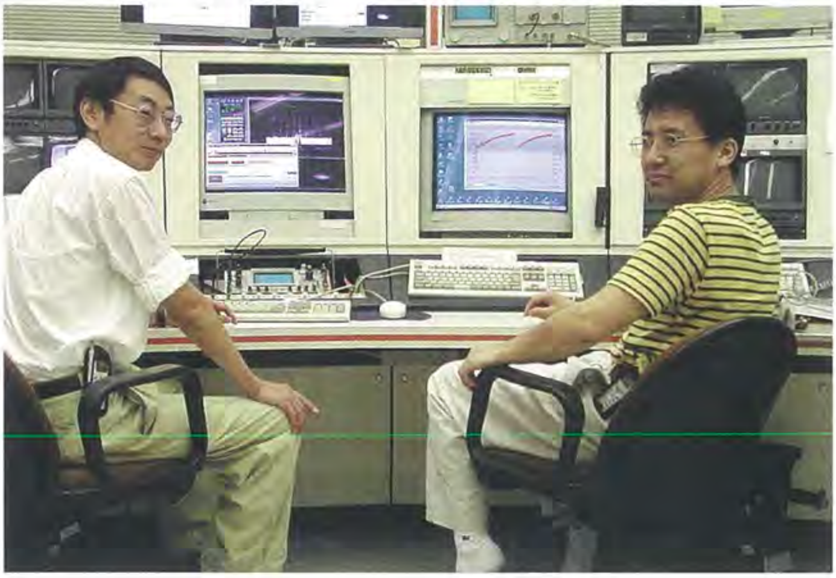

1 PF Storage Ring

1-1 Operations

1-1-1 Summary of Operations

In fiscal 1999, the PF ring was operated without any serious problems. On April 12, the ring operation started, but the beam injection was not very good. The e^+/e^- linac of KEK must inject the electron beam (2.5 GeV) to the PF and the PF-AR rings, and also the electron beam (8.0 GeV) and the positron beam (3.5 GeV) to the KEKB rings. The reproducibility in switching to the different conditions was not good. Thus, the staff members in both divisions of the light source and the linac joined to improve the reproducibility. After machine studies, they could fix the position and angle of the beam within ±0.3 mm and ±0.3 mrad, respectively, at the end of the linac. Finally, we could maintain the reproducibility in user operation. The orbit group investigated the capture rate from the linac to the ring using a turn-by-turn monitor system, and improved the injection rate, which was normally from 0.7 to 1.0 mA/s and more than 2.5 mA/s at the maximum. As a result, the radiation loss in the injection period became lower around the PF ring.

In December, 1996, we succeeded to store 788 mA before upgrading the ring. We could then store 500 mA for the low-emittance optics. However, the maximum stored current was 400 mA in user runs, as before. At the begining of July, we tried to utilize more intense synchrotron radiation to the beamlines by increasing the stored current up to 500 mA. At that time, the beamline performance of durability against the higher power radiation of a 500 mA beam was checked. After evaluating the optical elements and the radiation safety of the beamlines, we decided to operate at an initial current of 450 mA in the autumn user runs. Although few problems occurred during the early stage, the operation was quite good at a higher current.

Before the high brilliant project, the product of the beam current (I) and the beam lifetime (τ) had been sufficiently large, I･τ =1200A･min or more. After the improvement, I･τ became short, butgradually recovered to 500-600 A･min according to a vacuum-pressure improvement. Afterwards, it was found that the beam lifetime could be remarkably improved by applying a small phase modulation on an rf accelerating voltage at a frequency of 2 times the synchrotron frequency. The phase modulation makes the bunch length of the beam longer, and thus the Touschek effect is reduced. As a result, we succeeded to obtain about two-times longer beam lifetime, i.e., I･τ = 1200 A･min, and adopted phase modulation in user runs as routine. The progress of I･τ is shown in Fig.1.

The circumference of the ring expands or contracts accompanying the distortion of the building, the source of which is considered to be the temperature difference between day and night. This causes horizontal orbit drift. We thus suppressed the drift using feedback of the rf frequency.

The operation statistics are presented in Table 1, and the trend is shown in Fig.2. The average stored beam current was 340 mA and the average injection interval was recovered to 20 hours (Fig. 3). The trend concerning the failure time is shown in Fig.4 (less than 1%).

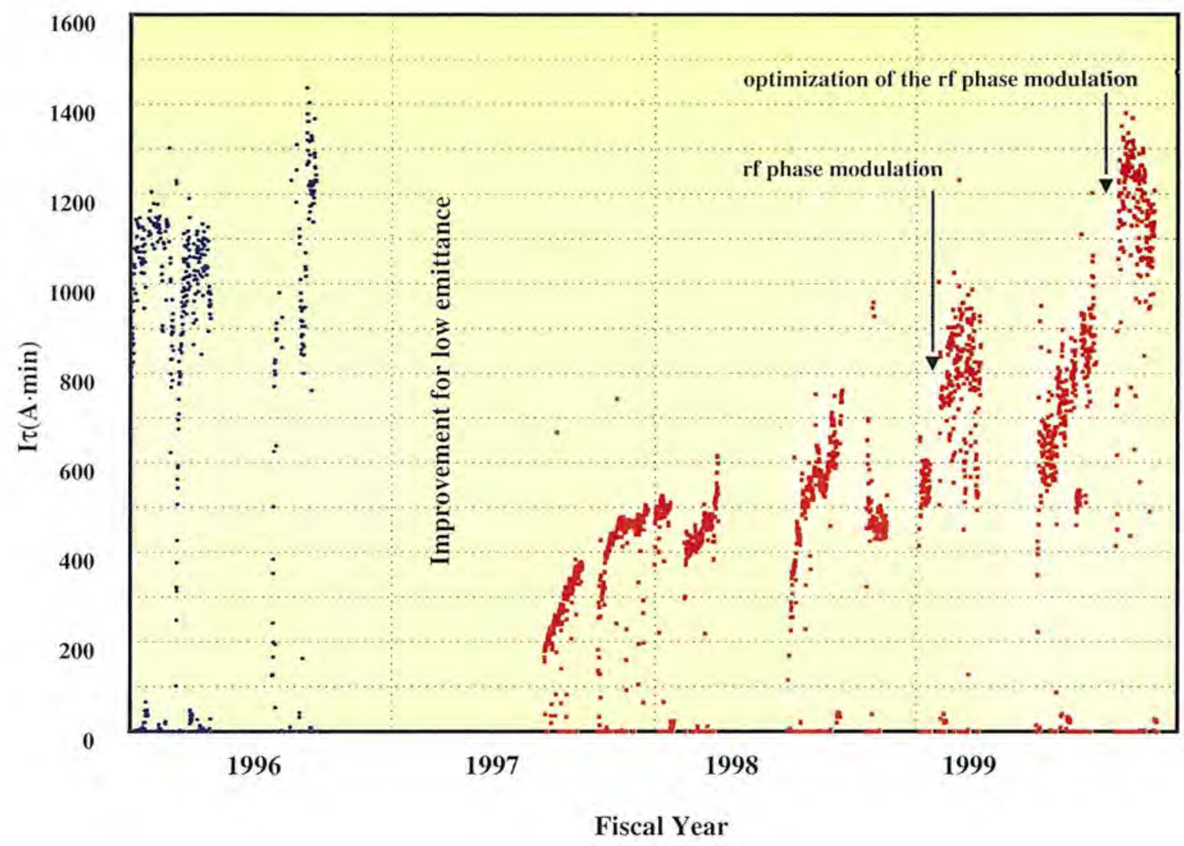

Figure 1. Progress of I・τ.

These results prove that the performance and the reliability of the PF ring are quite excellent. They have been accomplished by continuous efforts to make improvements.

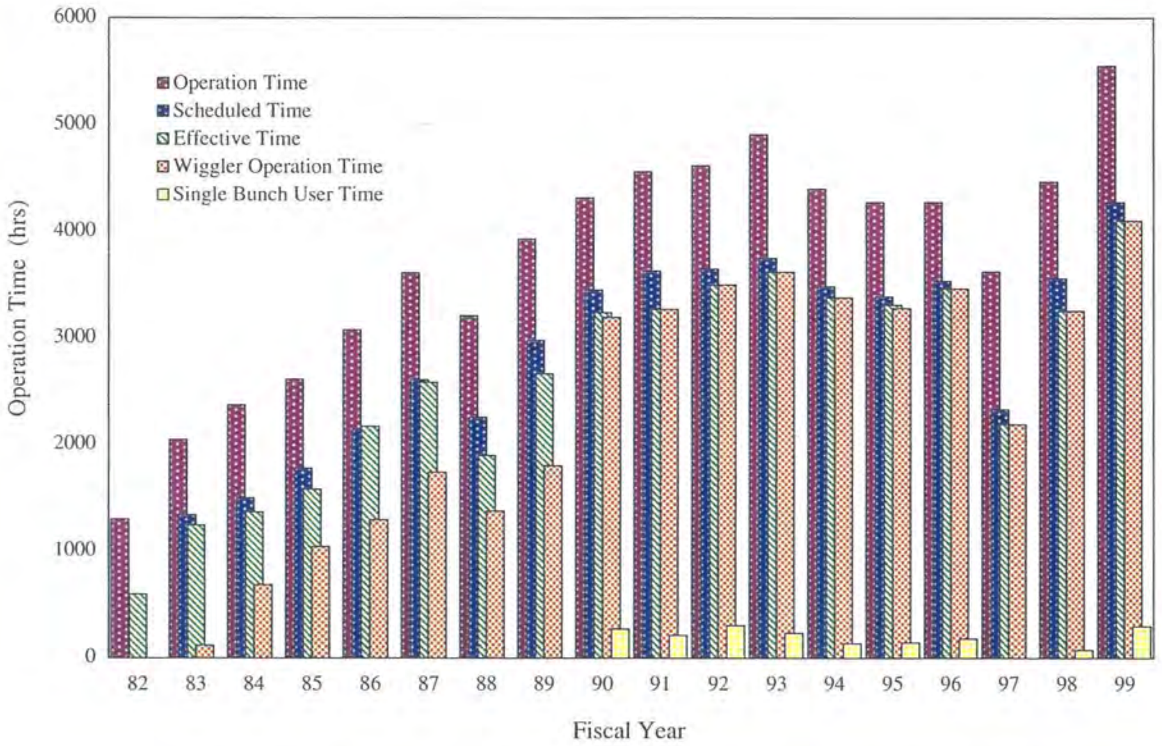

Figure 2.
Trend of the operation statistics.

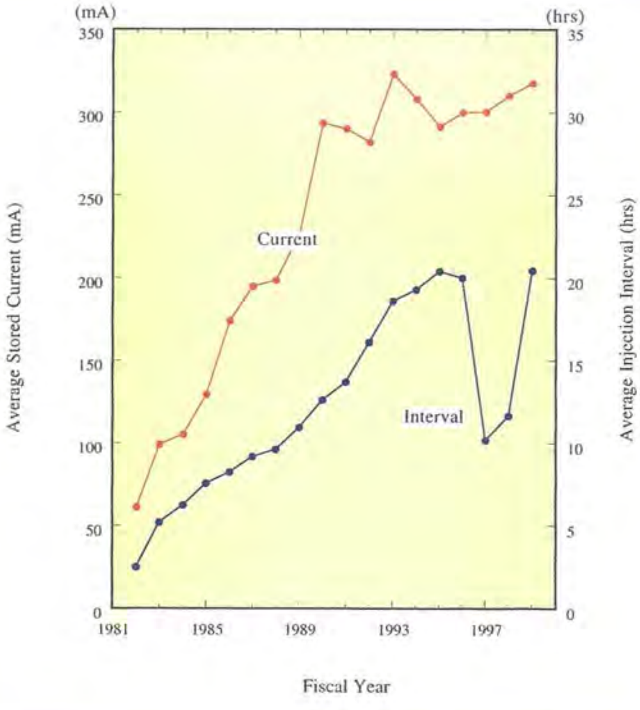

Figure 3.
Average stored current and injection interval.

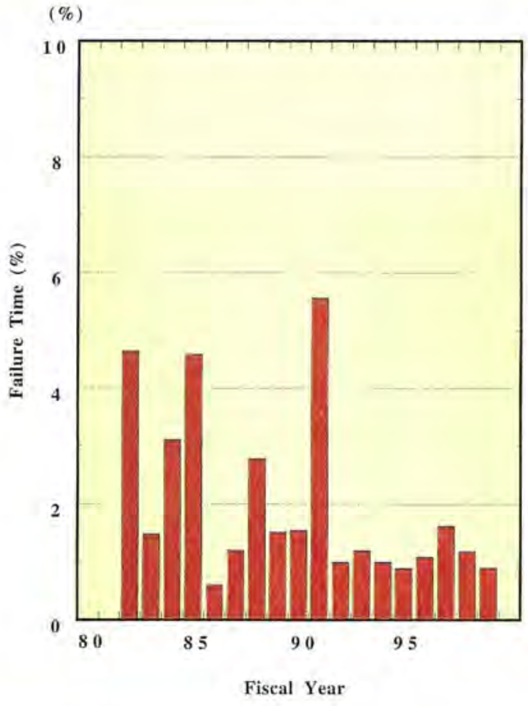

Figure 4.
Trend of the failure time.

Table 1 Statistics of the storage-ring operation during fiscal year 1999 (from Apr. 1999 to Mar. 2000).

	Multi-bunch	Single-bunch	Total
Ring operation time (hours)	5264.0	288	5552.0
Scheduled user time (hours)	3984.0	288	4272.0
Net user time (hours)	3842.8	258.6	4101.4
Time used for injection (hours)	88.9	25.6	114.5
Integrated current in $I \cdot \tau$ (A·hours)	1219.7	10.6	1230.3
Average current (mA)	317.4	41.0	
Number of injections	188	39	227
Interval between injections (hours)	20.4	6.6	

1-1-2 New Kicker System

We employ four kicker magnets to produce a pulse bump orbit to inject the electron beam into the PF ring. The pulse falling time (from 90% to 10%) of the old kicker magnet was 1.8 μsec. Since the revolution period of the PF ring is 0.624 μsec, the injected beam was kicked three times by the old ones. The available horizontal betatron tune for the injection was restricted because the injection beam may collide with the wall of the septum magnet due to the value of the tune. In order to solve this problem, new travelling wave-type kicker magnets (TW kicker magnet) with a shorter pulse length were developed. The new kicker magnets were installed in the PF ring in January, 2000, and have been successfully operated.

The TW kicker magnet consists of 30 segmented LC circuits (30 cells), like the equivalent circuit of the transmission line. A power supply system with a line type pulser was also designed and constructed to drive the magnet. An outline of the structure cell is shown in Fig.5. A general view of the new kicker magnet system is shown in Fig.6. The pulse falling time has been improved to 0.55 μsec, less than the revolution period, considering the following descriptions.

In general, the TW kicker magnet is set inside the vacuum chamber to insulate the high-voltage plates from the earth plates. However, a large space for the vacuum insulation is necessary and the impedance of the wall becomes too large. Thus, new magnets were installed outside of the vacuum chamber made of ceramics. To insulate the high-voltage plates from earth plates, a silicone rubber

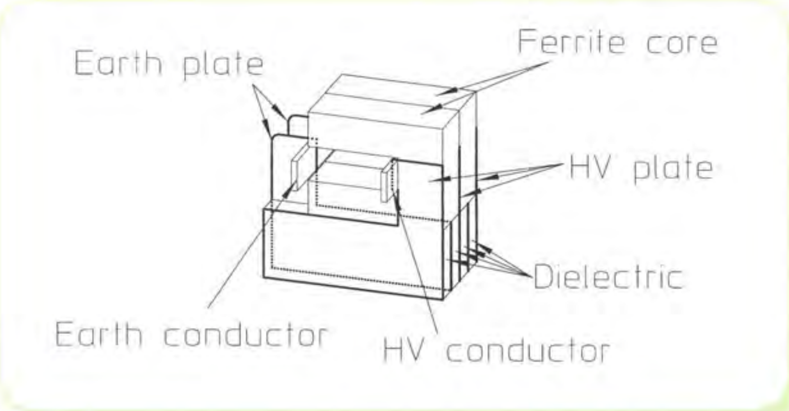

Figure 5.
Outline of the structure cell.

Figure 6.
General view of the new kicker magnet system.

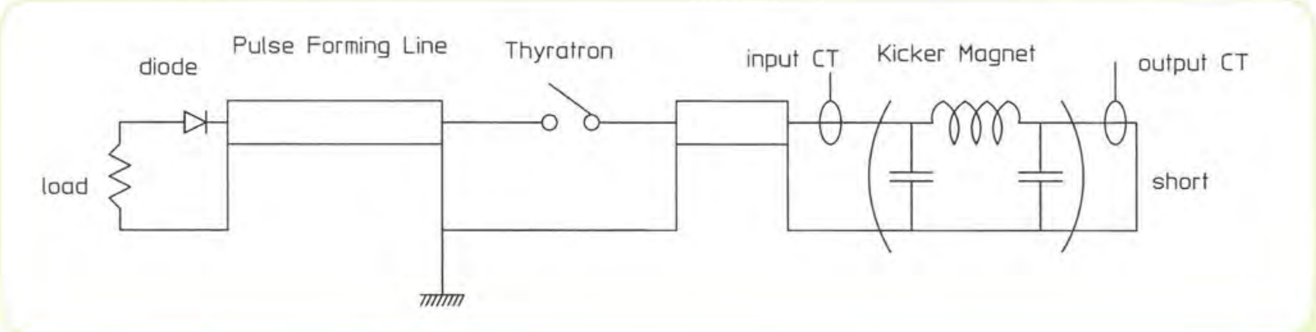

Figure 7. Block diagram of the TW-kicker system with the totally-reflection type.

molding was employed. Since the electric breakdown voltage of the molding is lower than that of the vacuum, the applied voltage for the magnet must be suppressed [1]. It was realized by lowering the impedance of the magnet to 6.25 Ω and adopting a total-reflection concept for the system. Though the lower impedance made the pulse falling time longer and the total-reflection concept made it double [2], the pulse falling time is still less than the revolution period. In producing magnets with low impedance, an alumina ceramic plate having a relative dielectric constant of 9.0 was used as insulation between the high-voltage plate and the earth plate. A block diagram of the TW-kicker system with the total-reflection type is shown in Fig.7.

References
[1] T.S. Mattison et al., Proc. of 1995 IEEE. Particle Accelerator Conference (Dallas),(1995)1915.
[2] Photon Factory Activity Report #15 Part A (1997)135.

1-1-3 Beam Position Monitor System for the Beam Transport Line

A nondestructive beam-position monitor system was provided for the beam transport line from the LINAC to the PF ring. The arrangement of the beam-position monitors (BPM) is shown in Fig.8 together with the energy-dispersion functions. There are 10 strip-line BPMs, which are indicated by the names started from "BPM_". Most of them are identified by the nearest quadrupole name, and some of them are named by the nearest components, such as "PM9". In the figure, profile monitors of a retractable scintillator screen, which have been used since commissioning of the PF ring, are described as "PM". Each BPM has four strip-line electrodes of 175 mm long, their back ends are short-circuited to a vacuum duct. The bunch signal of the strip-line is stored by a digital waveform analyzer having an adequate

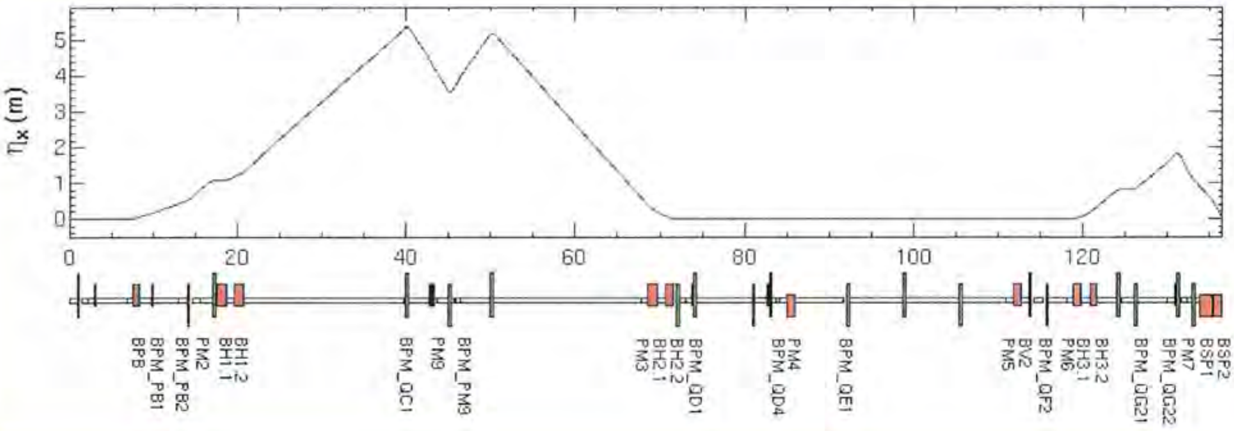

Figure 8. Arrangement of the strip-line BPMs along the beam transport line.

sampling speed. The signals from 10 BPMs are connected into the single waveform analyzer using rf signal combiners. Thus, the beam positions at all the BPMs can be deduced for the identical bunch. The resolution of the measurement using an 8-bit digitizer is about 0.1 mm.

During injection, the beam-transport orbits are continuously monitored at a second interval. Figure 9 shows the BPM graphics used at the control room. Summation of the four-electrode signals is used as a charge monitor. After the intensity of the signal is corrected on the cable loss, the charge at each BPM is deduced in nC unit. Under the usual injection condition, the beam positions along the beam transport are stable, except for the region with a large horizontal dispersion function. At the BPM for a dispersion function of 5 m, an energy difference of 0.1% is detected as the position variation of 5.0 mm. We have two BPMs in the dispersive region, BPM_QC1 and BPM_PM9. The profile monitor PM9 has been used for the monitor of energy spread and energy itself. The fluctuations of the beam positions are plotted in strip charts on the BPM graphics. The energy feedback following the horizontal beam position is usually performed at the LINAC. It is effective to reduce the slow energy drift during the injection period. All BPM data are delivered to the LINAC control through the data channel. At both control rooms, the beam orbit along the LINAC and the beam transport line are displayed in unified graphics.

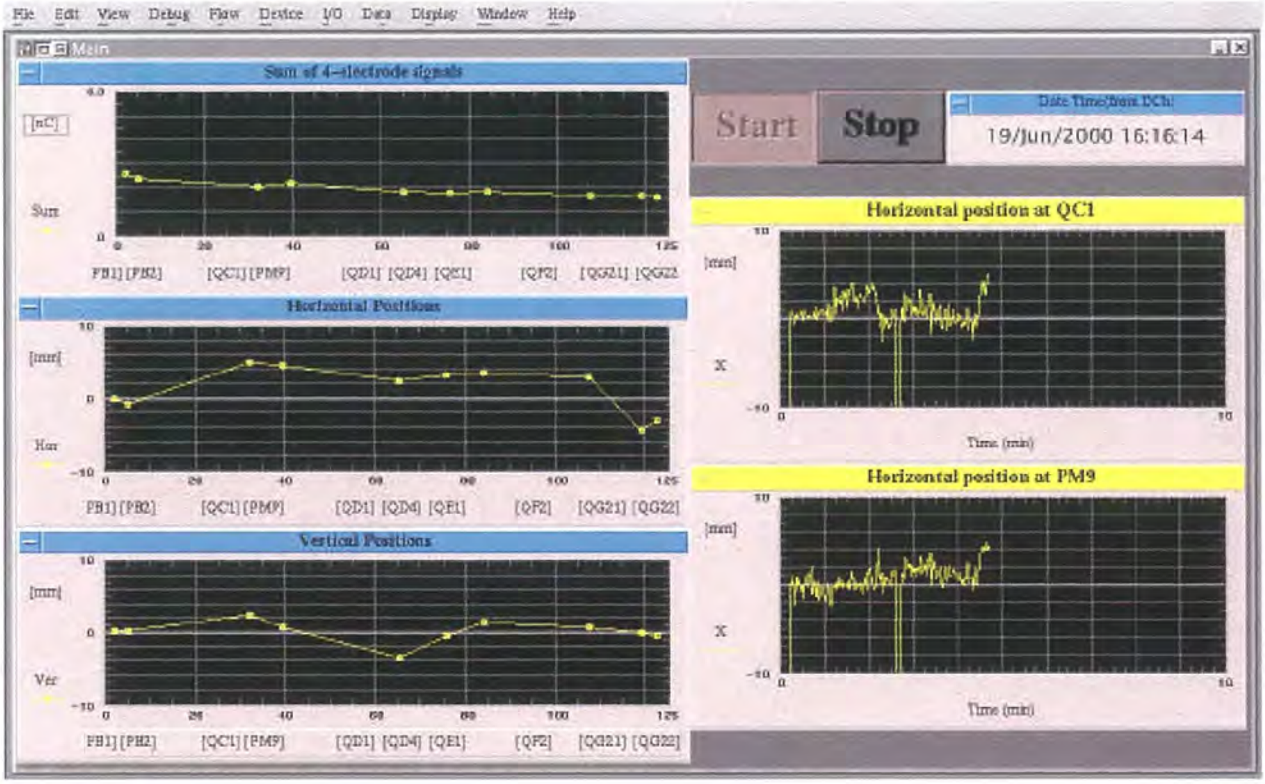

Date Time(from DCh): 19/Jun/2000 16:16:14

Figure 9. Graphics of the BPM system for the beam transport.

1-1-4 Improvements of the Injection Efficiency

Figure 10 shows the progress of the injection efficiency in fiscal 1999. The injection efficiency was calculated at a repetition rate of 25 Hz. There was a great improvement of the injection efficiency at the beginning of October, 1999. At that time, we investigated the cause of the deterioration of the injection efficiency. We measured the capture rate into the PF ring from the injector linac using a turn-by-turn monitor system [1]. As a result, it was found that the acceptance of the injection beam became narrower due to the horizontal scraper, which

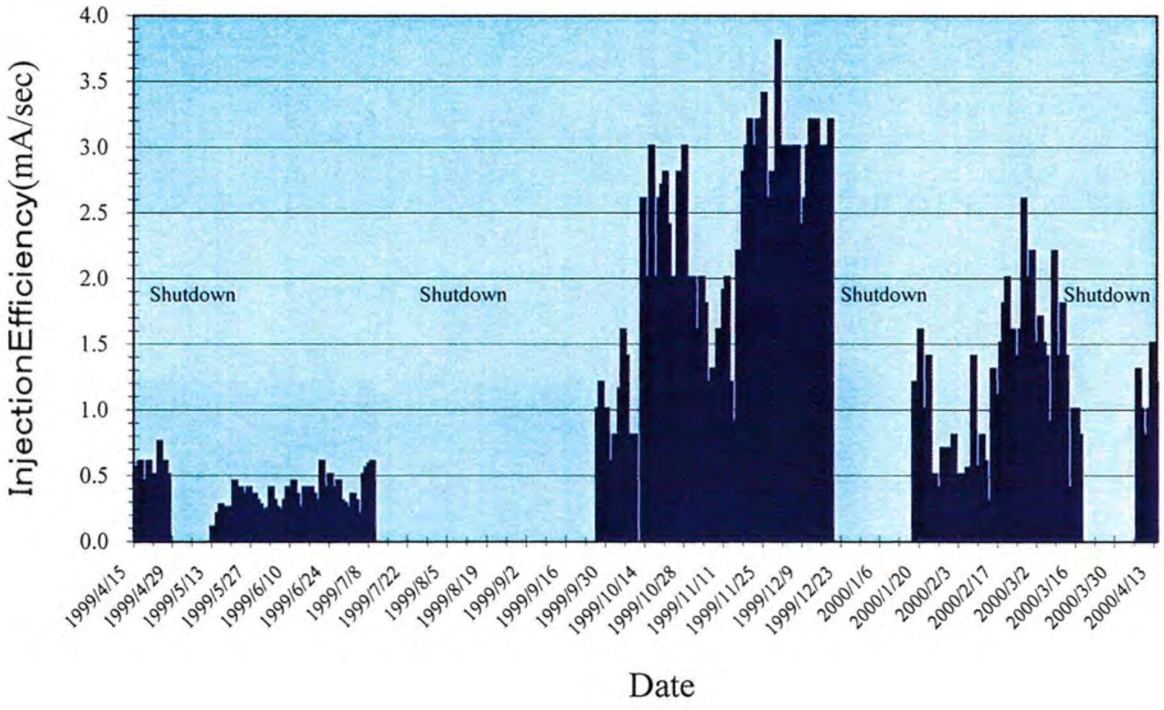

Figure 10. Progress of the injection efficiency in fiscal 1999.

Figure 11.
Capture rate of the injection beam for the injection phase between the ring and the linac.

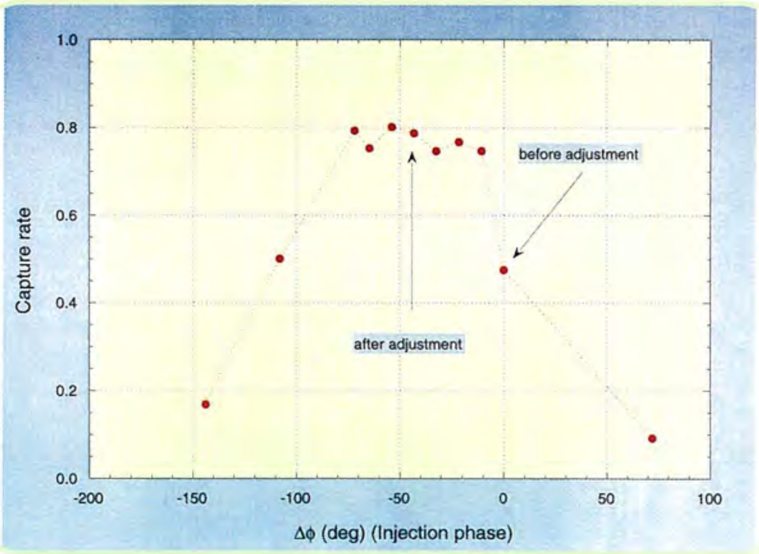

is inserted to remove those electrons with bad quality in the injection beam. Moreover, it was also proven that the injection phase between the ring and the linac had slightly deviated, as shown in Fig.11. Therefore, the injection phase was adjusted so that the capture rate increased. In addition, it became possible that the position of the scraper was extended much more by improvements of the beam quality performed in the injector linac and the beam-transport line. Thus, the injection efficiency was drastically improved and achieved to be six-times higher (more than 3.0 mA/sec) compared to the previous one. Afterwards, the good condition of the injection efficiency (more than 1.0 mA/sec) has been maintained, though it became temporarily bad in January and February, 2000, since the adjustment for the new kicker system was insufficient.

Reference

[1] Y. Kobayashi and T. Obina, Proc. of the 12th Symposium on Accelerator Science and Technology, (1999)516.

1-1-5 Improvement in the Beam Lifetime by means of an RF Phase Modulation

Four 500-MHz rf cavities are used to produce an accelerating voltage of 1.7 MV (typically) in the PF ring. It was recently found that the beam lifetime could be remarkably improved by applying a small phase modulation on an rf accelerating voltage at a frequency of 2 times the synchrotron frequency ($2f_s$) [1]. A typical improvement in the beam lifetime is shown in Fig.12. By applying phase modulation, the lifetime was improved by a factor of about 2.1.

Another benefit gained by phase modulation is a remarkable suppression of longitudinal coupled-bunch instabilities. Although excellent damped accelerating cavities are used in the PF ring, there

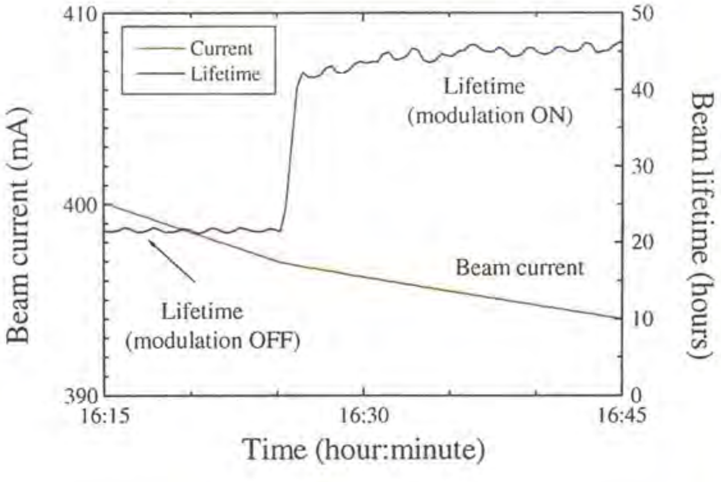

Figure 12.
Improvement in the beam lifetime by rf phase modulation. The beam lifetimes were measured with and without applying phase modulation (modulation frequency: 46.7 kHz, amplitude: 4.6° p-p).

arise many spectrum lines in a button-type monitor signal at high currents, due to the longitudinal coupled-bunch instabilities. Since these spectrum lines do not correspond to any frequencies of the cavity higher order modes, it is considered that this instability is induced by some resonant structures in the vacuum components. This instability causes a harmful fluctuation in the brightness of the synchrotron radiation. Figure 13 shows the measured beam spectra with and without applying phase modulation. It can be seen that the longitudinal coupled-bunch oscillations were largely suppressed by applying phase modulation.

The improvement in the lifetime can be understood by the following mechanism. By applying phase modulation at a frequency of $2f_s$, the longitudinal oscillations of stored electrons are excited by a parametric resonance process. A small-amplitude oscillation is described by a similar equation to the Mathieu equation. Since each electron tends to oscillate in one of the two states of oscillations, the

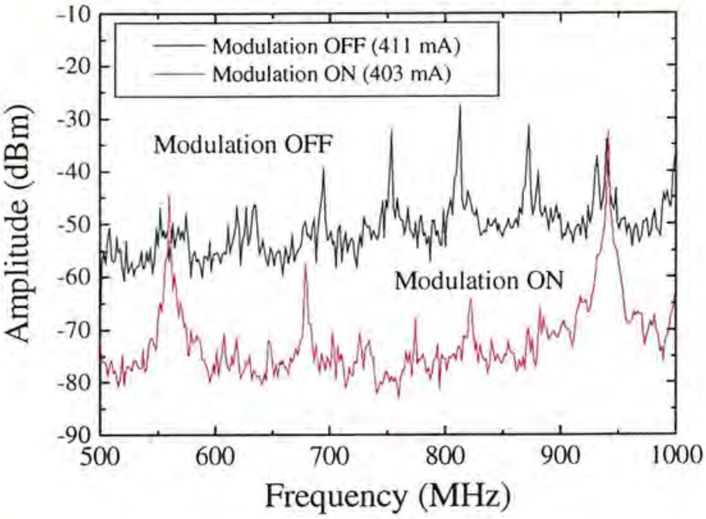

Figure 13.
Suppression of the longitudinal coupled-bunch instability by applying phase modulation (46.7 kHz, 4.6° p-p). Spectrum lines due to the longitudinal instability were measured with and without applying phase modulation.

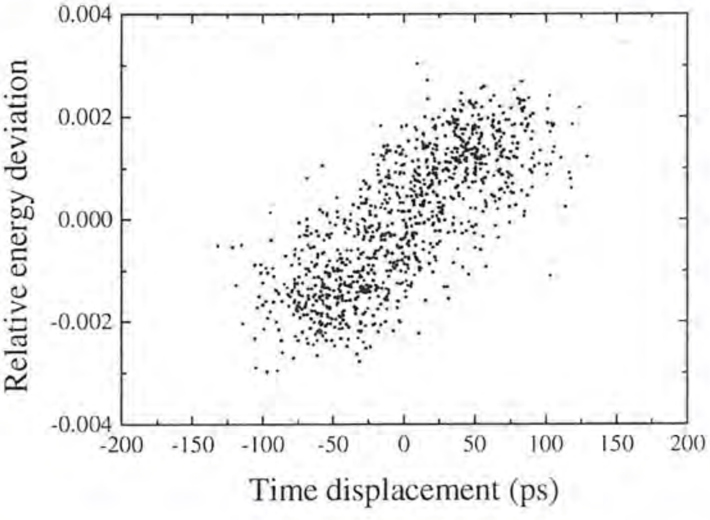

Figure 14.
Distribution of particles in phase space under phase modulation. The result of a multiparticle tracking simulation is shown. Modulation frequency: 45.36 kHz, amplitude 4.6° p-p.

phases of which are opposite to each other, the electrons form two subbunches. As a result, a quadrupole mode of the longitudinal oscillation of the bunch is excited, which results in a long average bunch length. This makes the Touschek lifetime longer. Figure 14 shows a typical simulation result of the longitudinal bunch motion under the phase modulation. It can be seen that the bunch is separated into two subbunches, which oscillate out of phase to each other.

We have been using this technique under routine operations since May, 1999. Thus, the beam performance in the PF ring has been largely improved regarding both lifetime and stability.

Reference

[1] S. Sakanaka, M. Izawa, T. Mitsuhashi, T. Takahashi, Phys. Rev. ST Accel. Beams 3(2000)050701.

1-1-6 Horizontal Orbit Feedback

An rf frequency feedback system was introduced to stabilize the horizontal orbit of the ring. The circumference of the storage ring expands or contracts accompanying the distortion of the building, whose source is the temperature difference between day and night. If the circumference (*C*) of the ring is changed, the beam energy (*E*) varies according to

$$\Delta C/C = \Delta f_{rf}/f_{rf} = -\alpha(\Delta E/E),$$

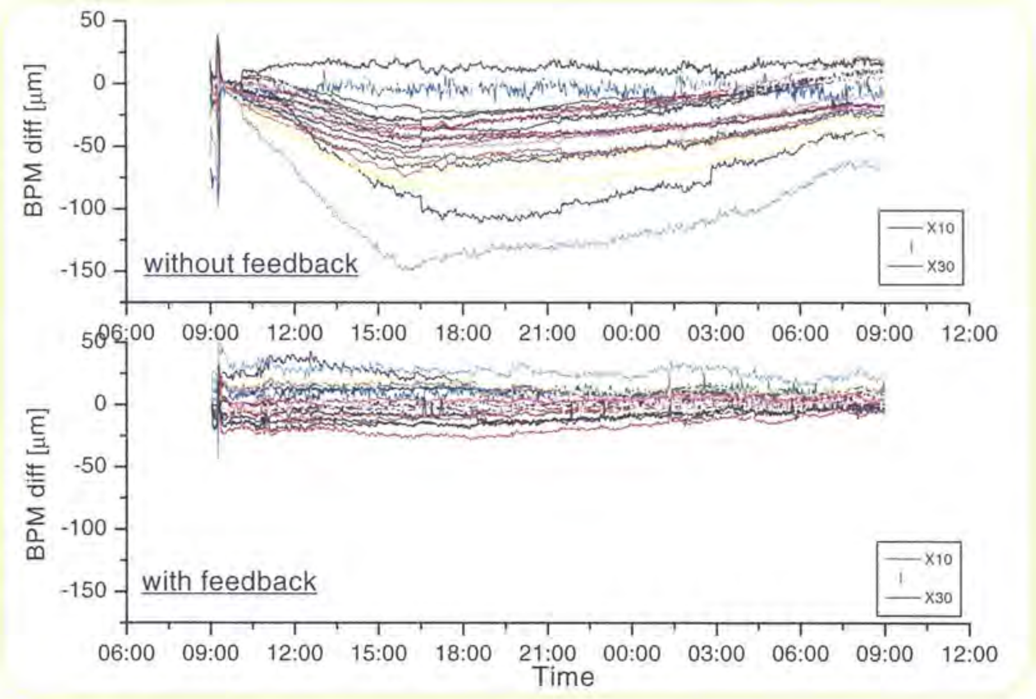

Figure 15. Typical horizontal orbit variation during one day with/without frequency feedback.

where α is a dimension less constant, called the momentum compaction factor. Moreover, the horizontal orbit difference ($\Delta \chi (s)$) is displayed as $\Delta \chi (s) = \eta (s)(\Delta E/E)$, where η is the dispersion function and $\Delta E/E$ is relative energy difference. Thus, we change the frequency of the rf with

$$\frac{\Delta f_{rf}}{f_{rf}} = -\alpha \frac{\sum \Delta x_i \eta_i}{\sum \eta_i^2},$$

where $\Delta \chi_i$ is the difference in the horizontal beam position from the standard orbit, η_i the dispersion at the BPM and i the BPM number from 1 to 65. Because the feedback period is not necessarily short, we calculate Δf every minutes and change the frequency if Δf exceeds 2 Hz. Figure 15 shows the typical horizontal orbit variation during one day with/without frequency feedback. The maximum orbit movement of about 150 μm (top) is successfully suppressed within 30 μm (bottom) using a feedback system. The change in the rf frequency is about 200-300 Hz during routine operation for users.

1-2 Developments and Machine Studies

1-2-1 Bunch-by-Bunch Beam Diagnostics

In the PF ring, a vertical instability has been observed in the multi-bunch mode. This instability can be suppressed by exciting octupole magnets during routine operation for users. However, the origin of the phenomenon has not yet been completely understood. We have developed an optical bunch-by-bunch beam diagnostic system using a high-speed light shutter [1], and observed the vertical instability of individual bunches with it. An observation of the vertical instability was performed in the multi-bunch mode (successive 280 bunches followed by 32 empty buckets) in which all bunches had almost equal beam currents (1.6 mA/bunch). In order to make the observation of the instability clear, we turned off the octupole magnets to avoid the Landau damping effect during the experiment. Figures 16 and 17 show the frequency spectra which correspond to the betatron sidebands of the 1st and 20th bunches in the bunch train, respectively. Although the beam currents of these two bunches were much the same, not only these spectral powers, but also these frequencies, are different, as can be seen in these figures. We analyzed the dependence of the betatron frequency on the position in the bunch train. Figure 18 shows the vertical betatron tunes of 20 bunches at the head of the train. It can be clearly seen that the vertical tune gradually increases along the train.

According to linear theory [2], the vertical motion of the trapped ion when a bunch passes through near the ion can be expressed by a matrix form. Namely, if we define the time (t) to be zero when the head of the bunch train passes, the ion motion after the first bunch in the train passes through the ion can be expressed as a matrix composed of a single focusing kick matrix followed by a drift space matrix whose drift length is equal to the bunch spacing:

$$\begin{pmatrix} y_i(s,t_{rf}) \\ \dot{y}_i(s,t_{rf}) \end{pmatrix} = \begin{pmatrix} 1 & t_{rf} \\ 0 & 1 \end{pmatrix} \begin{pmatrix} 1 & 0 \\ a(s) & 1 \end{pmatrix} \begin{pmatrix} y_i(s,0) \\ \dot{y}_i(s,0) \end{pmatrix}$$

$$= DB(s) \begin{pmatrix} y_i(s,0) \\ \dot{y}_i(s,0) \end{pmatrix},$$

where *D* and *B(s)* denote the drift motion and the one bunch passing matrix, *a(s)* is a focusing factor due to one bunch passing,

$$a(s) = -\frac{2r_p c N_b}{A\sigma_y(s)\left(\sigma_x(s)+\sigma_y(s)\right)},$$

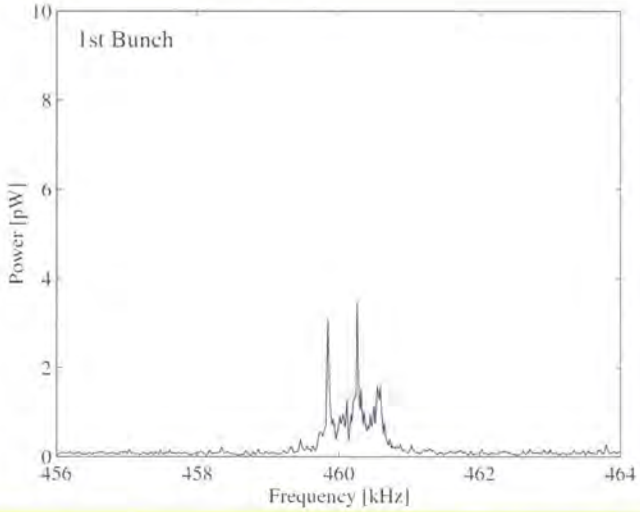

Figure 16.
Frequency spectra which correspond to the betatron sidebands of the 1st bunch in the train.

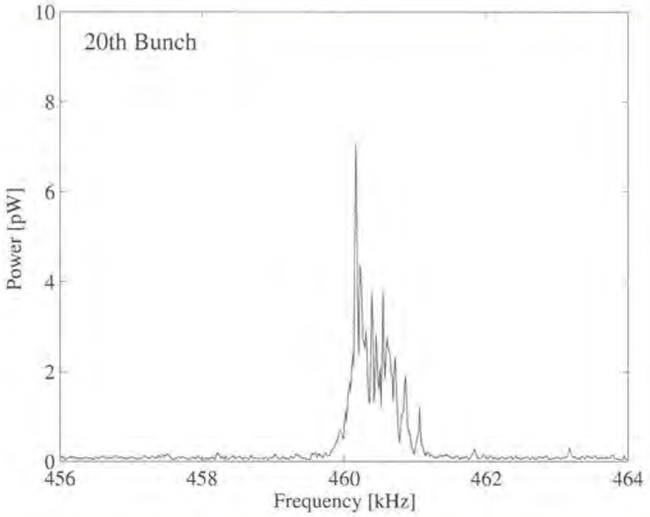

Figure 17.
Frequency spectra which correspond to the betatron sidebands of the 20th bunch in the bunch train.

where r_p represents the classical proton radius, *c* the speed of light, N_b the number of electrons in the bunch. *A* is the mass number of the ion, and $\sigma_x(s)$ and $\sigma_y(s)$ are the horizontal/vertical beam sizes at the longitudinal position *s* along the ring, respectively. The matrix that denotes the whole bunch train can be written by multiplying *DB(s)* and *D*, namely:

$$\begin{pmatrix} y_i(s,t_{rev}) \\ \dot{y}_i(s,t_{rev}) \end{pmatrix} = D^{h-L}[DB(s)]^L \begin{pmatrix} y_i(s,0) \\ \dot{y}_i(s,0) \end{pmatrix},$$

where *h* denotes the harmonic number, *L* the number of bunches in the train, and t_{rev} the revolution time around the storage ring, respectively.

An ion is affected by a periodic focusing force due to the passing of the bunch train, and oscillates around the beam orbit. Such motion of the ion can be discussed in a manner analogous to the "betatron oscillation" in linear beam-dynamics theory. Because the focusing factor depends on the longitudinal position along the ring, the "Twiss parameters of the ions" depend on *s*. Moreover, these parameters also depend on *t*, which means that they vary along the bunch train. Using this theory, the Twiss parameters of the ions at the longitudinal position *s* at the *n*-th bunch is as follows:

$$\begin{pmatrix} \beta_i(s,nt_{rf}) \\ \alpha_i(s,nt_{rf}) \\ \gamma_i(s,nt_{rf}) \end{pmatrix} = N^n_{bunch}(s) \begin{pmatrix} \beta_i(s,0) \\ \alpha_i(s,0) \\ \gamma_i(s,0) \end{pmatrix},$$

where β_i(s,t), α_i (s,t), γ_i (s,t) denote the Twiss parameters of the ion, and $N_{bunch}(s)$ is a transformation matrix of these parameters composed of matrix elements of *DB(s)*. The transformation matrix of a whole bunch train (*N(s)*) is written as follows;

$$N(s) = N^{h-L}_{drift} N^L_{bunch}(s),$$

where N_{drift} denotes a transformation matrix composed of the matrix

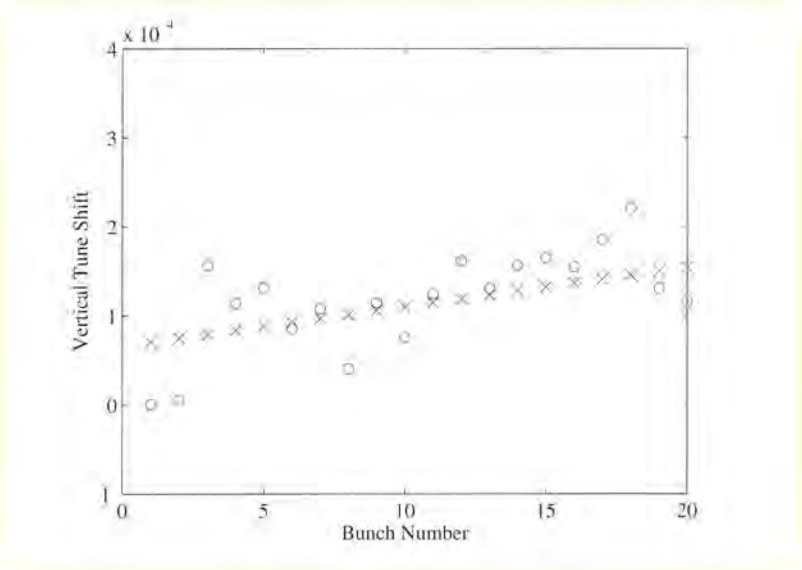

Figure 18.
Vertical betatron tunes of 20 bunches at the head of the train. Open circles denote the experimental result and crosses denote the theoretical values.

elements of *D*. The Twiss parameters of the ion at the head of the bunch can be defined by the matrix elements of *N(s)*.

Trapped ions take the "betatron oscillation" around the electron beam with amplitudes proportional to $\sqrt{\beta_i}$. Because $\sqrt{\beta_i}$ is a function of t, the size of the ion-cloud proportional to $\sqrt{\beta_i}$, or the density of the ions also changes with t . According to linear theory [2], the trapped ions can cause tune shifts, which are proportional to the ion density. Therefore, the modulation of the ion density could cause tune shifts that depend on the position of the train. The theoretical value according to a model in which the modulation of the ion density is taken into account are plotted in Fig.18. The theory agrees well with the experimental result.

References
[1] A. Mochihashi et al., Proc. of the 12th Symposium on Accelerator Science and Technology, (1999)421.
[2] Y. Baconnier, G. Brianti, CERN Int. Rep., CERN/SPS/80-2(DI).

1-2-2 Vibration Measurements

The vibration measurement system consists of vibrational gauges, amplifiers and a digital data recorder. Small vibration was detected by twelve sets of seismometers and six piezoelectric accelerometers. Each signal generated in gauges was amplified and sent to a digital data recorder that performs analog-to-digital transformations and data storage. The data-sampling rate was 500 Hz. The measured acceleration data were analyzed in the FFT and represented as a frequency spectrum. We represent the magnitude of the vibration using the root mean square (RMS) displacements converted from the measured acceleration in the frequency range of 1-100 Hz.

The vibrations of the air-conditioner (AC) have been recognized as the main source of the beam motion. In the light-source building, there were eight air-conditioners located above the storage ring tunnel and around the experimental hall that surrounds the storage-ring tunnel. Before measuring the vibrations of various parts of the light source building, the vibration of eight air-conditioners, themselves, were measured, in order to identify the frequency components of the measured data. Each air-conditioner has its fundamental mode of vibration in the frequency range from 14.8 to 22.5 Hz. Because there are only thin viscoelastic damping pads under these air-conditioners, these vibrations propagated around the light-source building.

The vibration of the storage ring tunnel floor was measured at twelve points using the twelve sets of probes situated along the storage ring. We measured the three components of the vibration with one set of probes. The displacement of the vertical direction is larger than the displacement of other two direction, but the magnitude of its displacement is only about 0.04 μm on the average.

The effects of the air-conditioners are evident from Fig.19, which presents the Fourier spectrum of the vertical ring tunnel floor displacement at a measuring point. One peak at 14.65 Hz corresponds to the fundamental vibration frequency of AC2, and another peak at 20.26 Hz also arises from AC4 (20.3 Hz). The magnitude of the 20.26 Hz peak amounts to 0.1 μm. This displacement is equivalent to a 0.07 μm RMS displacement. Thus, the vibration arising from the air-conditioners exhaust represents almost all of the RMS displacement measured at the point.

The vibration of the quadrupole magnet (Q-magnet) of the storage ring affects mostly the behavior of the stored electron beam motion. Thus, the vibration of the twelve Q-magnets selected from all storage ring Q-magnets were measured. Twelve sets of the probes were situated on top of the Q-magnets.

The magnitude of the RMS displacement of the Q-magnet vibration in the lateral (y) direction exceeds those in the other two directions. In the case of ring floor vibration, the displacement in the vertical (z) direction was prominent. On the contrary, the vibration of the Q-magnet in the lateral (y) direction was ten-times as large as the lateral (y) vibration of the floor. The Fourier spectrum of the Q-magnet displacement at the point is shown in Fig.20. Two major peaks at 14.53 and 20.26 Hz (already seen in the spectrum of the floor

Figure 19.
Fourier spectrum of the vertical displacement of the ring tunnel floor at a measuring point. The solid line shows the vibration with all AC stopped, and the dotted line shows that with all AC working.

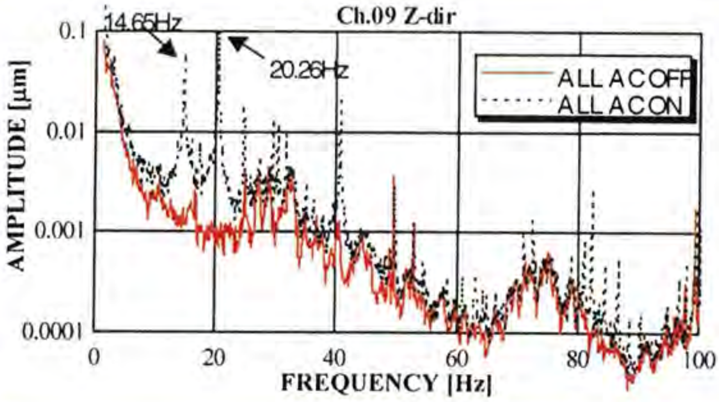

Figure 20.
Fourier spectrum of the Q-magnet vibration.

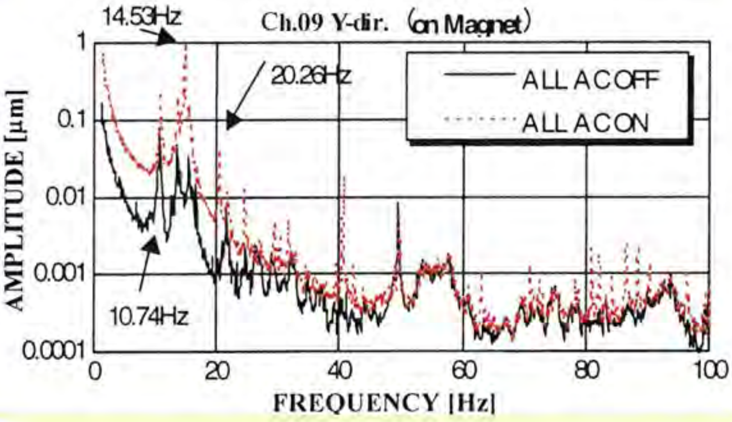

vibration) are also seen in this spectrum. Adding to these two peaks arising from the vibration of the air-conditioners, a new peak at 10.74 Hz appears. Because this peak can be seen when all air-conditioners stopped, it can be estimated that it arises from the fundamental resonant vibration of the girder and the Q-magnet.

After a lattice change of the PF ring for reducing the beam emittance, two Q-magnets and two sextupole magnets in a normal cell have been settled on a common girder. To investigate the vibrational properties of the girder and the Q-magnet, we have performed a hammering test and measured the fundamental resonant frequencies. The peak at 10.38 Hz, already seen in Fig.20, arises when the Q-magnet swayed on the girder in the lateral direction. Another remarkable peak at 13.18 Hz arises from twisting the girder's leg. The picture of the vibrational state of the Q-magnet and the girder is presented in Fig.21. This picture shows that the top of the Q-magnet vibrates heavily comparing to other part of the magnet and girder.

An obvious cure for the propagation of the air-conditioner vibration is to install a thick viscoelastic damping pad beneath the air-conditioner. From a simulation of this damping pad, the reduction of the propagated vibration amounts to -20 dB. We plan to measure the vibration of the stored electron beam and the synchrotron radiation beam more accurately, together with the vibration of the Q-magnets, in order to understand the correlation between these vibrations.

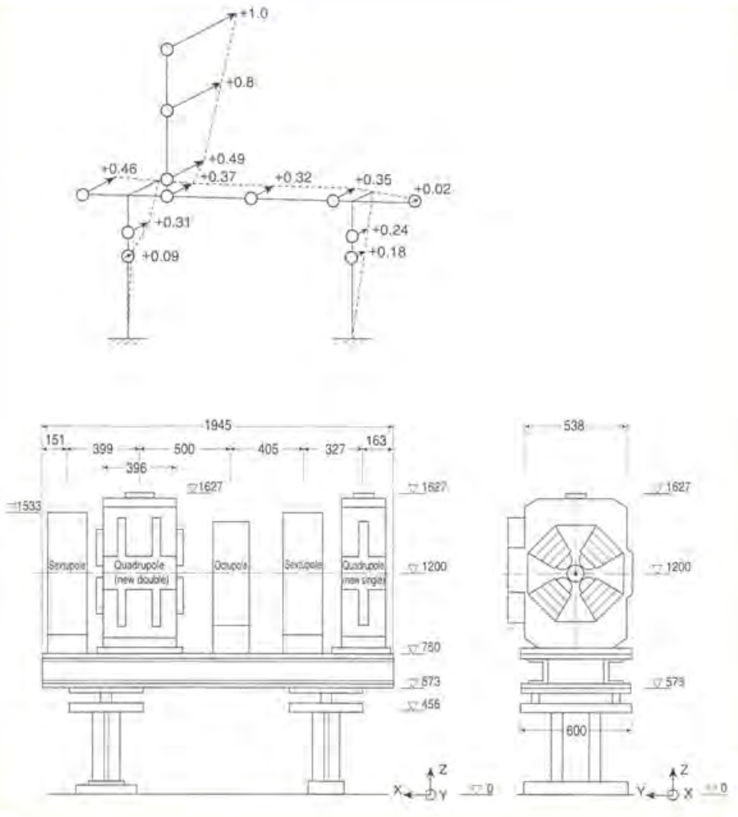

Figure 21.
Vibrational state of the Q-magnet and girder. Lower part of the figure shows the size of the Q-magnets and girder (in mm). Upper part presents the magnitudes of their swaying motion at 10.38 Hz in the lateral direction (arbitrary unit).

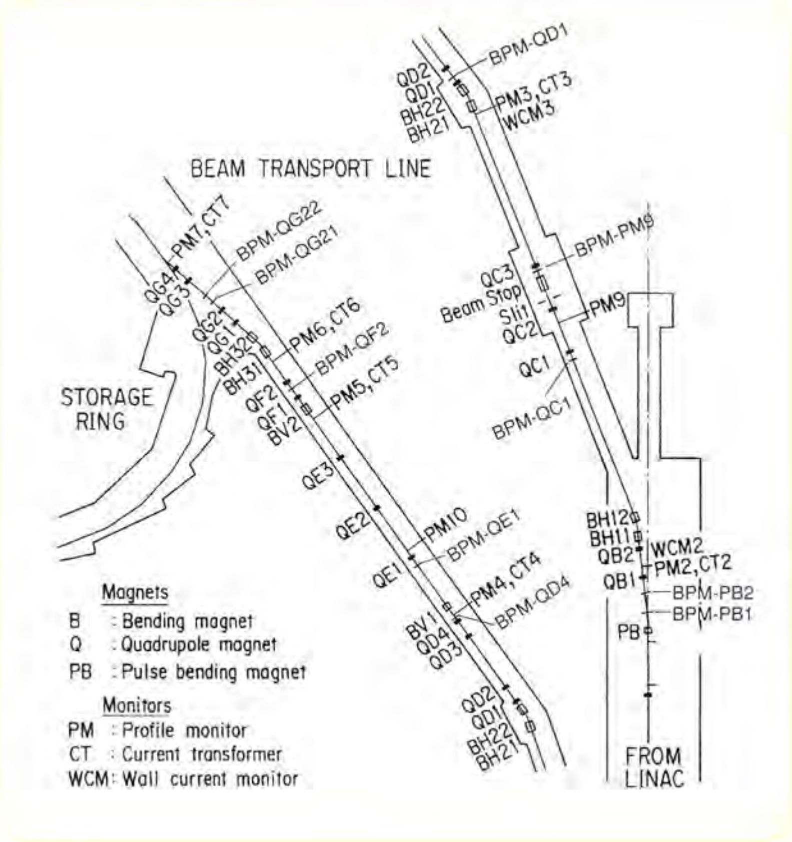

Figure 22.
Beam transport line.

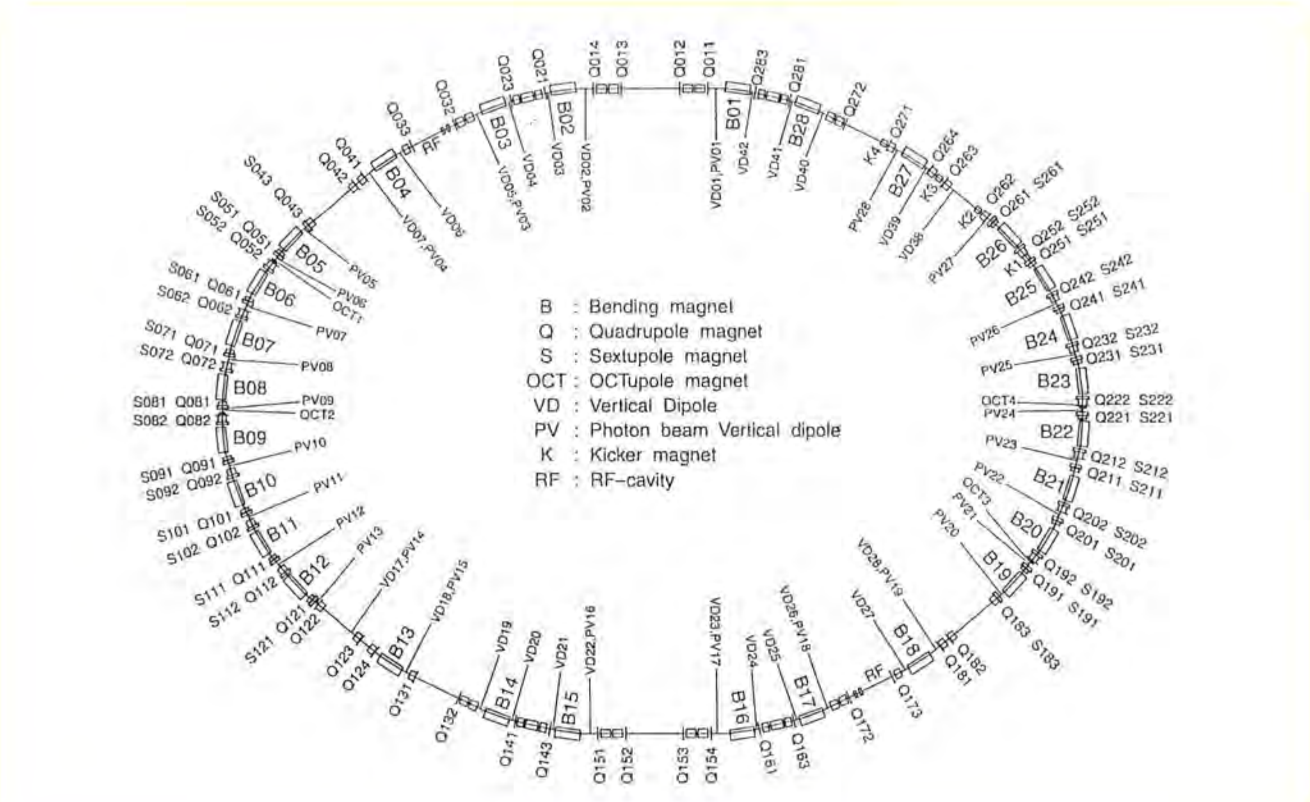

Figure 23.
Ring lattice components.

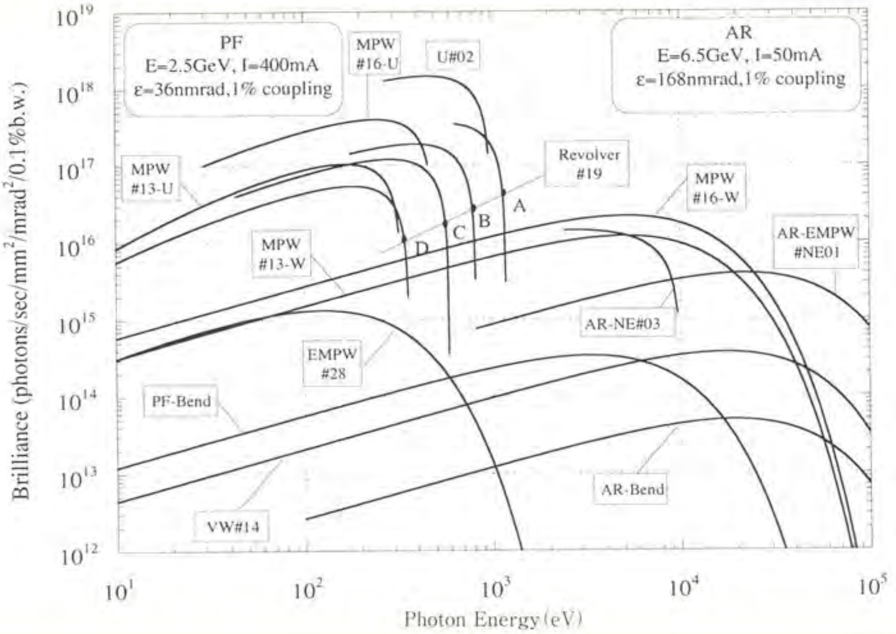

Figure 24.
Synchrotron radiation spectra.
Brilliance of radiation vs. photon energy for the insertion devices (U#02, MPW#13, VW#14, MPW#16, Revolver#19 and EMPW#28) and the bending magnet (Bend) of the PF, and for the insertion device (EMPW#NE1 and UNE3) of the AR. The name of each source of the PF is assigned in Table 2. Several insertion devices have both undulator and wiggler modes, which are denoted by U or W, respectively. The spectral curve of each undulator (or undulator mode of multipole wiggler) is a locus of the peak of the first harmonic within the allowable range of K-parameter. Spectra of Revolver#19 are shown for four kinds of period lengths.

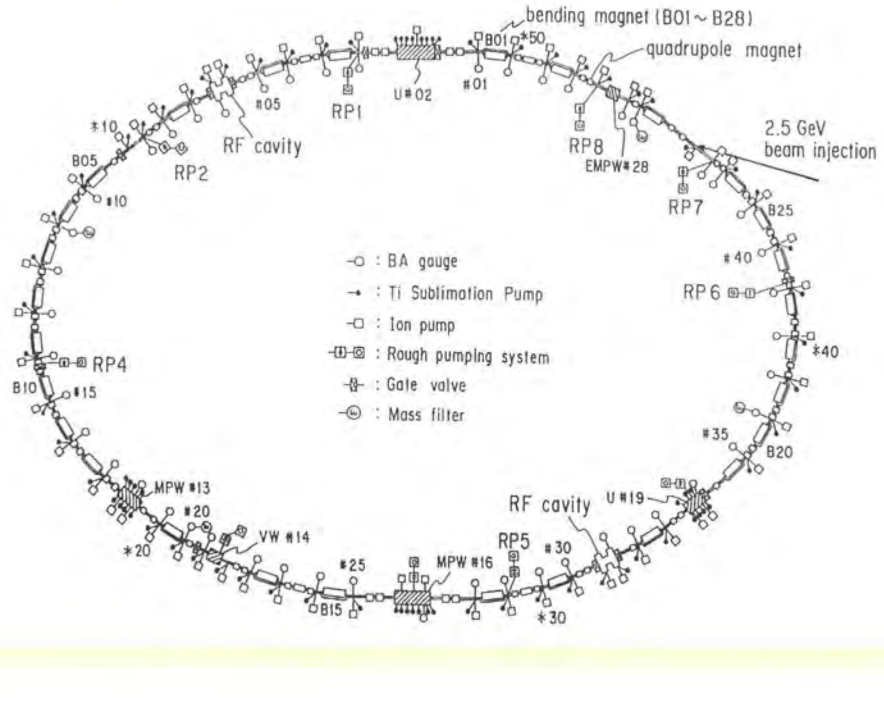

Figure 25.
Vacuum system components.

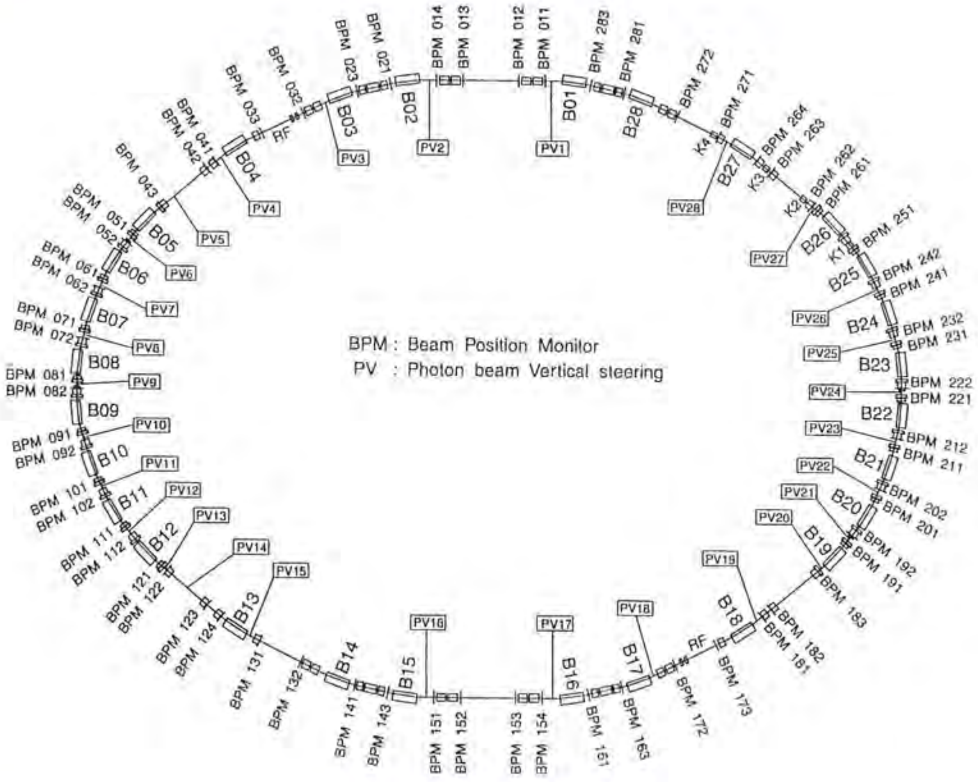

Figure 26.
Beam position monitors.

Table 2 Insertion devices

Caiculated spectral performances of the bend source and 6 insertion devices at the Photon Factory. E/I:beam energy and current, λ_u: period length, N: number of periods, L: length of undulator or wiggler, G_y (G_x) :minimum vertical (horizontal) gap height, B_y (B_x) maximum vertical (horizontal) magnetic field, P: pure configuration, H:hybrid configuration, S.C.: superconducting magnet, $\sigma_{x,y}$: horizontal or vertical beam size, $\sigma'_{x,y}$: horizontal or vertical beam divergence, K_h (K_v): horizontal (vertical) deflection parameter, $\varepsilon_1/\varepsilon_c$: photon energy of the first harmonic (critical energy in the case of bend source or wiggler), D: photon flux in unit solid angle (photons/s・mrad^2・0.1%b.w.), *B*: brilliance (photons/s・mm^2・mrad^2・0.1% b.w.), P_T: total radiated power, dP/dΩ: power in unit solid angle. Different operating modes of undulator and wiggler are denoted by - U and -W, respectively.

Name	E/I GeV/mA	λ_u cm	N	L m	$G_y(G_x)$ cm	$B_y(B_x)$ T	Type of magnet	σ_x mm	σ_y mm	σ'_x mrad	σ'_y mrad	$K_h(K_v)$	$\varepsilon_1/\varepsilon_c$ keV	D	*B*	P_T kW	dP/dΩ kW/mrad
Bend	2.5/300					0.96		0.39	0.059	0.186	0.013		4	4.80E+13	3.31E+14		0.081
U#02	2.5/300	6	60	3.6	2.8	0.4	H(NdFeB)	0.42	0.042	0.084	0.008	2.3	0.2	1.49E+17	1.30E+18	0.95	3.93
MPW#13-W	2.5/300	18	13	2.5	2.7	1.5	H(NdFeB)	0.86	0.019	0.117	0.018	25	6.2	1.29E+15	1.18E+16	8.64	3.38
MPW#13-U	2.5/300	18	13	2.5	2.7	1.5	H(NdFeB)	0.86	0.019	0.117	0.018	2	0.108	1.08E+16	9.25E+16	0.055	0.25
VW#14	2.5/300				5	5	S.C.	0.58	0.036	0.083	0.01		20.8	4.84E+13	3.67E+14		0.42
MPW#16-W	2.5/300	12	26	3.12	1.9	1.5	H(NdFeB)	0.42	0.042	0.084	0.008	16.8	6.2	1.03E+15	8.95E+15	10.89	6.46
MPW#16-U	2.5/300	12	26	3.12			H(NdFeB)	0.42	0.042	0.084	0.008	2	0.163	4.23E+16	3.63E+17	0.16	0.74
Revolver#19	2.5/300	5	46	2.3	3	0.28	H(NdFeB)	0.85	0.056	0.088	0.008	1.3	0.639	1.05E+17	3.47E+17	0.28	1.89
	2.5/300	7.2	32	2.3	3	0.4	H(NdFeB)	0.85	0.056	0.088	0.008	2.7	0.176	4.39E+16	1.44E+17	0.56	1.92
	2.5/300	10	23	2.3	3	0.54	H(NdFeB)	0.85	0.056	0.088	0.008	5	0.0437	1.28E+16	4.01E+16	1.02	2.02
	2.5/300	16.4	14	2.3	3	0.62	P(NdFeB)	0.85	0.056	0.088	0.008	9.5	0.0078	1.71E+15	4.29E+15	1.35	1.41
EMPW#28-W	2.5/300	16	12	1.92	3(11)	1(0.2)	P(NdFeB)	0.58	0.036	0.083	0.01	15(3)	4.1(90%)	3.07E+14	2.28E+15	2.84	0.46
EMPW#28-U	2.5/300	16	12	1.92			P(NdFeB)	0.58	0.036	0.083	0.01	3(3)	0.182(99%)	1.81E+16	1.33E+17	0.03	0.087

Table 3 General parameters of the PF storage ring.

Energy	2.5 GeV	(max 3 GeV)
Initial stored current (multi-bunch)	400mA	(max 500 mA at 2.5 GeV)
(single bunch)		65 mA (max 100 mA)
Emittance	36 nm · rad (horizontal) ~0.4 nm · rad (vertical)	
Circumference	187 m	(bending radius=8.66m)
RF frequency	500.1 MHz	(harmonic number=312)
Injection	2.5-GeV Linac	(positron/electron)
Beam lifetime	50 h (at 400 mA)	$I \cdot \tau \gtrsim 20$ A · h (at 400 mA)
Average vacuum pressure	$\lesssim 2 \times 10^{-8}$ Pa (at 300 mA) $P/I \times 6\text{-}7 \times 10^{-8}$ Pa/A (at 300 mA) $\sim 9 \times 10^{-8}$ Pa (at 0 mA)	
Insertion devices	Superconducting vertical wiggler 5T 60 period undulator K=2.3~0.1 26 period multipole wiggler/undulator 1.5T~0.04T Four way revolver type undulator 13 period multipole wiggler Elliptically polarized multipole wiggler	
SR channels	SR experiment 22 Beam diagnosis 3	

Table 4 Beam parameters.

Horizontal tune ν_x	9.60
Vertical tune ν_y	4.28
Momentum compaction factor α	0.0061
Natural chromaticity ξ_x	-12.5
ξ_y	-12.3
Bunch length σ_z	1.0 cm
Transverse damping time	7.8 msec
Longitudinal damping time	3.9 msec
Energy spread	7.3×10^{-4}
Radiation loss	400 keV

Table 5 Principal parameters of the accelerator system.

Magnet system

	number of magnets	number of power supplies
Bending	28	1
Quadrupole	74	15
Sextupole	32	3
Octupole	4	4
Vertical steerers	24	24
Fast vertical steerers for global orbit FB	28	28
Backleg windings		
on bendings for horizontal steerers	28	28
on sextupoles for vertical steerers	28	28
on sextupoles for skew quadrupoles	14	14
on sextupoles for field compensation	32	3
Electronic shunts on quadrupoles		
for optics matching and tune compensation	34	48

RF system

Number of RF stations	4
Number of klystrons	4 (180kW/klystron)
Number of RF cavities	4 (single cell cavity)
Shunt impedance	27.6MΩ (four cavities)
Unloaded Q	39000
Total power dissipated in cavity wall	105 kW
Total cavity gap voltage	1.7 MV
Synchrotron frequency	23 kHz

Vacuum system

Main pumping system		
pump	pumping speed	number
SIP(Sputter Ion Pump)	128 l/sec	54
DIP(Distributed Ion Pump)	150 l/sec	26
Ti sublimation	……	71
NEG(Non-Evaporable Getter)	……	2
total effective pumping speed $=2\times10^{4}$ l/sec(for CO)		
Rough pumping system	pumping speed	number
TMP(Turbo Molecular Pump)	300 l/sec	12
Measurement	number	
B-A gauge	48	
mass filter	4	
cold cathode gauge	24	
Sector gate valve	number	
all metal with RF shield	4	
viton seal with RF shield	7	

Injection system

Septum magnet		
name	Septum I (S1)	Septum II (S2)
core material	laminated silicon steel(passive type)	
length [mm]	1500	1000
maximum current [A]	6000	6000
deflection angle [degree]	7.0	5.0
pulse width [μ sec]	120	100

Kicker magnet	
name	K1, K2, K3, K4
core material	ferrite (Traveling wave type)
core length [mm]	345
	15000
maximum voltage [V]	4.1
pulse width [μ sec]	1.7

Superconducting vertical wiggler

Maximum field strength on the beam orbit	5 Tesla
Magnet gap	66 mm
Magnet pole size (width × hight)	40 mm×260 mm
Number of magnetic poles	5 poles (3 poles at nomal operation) installedat exery 200 mm
Rated exciting current	210 A at 4.8 Tesla
Superconducting wire	NbTi:Cu 1:1 size 1.70×0.85mm^2
Cross section of coils	65 mm×70 mm
Number of turn	2520
Liquid helium consumption in the permanent current mode	1.1 L/h
Damping rate of the permanent current	1.4×10^{-5}/h
Inductance	1.31 H/coil

Monitor system

I . Orbiting beam monitors

PM (Position Monitor)	65
DCCT (Direct Current Current Transformer)	2
RFKO (Radio Frequency Knock-Out system)	1
WCM (Wall Current Monitor)	1
LS (Loss monitor)	30
Visible Light Monitors	
CCD TV camera	1
streak camera	2
photon counting system	1

II .Photon beam position monitors installed in beamlines

Beamline	Source	Upstream	Downstream	Ver./Hor.
BL3A	B	SPM		V
BL3C	B	SPM	SPM	V
BL4C	B	SPM	SPM	V
BL6B	B	SIC		V
BL6C	B	SIC		V
BL6C	B	SPM	SPM	V
BL7C	B	SIC	SPM	V
BL10B	B	SIC		V
BL12C	B	WM	WM	V
BL21	B	WM		V
BL27	B	SPM		

Note: SPM: Split Photoemission Monitor B: Bending magnet
SIC: Split Ion Chamber
WM: Wire Monitor Superconducting Vertical Wiggler

Control system

Computers				
	Server	Workstation	PC	VME
Presentation/Console	—	3	17	—
Control/DB Engine	1	16	5	6
Equipment Control	—	—	3	9
Network Management	—	2	1	—
Network				
	Number	Port		
ATM Switch (155Mbps)	1	single mode 12		
			multi-mode 4	
ATM-Ethernet Switching Hub	12	10BASE-T 12/hub		

Table 6 Beam parameters at source points.

B.L.	Source	σ_x[mm]	σ'_x[mrad]	σ_y[mm]	σ'_y[mrad]
BL01	B01(+2.5)	0.203	0.245	0.061	0.0125
BL02	U#02	0.422	0.084	0.042	0.0084
BL03	B02(-0.0)	0.238	0.263	0.066	0.0125
	B03(+0.0)	0.288	0.228	0.084	0.0066
BL04	B04(+2.5)	0.319	0.161	0.066	0.0173
BL06	B06(+2.5)	0.391	0.185	0.059	0.0129
BL07	B07(+2.5)	0.391	0.185	0.059	0.0129
BL08	B08(+2.5)	0.391	0.185	0.059	0.0129
BL09	B09(+2.5)	0.391	0.185	0.059	0.0129
BL10	B10(+2.5)	0.391	0.185	0.059	0.0129
BL11	B11(+2.5)	0.391	0.185	0.059	0.0129
BL12	B12(+2.5)	0.447	0.138	0.054	0.0092
BL13	MPW#13	0.859	0.115	0.020	0.0186
BL14	VW#14	0.580	0.083	0.036	0.0098
BL15	B15(+2.5)	0.203	0.245	0.061	0.0125
BL16	MPW#16	0.422	0.084	0.042	0.0084
BL17	B16(-0.0)	0.238	0.263	0.066	0.0125
	B17(+0.0)	0.288	0.228	0.084	0.0066
BL18	B18(+2.5)	0.319	0.161	0.066	0.0173
BL19	U#19	0.847	0.088	0.057	0.0078
BL20	B20(+2.5)	0.391	0.185	0.059	0.0129
BL21	B21(+2.5)	0.391	0.185	0.059	0.0129
BL27	B27(+1.2)	0.259	0.218	0.090	0.0176
BL28	EMPW#28	0.580	0.083	0.036	0.0098

Table 7. Summary of beamline front ends in FY 1999.

Beamline	Affiliation	Source	Spectral range	Status
BL-1	KEK-PF	Bending magnet (B1)	VUV and X-ray	in operation
BL-2	KEK-PF	60-period undulator	soft X-ray	in operation
BL-3	KEK-PF	Bending magnet (B2&B3)	VUV and soft X-ray	in operation
BL-4	KEK-PF	Bending magnet (B4)	X-ray	in operation
BL-5	KEK-PF		-	in design
BL-6	KEK-PF	Bending magnet (B6)	X-ray	in operation
BL-7	KEK-PF and University of Tokyo	Bending magnet (B7)	VUV and X-ray	in operation
BL-8	Hitachi Ltd.	Bending magnet (B8)	VUV and X-ray	in operation
BL-9	Nippon Electrical Co. (NEC)	Bending magnet (B9)	VUV and X-ray	in operation
BL-10	KEK-PF	Bending magnet (B10)	X-ray	in operation
BL-11	KEK-PF	Bending magnet (B11)	VUV and soft X-ray	in operation
BL-12	KEK-PF	Bending magnet (B12)	VUV	in operation
BL-13	KEK-PF	27-pole wiggler/undulator	Soft and hard X-ray	in operation
BL-14	KEK-PF	Superconducting vertical wiggler	hard X-ray	in operation
BL-15	KEK-PF	Bending magnet (B15)	X-ray	in operation
BL-16	KEK-PF	53-pole wiggler/undulator	Soft and hard X-ray	in operation
BL-17	Fujitsu Ltd.	Bending magnet (B16&B17)	VUV and X-ray	in operation
BL-18	ISSP and KEK-PF	Bending magnet (B18)	VUV and X-ray	in operation
BL-19	ISSP and KEK-PF	Multi-undulator	VUV	in operation
BL-20	KEK-PF	Bending magnet (B20)	VUV and X-ray	in operation
BL-21	KEK-PF	Bending magnet (B21)	Beam diagnosis	in operation
BL-27	KEK-PF	Bending magnet (B27)	Soft X-ray and X-ray	in operation
BL-28	KEK-PF	25-pole wiggler/undulator	Circularly polarized VUV and soft X-ray	in operation

2 PF-AR

2-1 Operations

2-1-1 Summary of Operations

The operation statistics of the PF-AR are shown in Fig.1 and Table 1. Although several problems caused by superannuation have been encountered, almost 80% in the total opeartion time (4148 hours) was user time, as shown in the table. The typical operation status in user time is shown in Fig.2. Operations for "medical application" were performed in May 1999 (total six days) and in March 2000 (total three days). Medically meaningful clear X-ray pictures of the arterises of patients were taken as "medical applications". Although the PF-AR has become a dedicated single-bunch synchrotron radiation source, the purity was not satisfactory during the previous year. A new single-bunch purifier was successfully tested and used routinely during user time. An impurity of less than 10^{-6} was achieved using the new system. The principal parameters of the PF-AR are tabulated in Table 2.

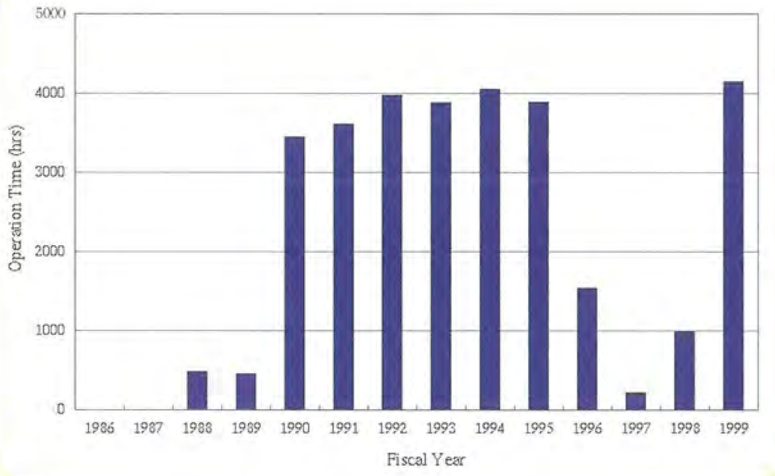

Figure 1.
Operation Time of PF-AR.

Table 1: Operation statistics of the PF-AR in fiscal 1999.

Operation time	SR experiment	Beam development	Failure	Miscellaneous
4148.0 h	3269.5 h	473.5 h	307.0 h	98.0 h
100 %	78.8 %	11.4 %	7.4 %	2.4 %

Table 2: Prencipal parameters of the PF-AR .

Energy	5.0/6.5 (GeV)
Bending radius	23.708 (m)
Circumference	377.26 (m)
RF frequency	508.58 (MHz)
Harmonic number	640
Betatron tune (H/V)	10.15/10.23
Emittance	294 (nm・rad)
Initial Current	40 (mA)

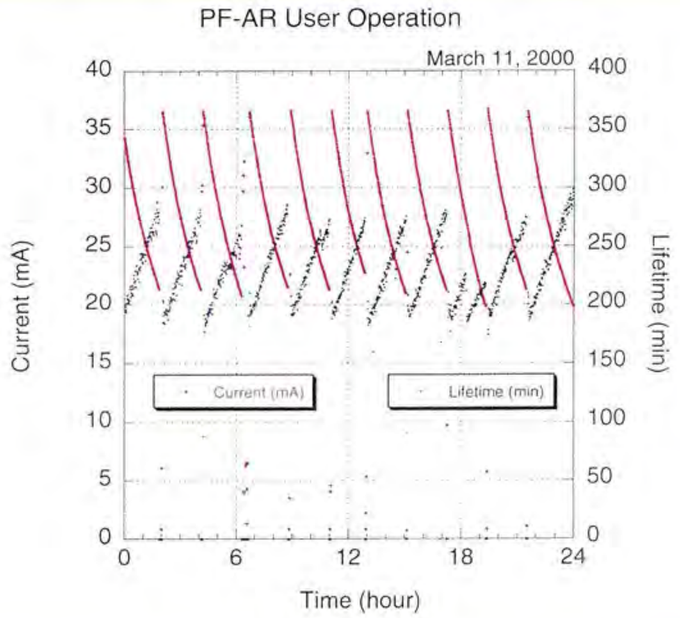

Figure 2.
Typical operation status during user time.

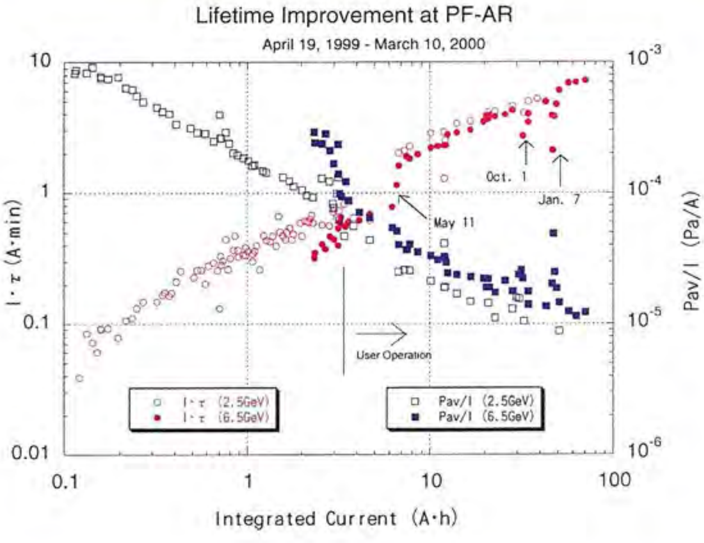

Figure 3.
Progress of the vacuum pressure improvement and the lifetime increase with the cumulative beam dose during fiscal 1999.

2-1-2 Vacuum Improvement

When we started to operate the PF-AR as a dedicated synchrotron light source in April 1998, the beam lifetime was only several ten minutes, because some vacuum pumps had become old for use. Since then, a longer beam lifetime has been strongly required because one injector linac is shared among four storage rings, and we can not basically inject the electron beam to the PF-AR more often than every two hours. Therefore, we had to improve the vacuum system in order to achieve a satisfactory beam lifetime and to increase the activity of the PF-AR.

The progress of the vacuum pressure improvement and the lifetime increase during fiscal 1999 is shown in Fig.3. When the user operation started on April 27, the lifetime of the 6.5 GeV - 38 mA beam was about ten minutes (i.e. $\mathrm{I}\cdot\tau$, the product of the stored current and the lifetime, was about 0.4 A·min). This short lifetime was caused by an after-effect of a vacuum leak which occurred in June, 1998. In addition, another leak occurred from a gate valve inserted into the vacuum ducts on April 28; thus, the $\mathrm{I}\cdot\tau$ was limited to 0.7 A·min until we found the source of the leak and fixed it on May 11. After that, the lifetime increased smoothly with the progress of the vacuum ducts baking by synchrotron radiation. In October, however, a vacuum leak occurred again from the same gate valve that leaked in April. We could fix it again, but not completely. Therefore, we removed the gate valve in December and simultaneously reinforced the pumping speed by installing several sputter ion pumps at some effective spots. As a result, the $\mathrm{I}\cdot\tau$ increased up to 7 A·min in February. In this case, if the electron beam is injected to 40 mA every 2 hours, the average stored beam current amounts to 30 mA, and every 4 hours, 25 mA.

After replacing the high-voltage cables for cold cathode gauges (CCGs) in 1998, the number of available CCGs increased by 35 to 51. To make use of these CCGs, we improved the pressure monitor system with EPICS, which was adopted in the KEKB control system. By increasing the number of CCGs, we could obtain more precise information about the change in the vacuum pressure, especially in case of a vacuum leak. This EPICS system also made it possible to log the pressure data, the beam lifetime, and time-integrated current. In the upgrading project of the PF-AR, we plan to use this EPICS system to control and monitor all vacuum devices.

2-2 Upgrading Project

2-2-1 General Description

The PF-AR was originally designed as a booster ring for the TRISTAN project. The ring had been partially used as a pulse X-ray source during this project. After the project was completed, the ring could be fully used for SR experiments. However, there are some problems since the ring was not designed as a dedicated light source. The first problem is that the beam lifetime is short, because the vacuum system performance is insufficient. The typical beam current and beam lifetime in user runs are shown in Fig.2 . We must inject the electron beam 10 times per day. The second one is that about half of the beam position monitors (BPMs), which are welded on the vacuum ducts, have lost their reliabilities. It is thus difficult for operators to maintain the beam orbit stabilities run by run. The third one is that the available beam lines for synchrotron-radiation experiments are insufficient; the undulator beam lines are only two, and the bending ones are also only two. Therefore, we have intended to make a ring change to a new pulsed X-ray source as the PF-AR. The main parameters of the new PF-AR are as follows: beam energy, 6.0-6.5 GeV; maximum beam current, 100 mA; and beam lifetime, 10 hours or more. Such a beam lifetime will give us an injection interval of 8 hours. In addition, we intend to reduce the beam emittance from 294 nm·rad to 165 by changing the horizontal betatron phase advance and to stabilize the beam orbit by using reliable BPM's and a feedback system.

The improvement to the PF-AR was started in the budget of fiscal 1999 prepared by KEK. A part of the vacuum duct was manufactured. We changed the duct materials from aluminum alloy to OFHC copper in order to endure a high heat load and to reduce the radiation damage of the accelerator components in the ring tunnel by high-energy photons. The BPM electrodes were newly designed and manufactured, which are mounted using vacuum flanges on the vacuum ducts.

In December, 1999, the Government gave a revised supplemental budget for the PF-AR project. We designed the vertical steering magnets and ordered to manufacture them. Some quadrupole and sextupole magnets are newly designed to extract SR without any geometrical interference. Because we have to enhance the pumping speed of the vacuum system to obtain a long beam lifetime, we arranged distributed ion pumps (DIP), sputter ion pumps (SIP), titanium sublimation pumps (TSP) and non-evaporable getter pumps (NEG) around the ring vacuum ducts. We arranged vacuum gauges every 5 meters and monitor vacuum pressure in the whole ring. The control system will be changed from the present NORDAL system to the EPICS system. The monitor beam line has been designed. It includes optical components and an in-vacuum-type insertion device. It will be useful to confirm the performance of the stored beam. Since the budget did not completely fulfill our requirements, we must reuse the present 11-cell APS cavities, of which HOM dummy loads will be reinforced. Thus, this may restrict the expected highest beam current of 70 mA.

We will start replacement work in the PF-AR tunnel in the middle of February, 2001, and finish them at the end of October. The commissioning will be conducted in the early stage of November, and the user run is expected to start in December.

2-2-2 Magnet System

The lattice configuration does not change basically in the present upgrade plan. Thus, all existing bending magnets, most quadrupole and sextupole magnets, and their power supplies are to be reused. These are elaborately maintained by exchanging with new parts, as possible; for example, the cooling water rubber hose, the cable, the coil and the flowmeter, etc. However, few quadrupole and sextupole magnets are newly manufactured to avoid interference with both the existing and future X-ray beam lines. Cross-sectional views and photographs of the new quadrupole and sextupole magnets are shown in Figs. 4 and 5. In addition, the vertical steering magnets are newly designed to ensure space for the vacuum system, and the number of the magnets is to increase from 44 to 79 for further orbit stabilization. Also, the existing power supplies for the steering magnets in both horizontal and vertical directions are to be replaced by new ones to improve both the resolution and the reliability.

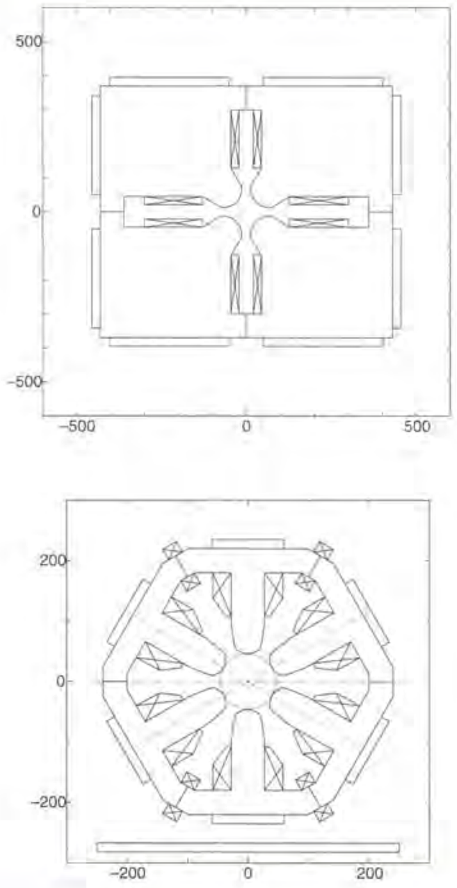

Figure 4.
Cross sectional views of the new quadrupole and sextupole magnets.

2-2-3 RF System

An rf system of the PF-AR comprises six 11-cell alternating periodic structure (APS) cavities, two 1-MW klystrons with their power supplies, and rf distribution networks. Two cavities, which are installed in the east straight section, are driven by a single klystron. The other four cavities are installed in the west straight section. The six cavities can provide an rf voltage of more than 16 MV, which is required to store a beam of 6.5 GeV. A total rf power of about 890 kW is required at the present beam current of 40 mA. After the reconstruction, a power of 1.12 MW will be required at an anticipated beam current of 70 mA (parasitic mode losses are not included).

The upgrade of the rf system is minimized in the present reconstruction plan. A further upgrade, including a possible change of the rf cavities, is planned in the next stage. In order to store a higher beam current in a single bunch, a reinforcement of the higher-order-mode (HOM) loads, which terminate the cavity HOM couplers, is essential. We plan to replace the present seventy-two 1-kW loads with new 3-5 kW ones. Furthermore, several upgrades, including an improvement in the crowbar circuit of the klystron power supply and a replacement of some overage devices, are on the way.

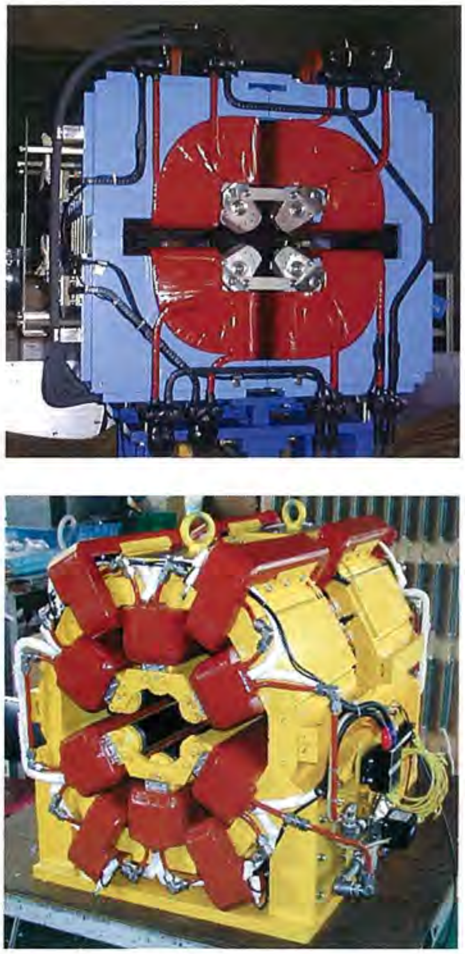

Figure 5.
Photographs of the the new quadrupole and sextupole magnets.

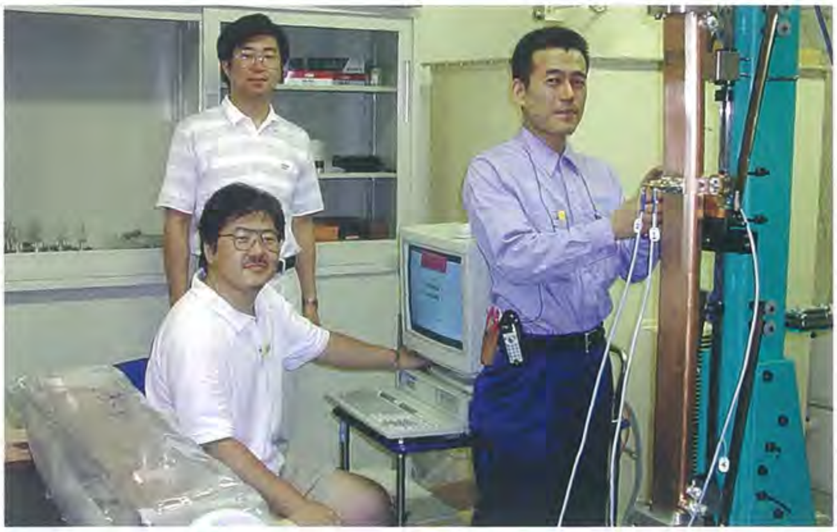

2-2-4 Vacuum System

The main problems of the new vacuum system are to achieve the low pressure necessary for a beam lifetime improvement and a countermeasure to the high thermal load due to the increased stored beam. The beam lifetime of the PF-AR depends upon the operating pressure, and it has been estimated that a pressure of 4×10^{-7} Pa or less is necessary at a stored current of 100 mA for the aimed lifetime. The beam chambers of the whole circumference should be replaced by new ones, except for the rf cavities, insertion devices and some beam-diagnostics equipment.

The pumping speeds and those locations have been examined so as to realize the required pressure without changing the main magnets and those arrangements. The beam chambers have been designed to be equipped at the required speeds. A typical chamber design for the arc sections is schematically shown in Fig.6. An OFHC (Oxygen Free High Conductivity) copper has been chosen as the main material of

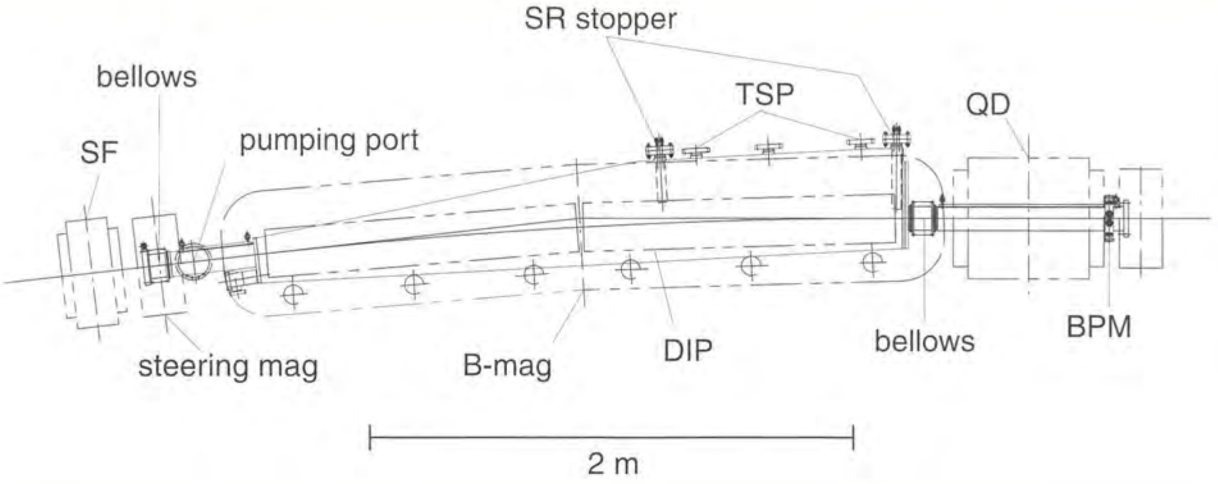

Figure 6. Typical chamber design for the arc sections.

the new beam chamber, because of its high thermal conductivity and property of suppressing the radiation leakage, though the flange and bellows are made of stainless steel. Every bellows is equipped with rf contacts. An arc chamber is composed of a straight part with a BPM, a part in a bending magnet and a bellows component. They are manufactured independently and will be assembled after calibrating the BPM at KEK. The production of the parts of 42 arc chambers and bellows of 12 arc chambers was finished in fiscal 1999.

An examination for selecting the vacuum pumps and gauges has advanced in parallel with the design and manufacture of the chambers. The following will be installed in the ring: 56 DIP's (Distributed Ion Pumps), TSP (Titanium Sublimation Pump) over 200, SIP (Sputter Ion Pump) over 80 and CCG (Cold Cathode Gauge) over 80.

2-2-5 Monitor System

In the present upgrade plan, several beam monitors will be renewed, owing to a replacement of the whole vacuum duct. We will prepare a beam-position monitor at each quadrupole magnet. The beam chambers of the new race track shape are made of copper tube, and the four feed-throughs with button type electrode will be attached by flanges. About 400 halogene-free coaxial rf cables and 100 coaxial mercury relay switches will be newly installed in the ring tunnel, but the electronics for the beam signal processing, which was situated in the four control buildings, is scheduled still to be used.

Synchrotron-light monitors are now being carefully designed for precise measurements of the beam profile. The beam scrapers and the beam stopper are also newly constructed, but the DCCT (Direct Current Current Transformer), CT (Current Transformer), WCM (Wall Current Monitor) and the beam damper system will be transferred to the empty straight sections.

2-2-6 Control System

There are many restrictions to improve the control system of the PF-AR. It is very important to make use of the existing hardware and to minimize the load of software development due to the limitation of human power. Seamless operation between the LINAC and the KEKB is also a point to be considered. It seems that it is the best way to adopt EPICS (Experimental Physics and Industrial Control System)[1] in order to achieve these requirements, since the control system of the KEKB is constructed by EPICS and has made great success [2,3]. The EPICS is a collection of software tools and other components, which has been developed by the collaboration of many laboratories around the world.

The control system can be classified into three layers: device interface layer, equipment control layer and operator interface layer. The operator interface layer is composed of UNIX workstations and X-terminals, while the equipment control layer is connected with a fast network interface. In order to control many kinds of input/output data of the accelerator equipment, the EPICS uses a distributed database on IOC (Input Output Controller), which can be accessed by the CA (Channel Access) protocol based on the TCP/IP protocol.

Four IOCs are already installed at each sub-control building (AR-N, W, S, E) and are operated for the beam-current monitor, calculation of beam lifetime and vacuum controllers. We are planning to use a total of 13 IOCs (RF:2, Magnet:2, Beam Monitor:5, Vacuum:2, Control:1) and VME modules, such as an auxiliary CAMAC crate controller, a GPIB interface, and an ARCNET module for the control of magnet power supply.

At the central control room, an X-terminal or its emulator on personal computers will be used as a console of man-machine interface program.

The development of the control system will be performed by the following procedure. At first, we will create a database of wiring information of the control system. The database will be used to create boot parameter files of various equipment connected to the IOCs. Although much equipment used in the AR is also used in the KEKB, we must develop some device driver software on VxWorks for new equipment as the next step.

References

[1] L.R.Dalesio, et al. 'EPICS Architecture', Proc. ICALEPCS'91, KEK, Tsukuba, Japan, (1991)278.

[2] T. Katoh, et al. Proc. ICALEPCS'95, Chicago, USA, (1995)899.

[3] T. Katoh, et al. Proc. ICALEPCS'97, Beijing, China (1997).

2-2-7 Schedule

The PF-AR will be operated until the middle of February, 2001 before the start of its renewal. All components will be delivered before December, 2000, as mentioned in the above sections. Previous to restructuring of the ring, we must remove the radiation shielding between the tunnel and the south experimental hall to ensure the access way from the entrance in that hall by the middle of February, 2001. After a survey and alignment of the magnet positions, old vacuum components will be removed and replaced with new ones. After connecting the vacuum chambers,the magnet system will be again aligned precisely. On the other hand, we must construct radiation shielding walls and a ceiling in the south experimental hall in

LIST OF PUBLICATIONS

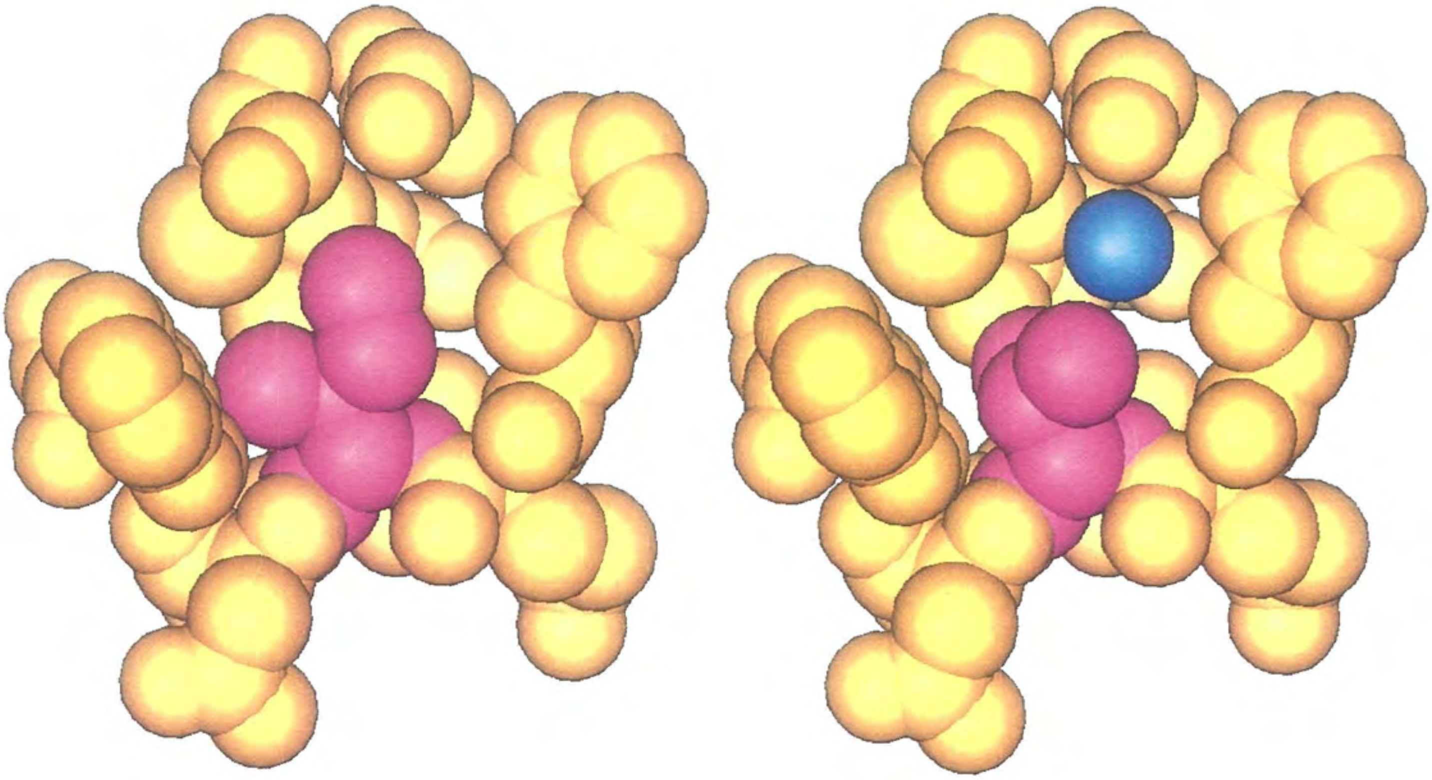

1A

M.Oshima, K.Ono, M.Mizuguchi, T.Uragami, H.Fujioka, M.Tanaka and Y.Watanabe
Photoelectron Spectroscopy and Magnetic Properties of Manganese Pnictides Nanocrystals Formed on Passivated GaAs Substrates
Jpn. J. Appl. Phys., **38** (1999) 373.

K.Ono, T.Uragami, M.Mizuguchi, H.Fujioka, M.Oshima, M.Tanaka, H.Akinaga and Y.Watanabe
Formation of Low-Dimensional Structures of Manganese Pnictides
J. Mag. Soc. Jpn., **23** (1999) 688.

K.Ono, M.Mizuguchi, T.Uragami, T.Mano, H.Fujioka, M.Oshima, M.Tanaka and Y.Watanabe
Formation on MnAs Dots on S-Passivated GaAs(100) Substrates
J. Mag. Soc. Jpn., **23** (1999) 691.

T.Uragami, K.Ono, M.Mizuguchi, T.Mano, H.Fujioka, M.Oshimam M.Tanaka and Y.Watanabe
Growth of MnAs on S- and Se-Passivated GaAs Substrates
J. Mag. Soc. Jpn., **23** (1999) 694.

T.Ikeda, H.Fujioka, K.Ono, M.Oshima, H.Akinaga, M.Yoshimoto, H.Maruta, H.Koinuma and Y.Watanabe
Epitaxial Growth of MnSb on Single Crystalline Ferrite Substrates
J. Mag. Soc. Jpn., **23** (1999) 685.

M.Oshima, K.Ono, M.Mizuguchi, H.Fujioka, M.Tanaka and H.Akinaga
Growth and Properties of Magnetic Nanostructures on Semiconductor Surfaces
J. Mag. Soc. Jpn., **24** (2000) 67. (*in Japanese*).

1B

Y.Kubozono, Y.Takabayashi, S.Fujiki, S.Kashino, T.Kambe, Y.Iwasa and S.Emura
Metal-Insulator Transition at 50 K in Na_2C_{60}
Phys. Rev., **B59** (1999) 15062.

Y.Maniwa, H.Kira, F.Shimizu and Y.Murakami
Development of Superstructure in Potassium-Loaded Zeolite LTA, $K_xK_{12}Si_{12}Al_{12}O_{48}$
J. Phys. Soc. Jpn., **68** (1999) 2902.

K.Ohwada, H.Nakao, Y.Fujii, M.Isobe and Y.Ueda
Structural Aspects of NaV_2O_5 under High Pressure
J. Phys. Soc. Jpn., **68** (1999) 3286.

K.Ishii, T.Watanuki, A.Fujiwara, H.Suematsu, Y.Iwasa, H.Shimoda, T.Takenobu and T.Mitani
Orientational Ordering of Alkali Ammonia Clusters in Ammoniated Alkali Fullerides $(NH_3)K_3C_{60}$ and $(ND_3)K_3C_{60}$
Proc. of XIIIth Int. Winterschool on Electronic Properties of Novel Materials, (1999) 60.

T.Watanuki, A.Fujiwara, K.Ishii, Y.Matsuoka, H.Suematsu, K.Ohwada, H.Nakao, Y.Fujii, K.Kikuchi and Y.Achiba
Structural Phase Transitions of Metallofullerene La@C_{82} Studied by Single Crystal X-Ray Diffraction
Proc. of XIIIth Int. Winterschool on Electronic Properties of Novel Materials, (1999) 124.

X.H.Chen, Z.S.Liu, D.H.Chi and Y.Iwasa
Structure and Properties of a Fulleride Sm_6C_{60}
Phys. Rev. B, **60** (1999) 6183.

K.Ishii, T.Watanuki, A.Fujiwara, H.Suematsu, Y.Iwasa, H. Shimoda, T.Takenobu and T.Mitani
Structural Phase Transition in Ammoniated Alkali Fullerides: Orientational Ordering of Alkali Ammonia Cluster
Mol. Cryst. Liq. Cryst., **340** (2000) 571.

T.Watanuki, A.Fujiwara, K.Ishii, Y.Matsuoka, H.Suematsu, K.Ohwada, H.Nakao, Y.Fujii, K.Kikuchi and Y.Achiba
Structural Phase Transitions of Endohedral Metallofullerene La@C_{82} Studied by Single Crystal X-Ray Diffraction
Mol. Cryst. Liq. Cryst., **340** (2000) 639.

A.Fujiwara, K.Ishii, T.Watanuki, H.Suematsu, H.Nakao, K.Ohwada, Y.Fujii, Y.Murakami, T.Mori, H.Kawada, T.Kikegawa, O.Shimomura, T.Matsubara, H.Hanabusa, S.Daicho, S.Kitamura and C. Katayama
Synchrotron Radiation X-Ray Powder Diffractometer Using a Cylindrical Imaging Plate
J. Appl. Crystallogr., **33** (2000) 1241.

X.H.Chen, D.H.Chi, Z.Sun, T.Takenobu, Z.S.Liu and Y.Iwasa
Synthesis, Structure, and Transport Properties of Novel Fullerides A_3C_{70} (A=Ba and Sm)
J. Am. Chem. Soc., **122** (2000) 5729.

K.Ohwada, H.Nakao, N.Takesue, Y.Fujii, M.Isobe, Y. Ueda, Y.Wakabayasi and Y.Murakami
Pressure-Induced Phase Transition in NaV_2O_5 at Low Temperature
J. Phys. Soc. Jpn., **69** (2000) 639.

K.Ishii, H.Ootoshi, Y.Nishi, A.Fujiwara, H.Suematsu and Y.Kubozono
Crystal Structure and Magnetic Properties of $Eu_xSr_{6-x}C_{60}$
Proc. of XIVth Int. Winterschool on Electronic Properties of Novel Materials, (2000) in press.

H.Ootoshi, K.Ishii, T.Watanuki, A.Fujiwara and H.Suematsu
Synthesis and Crystal Structure of Europium Fullerides
Mol. Cryst. Liq. Cryst., **340** (2000) 565.

2A

K.Sugawara, T.Sugawara and M.Shirai
Sulfur Behavior in Rapid Pyrolysis of Coals with Chemical Pretreatments
Jpn. J. Appl. Phys., **38** (1999) 608.

K.Sugawara, T.Takusari, T.Sugawara, M.Shirai and Y.Nishiyama
Effect of Aromaticity on Organic Sulfur Release in Rapid Pyrolysis of Coal
Int. J. Soc. Mat. Eng. Resources, **7** (1999) 312.

M.Shirai and K.Sugawara
Determination of Sulfur Species in Coal by X-Ray Absorption Near Edge Structure Spectroscopy
Int. J. Soc. Mat. Eng. Resources, **7** (1999) 320.

2B

H.I.Sekiguchi and T.Sekiguchi
Adsorption Structure of Formic Acid on Si(100) Studied by Surface NEXAFS
Surf. Sci., **433** (1999) 549.

J.Okamoto, T.Mizokawa, A.Fujimori, I.Hase, M.Nohara, H.Takagi, Y.Takeda and M.Takano
Correlation Effects in the Electronic Structure of $SrRuO_3$
Phys. Rev. B, **60** (1999) 2281.

K.Kobayashi, T.Mizokawa, A.Ino, J.Matsuno, A.Fujimori, H.Samata, A.Mishiro, Y.Nagata and F.M.F.de Groot
Doping Dependence of the Electronic Structure of $Ba_{1-x}K_xBiO_3$ Studied by X-Ray-Absorption Spectroscopy
Phys. Rev. B, **59** (1999) 15100.

T.Iwasaki, S.Suga, S.Imada, A.Sekiyama, K.Matsuda, M.Kotsugi, K.-S.An, T.Muro, S.Ueda, T.Matsushita, Y.Saitoh, T.Nakatani, H.Ishii, O.Sakai, R.Takayama, T.Suzuki, T.Oguchi, K.Katoh and A.Ochiai
Bulk and Surface Electronic Structures of CePdX (X=As,Sb) Studied by $3d$-$4f$ Resonace Photoemission
Phys. Rev. B, **61** (2000) 4621.

2C

N.A.Cherepkov, S.K.Semenov, Y. Hikosaka, K.Ito, S.Motoki, and A.Yagishita
Manifestation of Many-electron Correlations in Photionization of the K-shell of N_2
Phys. Rev. Lett., **84** (2000) 250.

3A

F.Saito, T.Toyoda, T.Mori, M.Tanaka, K.Hirano and S.Sasaki
Site- and Valence-Selective Study on the Origin of Fe Peaks in X-ray Magnetic Circular Dichroism of Ni Ferrites, $Fe[Ni_xFe_{2-x}]O_4$
Physhica B, **270** (1999) 35.

M.Takata, E.Nishiobori, K.Kato, M.Sakata and Y.Moritomo
Direct Observation of Orbital Order in Manganites by MEM Charge-Density Study
J. Phys. Soc. Jpn., **68** (1999) 2190.

E.Matsubara and K.Shinoda
Structural Study of Poly-Molybdate Ions in Acid Mo-Ni Aqueous Solutions
Jpn. J. Appl. Phys., **38** (1999) 576.

S.Sato, E.Matsubara, Y.Waseda. T.Zhang and A.Inoue
Fast X-Ray Measurement System for Structural Study in $Zr_{60}Al_{15}Ni_{25}$ Supercooled Liquid
Mat. Res. Soc. Symp. Proc., **554** (1999) 101.

K.Ohkubo, F.Saito and S.Sasaki
Linear Response Calculation of XMCD Spectra for Fe Ions in Ferrimagnetic Oxides
Proc. of 4th Symposium on ASID, (2000) 445.

3B

H.Harada, A.Sekiyama, S.Suga, S.Imada, T.Muro, R.-J.Jung, K.Matsuda, H.Takagi, A.Ochiai, T.Suzuki and H.Harima
Temperature Dependence of the Yb 4f Sperctra in Yb_4Bi_3 Probed by Photoemission Spectroscopy
J. Phys. Soc. Jpn., **68** (1999) 2844.

A.Sekiyama, S.Suga, Y.Saitoh, S.Ueda, H.Harada, T.Matsushita, T.Nakatani, T.Iwasaki, K.Matsuda, M.Kotsugi, S.Imada, T.Takabatake, T.Yoshino, D.T.Adroja, R.Takayama, O.Sakai, H.Harima and T.Nanba
High Resolution Ce 3d-4f Resonant Photoemission Study of CeNiSn and CePdSn
Solid State Commun., **111** (1999) 373.

A.Sekiyama, S.Suga, M.Fujikawa, S.Imada, T.Iwasaki, K.Matsuda, T.Matsushita, K.V.Kaznacheyev, A.Fujimori, H.Kuwahara and Y.Tokura
Electronic States of Charge-Ordering $Nd_{0.5}Sr_{0.5}MnO_3$ Probed by Photoemission
Phys. Rev. B, **59** (1999) 15528.

Y.Enta, D.Shoji, M.Shinohara, M.Suemitsu, M.Niwano, N.Miyamoto, Y.Azuma and H.Kato
Si 2p Spectra of Initial Thermal Oxdies on Si(100) Oxidized by H_2O
Jpn. J. Appl. Phys., **38** (1999) 253.

K.Soda, T.Takeuchi, Y.Yanagida, U.Mizutani, M.Kato, Y.Nishino, A.Sekiyama. S.Imada, S.Suga, T.Matsushita and Y.Saito
Photoemission Study of DO_3-Related $(Fe_{1-x}V_x)_3Al$ Alloys
Jpn. J. Appl. Phys., **38-1** (1999) 496.

M.-T.Huang, R.Wehlitz, Y.Azuma, L.Pibida, I.A.Sellin, J.W.Cooper, M.Koide, H.Ishijima and T.Nagata
Single and Double Photoionization of Lithium
Phys. Rev. A, **59** (1999) 3397.

R.Wehlitz, M.-T.Huang, I.A.Sellin and Y.Azuma
The Wannier Threshold Law Examined by Photoelectron Satellite Measurements
J. Phys. B, **32** (1999) L635.

Y.Takeda, M.Arita, H.Sato, K.Shimada, H.Namatame, M.Taniguchi, K.Katoh, F.Iga and T.Takabatake
Temperature-Dependent High-Resolution Photoemission Study of the Kondo Insulator $Ce_3Bi_4Pt_3$
J. Elec. Spec. Relat. Phenom., **101** (1999) 721.

M.Arita, Y.Takeda, Y.Okamura, H.Sato, K.Shimada, K.Mamiya, H.Namatame, M.Taniguchi, M.Tsubota, F.Iga and T.Takabatake
Temperature-Dependent High-Resolution Photoemission Study of $Y_{1-x}Ca_xTiO_3$
Jpn. J. Appl. Phys., **38** (1999) 206.

Y.Takeda, M.Arita, Y.Okamura, H.Sato, K.Shimada, K.Mamiya, H.Namatame, M.Taniguchi, K.Katoh, F.Iga and T.Takabatake
Low-Temperature High-Resolution Resonant Photoemission Study of Kondo Insulator $Ce_3Bi_4Pt_3$
Jpn. J. Appl. Phys., **38** (1999) 209.

T.Susaki, Y.Takeda, M.Arita, K.Mamiya, A.Fujimori, K.Shimada, H.Namatame, M.Taniguchi, N.Shimizu, F.Iga and T.Takabatake
Temperature-Dependent High-Resolution Photoemission Study of the Kondo Insulator YbB_{12}
Phys. Rev. Lett., **82** (1999) 992.

J.Matsuno, T.Mizokawa, A.Fujimori, K.Mamiya, S.Kawasaki and M.Takano
Photoemission and Hartree-Fock Studies of Oxygen-Hole Ordering in Change-Disproportionated $La_{1-x}Sr_xFeO_3$
Phys. Rev. B, **60** (1999) 4605.

M.Nakamura, T.Yoshida, K.Mamiya, A.Fujimori, Y.Taguchi and Y.Tokura
Resonant Photoemission Study of $LaTiO_{3.04}$
Mater. Sci. Eng., **68** (1999) 123.

T.Iwasaki, S.Suga, S.Imada, A.Sekiyama, K.Matsuda, M.Kotsugi, K.-S.An, T.Muro, S.Ueda, T.Matsushita, Y.Saitoh, T.Nakatani, H.Ishii, O.Sakai, R.Takayama, T.Suzuki, T.Oguchi, K.Katoh and A.Ochiai
Bulk and Surface Electronic Structures of CePdX (X=As,Sb) Studied by $3d$-$4f$ Resonace Photoemission
Phys. Rev. B, **61** (2000) 4621.

A.Sekiyama, T.Iwasaki, K.Matsuda, Y.Saitoh, Y.Onuki and S.Suga
Probing Bulk States of Correlated Electron Systems by High-Resolution Resonance Photoemission
Nature, **403** (2000) 396.

T.Takiya, H.Sugiyama, X.Zhang, S.Shimada, K.Yamazato, A.Komura and M.Ando
New Mounting Method of Diamond Monochromator for High Brilliance Synchrotron Radiation
Rev. Sci. Instrum., **70** (1999) 3523.

4A

Y.Takahashi, A.Iida, K.Ishikawa, H.Takezoe and A.Fukuda
Structure of Needlelike Defect in Homogenously Aligned Cells of a Ferroelectric Liquid Crystal Mixture, Studied Using X-Ray Microbeam
Jpn. J. Appl. Phys., **38** (1999) 4132.

Y.Takanishi, T.Izumi, J.Watanabe, K.Ishikawa, H.Takezoe and A.Iida
Field-Induced Molecular Reorientation Keeping a Frustrated Strucuture in an Achiral Bent-Shaped Liquid Crystal
J. Mater. Chem., **9** (1999) 2771.

W.Nozaki, T.Nakamura, A.Iida, K.Matsuoka and N.Takaoka
Trace Element Concentrations in Iron type Cosmic Spherules Determined by the SR-XRF Method
Antarctic Meteorite Research, **12** (1999) 199.

S.Hayakawa, J.Noda and Y.Gohshi
Conversion Electron Yield XAFS Measurements under Atmospheric Conditions
Spectrochim. Acta B, **54B** (1999) 235.

S.Hayakawa, T.Hirose, L.Yan, M.Morishita, H.Kuwano and Y.Gohshi
Synchrotron Radiation X-Ray Excited Optical Luminescence for Chemical State Selective Analysis
X-ray Spectrometry, **28** (1999) 515.

Y.Hasegawa, Y.Ueji, K.Okitsu, Y.Amemiya, J.M.Ablett and D.P.Siddons
Tunable X-Ray Polarization Reflector with Perfect Crystals
Acta Cryst. A, **55** (1999) 955.

S.Hayakawa, X.-P.Jia, M.Wakatsuki, Y.Gohshi and T.Hirokawa
Analysis of Trace Co in Synthetic Diamonds using Synchrotron Radiation Excited X-Ray Fluorescence Analysis
J. Cryst. Growth, **210** (2000) 388.

S.Hayakawa, K.Kobayashi and Y.Gohshi
A Compact X-Ray Beam Intensity Monitor using Gas Amplified Sample Current Measurement
Rev. Sci. Instrum., **71** (2000) 20.

4B1

M.Ohkawa, S.Takeno, A.Yoshiasa and K.Ohsumi
The Structural Study on Fe-Pumpellyite: An Application of Weissenberg Technique Combined with a Synchrotron Radiation and an Imaging Plate
Mineral. J., **21** (1999) 151.

4B2

Y.Xiao, S.Hayakawa, Y.Gohshi, M.Oshima, F.Izumi, H.Okudera, H.Toraya and K.Ohsumi
A Rietveld-Analysis Program for X-Ray Powder Spectro-Diffractometry
Powder Diffraction, **14** (1999) 106.

Y.Xiao, S.Hayakawa, Y.Gohshi, M.Oshima, H.Okudera, H.Toraya and K.Ohsumi
Site-Selective Chemical State Analysis for Magnetite Structure using Powder Spectro-Diffractometry
Jpn. J. Appl. Phys., **38-1** (1999) 381.

4C

K.Nakamura, T.Arima, A.Nakazawa, Y.Wakabayashi and Y.Murakami
Polarization-Dependent Resonant-X-Ray Diffraction in Charge- and Orbital-Ordering Phase of $Nd_{1/2}Sr_{1/2}MnO_3$
Phys. Rev., **60** (1999) 2425.

Y.Endoh, K.Hirota, S.Ishihara, S.Okamoto, Y.Murakami, A.Nishizawa, T.Fukuda, H.Kimura, H.Nojiri, K.Kaneko and S.Maekawa
Transition between Two Ferromagnetic States Driven by Orbital Ordering in $La_{0.88}Sr_{0.12}MnO_3$
Phys. Rev. Lett., **82** (1999) 4328.

Y.Murakami, J.P.Hill, D.Gibbs, M.Blume, H.Kawada, I.Koyama, M.Tanaka, H.Kawata, T.Arima, Y.Moritomo, Y.Tokura, K.Hirota and Y.Endoh
Direct Observation of Charge and Orbital Ordering by Resonant X-Ray Scattering
Jpn. J. Appl. Phys., **38** (1999) 360.

Y.Endoh, H.Nojiri, K.Kaneko, K.Hirota, T.Fukuda H. H.Kimura, Y.Murakami, S.Ishihara, S.Maekawa, S.Okamoto and M.Motokawa
Field Induced Transition from Metal to Insulator in the Colossal Magneto-Resistance Manganites
Mater. Sci. Eng., **63** (1999) 151.

T.Inami, N.Ikeda, Y.Murakami, I.Koyama, Y.Wakabayashi and Y.Yamada
Charge Ordering in $La_{1-x}Sr_xMno_3$ ($x \sim 0.12$)
Jpn. J. Appl. Phys., **38** (1999) 212.

H.Nakao, K.Ohwada, N.Takesue, Y.Fujii, M.Isobe and Y.Ueda
Critical Behavior of Crystal Lattice of NaV_2O_5
J. Phys. Chem. Solids, **60** (1999) 1101.

T.Watanuki, A.Fujiwara, K.Ishii, Y.Matsuoka, H.Suematsu, K.Ohwada, H.Nakao, Y.Fujii, K.Kikuchi and Y.Achiba
Structural Phase Transitions of Metallofullerene La@C_{82} Studied by Single Crystal X-Ray Diffraction
Proc. of XIIIth Int. Winterschool on Electronic Properties of Novel Materials, (1999) 124.

T.Shimura, T.Hosoi, R.Ejiri and M.Umeno
Ordered Structure in Buried Oxide Layers of SOI Wafers
Jpn. J. Appl. Phys., **38** (1999) 297.

K.Hirota, N.Oumi, T.Matsumura, H.Nakao, Y.Wakabayashi, Y.Murakami and Y.Endoh
Direct Observation of Antiferroquadrupolar Ordering: Resonant X-Ray Scattering Study of DyB_2C_2
Phys. Rev. Lett., **84** (2000) 2706.

M.Noguchi, A.Nakazawa, S.Oka, T.Arima, Y.Wakabayashi, H.Nakao, and Y.Murakami
Synchrotron X-Ray-Diffraction Study of Orbital Ordering in YVO_3
Phys. Rev. B, **62** (2000) R9271.

T.Shimura, T.Hosoi and M.Umeno
Analysis of Ordered Structure of Buried Oxide Layers in SIMOX Wafers
SILICON-ON-INSULATOR TECHNOLOGY AND DEVICES IX, **99-3** (2000) 155.

T.Shimura, T.Hosoi and M.Umeno
Characterization of SOI Wafers by X-Ray CTR Scattering
J. Cryst. Growth, **210** (2000) 98.

T.Shimura, T.Hosoi and M.Umeno
Ordered SiO_2 in the Buried Oxide of SIMOX SOI Wafers
Proc. of the 4th Symp. on Atomic-scale Surface and Interface Dynamics, **4** (2000) 395.

T.Shimura, T.Hosoi and M.Umeno
The Crystalline SiO_2 Phase in the BOX Layers of SIMOX Wafers
The 3rd SANKEN Int. Symp. on Advanced Nanoelectronics: Devices, Materials, and Computing, **57** (2000) 128.

6A

T.Inoue, H.Sugawara, S.Hamanaka, H.Tsukui, E.Suzuki, T.Kohzuma and Y.Kai
Crystal Structure Determinations of Oxidized and Reduced Plastocyanin from the Cyanobacterium *Synechococcus* sp.
Biochem., **38** (1999) 6063.

N.Shibata, T.Inoue, C.Nagano, N.Nishio, T.Kohzuma, K.Onodera, F.Yoshizaki, Y.Sugimura and Y.Kai
Novel Insight into the Copper-Ligand Geometry in the Crystal Structure of *Ulva pertusa* Plastocyanin at 1.6-ÅResolution
J. Biol. Chem., **274** (1999) 4225.

T.Inoue, H.Sugawara, S.Hamanaka, H.Tsukui, E.Suzuki, T.Kohzuma and Y.Kai
Crystallization and Preliminary X-Ray Analysis of Plastocyanin from Cyanobacterium *Synechococcus* sp. PCC 7942
Acta Cryst. D, **D55** (1999) 683.

T.Kohzuma, T.Inoue, F.Yoshizaki, Y.Sasakawa, K.Onodera, S.Nagatomo, T.Kitagawa, S.Uzawa, T.Isobe, Y.Sugimura, M.Gotowda and Y.Kai
The Structure and Unusual pH Dependence of Plastocyanin from the Fern *Dryoperis crassirhizoma*
J. Biol. Chem., **274** (1999) 11817.

T.Inoue, N.Nishino, S.Suzuki, K.Kataoka, T.Kohzuma and Y.Kai
Crystal Structure Determinations of Oxidized and Reduced Pseudoazurins from *Achromobacter cycloclastes*
J. Biol. Chem., **274** (1999) 17845.

H.Hashimoto, T.Matsumoto, M.Nishioka, T.Yuasa, S.Takeuchi, T.Inoue, S.Fujiwara, M.Takagi, T.Imanaka and Y.Kai
Crystallographic Studies on a Family B DNA Polymerase from Hyperthermophilic Archaeon *Pyrococcus kodakaraensis* Strain KOD1
J. Biochem., **125** (1999) 983.

H.Sugawara, H.Yamamoto, N.Shibata, T.Inoue, S.Okada, C.Miyake, A.Yokota and Y.Kai
Crystal Structure of Carboxylase Reaction-Oriented Ribulose 1,5-Bisphosphate Carboxylase/Oxygenase from a Thermophilic Red Alga, *Galdieria partita*
J. Biol. Chem., **274** (1999) 15655.

Y.Kai, H.Matsumura, T.Inoue, K.Terada, Y.Nagara, T.Yoshinaga, A.Kihara, K.Tsumura and K.Izui
Three-Dimensional Structure of Phospho*enol*pyruvate Carboxylase: A Proposed Mechanism for Allosteric Inhibition
Proc. Natl. Acad. Sci. USA, **96** (1999) 823.

T.Oyama, M.Kusunoki, Y.Kishimoto, Y.Takasaki and Y.Nitta
Crystal Structure of β-Amylase from *Bacillus cereus* var. *mycoides* at 2.2 ÅResolution
J. Biolchem., **125** (1999) 1120.

H.Ago, T.Adachi, A.Yoshida, M.Yamamoto, N.Habuka, K.Yatsunami and M.Miyano
Crystal Structure of the RNA-Dependent RNA Polymerase of Hepatitis C Virus
Structure, **7** (1999) 1417.

K.Takano, M.Ota, K.Ogasahara, Y.Yamagata, K.Nishikawa and K.Yutani
Experimental Verification of the 'Stability Profile of Mutant Protein' (SPMP) Data using Mutant Human Lysozymes
Protein Engineering, **12** (1999) 663.

K.Takano, Y.Yamagata, M.Kubota, J.Funahashi, S.Fujii and K.Yutani
Contribution of Hydrogen Bonds to the Conformational Stability of Human Lysozyme: Calorimetry and X-ray Analysis of Six Ser $\rightarrow AlaMutants$
Biochem., **38** (1999) 6623.

N.Nakagawa, M.Sugahara, R.Masui, R.Kato, K.Fukuyama and S.Kuramitsu
Crystal Strucuture of *Thermus thermophilus*HB8 UvrB Protein, a Key Enzyme of Nucleotide Excision Repair
J. Biochem.(Tokyo), **126** (1999) 986.

T.Nakai, K.Okada, S.Akutsu, I.Miyahara, S.Kawaguchi, R.Kato, S.Kuramitsu and K.Hirotsu
Structure of *Thermus thermophilus* HB8 Aspartate Aminotransferase and Its Complex with Maleate
Biochem., **38** (1999) 2413.

T.Nogi, T.A.Fukami, M.Ishida, M.Yoshida and K.Miki
Purification, Crystallization, and Preliminary X-Ray Crystallographic Analysis of *Thermus thermophilus* V_1-ATPase B Subunit
J. Struct. Biol., **127** (1999) 79.

K.Kitano, Y.Niimura, Y.Nishiyama and K.Miki
Stimulation of Peroxidase Activity by Decamerization Related to Ionic Strength: AhpC Protein from *Amphibacillus xylanus*
J. Biochem., **126** (1999) 313.

H.Komori, F.Matsunaga, Y.Higuchi, M.Ishiai, C.Wada and K.Miki
Crystal Structure of a Prokaryotic Replication Initiator Protein Bound to DNA at 2.6 ÅResolution
EMBO J., **18** (1999) 4597.

M.Fujihashi, N.Shimizu, Y.-W.Zhang, T.Koyama and K.Miki
Crystallization and Preliminary X-Ray Diffraction Studies of Undecaprenyl Diphosphate Synthase from *Micrococcus luteus* B-P 26
Acta Crystallogr., **D55** (1999) 1606.

N.Maeda, K.Kitano, T.Fukui, S.Ezaki, H.Atomi, K.Miki and T.Imanaka
Ribulose Bisphosphate Carboxylase/Oxygenase from the Hyperthermophilic Archaeon *Pyrococcus kodakaraensis* KOD1 is Composed Solely of Large Subunits and Forms a Pentagonal Structure
J. Mol. Biol., **293** (1999) 57.

J.Saito, A.Kita, Y.Higuchi, Y.Nagata, A.Ando and K.Miki
Crystal Structure of Chitosanase from *Bacillus circulans* MH-K1 at 1.6-ÅResolution and its Substrate Recognition Mechanism
J. Biol. Chem., **274** (1999) 30818.

T.Kobori, W.C.Lee, T.Akagi, H.Sasaki, S.Zenno, K.Saigo and M.Tanokura
Crystallization and Preliminary Crystallographic Analysis of Major Nitroreductase from *Escherichia coli*
Act. Cryst., **D55** (1999) 1901.

List of Publications

H.Hashimoto, T.Inoue, M.Nishioka, S.Fujiwara, M.Takagi, T.Imanaka and Y.Kai
Hyperthermostable Protein Structure Maintained by Intra- and Inter-Helix Ion-Pairs in Archaeal O^6 Methylguanine-DNA Methyltransferase
J. Mol. Biol., **192** (1999) 245.

H.Matsumura, M.Terada, S.Shirakata, T.Inoue, T.Yoshinaga, K.Izui and Y.Kai
Plausible Phospho*enol*pyruvate Binding Site Revealed by 2.6ÅStructure of Mn^{2+}-bound Phospho*enol*pyruvate Carboxylase from *Escherichia coli*
FEBS Letters, **458** (1999) 93.

T.Inoue, M.Gotowda, H.Sugawara, T.Kohzuma, F.Yoshizaki, Y.Sugimura and Y.Kai
Structure Comparison between Oxidized and Reduced Plastocyanin from a Fern, *Dryopteris crassirhizoma*
Biochem., **38** (1999) 13853.

T.Shirai, M.Fujikake, T.Yamane, K.Inaba, K.Ishimori and I.Morishima
Crystal Structure of a Protein with an Artificial Exon-shuffling, module M4-substituted Chimera Hemoglobin $\beta\alpha$, at 2.5 ÅResolution
J. Mol. Biol., **287** (1999) 369.

M.G.Lee, J.Y.Lee, H.K.Song and S.W.Suh
Crystallization and Preliminary X-Ray Analysis of*Saccharomyces Cerevisiae* Ypd1p, a Key Intermediate in Phosphorelay Signal Transduction
Acta Cryst., **D 55** (1999) 1219.

C.Chang, B.Chul Park, D.-S. Lee and S.W.Suh
Crystal Structures of Thermostable Xylose Isomerases from *Thermus caldophilus* and *Thermus thermophilus:* Possible Structural Determinants of Thermostability
J. Mol. Biol., **288** (1999) 623.

H.K.Song, Y.S.Kim, J.K.Yang, J.Moon, J.Y.Lee and S.W.Suh
Crystal Structure of a 16 kDa Double-Headed Bowman-Birk Trypsin Inhibitor from Barley Seeds at 1.9 ÅResolution
J. Mol. Biol., **293** (1999) 1133.

H.K.Song, J.Y.Lee, M.G.Lee, J.Moon, K.Min, J.K.Yang and S.W.Suh
Insights into Eukaryotic Multistep Phosphorelay Signal Transduction Revealed by the Crystal Structure of Ypd1p from *Saccharomyces cerevisiae*
J. Mol. Biol., **293** (1999) 753.

C.Chang, H.K.Song, B.C.Park, D.-S.Lee and S.W.Suh
A Thermostable Xylose Isomerase from *Thermus caldphilus:* Biochemical Characterization, Crystallization, and Preliminary X-Ray Analysis
Acta Cryst., **D 55** (1999) 294.

Y.S.Kim, H.K.Song and S.W.Suh
Crystallization and Preliminary X-Ray Analysis of a Complex between the Bowman-Birk Trypsin Inhibitor from Barley and Porcine Pancreatic Trypsin
Acta Cryst., **D 55** (1999) 1244.

H.-M.Li, T.Zhao, L.Jin, M.Wang, Y.Zhang and D.-C.Wang
A Series of Bioactivity-Variant Neurotoxins from Scorpion *Buthus martensii* Karsch: Purification, Crystallization and Crystallographic Analysis
Acta Cryst., **D55** (1999) 341.

X.-L.He, H.-M.Li, Z.-H.Zeng, X.-Q.Liu, M.Wang and D.-C.Wang
Crystal Structures of Two α-like Scorpion Toxins: Non-Proline *cis* Peptide Bonds and Implications for New Binding Site Selectivity on the Sodium Channel
J. Mol. Biol., **292** (1999) 125.

S.Kim, D.W.Shin, D.Kim and S.H.Eom
Crystallization and Preliminary X-Ray Crystallographic Studies of the D2 Region of the Skeletal Muscle Ryanodine Receptor
Acta Cryst. D, **D55** (1999) 1601.

S.Misaki, Y.Morimoto, M.Ogata, T.Yagi, Y.Higuchi and N.Yasuoka
Structure Determination of Rubredoxin from *Desulfovibrio vulgaris* Miyazaki F in Two Crystal Forms
Acta Cryst., **D55** (1999) 408.

K.Suto, K.Kawagoe, N.Shibata, Y.Morimoto, Y.Higuchi, M.Kitamura, T.Nakaya and N.Yasuoka
Crystallization and Preliminary Crystallographic Studies of FMN-Binding Protein from *Desulfovibrio vulgaris* Miyazaki F
Acta Cryst., **D55** (1999) 1089.

Y.Higuchi
Small Molecular Ligands (SO, CO, CN, SH) to the Metals Found in B
Chemistry, **54** (1999) 36. (*in Japanese*).

S.Fushinobu and H.Matsuzawa
X-Ray Crystallography of a Xylanase from *Aspergillus Kawachii* and the Mechanism of its Extremely Low pH Optimum and Acid Stability
J. Brewing Soc. Jpn, **94** (1999) 640. (*in Japanese*).

A.Ibuka, A.Taguchi, M.Ishiguro, S.Fushinobu, Y.Ishii, S.Kamitori, K.Okuyama, K.Yamaguchi, M.Konn and H.Matsuzawa
Crystal Structure of the E166A Mutant of Extendedspectrum β-Lactamase Toho-1 at 1.8ÅResolution
J. Mol. Biol., **285** (1999) 2079.

K.T.Chong, G.Miyazaki, H.Morimoto, Y.Oda and S.-Y.Park
Structures of the Deoxy and CO Forms of Hemoglobin from *Dasyatis akajei*, a Cartilaginous Fish
Acta Cryst., **D55** (1999) 1291.

G.Miyazaki, H.Morimoto, K.-M.Yun, S.-Y.Park, A.Nakagawa, H.Minagawa and N.Shibayama
Magnesium(II) and Zinc(II)-Protoporphyrin IX's Stabilize the Lowest Oxygen Affinity State of Human Hemoglobin even more Strongly than Deoxyheme
J. Mol. Biol., **292** (1999) 1121.

T.Matsumoto, Y.Morimoto, N.Shibata, T.Kinebuchi, N.Shimamoto, T.Tsukihara and N.Yasuoka
Roles of Functional Loops and the C-Terminal Segment of a Single-Stranded DNA Binding Protein Elucidated by X-Ray Structure Analysis
J. Biochem., **127** (2000) 329.

K.Fukuda, H.Mizuno, H.Atoda and T.Morita
Crystal Structure of Flavocetin-A, a Platelet Glycoprotein Ib-Binding Protein, Reveals a Novel Cyclic Tetramer of C-type Lectin-like Heterodimers
Biochem., **39** (2000) 1915.

K.Suto, K.Kawagoe, N.Shibata, Y.Morimoto, Y.Higuchi, M.Kitamura, T.Nakaya and N.Yasuoka
How do the X-Ray Structure and the NMR Structure of FMN-Binding Protein Differ?
Acta. Cryst., **D56** (2000) 368.

Y.-Q.Shen, J.Li, S.-Y.Song and Z.-J.Lin
Structure of Apo-glyceraldehyde-3-phosphate Dehydrogenase from *Palinurus versicolor*
J. Structural Biol., **130** (2000) 1.

I.Sugiura, O.Nureki, Y.U.Yoshikawa, S.Kuwabara, A.Shimada, M.Tateno, B.Lorber, R.Giege, D.Moras, S.Yokoyama and M.Konno
The 2.0 ÅCrystal Structure of *Thermus thermophilus* Methionyl-tRNA Synthetase Reveals Two RNA-Binding Modules
Structure, **8** (2000) 197.

6B

T.Inoue, H.Sugawara, S.Hamanaka, H.Tsukui, E.Suzuki, T.Kohzuma and Y.Kai
Crystal Structure Determinations of Oxidized and Reduced Plastocyanin from the Cyanobacterium *Synechococcus* sp.
Biochem., **38** (1999) 6063.

N.Shibata, T.Inoue, C.Nagano, N.Nishio, T.Kohzuma, K.Onodera, F.Yoshizaki, Y.Sugimura and Y.Kai
Novel Insight into the Copper-Ligand Geometry in the Crystal Structure of *Ulva pertusa* Plastocyanin at 1.6-ÅResolution
J. Biol. Chem., **274** (1999) 4225.

T.Inoue, H.Sugawara, S.Hamanaka, H.Tsukui, E.Suzuki, T.Kohzuma and Y.Kai
Crystallization and Preliminary X-Ray Analysis of Plastocyanin from Cyanobacterium *Synechococcus* sp. PCC 7942
Acta Cryst. D, **D55** (1999) 683.

T.Kohzuma, T.Inoue, F.Yoshizaki, Y.Sasakawa, K.Onodera, S.Nagatomo, T.Kitagawa, S.Uzawa, T.Isobe, Y.Sugimura, M.Gotowda and Y.Kai
The Structure and Unusual pH Dependence of Plastocyanin from the Fern *Dryoperis crassirhizoma*
J. Biol. Chem., **274** (1999) 11817.

T.Inoue, N.Nishino, S.Suzuki, K.Kataoka, T.Kohzuma and Y.Kai
Crystal Structure Determinations of Oxidized and Reduced Pseudoazurins from *Achromobacter cycloclastes*
J. Biol. Chem., **274** (1999) 17845.

H.Hashimoto, T.Matsumoto, M.Nishioka, T.Yuasa, S.Takeuchi, T.Inoue, S.Fujiwara, M.Takagi, T.Imanaka and Y.Kai
Crystallographic Studies on a Family B DNA Polymerase from Hyperthermophilic Archaeon *Pyrococcus kodakaraensis* Strain KOD1
J. Biochem., **125** (1999) 983.

H.Sugawara, H.Yamamoto, N.Shibata, T.Inoue, S.Okada, C.Miyake, A.Yokota and Y.Kai
Crystal Structure of Carboxylase Reaction-Oriented Ribulose 1,5-Bisphosphate Carboxylase/Oxygenase from a Thermophilic Red Alga, *Galdieria partita*
J. Biol. Chem., **274** (1999) 15655.

Y.Kai, H.Matsumura, T.Inoue, K.Terada, Y.Nagara, T.Yoshinaga, A.Kihara, K.Tsumura and K.Izui
Three-Dimensional Structure of Phospho*enol*pyruvate Carboxylase: A Proposed Mechanism for Allosteric Inhibition
Proc. Natl. Acad. Sci. USA, **96** (1999) 823.

H.Ago, T.Adachi, A.Yoshida, M.Yamamoto, N.Habuka, K.Yatsunami and M.Miyano
Crystal Structure of the RNA-Dependent RNA Polymerase of Hepatitis C Virus
Structure, **7** (1999) 1417.

H.Tsuge, T.Nishimura, Y.Tada, T.Asano, D.Turk, V.Turk and N.Katunuma
Inhibition Mechanism of Cathepsin L-Specific Inhibitors Based on the Crystal Structure of Papain-CLIK148 Complex
Biochem. Biophys. Res. Commun., **266** (1999) 411.

H.Tsuge, M.Nagahama, T.Nishimura, Y.Sakaguchi, N.Katunuma and J.Sakurai
Crystallization and Preliminary X-Ray Studies of the Component of *Clostridium perfringens* Iota Toxin Complexed with NADPH
J. Structural Biol., **126** (1999) 175.

K.Takano, Y.Yamagata, M.Kubota, J.Funahashi, S.Fujii and K.Yutani
Contribution of Hydrogen Bonds to the Conformational Stability of Human Lysozyme: Calorimetry and X-ray Analysis of Six Ser → *AlaMutants*
Biochem., **38** (1999) 6623.

K.Takano, Y.Yamagata, J.Funahashi, Y.Hioki, S.Kuramitsu and K.Yutani
Contribution of Intra- and Intermolecular Hydrogen Bonds to the Conformational Stability of Human Lysozyme
Biochem., **38** (1999) 12698.

S.-H.Liaw, K.Y.Lee, S.-Y.Yang and S.-N.Su
Crystallization and Preliminary Diffraction Data of 60-kDa Glycosylated Pollen Isoallergens from Bermuda Grass
J. Structural Biol., **127** (1999) 83.

M.Fujihashi, N.Shimizu, Y.-W.Zhang, T.Koyama and K.Miki
Crystallization and Preliminary X-Ray Diffraction Studies of Undecaprenyl Diphosphate Synthase from *Micrococcus luteus* B-P 26
Acta Crystallogr., **D55** (1999) 1606.

N.Maeda, K.Kitano, T.Fukui, S.Ezaki, H.Atomi, K.Miki and T.Imanaka
Ribulose Bisphosphate Carboxylase/Oxygenase from the Hyperthermophilic Archaeon *Pyrococcus kodakaraensis* KOD1 is Composed Solely of Large Subunits and Forms a Pentagonal Structure
J. Mol. Biol., **293** (1999) 57.

J.Saito, A.Kita, Y.Higuchi, Y.Nagata, A.Ando and K.Miki
Crystal Structure of Chitosanase from *Bacillus circulans* MH-K1 at 1.6-ÅResolution and its Substrate Recognition Mechanism
J. Biol. Chem., **274** (1999) 30818.

H.K.Song, J.Y.Lee, M.G.Lee, J.Moon, K.Min, J.K.Yang and S.W.Suh
Insights into Eukaryotic Multistep Phosphorelay Signal Transduction Revealed by the Crystal Structure of Ypd1p from *Saccharomyces cerevisiae*
J. Mol. Biol., **293** (1999) 753.

S.H.Sohn, H.K.Song, K.Min, S.-J.Cho, J.Moon, J.Y.Lee, H.J.Ahn, C.Chang, H.-J.Kim and S.W.Suh
Crystallization and Preliminary X-Ray Crystallographic Analysis of Deoxycytidylate Hydroxymethylase from Bacteriophage T4
Acta Cryst., **D 55** (1999) 1061.

Y.Matsuura, M.Stewart, M.Kawamoto, N.Kamiya, K.Saeki, T.Yasunaga and T.Wakabayashi
Structural Basis for the Higher Ca^{2+}-Activation of the Regulated Actin-Activated Myosin ATPase Observed with *Dictyostelium/Tetrahymena* Actin Chimeras
J. Mole. Biol., **296** (2000) 579.

6C

A.Fujiwara, K.Ishii, T.Watanuki, H.Suematsu, H.Nakao, K.Ohwada, Y.Fujii, Y.Murakami, T.Mori, H.Kawada, T.Kikegawa, O.Shimomura, T.Matsubara, H.Hanabusa, S.Daicho, S.Kitamura and C. Katayama
Synchrotron Radiation X-Ray Powder Diffractometer Using a Cylindrical Imaging Plate
J. Appl. Crystallogr., **33** (2000) 1241.

7A

T.Tsuduki, A.Imanishi, K.Isawa, S.Terada, F.Matsui, M.Kiguchi, T.Yokoyama and T.Ohta
Adsorption Structures of Alkanethiols Self-Assembled Monolayers on the Cu(100) Surface Studied by S-*K* EXAFS and C-*K* NEXAFS Spectroscopies
J. Synchrotron Rad., **6** (1999) 787.

Y.Baba and T.Sekiguchi
Desorption of Fragment Ions from Condensed $Si(OCH_3)_4$ by Localized Inner-Shell Electron Excitation at the Silicon, Oxygen, and Carbon *K* Edges
J. Vac. Sci. Technol. A, **18** (2000) 334.

7B

K.Sakamoto, S.Doi, Y.Ushimi, K.Ohno, H.W.Yeom, T.Ohta, S.Suto and W.Uchida
Adsorption Process of Metastable Molecular Oxygen on a Si(111)-(7×7) Surface
Phys. Rev. B, **60** (1999) R8465.

7C

A.Kuno, M.Matsuo and C.Numako
In situ Chemical Speciation of Iron in Estuarine Sediments using XANES Spectroscopy with Partial Least-Squares Regression
J. Synchrotron Rad., **6** (1999) 667.

M.Shirai, K.Murakami and M.Arai
XAFS Study on the Thermal Behavior of Nickel Species Dispersed in Brown Coals
Jpn. J. Appl. Phys., **38** (1999) 77.

M.Shirai, K.Torii and M.Arai
XAFS Study on Metal Particle Formation in Noble Metal Cation Loaded Synthesized Smectite Containing Several Devalent Cations during Hydrogen Reduction
Jpn. J. Appl. Phys., **38** (1999) 69.

E.Yanase, I.Watanabe, M.Harada, M.Takahashi and Y.Dake
Conversion Electron/He Ion Yield XAFS of $SrTiO_3$ Thin Films
Jpn. J. Appl. Phys, **38** (1999) 198.

Y.Shimizugawa, N.Umesaki, J.R.Qiu and K.Hirao
Local Structure around Europium Ions Doped in Borate Glasses
J. Synchrotron Rad., **6** (1999) 624.

T.Yokoyama, M.Kiguchi, T.Ohta, O.Sato, Y.Einaga and K.Hashimoto
Local Structure of a Trapped Photoexcited State of a Fe-Co Cyanide Studied by X-Ray-Absorption Fine-Structure Spectroscopy
Phys. Rev. B, **60** (1999) 9340.

Y.Okamoto and T.Kubota
Structure of Active Site and Molecular Design of Desulfurization Catalysts
Hyomen, **37** (1999) 95. (*in Japanese*).

M.Arai, Y.Minato, K.Torii and M.Shirai
Cobalt-Containing Smectite-like Mesoporous Materials as a New Type of Catalyst for Hydrodesulfurization of Thiophene
Catal. Lett., **61** (1999) 83.

Y.Okamoto, H.Okamoto, T.Kubota, H.Kobayashi and O.Terasaki
Preparation and Structure Analysis of Co-Mo Binary Sulfide Clusters Encapsulated in an NaY Zeolite
Phys. Chem. B, **103** (1999) 7160.

I.Nakai, H.Maeda and S.Ishio
The Local Structure of Amorphous $Gd_{80}Si_{12}B_8$
Jpn. J. Appl. Phys., **38** (1999) 512.

T.Yamamoto, T.Tanaka, S.Takenaka, S.Yoshida, T.Onari, Y.Takahashi, T.Kosaka and S.Hasegawa
XAFS Study of Fe- and Mn- Promoted Sulfated Zirconia
J. Synchrotron Rad., **6** (1999) 425.

T.Tanaka, T.Yamamoto, Y.Kohno, T.Yoshida and S.Yoshida
Application of XANES Spectra to Supported Catalysts
Jpn. J. Appl. Phys., **38** (1999) 30.

T.Yamamoto, T.Tanaka, S.Takenaka, S.Yoshida, T.Onari, Y.Takahashi, T.Kosaka, S.Hasegawa and M.Kudo
Structural Analysis of Iron and Manganese Species in Iron- and Manganese-Promoted Sulfated Zirconia
J. Phys. Chem. B, **103** (1999) 2385.

K.Fukumi, A.Chayahara, H.Kageyama, K.Kadono, T.Akai, N.Kitamura, H.Mizoguchi, Y.Horino, M.Makihara, K.Fujii and J.Hayakawa
Formation Process of CuCl Nano-Particles in Silica Glass by Ion Implantation
J. Non-Cryst. Solids, **259** (1999) 93.

Y.Yuan, K.Asakura, H.Wan, K.Tsai and Y.Iwasawa
Characterization of CO-and H_2-Adsorbed Au_6Pt-Phosphine Clusters Supported on SiO_2 by EXAFS, TPD, and FTIR
Bull. Chem. Soc. Jpn., **72** (1999) 2643.

M.Saito, S.Kang and Y.Waseda
Partial Structural Functions of Molten RbBr Estimated from the Anomalous X-ray Scattering Data
Jpn. J. Appl. Phys., **38** (1999) 596.

K.Yano, T.Masaki, Y.Fujiwara, X.Y.Yu, S.Iwata and S.Tsunashima
Structural Anisotropy in Sputter- and Vacuum-Deposited Dy/Fe Multilayers
J. Magnetic Soc. Jpn., **23** (1999) 91.

Y.Arita, S.Yamasaki, T.Matsui, T.Harami and K.Kobayashi
EXAFS study of $SrCeO_3$ doped with Yb
Solid State Ionics, **121** (1999) 225.

A.P.Kozlova, A.I.Kozlov, S.Sugiyama, Y Matsui, K.Asakura and Y.Iwasawa
Study of Gold Species in Iron-Oxide-Supported Gold Catalysts Derived from Gold-Phosphine Complex $Au(PPh_3)(NO_3)$ and As-Precipitated Wet $Fe(OH)_3$
J. Catal., **181** (1999) 37.

S.Sato, R.Kakiuchi, M.Yoshiya, E.Matsubara, M.Saito, Y.Waseda and S.Takayama
Structural Study of Thin Amorphous SiO_2 and Si_3N_4 Films by the Grazing Incidence X-Ray Scattering(GIXS) Method
High Temp. Mater. Proc., **18** (1999) 99.

T.Inoue, S.T.Oyama, H.Imoto, K.Asakura and Y.Iwasawa
Characterization and Selective Oxidation Catalysis of Modified Pt Particles on SbOx
Appl. Catal. A. General, **191** (2000) 131.

M.Shirai, K.Aoki, Y.Minato, K.Torii and M.Arai
Porous Smectite-type Materials Containing Catalytically Active Divalent Cations in Octahedral Sheets
Studies in Sur. Sci. Catal., **129** (2000) 435.

S.Kim, T.Ohta and G.Kwag
In situ Structural Investigation of Iron Phthalocyanine Monolayer Adsorbed on Electrode Surface by X-ray Absorption Fine Structure
Bull. Korean Chem. Soc., **21** (2000) 588.

T.Hayaishi, Y.Fujita, M.Izumisawa, T.Tanaka, E.Murakami, E.Shigemasa, A.Yagishita and Y.Morioka
Multi-Step Post-Collision Interaction Effects in K-Shell Photoionization of Kr
J. Phys. B: At. Mol. Opt. Phys., **33** (2000) 37.

Y.Izumi, T.Shimizu, T.Kobayashi and K.Aika
Nitrous Oxide Decomposition Active Site on Ni-MgO Catalysts Characterized by X-Ray Absorption Fine Structure Spectroscopy
Chem. Commun., (2000) 1053.

8B

A.Yoshiasa, T.Tamura, O.Kamishima, K.Murai, K.Ogata and H.Mori
Local Structure and Mean-Square Relative Displacement in SiO_2 and GeO_2 polymorphs
J. Synchrotron Rad., **6** (1999) 1051.

10A

Y.Konoike, T.Toyoda, K.Yamawaki and S.Sasaki
Observation of Charge Ordering in Mixed-Valence Compounds by X-Ray Anomalous Scattering Measurement
Proc. of 4th Symposium on ASID, (2000) 437.

10B

M.Shirai, K.Murakami and M.Arai
XAFS Study on the Thermal Behavior of Nickel Species Dispersed in Brown Coals
Jpn. J. Appl. Phys., **38** (1999) 77.

M.Shirai, K.Torii and M.Arai
XAFS Study on Metal Particle Formation in Noble Metal Cation Loaded Synthesized Smectite Containing Several Devalent Cations during Hydrogen Reduction
Jpn. J. Appl. Phys., **38** (1999) 69.

I.Nakai and T.Tokuyoshi
XANES Study on Phase Transformation of Amorphous Y_2Fe
Jpn. J. Appl. Phys., **38** (1999) 484.

K.Asakura, Y.Noguchi and Y.Iwasawa
XAFS Study on the Structure of Mo Species in NaY Zeolite Derived from $Mo(CO)_6$
Jpn, J. Appl. Phys., **38** (1999) 85.

K.Asakura, T.Kubota, W-J.Chun, Y.Iwasawa, K.Ohtani and T.Fujikawa
Pt L_3-edge XANES Studies about the Hydrogen Adsorption on Small Pt Particle
J. Synchrotron Rad., **6** (1999) 439.

T.Yokoyama, M.Kiguchi, T.Ohta, O.Sato, Y.Einaga and K.Hashimoto
Local Structure of a Trapped Photoexcited State of a Fe-Co Cyanide Studied by X-Ray-Absorption Fine-Structure Spectroscopy
Phys. Rev. B, **60** (1999) 9340.

Z.H.Zhou, K.Kamiya, K.Tsutsumi, T.Hashimoto and H.Nasu
Structure of Na_2S-GeS_2 Sulphide Glasses – Comparison with Na_2O-GeO_2 Oxide Glasses
Phys. Chem. Glasses, **40** (1999) 146.

Y.Okamoto and T.Kubota
Structure of Active Site and Molecular Design of Desulfurization Catalysts
Hyomen, **37** (1999) 95. (*in Japanese*).

M.Arai, Y.Minato, K.Torii and M.Shirai
Cobalt-Containing Smectite-like Mesoporous Materials as a New Type of Catalyst for Hydrodesulfurization of Thiophene
Catal. Lett., **61** (1999) 83.

T.Yokoyama
Path-Integral Effective-Potential Theory for EXAFS Cumulants Compared with the Second-Order Perturbation
J. Syncrotron Rad., **6** (1999) 323.

Y.Okamoto, H.Okamoto, T.Kubota, H.Kobayashi and O.Terasaki
Preparation and Structure Analysis of Co-Mo Binary Sulfide Clusters Encapsulated in an NaY Zeolite
Phys. Chem. B, **103** (1999) 7160.

K.K.Bando, N.Ichikuni, H.Arakawa and K.Asakura
EXAFS Observation of Li Additive Effect on Structure of Rh Particles Supported on Zeolite
Jpn. J. Appl. Phys., **38** (1999) 81.

T.Tanaka, T.Yamamoto, Y.Kohno, T.Yoshida and S.Yoshida
Application of XANES Spectra to Supported Catalysts
Jpn. J. Appl. Phys., **38** (1999) 30.

A.Yoshiasa and H.Maeda
Anharmonic Effective Pair Potentials of β- and α-AgI Determined by I K-edge EXAFS
Solid State Ionics, **121** (1999) 175.

M.Sasaki, M.Osada, N.Higashimto, T.yamamotot, A.Fukuoka and M.Ichikawa
Templating Fabrication of Platinum Nanoparticles and Nanowires using the Cofined Mesoporous Channels of FSM-16– Their Structural Characterization and Catalytic Performances in Water Gas Shift Reaction
J. Mol. Catal. A, **141** (1999) 223.

K.Asakura, H.Nagahiro, N.Ichikuni and Y.Iwasawa
Structure and Catalytic Combustion Activity of Atomically Dispersed Pt Species at MgO Surface
Appl. Catal. A: General, **188** (1999) 313.

S.Yoshioka, Y.Kawakita, M.Kanehira and S.Takeda
Local Structure of Liquid IVb-Te Mixtures
Jpn. J. Appl. Phys., **38** (1999) 468.

J.-H.Choy, W.Lee and S.-J.Hwang
Evolution of Crystal and Electronic Structures of Sr_2CuO_3 upon Fluorination Reaction
Physica C, **322** (1999) 93.

T.Miyanaga, H.Hoshino, H.Ikemoto, I.Yamamoto and H.Endo
EXAFS Studies of Liquid Arsenic Chalcogenides
Jpn. J. Appl. Phys., **38** (1999) 560.

H.Ikemoto, H.Hoshino, T.Miyanaga, I.Yamamoto and H.Endo
The Semiconductor-Metal Transition of Liquid Tellurium-Arsenic Mixtures
J. Non-Cryst. Solids, **250** (1999) 458.

H.Hoshino, I.Yamamoto, T.Miyanaga, H.Ikemoto and H.Endo
The Electronic and Structural Changes in the Supercooled Liquid and Glassy As_2Se_3
J. Non-Cryst. Solids, **250** (1999) 478.

T.Ishioka, K.Maeda and I.Kanesaka
Vibrational Spectra and Structure of Zinc Stearate
8th Europian Conf. on the Spectroscopyof Biol. Mol., **8** (1999) 313.

M.Shirai, K.Aoki, Y.Minato, K.Torii and M.Arai
Porous Smectite-type Materials Containing Catalytically Active Divalent Cations in Octahedral Sheets
Studies in Sur. Sci. Catal., **129** (2000) 435.

T.Ishioka, M.Shimizu, I.Watanabe, S.Kawauchi and M.Harada
Infrared and XAFS Study on Internal Structural Change of Ion Aggregate in a Zinc Salt of Poly(ethylene-*co*-methacrylic acid) Ionomer on Water Absorption
Macromolecules, **33** (2000) 2722.

T.Shido, K.Asakura, Y.Noguchi and Y.Iwasawa
Structure and Catalytic Performance of Mo Dimer Oxy-Carbide Species in NaY Supercages
Appl. Catal. A: General, **194** (2000) 365.

10C

T.Izumoto, H.Umeda, S.Sakurai, J.Masamoto, S.Nomura, Y.Kitagawa and Y.Suda
Solubility of Poly(phenylene ether) to Polystyrene-*block*-polyethylenebutylene-*block*-polystyrene Triblock Copolymers
Sen'I Gakkaishi, **55** (1999) 13. (*in Japanese*).

S.Nojima
Analysis of Morphology Formation in Crystalline-Amorphous Block Copolymers by Synchrotron Radiation
Koubunshikakou, **48** (1999) 322. (*in Japanese*).

S.Sakurai, J.Masamoto and S.Nomura
Control of Microdomain Structures and Mechanical Properties in Styrenic Block Copolymers
Nihon Gomu Kyokaishi, **72** (1999) 526. (*in Japanese*).

H.Yoshida
Crystallization Process of Plymers Observed by the Simultaneous DSC-XRD and DSC-FTIR Methods
Netsu Sokutei, **26** (1999) 141. (*in Japanese*).

J.K.Kim, H.H.Lee, S.Sakurai, S.Aida, J.Masamoto, S.Nomura, Y.Kitagawa and Y.Suda
Lattice Disordering and Domain Dissolution Transitions in Polystyrene-*block*-poly(ethylene-*co*-but-1-ene)-*block*-polystyrene Triblock Copolymer Having a Highly Asymmetric Composition
Macromolecules, **32** (1999) 6707.

T.Fujisawa, Y.Inoko and N.Yagi
The Use of Hamamatsu X-ray Image Intensifier with a Cooled CCD as a Solution X-Ray Scattering Detector
J. Synchrotron Rad., **6** (1999) 1106.

P.J.Gualfetti, M.Iwakura, J.C.Lee, H.Kihara, O.Bilsel, J.A.Zitzewitz and C.R.Matthews
Apparent Radii of the Native, Stable Intermediates and Unfolded Conformers of the α-Subunit of Tryptophan Synthase from *E. coil*, a TIM Barrel Protein
Biochem., **38** (1999) 13367.

M.Sugiyama, S.Kuwajima, Y.Soejima, A.Nakamura, N.Hiramatsu, T.Kikukawa, A.Suzuki and K.Hara
Microphase Separatiom in Dehydrated *N*-isopropylacrylamide/Sodium Acrylate Gel
Jpn. J. Appl. Phys., **38** (1999) 1360.

D.-P.Hong, M.Hoshino, R.Kuboi and Y.Goto
Clustering of Fluorine-Substituted Alcohols as a Factor Responsible for their Marked Effects on Proteins and Peptides
J. Am. Chem. Soc., **121** (1999) 8427.

S.Sasaki, K.Tashiro, M.Kobayashi, Y.Izumi and K.Kobayashi
Microscopically Viewed Structural Change of PE during the Isothermal Crystallization from the Melt II. Conformational Ordering and Lamellar Formation Mechanism Derived from the Coupled Interpretation of Time-Resolved SAXS and FTIR Data
Polymer, **40** (1999) 7125.

M.Hirai, R.K.Hirai, M.Sanada, H.Iwase and S.Mitsuya
Characteristics of AOT Microemulsions Structure Depending on Apolar Solvents
Phys. Chem. B, **103** (1999) 9658.

M.Hirai, H.Iwase and T.Hayakawa
Thermal Induced Modulation of Surface Change of Sialoglycosphingolipid Micelles
Phys. Chem. B, **103** (1999) 10136.

S.Kutsumizu, H.Tagawa, Y.Moroga and S.Yano
Small-Angle X-ray Scattering Investigation of Noncrystalline Poly(ethylene-*co*-methacrylic acid) Ionomers
Macromolecules, **33** (2000) 3818.

11A

K.Fujii, H.Tomimoto, K.Isshiki, M.Tooyama, T.Sekitani and K.Tanaka
Photon Stimulated Ion Desorption of Polymer Thin Films Following Core Excitation
Jpn. J. Appl. Phys., **38** (1999) 321.

T.Maruyama, H.Sasaki, S.Morishima and K.Akimoto
Emission Quantum Efficiency of Undoped and Eu Doped GaN Determined by Photocalorimetric Spectroscopy
Phys. stat. sol. (b), **216** (1999) 629.

A.Yamada, K.P.Ho, T.Akaogi, T.Maruyama and K.Akimoto
Layered Compound Substrates for GaN Growth
J. Cryst. Growth, **201/202** (1999) 332.

K.Amemiya, T.Yokoyama, Y.Yonamoto, M.Miyachi, Y.Kitajima and T.Ohta
Observation of O K-Edge X-Ray Magnetic Circular Dichroism of CO Adsorbed on an Ultrathin Co/Cu(001) Film
Jpn. J. Appl. Phys., **39** (2000) L63.

11B

K.Sugawara, T.Sugawara and M.Shirai
Sulfur Behavior in Rapid Pyrolysis of Coals with Chemical Pretreatments
Jpn. J. Appl. Phys., **38** (1999) 608.

T.Tsuduki, A.Imanishi, K.Isawa, S.Terada, F.Matsui, M.Kiguchi, T.Yokoyama and T.Ohta
Adsorption Structures of Alkanethiols Self-Assembled Monolayers on the Cu(100) Surface Studied by S-*K* EXAFS and C-*K* NEXAFS Spectroscopies
J. Synchrotron Rad., **6** (1999) 787.

K.Sugawara, T.Takusari, T.Sugawara, M.Shirai and Y.Nishiyama
Effect of Aromaticity on Organic Sulfur Release in Rapid Pyrolysis of Coal
Int. J. Soc. Mat. Eng. Resources, **7** (1999) 312.

M.Shirai and K.Sugawara
Determination of Sulfur Species in Coal by X-Ray Absorption Near Edge Structure Spectroscopy
Int. J. Soc. Mat. Eng. Resources, **7** (1999) 320.

M.Kiguchi, T.Yokoyama, T.Tsuduki, S.Terada, Y.Kitajima and T.Ohta
Heteroepitaxial Growth of KCl on a Cleaved (001) Face of KBr Studied by Extended X-Ray-Absorption Fine Structure
Surf. Sci., **433-435** (1999) 595.

J.Kawai, M.Sai, T.Sugimura, K.Hayashi, H.Takenaka and Y.Kitajima
Total Reflection X-Ray Photoelectron Spectroscopy of a Tantalum-Titanium Multilayer
X-Ray Spectrom., **28** (1999) 519.

M.Kiguchi, T.Yokoyama, D.Matsumura, H.Kondoh, T.Ohta and Y.Kitajima
Interface Structure of Alkali-Halide Heteroepitaxial Films Studied by X-Ray-Absorption Fine Structure
Phys. Rev. B, **60** (1999) 16205.

S.Terada, T.Yokoyama, Y.Okamoto, M.Kiguchi, Y.Kitajima and T.Ohta
SO_2 Adsorption on Thin Pd/Ni(111) Films Studied by X-Ray Absorption Fine Structure Spectroscopy
Surf. Sci., **442** (1999) 141.

T.Maruyama, T.Hasegawa, N.Komura, H.Yamada, W.Ohtsuka, K.Akimoto, Y.Kitajima, K.Maeda and E.Yagi
Compensation Centers in ZnSeTe
J. Appl. Phys., **86** (1999) 5993.

T.Ohta, T.Yokoyama, S.Terada, A.Imanishi and Y.Kitajima
Structures and Chemical Reactions of SO_2 Adsorbates Studied by Surface XAFS
Res. Chem. Intermed., **26** (2000) 29.

S.Nakai, Y.Megawa, F.Terasaki, C.Gang, T.Ohuchi, K.Obara, T.Kojima, H.Arai, T.Kashiwakura and Y.Kitajima
Resonant Emission Spectra of YF_3, YCl_3, Y_2O_3 and Y-Metal in the YL_{III} Absorption Region
Phys. Rev. B, **61** (2000) 7433.

11C

K.Edamoto, M.Yamazaki, K.Ozawa and S.Otani
Angle-Resolved Photoemission Study of the Clean and Oxygen-Covered ZrC(111) Surface
Jpn. J. Appl. Phys., **38** (1999) 257.

Y.Takakuwa
Real-Time Monitoring of the Surface Dynamics by Photoelectron Spectroscopy using Synchrotron Radiation
Denki-gakkai, **44** (1999) 23. (*in Japanese*).

K.Edamoto
Angle-Resolved Photoemission Spectroscopy Study of Transition Metal Carbide Polar Surfaces
J. Jpn. Soc. Synchrotron Rad. Res., **12** (1999) 268. (*in Japanese*).

Y.Takakuwa
Surface Dynamics on a High-Temperature Si Surface under a High-Pressure Reactive Gas Atmosphere Studied by Time-Resolved UPS
J. Elec. Spec. Relat. Phenom., **101** (1999) 211.

K.Ozawa, T.Noda, T.Nakane, M.Yamazaki, K.Edamoto and S.Otani
Photoemission Study of K Adsorption on ZrC(111)
Surf. Sci., **433** (1999) 700.

T.Noda, M.Yamazaki, K.Ozawa, K.Edamoto and S.Otani
Oxygen Adsorption on a ZrC(111) Surface: Angle-Resolved Photoemission Study
Surf. Sci., **450** (2000) 27.

K.Ozawa, T.Noda, T.Nakane, M.Yamazaki, K.Edamoto, S.Tanaka and S.Otani
Potassium Adsorption on the Polar ZrC(111) Surface: Photoemission Spectroscopy Study
Surf. Sci., **446** (2000) 229.

11D

Y.Takakuwa
Real-Time Monitoring of the Surface Dynamics by Photoelectron Spectroscopy using Synchrotron Radiation
Denki-gakkai, **44** (1999) 23. (*in Japanese*).

K.Edamoto
Angle-Resolved Photoemission Spectroscopy Study of Transition Metal Carbide Polar Surfaces
J. Jpn. Soc. Synchrotron Rad. Res., **12** (1999) 268. (*in Japanese*).

T.Hori, H.Sakamoto, Y.Takakuwa, Y.Enta, H.Kato and N.Miyamoto
In *situ* Observation of a High-Temperature Si(001) Surface During SiH_2Cl_2 Exposure by Photoelectron Spectroscopy
Thin Solid Films, **343** (1999) 354.

Y.Takakuwa
Surface Dynamics on a High-Temperature Si Surface under a High-Pressure Reactive Gas Atmosphere Studied by Time-Resolved UPS
J. Elec. Spec. Relat. Phenom., **101** (1999) 211.

T.Maruyama, Y.Miyajima, S.H.Cho, K.Akimoto and H.Kato
Angle-Resolved Photoemissoin Study of the Wurtzite GaN (0001)
Physica B, **262** (1999) 240.

12A

T.Sekitani, E.Ikenaga, K.Fujii, K.Mase, N.Ueno, K.Tanaka
Control of Chemical Bond Scission by using Site-Specific Photochemical Surface Reactions
J. Elect. Spec. Relat. Phenom., **101** (1999) 135.

A.Yokoya, R.Watanabe and T.Hara
Single- and Double-Strand Breaks in Solid pBR322 DNA Induced by Ultrasoft X-Rays at Photon Energies of 388, 435 and 573 eV
J. Rad. Res., **40** (1999) 145.

M.Yamamoto, K.Sakano and Y.Hotta
High Reflectance Multilayer Mirrors for the Water Window Region
Inst. Phys. Conf. Ser., **159** (1999) 601.

12B

T.Imajo, K.Yoshino, J.R.Esmond, W.H.Parkinson, A.P.Thorne, J.E.Murray, R.C.M.Learner, G.Cox, A.S.-C.Cheung, K.Ito and T.Matsui
The Application of a VUV Fourier Transform Spectrometer and Synchrotron Radiation Source to Measurements of: II. The $\delta(1,0)$ band of NO
J. Chem. Phys., **112** (2000) 2251.

K.Yoshino, A.P.Thorne, K.Ito, T.Matsui, K.W.-S.Leung, A.S.-C.Cheung and T.Imajo
The Application of a VUV-FT Spectrometer and Synchrotron Radiation Source to Measurements of the NO and O_2 Bands at 295 K
Phys. Chem. Earth(C), **25** (2000) 199.

12C

T.Tokuyoshi and I.Nakai
XANES Spectra of Mechanically Alloyed YFe
Jpn. J. Appl. Phys., **38** (1999) 476.

M.Shirai, K.Murakami and M.Arai
XAFS Study on the Thermal Behavior of Nickel Species Dispersed in Brown Coals
Jpn. J. Appl. Phys., **38** (1999) 77.

M.Shirai, K.Torii and M.Arai
XAFS Study on Metal Particle Formation in Noble Metal Cation Loaded Synthesized Smectite Containing Several Devalent Cations during Hydrogen Reduction
Jpn. J. Appl. Phys., **38** (1999) 69.

E.Yanase, I.Watanabe, M.Harada, M.Takahashi and Y.Dake
Conversion Electron/He Ion Yield XAFS of $SrTiO_3$ Thin Films
Jpn. J. Appl. Phys, **38** (1999) 198.

I.Nakai and T.Tokuyoshi
XANES Studies of Mechanical Alloying Y_2Co
Jpn. J. Appl. Phys., **38** (1999) 480.

Y.Okamoto and T.Kubota
Structure of Active Site and Molecular Design of Desulfurization Catalysts
Hyomen, **37** (1999) 95. (*in Japanese*).

Y.Okamoto, H.Okamoto, T.Kubota, H.Kobayashi and O.Terasaki
Preparation and Structure Analysis of Co-Mo Binary Sulfide Clusters Encapsulated in an NaY Zeolite
Phys. Chem. B, **103** (1999) 7160.

H.Yamaguchi and H.Takebe
Local Structure of Rare-Earth Ions in Alkali Silicae Glasses Studied by Extended X-Ray Absorption Fine Structure
Jpn. J. Appl. Phys. Suppl., **38** (1999) 168.

T.Yamamoto, T.Tanaka, S.Takenaka, S.Yoshida, T.Onari, Y.Takahashi, T.Kosaka and S.Hasegawa
XAFS Study of Fe- and Mn- Promoted Sulfated Zirconia
J. Synchrotron Rad., **6** (1999) 425.

T.Tanaka, T.Yamamoto, Y.Kohno, T.Yoshida and S.Yoshida
Application of XANES Spectra to Supported Catalysts
Jpn. J. Appl. Phys., **38** (1999) 30.

T.Yamamoto, T.Tanaka, S.Takenaka, S.Yoshida, T.Onari, Y.Takahashi, T.Kosaka, S.Hasegawa and M.Kudo
Structural Analysis of Iron and Manganese Species in Iron- and Manganese-Promoted Sulfated Zirconia
J. Phys. Chem. B, **103** (1999) 2385.

H.Miyake, M.Mukai, S.Adachi, H.Nakamura, K.Tamura, T.Iizuka, Y.Shiro, R.W.Strange and S.S.Hasnain
Iron Coordination Structures of Oxygen Sensor FixL Characterized by Fe K-Edge Extended X-Ray Absorption Fine Structure and Resonance Raman Spectroscopy
J. Biol. Chem., **274** (1999) 23176.

M.Yao, T.Hayakawa, K.Nagaya, Y.Ohmasa, K.Hamada, M.Tai, I.Yamamoto and M.Nomura
X-Ray Absorption Near Edge Structure of Selenium Free Clusters
Jpn. J. Appl. Phys., **38** (1999) 564.

U.Tanaka, T.Maruyama and K.Akimoto
Epitaxial Growth of GaN/Pd/GaN Sandwich Structure
J. Cryst, Growth, **201/202** (1999) 444.

A.Yamada, K.P.Ho, T.Maruyama and K.Akimoto
Molecular Beam Epitaxy of GaN on a Substrate of MoS_2 Layered Compound
Appl. Phys. A, **69** (1999) 89.

S.Morishima, T.Maruyama, M.Tanaka, Y.Masumoto and K.Akimoto
Growth of Eu Doped GaN and Electrominescence from MIS Structure
Phys. stat. sol. (a), **176** (1999) 113.

T.Maruyama, M.Sasaki, S.Morishima and K.Akimoto
Red Emission from Eu-Doped GaN Studied by Photoluminescence and Photo-Calorimetric Spectroscopy
Jpn. J. Appl. Phys., **38** (1999) 1306.

O.Endo, M.Kiguchi, T.Yokoyama, M.Ito and T.Ohta
In-situ X-ray absorption studies of bromine on the Ag(100) electrode
J. Electroanalytical Chem., **473** (1999) 19.

13B1

C.H.Lee, H.Oyanagi, C.Sekine, I.Shirotani and M.Ishii
XANES Study of Rare-earth Valency in $L\mathrm{Ru}_4\mathrm{P}_{12}(L=\mathrm{Ce}$ and Pr)
Phys. Rev. B, **60** (1999) 13253.

13C

T.Sekitani, E.Ikenaga, K.Fujii, K.Mase, N.Ueno, K.Tanaka
Control of Chemical Bond Scission by using Site-Specific Photochemical Surface Reactions
J. Elect. Spec. Relat. Phenom., **101** (1999) 135.

K.Kosugi, T.Abukawa, M.Shimomura, S.Sumitani, H.-W.Yeom, T.Hanano, K.Tono, S.Suzuki, S.Sato, T.Ohta, S.Kono and Y.Takakuwa
Photoelectron Diffraction Study of the Si(001)$c(4\times4)$-C Surface
J. Elec. Spec. Relat. Phenom., **101** (1999) 239.

14A

K.Asakura, W-J.Chun and Y.Iwasawa
Anisotropic Arrangement of Mo Species Highly Dispersed on TiO_2 (110) Surface Demonstrated by Polarization Dependent Total Reflection Fluorescence EXAFS
Jpn. J. Appl. Phys., **38** (1999) 40.

N.Ishizawa, Y.Matsushima, M.hayashi and M.Ueki
Synchrotron Radiation Study of Yttria-Stabilized Zirconia, $\mathrm{Zr}_{0.758}Y_{0.242}O_{1.879}$
Acta. Cryst. B, **B55** (1999) 726.

H.Kitahara-Eba, N.Ishizawa, F.Marumo and Y.Noda
Synchrotron X-Ray Study of the Monoclinic High-pressure Structure of $AgGaS_2$
Phys. Rev. B, **61** (2000) 3310.

K.Asakura, W.-J.Chun and Y.Iwasawa
Polarization-dependent Total-reflection Fluorescence EXAFS Study about Active Structures on Single Crystal Oxides as Model Catalyst Surfaces
Topics in Catal., **10** (2000) 209.

N.Ishizawa
Precise Structure Analysis under Virtually Extinction-free Conditions using Small Crystals
J. Cryst. Soc. Jpn., **42** (2000) 155.

14B

O.Sakata, N.Matsuki and H.Hashizume
In-plane Structure of an Arsenic-Adsorbed Si(001) Surface Probed with Grazing-Angle X-Ray Standing Waves
Phys. Rev. B, **60** (1999) 15546.

T.Takeda, A.Momose, K.Hirano, S.Haraoka, T.Watanabe and Y.Itai
Human Carcinoma: Early Experience with Phase-Contrast X-ray CT with Synchrotron Radiation–Comparative Specimen Study with Optical Microscopy
Radiology, **214** (2000) 298.

14C

S.Iida, R.Kitamura, T.Abe and H.Kawata
Section Topography in Bragg-Case Used for Kinematical Imaging of Microdefects in Si Crystals
Jpn. J. Appl. Phys., **38** (1999) 531.

K.Mori, K.Hyodo, N.Shikano and M.Ando
First Observatin of Small Fractures on a Human Dried Proximal Phalanx by Synchrotron X-Ray Interference Radiography
Jpn. J. Appl. Phys., **38** (1999) L1339.

15A

K.Sato, S.Ueno and J.Yano
Molecular Interactions and Kinetic Properties of Fats
Prog. Lipid Res., **38** (1999) 91.

K.Boubekri, J.Yano, S.Ueno and K.Sato
Polymorphic Transformations in *sn*-1,3-Distearoyl-2-ricinoleyl-glycerol
J. American Oil Chem. Soc., **76** (1999) 949.

T.Asano, F.J.Balta Calleja, A.Flores, M.Tanigaki, M.F.Mina, C.Sawatari, H.Itagaki, H.Takahashi and I.Hatta
Crystallization of Oriented Amorphous Poly(ethyleneterephthalate) as Revealed by X-Ray Diffraction and Microhardness.
Polymer, **40** (1999) 6475.

T.Asano, T.Yamamoto, M.F.Mina, Y.Fujiwara, H.Takahashi and I.Hatta
Melting Behavior of the Oriented β-Phase Polypropylene Texture Crystallized by the Temperature Slope Method
J. Macromol. Sci. Phys., **D38** (1999) 163.

M.F.Mina, T.Asano, R.Nuryadi, C.Sawatari, H.Takahashi and I.Hatta
Effect of Homologous Impurity on the Solid-Solid Phase Transition of Normal-Alkane(Hexatriacontane) Crystal Studied by Time-Resolved X-Ray Measurements
Jpn. J. Appl. Phys., **38** (1999) 164.

H.Okuda, H.Suzuki, H.Hiramatsu, K.Ito, K.Osamura and Y.Amemiya
Phase Decomposition in Al-Ag Alloys under Deformation
Proc. of International Conf. on Solid-Solid Phase Transformations, **12** (1999) 137.

H.Okuda, K.Ito, K.Osamura and Y.Amemiya
Time-Resolved SWAXS on Phase Decomposition with Ordering
Proc. of the International Conf. on Solid-Solid Phase Transformations, **12** (1999) 257.

K.Wakabayashi and N.Yagi
Muscle Contraction: Challenges for Synchrotron Radiation
J. Synchrotron Rad., **9** (1999) 875.

Y.Sugimoto and K.Wakabayashi
Level-Arm Motion and Power Stroke in Myosin Motor Protein
PNE, **44** (1999) 102. (*in Japanese*).

Y.Takezawa, D.-S.Kim, M.Ogino, Y.Sugimoto, T.Kobayashi, T.Arata and K.Wakabayashi
Backward Movements of Cross-Bridges by Application of Stretch and by Binding of MgADP to Skeletal Muscle Fibers in the Rigor State as Studied by X-Ray Diffraction
Biophys. J., **76** (1999) 1770.

S.Maruta, Y.Uyehara, K.Homma, Y.Sugimoto and K.Wakabayashi
Formation of the Myosin-ADP-Gallium Fluoride Complex and its Solution Structure by Small-Angle Synchrotron X-Ray Scattering
J. Biochem., **125** (1999) 177.

Y.Takezawa, D.-S.Kim, M.Ogino, Y.Sugimoto, T.Kobayashi, T.Arata and K.Wakabayashi
Similar Effects of the Applied Stretch and MgADP Binding on the Structure of Skeletal Muscle Fibers in the Rigor State as Studied by X-Ray Diffraction
J. Muscle Res. Cell Motil., **20** (1999) 336.

T.Arata, S.Kimura, Y.Sugimoto, Y.Takezawa and K.Wakabayashi
X-Ray Solution Scattering Study of the Actin Dimer-Myosin Head Complex
J. Muscle Res. Cell Motil., **20** (1999) 335.

M.Kojima, M.Tanokura, M.Maeda, K.Kimura, Y.Amemiya, H.Kihara and K.Takahashi
pH-Dependent Unfolding of Aspergilloperpsin II Studied by Small-Angle X-Ray Scattering
Biochem., **39** (2000) 1364.

K.Nishikawa and T.Morita
Inhomogeneity of molecular distribution in supercritical fluids
Chem. Phys. Lett., **316** (2000) 238.

T.Morita, K.Kusano, H.Ochiai, K.Satow and K.Nishikawa
Study of inhomogeneity of supercritical water by small-angle x-ray scattering
J. Chem. Phys., **112** (2000) 4203.

15B1

K.Mizuno, S.Nagai, A.Tamiya, Y.Noda, K.Okitsu, E.Hashimoto and T.Kino
Identification of Nature of Dislocation Loops Grown as Vacancy Source after Up-Quenching
Jpn. J. Appl. Phys. Suppl., **38** (1999) 460.

K.Izumi, K.Taguchi, Y.Kobayashi, M.Tachibana, K.Kojima and M.Ataka
Screw Dislocation Lines in Lysozyme Crystals Observed by Laue Topography Using Synchrotron Radiation
J. Crystal Growth, **206** (1999) 155.

M.Tachibana, K.Kono, M.Shimizu, and K.Kojima
Growth and Dislocation Characteristics of Organic Molecular Crystals: 2,3-dimethylnaphthalene
J. Cryst. Growth, **198** (1999) 665.

K.Mizuno, S.Nagai, A.Tamiya, Y.Noda, K.Ito, M.Iwami, M.Kunimoto and T.Kino
Indistinct Defect Images in Topographs of Nearly Perfect Aluminum Crystals Just Prior to Appearance of Dislocation Loops
J. Phys. Soc. Jpn., **69** (2000) 1271.

15C

Y.Hasegawa, Y.Ueji, K.Okitsu, Y.Amemiya, J.M.Ablett and D.P.Siddons
Tunable X-Ray Polarization Reflector with Perfect Crystals
Acta Cryst. A, **55** (1999) 955.

Y.Kudo, K.-Y.Liu, S.Kawada, A.Kashiwagi and K.Hirano
Determination of the Density and the Thichness of SiO_2 Films using Extremely Asymmetric X-Ray Diffraction
Jpn. J. Appl. Phys., **39** (2000) 1409.

Y.Kudo, K.Liu, S.Kawado and K.Hirano
Elimination of Exttrinsic Components Overlapping Lattice Distortion Variations of a Silicon Single Crystal Obtained by Double-Crystal X-Ray Topography
J. Appl. Cryst., **33** (2000) 226.

16A2

Y.Endoh, K.Hirota, S.Ishihara, S.Okamoto, Y.Murakami, A.Nishizawa, T.Fukuda, H.Kimura, H.Nojiri, K.Kaneko and S.Maekawa
Transition between Two Ferromagnetic States Driven by Orbital Ordering in $La_{0.88}Sr_{0.12}MnO_3$
Phys. Rev. Lett., **82** (1999) 4328.

Y.Murakami, J.P.Hill, D.Gibbs, M.Blume, H.Kawada, I.Koyama, M.Tanaka, H.Kawata, T.Arima, Y.Moritomo, Y.Tokura, K.Hirota and Y.Endoh
Direct Observation of Charge and Orbital Ordering by Resonant X-Ray Scattering
Jpn. J. Appl. Phys., **38** (1999) 360.

Y.Endoh, H.Nojiri, K.Kaneko, K.Hirota, T.Fukuda H. H.Kimura, Y.Murakami, S.Ishihara, S.Maekawa, S.Okamoto and M.Motokawa
Field Induced Transition from Metal to Insulator in the Colossal Magneto-Resistance Manganites
Mater. Sci. Eng., **63** (1999) 151.

K.Hirota, N.Oumi, T.Matsumura, H.Nakao, Y.Wakabayashi, Y.Murakami and Y.Endoh
Direct Observation of Antiferroquadrupolar Ordering: Resonant X-Ray Scattering Study of DyB_2C_2
Phys. Rev. Lett., **84** (2000) 2706.

16B

R.Z.Tai, Y.Takayama, N.Takaya, T.Miyahara, S.Yamamoto, H.Sugiyama, J.Urakawa, H.Hayano and M.Ando
Chaotic Nature of the Stored Current in an Electron Storage Ring Detected by a Two-Photon Correlator for Soft-X-Ray Synchrotron Radiation
Phys. Rev. A, **60** (1999) 3262.

M.-T.Huang, R.Wehlitz, Y.Azuma, L.Pibida, I.A.Sellin, J.W.Cooper, M.Koide, H.Ishijima and T.Nagata
Single and Double Photoionization of Lithium
Phys. Rev. A, **59** (1999) 3397.

R.Wehlitz, M.-T.Huang, K.A.Berrington, S.Nakazaki and Y.Azuma
One-Step Double Autoionization into the Double-Photoionization Continuum
Phys. Rev. A, **60** (1999) R17.

R.Wehlitz, M.-T.Huang, I.A.Sellin and Y.Azuma
The Wannier Threshold Law Examined by Photoelectron Satellite Measurements
J. Phys. B, **32** (1999) L635.

R.Z.Tai, Y.Takayama, N.Takaya, T.Miyahara, S.Yamamoto, H.Sugiyama, J.Urakawa, H.Hayano, and M.Ando
Chaotic Nature of the Stored Current in an Electron Storage Ring Detected by a Two-photon Correlator for Soft-X-Ray Synchrotron Radiation
Phys. Rev.A, **60** (1999) 3262-3266.

K.Ito, J.Adachi, R.Hall, S.Motoki, E.Shigemasa, K.Soejima and A.Yagishita
Photoelectron Angular Distributions from Dissociative Photoionization Channels of Fixed-in-Space Molecular Hydrogern
J. Phys. B, **33** (2000) 527.

17A

X.Jiang, Q.Jia, Z.Jiang and A.Iida
Depth Profile of Delta-Doped Semiconductors by X-Ray Reflection Technique
Jpn. J. Appl. Phys., **38** (1999) 261.

18A

S.Suto, K.Sakamoto, D.Kondo, T.Wakita, A.Kimura and A.Kakizaki
Bonding Nature of C_{60} Adsorbed on Si(111)7×7 and Si(100)2×1 Surfaces Studied by HREELS and PES
Surf. Sci., **427** (1999) 85.

D.Kondo, K.Sakamoto, Y.Ushimi, M.Harada, A.Kimura, A.Kakizaki and S.Suto
Change in Electronic Structure of C_{60} Molecules Adsorbed on a Si(001)-(2×1) Surface by Thermal Effect
Jpn. J. Appl. Phys., **38** (1999) 328.

K.Sakamoto, D.Kondo, Y.Ushimi, M.Harada, A.Kimura, A.Kakizaki and S.Suto
Temperature Dependence of the Electronic Structure of C_{60} Films Adsorbed on Si(001)-(2×1) and Si(111)-(7×7) Surfaces
Phys. Rev. B, **60** (1999) 2579.

S.Suto, K.Sakamoto, D.Kondo, T.Wakita, A.Kimura, A.Kakizaki, C.-W.Hu and A.Kasuya
Interaction of C_{60} with Si(111)7×7 and Si(100)2×1 Surfaces Studied by STM, PES and HREELS: Annealing Effect
Surf. Sci., **438** (1999) 242.

K.Sakamoto, D.Kondo, Y.Ushimi, A.Kimura, A.Kakizaki and S.Suto
Thermal-Dependent Electronic Structure at the Interface of C_{60}-Adsorbed Si(111)-(7×7) Surface
Surf. Sci., **438** (1999) 248.

K.Sakamoto, K.Kondo, M.Harada, A.Kimura, A.Kakizaki and S.Suto
Electronic Structure of C_{60} Adsorbed on Si(111)-(7×7) and Si(001)-(2×1) Surfaces
Surf. Sci., **433** (1999) 642.

J.Okabayashi, A.Kimura, T.Mizokawa, A.Fujimori, T.Hayashi and M.Tanaka
Mn 3d Partial Density of States in $Ga_{1-x}Mn_xAs$ Studied by Resonant Photoemission Spectroscopy
Phys. Rev. B, **59** (1999) 2486.

H.Sasaki, T.Jikimoto, A.Kinoshita, M.Hirai, M.Kusaka, M.Iwami and T.Nakata
Electronic and Structural Analysis of 6H-SiC(0001)3×3 Reconstructed Surface
Jpn. J. Appl. Phys., **38** (1999) 309.

18B

T.Inoue, H.Sugawara, S.Hamanaka, H.Tsukui, E.Suzuki, T.Kohzuma and Y.Kai
Crystal Structure Determinations of Oxidized and Reduced Plastocyanin from the Cyanobacterium *Synechococcus* sp.
Biochem., **38** (1999) 6063.

N.Shibata, T.Inoue, C.Nagano, N.Nishio, T.Kohzuma, K.Onodera, F.Yoshizaki, Y.Sugimura and Y.Kai
Novel Insight into the Copper-Ligand Geometry in the Crystal Structure of *Ulva pertusa* Plastocyanin at 1.6-ÅResolution
J. Biol. Chem., **274** (1999) 4225.

T.Inoue, H.Sugawara, S.Hamanaka, H.Tsukui, E.Suzuki, T.Kohzuma and Y.Kai
Crystallization and Preliminary X-Ray Analysis of Plastocyanin from Cyanobacterium *Synechococcus* sp. PCC 7942
Acta Cryst. D, **D55** (1999) 683.

T.Kohzuma, T.Inoue, F.Yoshizaki, Y.Sasakawa, K.Onodera, S.Nagatomo, T.Kitagawa, S.Uzawa, T.Isobe, Y.Sugimura, M.Gotowda and Y.Kai
The Structure and Unusual pH Dependence of Plastocyanin from the Fern *Dryoperis crassirhizoma*
J. Biol. Chem., **274** (1999) 11817.

T.Inoue, N.Nishino, S.Suzuki, K.Kataoka, T.Kohzuma and Y.Kai
Crystal Structure Determinations of Oxidized and Reduced Pseudoazurins from *Achromobacter cycloclastes*
J. Biol. Chem., **274** (1999) 17845.

H.Hashimoto, T.Matsumoto, M.Nishioka, T.Yuasa, S.Takeuchi, T.Inoue, S.Fujiwara, M.Takagi, T.Imanaka and Y.Kai
Crystallographic Studies on a Family B DNA Polymerase from Hyperthermophilic Archaeon *Pyrococcus kodakaraensis* Strain KOD1
J. Biochem., **125** (1999) 983.

H.Sugawara, H.Yamamoto, N.Shibata, T.Inoue, S.Okada, C.Miyake, A.Yokota and Y.Kai
Crystal Structure of Carboxylase Reaction-Oriented Ribulose 1,5-Bisphosphate Carboxylase/Oxygenase from a Thermophilic Red Alga, *Galdieria partita*
J. Biol. Chem., **274** (1999) 15655.

Y.Kai, H.Matsumura, T.Inoue, K.Terada, Y.Nagara, T.Yoshinaga, A.Kihara, K.Tsumura and K.Izui
Three-Dimensional Structure of Phospho*enol*pyruvate Carboxylase: A Proposed Mechanism for Allosteric Inhibition
Proc. Natl. Acad. Sci. USA, **96** (1999) 823.

J.Masuda, T.Yamaguchi, T.Tobimatsu, T.Toraya, K.Suto, N.Shibata, Y.Morimoto, Y.Higuchi and N.Yasuoka
Crystallization and Preliminary X-Ray Study of Two Crystal Forms of *Klebsiella Oxytoca* Diol Dehydratase-cynacobalamin Complex
Acta Cryst., **D55** (1999) 907.

N.Shibata, J.Masuda, T.Tobimatsu, T.Toraya, K.Suto, Y.Morimoto and N.Yasuoka
A New Mode of B_{12} Binding and the Direct Participation of a Potassium Ion in Enzyme Catalysis: X-Ray Structure of Diol Dehydratase
Structure, **7** (1999) 997.

S-S.Cha, M-S.Kim, Y.H.Choi, B-J.Sung, N.K.Shin, H-C.Shin, Y.C.Sung and B-H.Oh
2.8ÅResolution Crystal Structure of Human TRAIL, a Cytokine with Selective Antitumor Activity
Immunity, **11** (1999) 253.

J-S.Kim, S-S.Cha, H-J.Kim, T-J.Kim, N-C.Ha, S-T.Oh, H-S.Cho, M-J.Cho, M-J.Kim, H-S.Lee, J-W.Kim, K.Y.Choi, K-H.Park and B-H.Oh
Crystal Structure of a Maltogenic Amylase Provides Insights into a Catalytic Versatility
J. Bilol. Chem., **274** (1999) 26279.

S-S.Cha, H-C.Shin, K.Y.Choi and B-H.Oh
Expression, Purification and Crystallization of Recombinant Human TRAIL
Acta Cryst. D, **55** (1999) 1101.

H.Tsuge, T.Nishimura, Y.Tada, T.Asano, D.Turk, V.Turk and N.Katunuma
Inhibition Mechanism of Cathepsin L-Specific Inhibitors Based on the Crystal Structure of Papain-CLIK148 Complex
Biochem. Biophys. Res. Commun., **266** (1999) 411.

List of Publications

H.Tsuge, M.Nagahama, T.Nishimura, Y.Sakaguchi, N.Katunuma and J.Sakurai
Crystallization and Preliminary X-Ray Studies of the Component of *Clostridium perfringens* Iota Toxin Complexed with NADPH
J. Structural Biol., **126** (1999) 175.

K.Takano, Y.Yamagata, M.Kubota, J.Funahashi, S.Fujii and K.Yutani
Contribution of Hydrogen Bonds to the Conformational Stability of Human Lysozyme: Calorimetry and X-ray Analysis of Six Ser → *AlaMutants*
Biochem., **38** (1999) 6623.

N.Nakagawa, M.Sugahara, R.Masui, R.Kato, K.Fukuyama and S.Kuramitsu
Crystal Strucuture of *Thermus thermophilus*HB8 UvrB Protein, a Key Enzyme of Nucleotide Excision Repair
J. Biochem.(Tokyo), **126** (1999) 986.

T.Nogi, T.A.Fukami, M.Ishida, M.Yoshida and K.Miki
Purification, Crystallization, and Preliminary X-Ray Crystallographic Analysis of *Thermus thermophilus* V_1-ATPase B Subunit
J. Struct. Biol., **127** (1999) 79.

K.Kitano, Y.Niimura, Y.Nishiyama and K.Miki
Stimulation of Peroxidase Activity by Decamerization Related to Ionic Strength: AhpC Protein from *Amphibacillus xylanus*
J. Biochem., **126** (1999) 313.

H.Komori, F.Matsunaga, Y.Higuchi, M.Ishiai, C.Wada and K.Miki
Crystal Structure of a Prokaryotic Replication Initiator Protein Bound to DNA at 2.6 ÅResolution
EMBO J., **18** (1999) 4597.

J.Saito, A.Kita, Y.Higuchi, Y.Nagata, A.Ando and K.Miki
Crystal Structure of Chitosanase from *Bacillus circulans* MH-K1 at 1.6-ÅResolution and its Substrate Recognition Mechanism
J. Biol. Chem., **274** (1999) 30818.

H.Hashimoto, T.Inoue, M.Nishioka, S.Fujiwara, M.Takagi, T.Imanaka and Y.Kai
Hyperthermostable Protein Structure Maintained by Intra- and Inter-Helix Ion-Pairs in Archaeal O^6 Methylguanine-DNA Methyltransferase
J. Mol. Biol., **192** (1999) 245.

H.Matsumura, M.Terada, S.Shirakata, T.Inoue, T.Yoshinaga, K.Izui and Y.Kai
Plausible Phospho*enol*pyruvate Binding Site Revealed by 2.6ÅStructure of Mn^{2+}-bound Phospho*enol*pyruvate Carboxylase from *Escherichia coli*
FEBS Letters, **458** (1999) 93.

T.Inoue, M.Gotowda, H.Sugawara, T.Kohzuma, F.Yoshizaki, Y.Sugimura and Y.Kai
Structure Comparison between Oxidized and Reduced Plastocyanin from a Fern, *Dryopteris crassirhizoma*
Biochem., **38** (1999) 13853.

M.Nakasako, M.Odaka, M.Yohda, N.Dohmae, K.Takio, N.Kamiya and I.Endo
Tertiary and Quaternary Structures of Photoreactive Fe-Type Nitrile Hydratase from *Rhodococcus* sp. N-771: Roles of Hydration Water Molecules in Stabilizing the Structures and the Structural Origin of the Substrate Specificity of the Enzyme
Biochem., **38** (1999) 9887.

J.Funahashi, K.Takano, Y.Yamagata and K.Yutani
Contribution of Amino Acid Substitutions at two Different Interior Positions to the Coformational Stability of Human Lysozyme
Protein Engineering, **12** (1999) 841.

K.Takano, K.Tsuchimori, Y.Yamagata and K.Yutani
Effect of Foreign N-Terminal Residues on the Conformational Stability of Human Lysozyme
Eur. J. Biochem., **266** (1999) 675.

Y.Higuchi
Small Molecular Ligands (SO, CO, CN, SH) to the Metals Found in B
Chemistry, **54** (1999) 36. (*in Japanese*).

K.T.Chong, G.Miyazaki, H.Morimoto, Y.Oda and S.-Y.Park
Structures of the Deoxy and CO Forms of Hemoglobin from *Dasyatis akajei*, a Cartilaginous Fish
Acta Cryst., **D55** (1999) 1291.

G.Miyazaki, H.Morimoto, K.-M.Yun, S.-Y.Park, A.Nakagawa, H.Minagawa and N.Shibayama
Magnesium(II) and Zinc(II)-Protoporphyrin IX's Stabilize the Lowest Oxygen Affinity State of Human Hemoglobin even more Strongly than Deoxyheme
J. Mol. Biol., **292** (1999) 1121.

T.Shimura, T.Hosoi, R.Ejiri and M.Umeno
Ordered Structure in Buried Oxide Layers of SOI Wafers
Jpn. J. Appl. Phys., **38** (1999) 297.

S.Goda, K.Takano, Y.Yamagata, Y.Katakura and K.Yutani
Effect of Extra N-Terminal Residues on the Stability and Folding of Human Lysozyme Expressed in *Pichia pastoris*
Protein Engineering, **13** (2000) 299.

K.Fukuda, H.Mizuno, H.Atoda and T.Morita
Crystal Structure of Flavocetin-A, a Platelet Glycoprotein Ib-Binding Protein, Reveals a Novel Cyclic Tetramer of C-type Lectin-like Heterodimers
Biochem., **39** (2000) 1915.

T.Koshiba, M.Yao, Y.Kobashigawa, M.Demura, A.Nakagawa, I.Tanaka, K.Kuwajima and K.Nitta
Structure and Thermodynamics of the Extraordinarily Stable Molten Globule State of Canine Milk Lysozyme
Biochem., **39** (2000) 3248.

T.Shimura, T.Hosoi and M.Umeno
Analysis of Ordered Structure of Buried Oxide Layers in SIMOX Wafers
SILICON-ON-INSULATOR TECHNOLOGY AND DEVICES IX, **99-3** (2000) 155.

T.Shimura, T.Hosoi and M.Umeno
Characterization of SOI Wafers by X-Ray CTR Scattering
J. Cryst. Growth, **210** (2000) 98.

T.Shimura, T.Hosoi and M.Umeno
Ordered SiO_2 in the Buried Oxide of SIMOX SOI Wafers
Proc. of the 4th Symp. on Atomic-scale Surface and Interface Dynamics, **4** (2000) 395.

T.Shimura, T.Hosoi and M.Umeno
The Crystalline SiO_2 Phase in the BOX Layers of SIMOX Wafers
The 3rd SANKEN Int. Symp. on Advanced Nanoelectronics: Devices, Materials, and Computing, **57** (2000) 128.

18C

A.Onodera, H.Hirano, T.Yuasa, N.F.Gao and Y.Miyamoto
Static Compression of Ti_3SiC_2 to 61 GPa
Appl. Phys. Lett., **74** (1999) 3782.

K.Takemura
Structure Analysis by Powder X-Ray Diffraction Experiments under Ultra High Pressure
J. Cryst. Soc. Jpn., **41** (1999) 11. (*in Japanese*).

K.Takemura
Absence of the c/a Anomaly in Zn under High Pressure with a Helium-Pressure Medium
Phys. Rev. B, **60** (1999) 6171.

T.Hattori, T.Matsuda, T.Tsuchiya, T.Nagai and T.Yamanaka
Clinopyroxene-Perovskite Phase Transition of $FeGeO_3$ under High Pressure and Room Temperature
Phys. Chem. Minerals, **26** (1999) 212.

A.Fujiwara, K.Ishii, T.Watanuki, H.Suematsu, H.Nakao, K.Ohwada, Y.Fujii, Y.Murakami, T.Mori, H.Kawada, T.Kikegawa, O.Shimomura, T.Matsubara, H.Hanabusa, S.Daicho, S.Kitamura and C. Katayama
Synchrotron Radiation X-Ray Powder Diffractometer Using a Cylindrical Imaging Plate
J. Appl. Crystallogr., **33** (2000) 1241.

27A

T.Sekiguchi and Y.Baba
Adsorbate Substrate Interaction in Photofragmentation of Trimethylsilyl Uoride $[Si(CH_3)_3F]$ Adsorbed on Cu(111) following Si K-Shell Excitation
Surf. Sci., **433** (1999) 849.

Y.Baba and T.Sekiguchi
Screening Effect of Metal, Semiconductor and Insulator Surfaces on the Photo-Fragmentation of Physisorbed Molecules
Surf. Sci., **433** (1999) 843.

Y.Yoshimura, K.Ono, H.Fujioka, S.Hayakawa, Y.Sato, M.Uematsu, Y.Baba, K.Hirose and M.Oshima
Chemical States of Piled-up Phosphorus and Arsenic Atoms at the SiO_2/Si Interface
Jpn. J. Appl. Phys., **38** (1999) 552.

Y.Baba and T.Sekiguchi
Desorption of Fragment Ions from Condensed $Si(OCH_3)_4$ by Localized Inner-Shell Electron Excitation at the Silicon, Oxygen, and Carbon *K* Edges
J. Vac. Sci. Technol. A, **18** (2000) 334.

H.Yamamoto and Y.Baba
Non-Destructive Depth Profile Analysis of SiO_2/Si Layer by High-Energy XPS
J. Surf. Anal., **7** (2000) 122.

28A

S.Kawaguchi, K.Ono, K.Horiba, M.Mizuguchi, S.Hayakawa, H.Fujioka, T.Koide, H.Miyauchi, N.Nakajima, H.Takenaka and M.Oshima
$M_{2,3}$ Edge Core-level Magnetic Circular Dichroism Measurements of Cu/Co Multilayers
Jpn. J. Appl. Phys., **38** (1999) 419.

K.Soejima, A.Danjo, K.Okuno and A.Yagishita
Linear and Circular Dichroism in the Double Photoionization of Helium
Phys. Rev. Lett., **83** (1999) 1546.

M.Sawada, A.Kimura and A.Kakizaki
Helicity Dependence of the Spin Polarization of Ni 6eV Satllite
J. Phys. Soc. Jpn., **69** (2000) 1891.

28B

T.Nakamura, Y.Watanabe, M.Mizumaki and S.Nanao
Short Range Order of Spin Moments in $NdCo_2$ Studied by Magnetic EXAFS
Jpn. J. Appl. Phys., **38** (1999) 436.

NE1A1

N.Shiotani
Fermiology by Compton Scattering
Jpn. J. Appl. Phys., **38** (1999) 18.

Y.Kubo, Y.Sakurai and N.Shiotani
Effects of Self-Interaction Correction on Momentum Density in Copper
J. Phys. Condens. Matter, **11** (1999) 1683.

Y.Sakurai, S.Kaprzyk, A.Bansil, Y.Tanaka, G.Stutz, H.Kawata and N.Shiotani
A High-Resolution Compton Scattering Study of Cu: Experiment and Theory
J. Phys. Chem. Solids, **60** (1999) 905.

G.Stutz, F.Wohlert, A.Kaprolat, W.Schülke, Y.Sakurai, Y.Tanaka, M.Ito, H.Kawata, N.Shiotani, S.Kaprzyk and A.Bansil
Electron Momentum-Space Densities and Fermi Surface of $\mathrm{Li}_{100-x}\mathrm{Mg}_x(0\leq x\leq 40)$ alloys: Compton scattering experiment versus theory
Phys. Rev. B, **60** (1999) 7099.

I.Matsumoto, J.Kwiatkowska, F.Maniawski, A.Bansil, S.Kaprzyk, M.Itou, H.Kawata and N.Shiotani
A Compton Scattering Study of an Al-Li Disordered Alloy Single Crystal
J. Phys. Chem. Sol., **61** (2000) 375.

Others

C.Uyama, K.Tokumori, F.Toyofuku, H.Sugiyama, K.Hyodo, M.Ando, K.Nishimura, T.Takeda, K.Yamazaki and M.Matsumoto
Proposal for Medical Application Beamline of the Spring-8
SPIE, **3770** (1999) 193.

M.Sato, S.Kitao, Y.Kobayashi, R.Haruki, T.Mitsui, Y.Yoda, X.W.Zhang and Y.Maeda
Nuclear Resonance Scattering of Synchrotron Radiation by ^{40}K
Phys. Rev. Lett., **84** (2000) 566.

R.Tai, Y.Takayama, N.Takaya, T.Miyahara, S.Yamamoto, H.Sugiyama, J.Urakawa, H.Hayano and M.Ando
A Novel Intensity Interferometer for Synchrotron Radiation in the Vacuum Ultraviolet and Soft X-Ray Regions
Rev. Sci. Inst., **71** (2000) 1256.

K.Mori, H.Shiwaku, N.Sekine, K.Hyodo, N.Shikano, H.Sato, M.Sato and M.Ando
Imaging of Bone by X-Ray Phase-Contrast Method and Synchrotron X-Radiation Photographing System
THE KONICA X-RAY PHOTOGRAPHIC REVIEW, **51** (2000) 101. (*in Japanese*).

K.Mori, N.Sekine, M.Sato, H.Sato, N.Shikano, T.Igarashi, K.Hyodo and M.Ando
Obnsarvation of Small Fractures by Phase Sensitive Radiography
ASVPI, **5** (2000) 47. (*in Japanese*).

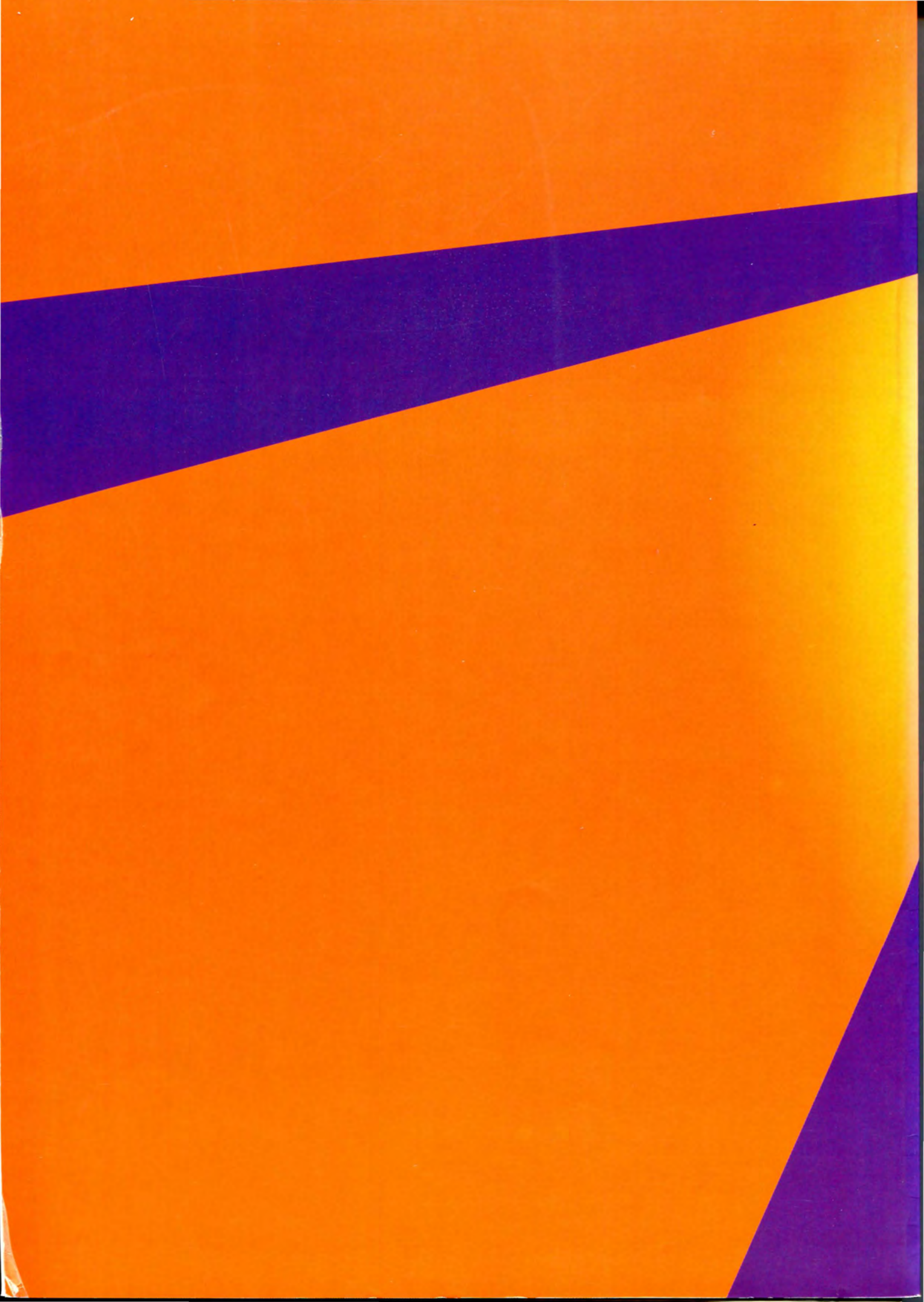

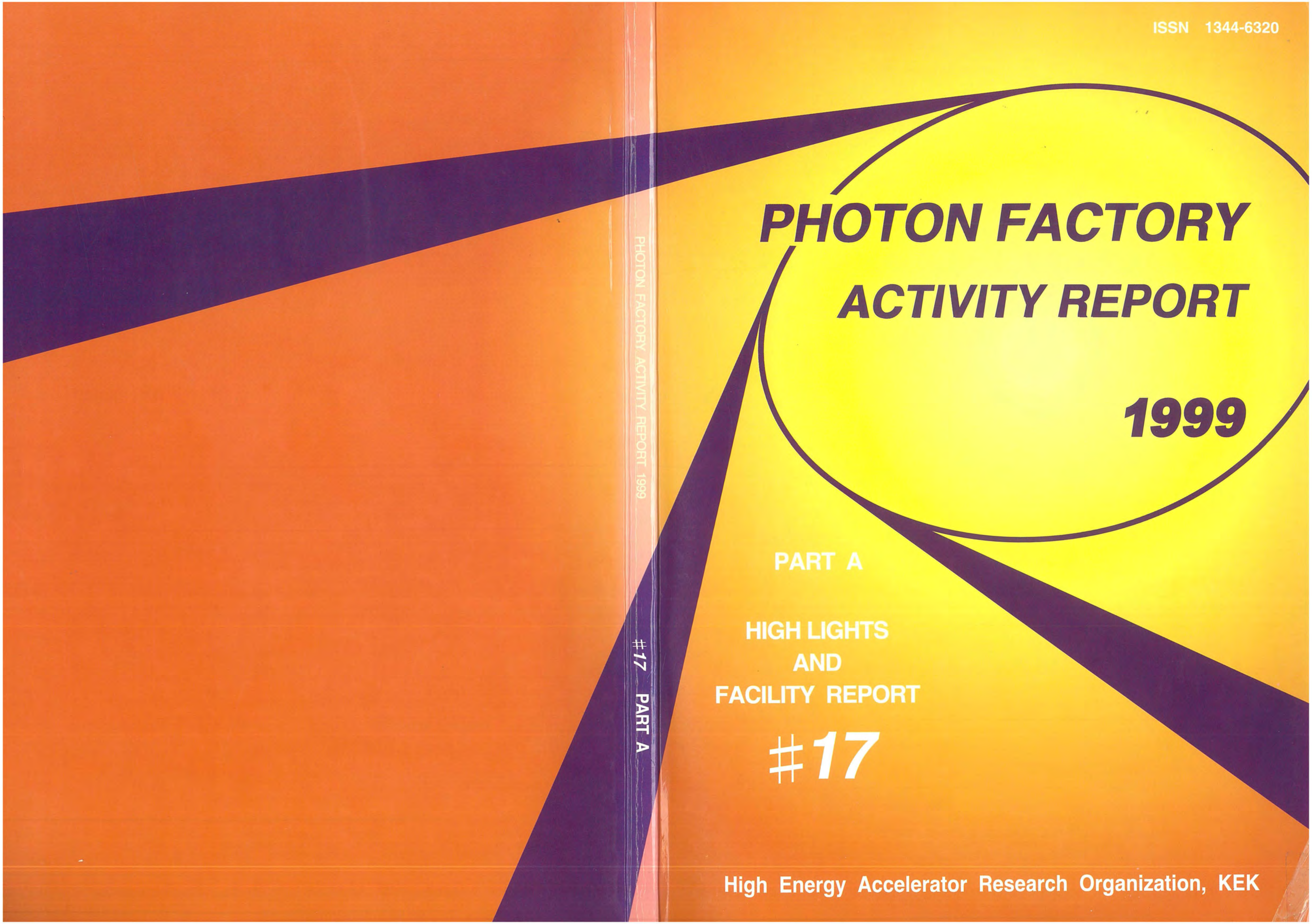

PHOTON FACTORY ACTIVITY REPORT 1999

#17 PART A

ISSN 1344-6320

PHOTON FACTORY
ACTIVITY REPORT
1999

PART A

HIGH LIGHTS
AND
FACILITY REPORT

#17

High Energy Accelerator Research Organization, KEK

M= 23.4, which is much improved compared with that of 9.5 μm when M=1.

Also, a two-dimensional imaging system has been realized by placing another set of X-ray magnifiers perpendicularly. Real-time X-ray micro-imaging will be realized by using this CCD detection system.

Reference

[1] K. Sato, Y. Hasegawa, K. Kondo, K. Miyazaki, T. Matsushita and Y. Amemiya, Rev. Sci. Instrum., to be published.

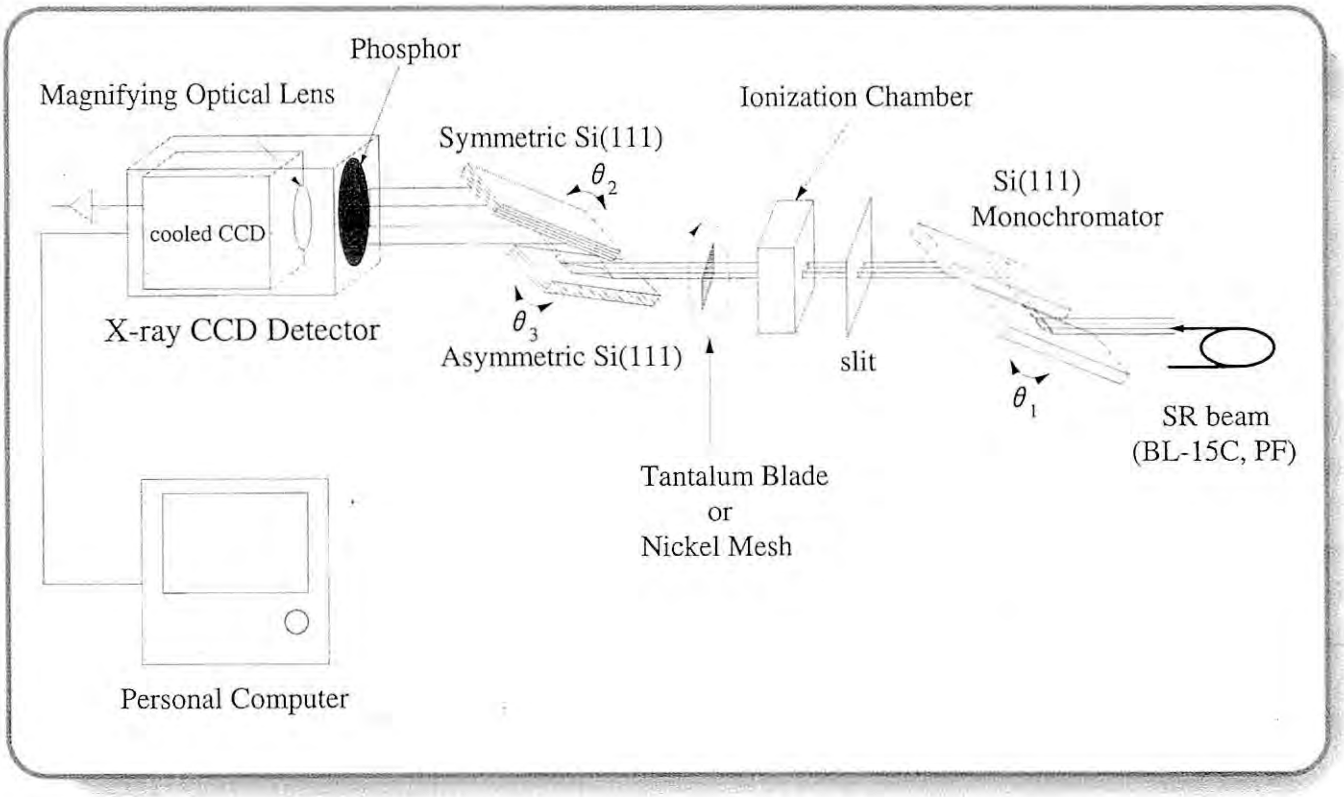

Figure 1.
Experimental setup of a high spatial-resolution x-ray CCD detector with a one-dimensional x-ray magnifier.

Figure 2.
Images of nickel meshes with 20 μm spacing taken with an X-ray CCD camera with one-dimensional X-ray magnification.